

Electronic Thesis and Dissertation Repository

---

2-17-2021 10:00 AM

## Finite Element Analysis of Buckling Capacity of Conical Steel Tanks Considering Field-measured Initiation Imperfections – A Case Study

Haoyi Zhang, *The University of Western Ontario*

Supervisor: Zhou, Wenxing, *The University of Western Ontario*

Co-Supervisor: El Ansary, Ayman M., *The University of Western Ontario*

A thesis submitted in partial fulfillment of the requirements for the Master of Engineering Science degree in Civil and Environmental Engineering

© Haoyi Zhang 2021

Follow this and additional works at: <https://ir.lib.uwo.ca/etd>



Part of the [Civil Engineering Commons](#)

---

### Recommended Citation

Zhang, Haoyi, "Finite Element Analysis of Buckling Capacity of Conical Steel Tanks Considering Field-measured Initiation Imperfections – A Case Study" (2021). *Electronic Thesis and Dissertation Repository*. 7636.

<https://ir.lib.uwo.ca/etd/7636>

This Dissertation/Thesis is brought to you for free and open access by Scholarship@Western. It has been accepted for inclusion in Electronic Thesis and Dissertation Repository by an authorized administrator of Scholarship@Western. For more information, please contact [wlsadmin@uwo.ca](mailto:wlsadmin@uwo.ca).

## Abstract

The geometric imperfection in elevated steel conical water tanks is a key factor that influences the buckling capacity of the tank. Current considerations of imperfections in the design of conical tanks are based on theoretical analysis, whereby the imperfection shapes and locations are assumed to have the most critical impact on the capacity. This thesis investigates the initial imperfections of an actual stiffened liquid-filled steel conical tank (LFCT) based on high-resolution laser scan measurement data of the tank geometry.

In the first part of this study, detailed analyses of the laser scan data were carried out to extract the global and local initial imperfections of the tank. The global imperfection represents the ovalization of the tank circumferences at difference elevations and shift of the tank central axis from the nominal central axis position. The local imperfection is the difference between the overall and global imperfections. As part of the evaluation of the tank's structural integrity the imperfections extracted from the laser scan data are compared with specified tolerances recorded in design standards (AWWA D100-11; EN 1993-1-6: 2007, etc.) and with theoretical expressions available in the literature. Analysis results have shown that local & total imperfections exceed the tolerances specified in the design standards at several locations on the tank and the discrepancy between the imperfection wavelengths specified in the standards and observed from the data.

In the second part of this study, three-dimensional finite element models of the stiffened conical steel water tank were established. Initial imperfections of various shapes have been incorporated into the models, including patterns extracted from the laser scan data and assumptions from previous studies. Their impacts on the buckling capacity were analyzed by a series of elastoplastic analyses and compared with each other. Conservativeness of assumed imperfection shapes have been verified with more impact than components of field measured imperfections of higher amplitude.

## Keywords

*Liquid-filled conical tanks, Stiffened tanks, Geometric imperfections, Buckling capacity, Global imperfections, Local imperfections, Ovalization, Finite element analysis, Least-square method, Arc-length method.*

## Summary for Lay Audience

Research on imperfect steel water tanks is important since the buckling capacity of these tanks can be significantly reduced with very small imperfections. Previous research and design codes assumed series of critical imperfection shapes which is close to the first buckling mode. However, the effect of imperfections is sensitive to their shapes, which requires deeper study on imperfections measured from real structures. Yet, the study on the geometric imperfections measured from a real liquid-filled conical tank (LFCT) is still lacking with only few investigations on cylindrical oil tanks and silos have been carried out. Geometric imperfections are considered as the critical shape in design standards which leads to conservative approach. To make an improvement, this study provided an investigation on the effect of geometric imperfections on a real LFCT.

The shape and amplitude of imperfections are evaluated in the first part. Geometric imperfections introduced in this study are measured on the exterior surface of a tank, which provided a set of high-resolution laser scan data. According to the consideration of imperfection components in design standards, the entire imperfections can be classified as global imperfections and local imperfections. A series of data analysis including least-square (LSQ) method was employed to decompose the laser scan data into global & local imperfections. Their shape and amplitudes were compared with tolerances in design codes to evaluate the quality of this imperfect tank based on various standards.

The second part employed elastoplastic finite element analyses (FEA) to evaluate the impact on buckling capacity of the tank by various imperfection shapes. This was realized by modelling a full-scale stiffened conical steel water tank with initial imperfections. Several imperfection shapes were applied on the tank including patterns extracted from laser scan data and conservative assumptions from previous studies. It was shown from the results that the conservativeness of assumptions reported in the literature have been confirmed by this experiment, while the effects of global, local and total imperfections from real measurements are complicated.



## **Co-Authorship Statement**

This thesis has been prepared as an integrated-article format stipulated by the Faculty of Graduate Studies at Western University. Chapter 2 and Chapter 3 of the thesis will be submitted to publication. Original data introduced in analysis were provided by Professor Ayman El Ansary. The devise of analyzing procedure, design of experiments, analysis works on data and models, draft writing and edition of this thesis was carried out by the candidate under direct supervision and with the aid from Professor Ayman El Ansary and Wenxing Zhou.

## **Acknowledgements**

I would like to express my great thankfulness and sincere gratitude to my supervisors Prof. Ayman El Ansary and Prof. Wenxing Zhou for providing me this opportunity in starting research works, for their inspiring guidance, warm encouragement, patient instructions and powerful support throughout this research experience. This will be beneficial to me for a lifelong time.

I would like to send deep appreciation to all my friends and colleagues in Western University who accompanied me throughout this study and research experience, providing me delightful times and endless help in all times. I will send my best wishes to them.

I would also like to express my gratitude to the faculty and staff members at Western University for their support and for the great experience provided in this research experience.

Finally, I would like to send my deepest appreciation to my family members, especially my parents. It is their everlasting support and sacrifice that provided me the opportunity to achieve success in the present time. No word and speech can express enough thankfulness to them.

# Table of Contents

|   |     |
|---|-----|
| Abstract.....   | ii  |
| Keywords .....  | iii |
| Summary for Lay Audience .....  | iv  |
| Co-Authorship Statement.....  | v   |
| Acknowledgements.....   | vi  |
| Table of Contents .....   | vii |
| List of Tables.....   | x   |
| List of Figures.....  | xi  |
| Nomenclature.....   | xvi |
| Chapter 1 Introduction .....  | 1   |
| 1.1 Background.....   | 1   |
| 1.2 Research objectives.....  | 4   |
| 1.3 Outline of thesis .....   | 5   |
| 1.4 References.....   | 6   |
| Chapter 2 Analysis of Imperfections in Conical Tanks – A Case Study ..... | 8   |
| 2.1 Background information .....  | 8   |
| 2.1.1 Representative works .....  | 8   |
| 2.1.2 Scopes .....  | 9   |
| 2.2 Specifications from design standards and literatures.....             | 9   |
| 2.3 Introduction of the LFCT in case study .....                          | 16  |
| 2.4 Data processing.....  | 20  |
| 2.4.1 Down-sampling of imperfection data .....                            | 20  |
| 2.4.1.1 Methodology and parameters.....                                   | 20  |
| 2.4.1.2 LSQ fitting with Ellipse .....                                    | 22  |
| 2.4.1.3 Imperfection analysis .....                                       | 28  |
| 2.4.1.4 Imperfection smoothing.....                                       | 38  |
| 2.4.3 Global imperfection .....   | 43  |
| 2.5 Comparison & evaluation .....   | 54  |

|  |     |
|--|-----|
| 2.5.1 Equivalent cylinder .....  | 54  |
| 2.5.2 Evaluation of meridional & circumferential imperfections .....   | 58  |
| 2.5.2.1 Evaluation with specification in AWWA D100-11 .....  | 58  |
| 2.5.2.2 Evaluation with specification in EN 1993-1-6: 2007 .....   | 64  |
| 2.5.2.3 Evaluation with specification in EN 1998-4: 2006.....  | 70  |
| 2.5.2.4 Evaluation with specification by Vandepitte et al. (1982).....   | 76  |
| 2.5.2.5 Evaluation with specification by El Damatty et al. (2001).....   | 81  |
| 2.6 Conclusion .....   | 85  |
| 2.7 References.....  | 87  |
| Chapter 3 Nonlinear Buckling analysis of Stiffened Conical Tanks Considering Various Imperfection Patterns ..... | 90  |
| 3.1 Introduction.....  | 90  |
| 3.2 Imperfection shape specifications.....   | 92  |
| 3.3 Introduction of the case.....  | 94  |
| 3.4 FEM verification.....  | 101 |
| 3.4.1 Introduction.....  | 101 |
| 3.4.2 Mesh sensitivity .....   | 106 |
| 3.5 Plastic deformation analysis .....   | 114 |
| 3.5.1 Introduction.....  | 114 |
| 3.5.2 Mesh sensitivity .....   | 119 |
| 3.6 Imperfection Analysis .....  | 129 |
| 3.6.1 Introduction.....  | 129 |
| 3.6.2 Mesh sensitivity .....   | 131 |
| 3.6.3 Multiple simulation & comparison .....   | 137 |
| 3.7 Conclusion .....   | 139 |
| 3.8 References.....  | 140 |
| Chapter 4 Conclusions .....  | 142 |
| 4.1 Summaries and conclusions.....   | 142 |
| 4.1.1 General.....   | 142 |
| 4.1.2 The evaluation of extracted circumferential & meridional geometric   |     |

|  |     |
|--|-----|
| imperfection shapes from cloud data in amplitude and wavelength.....                                   | 142 |
| 4.1.3 Impact of real & simplified geometrical imperfections on the buckling capacity<br>of a LFCT..... | 143 |
| 4.1.4 Research significance and novelty.....   | 144 |
| 4.2 Recommendations for future work .....  | 145 |
| Appendix.....  | 146 |
| Curriculum Vitae.....  | 205 |

## List of Tables

|   |     |
|---|-----|
| Table 2.1 Specified imperfection tolerance in EN 1993-1-6: 2007 .....                   | 12  |
| Table 2.2 Coefficient value for different construction quality in EN 1998-4: 2006 ..... | 13  |
| Table 2.3 AWWA D100-11 global imperfection tolerance .....                              | 13  |
| Table 2.4 Local imperfection amplitude tolerance in EN 1993-1-6: 2007 .....             | 65  |
| Table 2.5 Imperfection tolerance for EN 1998-4 seismic design.....                      | 70  |
| Table 2.6 Tolerance and assumption by Vandepitte et al. (1982).....                     | 76  |
| Table 3.1 Material properties in verification.....                                      | 103 |
| Table 3.2 Loads on Fredericton tank.....  | 104 |
| Table 3.3 Configurations of model in each step .....                                    | 108 |
| Table 3.4 Verification analysis results for ‘good’ shell .....                          | 110 |
| Table 3.5 Verification analysis results for ‘mediocre’ shell .....                      | 111 |
| Table 3.6 Material properties of FEM model.....   | 115 |
| Table 3.7 Water load applied on FEM model .....   | 118 |
| Table 3.8 Configurations of model in each step .....                                    | 119 |
| Table 3.9 Sensitivity analysis results .....  | 122 |
| Table 3.10 Material properties of FEM model.....  | 129 |
| Table 3.11 Loads applied on FEM model .....   | 131 |
| Table 3.12 Configurations of model in each step .....                                   | 132 |
| Table 3.13 Sensitivity analysis results .....   | 135 |
| Table 3.14 $P_{cr}$ results of FEA.....   | 138 |

## List of Figures

|  |    |
|--|----|
| Figure 2.1 Specified global imperfection in EN 1993-1-6: 2007 .....                                  | 10 |
| Figure 2.2 Specified eccentricities in EN 1993-1-6: 2007 (elevation view).....                       | 11 |
| Figure 2.3 Specified dimple in EN 1993-1-6: 2007.....  | 12 |
| Figure 2.4 Ring stiffener in cylindrical shell by Chen et al. (2001) .....                           | 15 |
| Figure 2.5 Stress resultants between ring pieces by Chen et al. (2001).....                          | 15 |
| Figure 2.6 Photo of a typical elevated combined conical tank in Canada .....                         | 17 |
| Figure 2.7 Elevation view of the studied conical tank.....   | 17 |
| Figure 2.8 Stiffeners configuration of the studied conical tank (top view) .....                     | 18 |
| Figure 2.9 Geometry of stiffeners (elevation view).....  | 18 |
| Figure 2.10 Side view of laser scan cloud data ( $y$ - $z$ plane).....                               | 19 |
| Figure 2.11 Plan view of laser scan cloud data ( $x$ - $y$ plane).....                               | 20 |
| Figure 2.12 Assumed distorted central axis & meridians .....   | 21 |
| Figure 2.13 Side view & plan view of sampling parameters.....  | 22 |
| Figure 2.14 Ellipse for LSQ fitting.....   | 23 |
| Figure 2.15 Calculated $x$ coordinate of deviated central axis.....                                  | 24 |
| Figure 2.16 Calculated $y$ coordinate of deviated central axis.....                                  | 25 |
| Figure 2.17 Calculated inclination angle of fitting ellipses .....                                   | 26 |
| Figure 2.18 Calculated semi-axes length of fitting ellipses.....                                     | 27 |
| Figure 2.19 Selected circumferences layout .....   | 28 |
| Figure 2.20 Coordinate systems employed for sampling procedure & imperfection<br>calculation.....    | 29 |
| Figure 2.21 Radial deviation & perpendicular deviation (geometric imperfections) .....               | 30 |
| Figure 2.22 Calculated circumferential imperfections with $d_i$ of 0.02 - 0.05 m.....                | 32 |
| Figure 2.23 Calculated meridional imperfections with $\theta_i$ of $0.36^\circ$ - $1.44^\circ$ ..... | 35 |
| Figure 2.24 Difference between sampling results with various resolution.....                         | 37 |
| Figure 2.25 Denoised circumferential imperfections.....  | 40 |
| Figure 2.26 Denoised meridional imperfections.....   | 43 |
| Figure 2.27 Difference between nominal radius and calculated semi-axes of fitting ellipse            |    |

|   |    |
|---|----|
| .....   | 44 |
| Figure 2.28 Plan view of ovalization effect on the top of cone (20 times scaled).....   | 45 |
| Figure 2.29 Smoothed profile of global imperfection parameters.....   | 49 |
| Figure 2.30 Meridional global imperfections .....   | 52 |
| Figure 2.31 Circumferential global imperfections (40 times scaled) .....  | 54 |
| Figure 2.32 Contribution of hydrostatic pressure to membrane stress .....   | 56 |
| Figure 2.33 Equivalent cylinders in (a) EN 1993-1-6: 2007; (b) AWWA D100-11 standards<br>.....  | 57 |
| Figure 2.34 Evaluation of local imperfection amplitude with specifications in AWWA<br>D100-11 .....                                     | 61 |
| Figure 2.35 Evaluation of local imperfection wavelength with specifications in AWWA<br>D100-11 .....                                    | 63 |
| Figure 2.36 Evaluation of meridional local imperfection amplitude with specifications in<br>EN 1993-1-6: 2007 .....                     | 67 |
| Figure 2.37 Evaluation of circumferential local imperfection amplitude with<br>specifications in EN 1993-1-6: 2007 .....                | 69 |
| Figure 2.38 Evaluation of total imperfection amplitude with specifications in EN 1998-4:<br>2006.....                                   | 75 |
| Figure 2.39 Evaluation of meridional local imperfection amplitude with specifications by<br>Vandepitte et al. (1982).....               | 78 |
| Figure 2.40 Evaluation of meridional local imperfection wavelength with specifications<br>by Vandepitte et al. (1982).....              | 80 |
| Figure 2.41 Comparison of circumferential local imperfections with specifications by El<br>Damatty et al. (2001) (40 times scaled)..... | 83 |
| Figure 2.42 Evaluation of circumferential local imperfection wavelength with<br>specifications by Vandepitte et al. (1982).....         | 84 |
| Figure 3.1 Imperfection specification by Vandepitte et al. (1982) .....   | 92 |
| Figure 3.2 Circumferential imperfection patterns by El Damatty et al. (2001).....   | 93 |
| Figure 3.3 Elevation view of the tank.....  | 94 |
| Figure 3.4 Stiffeners configuration of the tank (top view) .....  | 95 |



|  |     |
|--|-----|
| Figure 3.5 Stiffener geometry (elevation view).....  | 95  |
| Figure 3.6 Circumferential imperfections from cloud data (40 times scaled).....            | 97  |
| Figure 3.7 Meridional imperfections from cloud data.....                                   | 100 |
| Figure 3.8 Geometry of the Fredericton tank.....   | 102 |
| Figure 3.9 Geometry of SHELL181 element.....   | 103 |
| Figure 3.10 Boundary conditions of verification model.....                                 | 104 |
| Figure 3.11 Geometric imperfections on Fredericton tank.....                               | 105 |
| Figure 3.12 Mesh of perfect Fredericton tank.....  | 106 |
| Figure 3.13 Mesh of imperfect Fredericton tank.....  | 107 |
| Figure 3.14 Generated mesh for the 1 <sup>st</sup> step.....                               | 108 |
| Figure 3.15 Generated mesh for the 4 <sup>th</sup> step.....                               | 109 |
| Figure 3.16 Generated mesh for the 7 <sup>th</sup> step.....                               | 109 |
| Figure 3.17 Verification analysis results $P_{cr}$ and $\sigma_{v,max}$ .....              | 112 |
| Figure 3.18 Difference between steps.....  | 113 |
| Figure 3.19 Load-deflection curve of ‘good’ shell (7 <sup>th</sup> step).....              | 113 |
| Figure 3.20 Load-deflection curve of ‘mediocre’ shell (7 <sup>th</sup> step).....          | 114 |
| Figure 3.21 Bilinear isotropic hardening.....  | 116 |
| Figure 3.22 Boundary conditions.....   | 117 |
| Figure 3.23 Generated mesh for sensitivity analysis (1 <sup>st</sup> step).....            | 120 |
| Figure 3.24 Generated mesh for sensitivity analysis (3 <sup>rd</sup> step).....            | 120 |
| Figure 3.25 Generated mesh for sensitivity analysis (5 <sup>th</sup> step).....            | 121 |
| Figure 3.26 Iterative analysis results.....  | 123 |
| Figure 3.27 Differences between iterative steps.....                                       | 123 |
| Figure 3.28 Residual deformation of El Damatty et al. (2001) ‘good cone’.....              | 125 |
| Figure 3.29 Residual deformation of El Damatty et al. (2001) ‘poor cone’.....              | 126 |
| Figure 3.30 Residual deformation of 100% measured imperfection (500 times scaled)<br>..... | 127 |
| Figure 3.31 Residual deformation of 40% measured imperfection (500 times scaled).          | 128 |
| Figure 3.32 Boundary conditions of the LFCT.....   | 130 |
| Figure 3.33 Generated mesh for the 1 <sup>st</sup> step.....                               | 132 |

|   |     |
|---|-----|
| Figure 3.34 Generated mesh for the 2 <sup>nd</sup> step.....  | 133 |
| Figure 3.35 Generated mesh for the 3 <sup>rd</sup> step .....   | 133 |
| Figure 3.36 Generated mesh for the 4 <sup>th</sup> step .....   | 134 |
| Figure 3.37 Generated mesh for the 5 <sup>th</sup> step .....   | 134 |
| Figure 3.38 Sensitivity analysis results.....   | 136 |
| Figure 3.39 Differences between steps .....   | 137 |
| Figure A.1 Calculated circumferential imperfections with $d_i$ of 0.02 - 0.05 m .....   | 148 |
| Figure A.2 Calculated meridional imperfections with $\theta_i$ of 0.36° - 1.44° .....   | 152 |
| Figure A.3 Denoised circumferential imperfections .....   | 155 |
| Figure A.4 Denoised meridional imperfections .....  | 159 |
| Figure A.5 Meridional global imperfections.....   | 163 |
| Figure A.6 Circumferential global imperfections (40 times scaled).....  | 166 |
| Figure A.7 Evaluation of local imperfection amplitude with specifications in AWWA<br>D100-11 .....                                      | 170 |
| Figure A.8 Evaluation of local imperfection wavelength with specifications in AWWA<br>D100-11 .....                                     | 172 |
| Figure A.9 Evaluation of meridional local imperfection amplitude with specifications in<br>EN 1993-1-6: 2007 .....                      | 176 |
| Figure A.10 Evaluation of circumferential local imperfection amplitude with<br>specifications in EN 1993-1-6: 2007 .....                | 179 |
| Figure A.11 Evaluation of total imperfection amplitude with specifications in EN 1998-4:<br>2006.....                                   | 186 |
| Figure A.12 Evaluation of meridional local imperfection amplitude with specifications by<br>Vandepitte et al. (1982).....               | 190 |
| Figure A.13 Evaluation of meridional local imperfection wavelength with specifications<br>by Vandepitte et al. (1982).....              | 192 |
| Figure A.14 Comparison of circumferential local imperfections with specifications by El<br>Damatty et al. (2001) (40 times scaled)..... | 195 |
| Figure A.15 Evaluation of circumferential local imperfection wavelength with<br>specifications by Vandepitte et al. (1982).....         | 197 |

|   |     |
|---|-----|
| Figure A.16 Circumferential imperfections from cloud data (40 times scaled) ..... | 200 |
| Figure A.17 Meridional imperfections from cloud data .....                        | 204 |

## Nomenclature

|                   |   |
|-------------------|---|
| $\delta$          | geometric imperfection amplitude                          |
| $\delta_{global}$ | global imperfection amplitude                             |
| $\delta_{local}$  | Local imperfection amplitude                              |
| $U_r$             | Global imperfection coefficient                           |
| $d_{max}$         | maximum internal diameter of tank                         |
| $d_{min}$         | minimum internal diameter of tank                         |
| $d_{nom}$         | nominal internal diameter                                 |
| $e_a$             | actual eccentricity                                       |
| $e_{tot}$         | the eccentricity between middle surfaces of joined plates |
| $e_{int}$         | intended offset between middle surfaces of joined plates  |
| $U_e$             | eccentricity parameter                                    |
| $t$               | shell thickness   |
| $t_{min}$         | minimum shell thickness at the weld                       |
| $R$               | tank radius   |
| $R_b$             | radius at the tank base                                   |
| $l$               | meridional length   |
| $l_{gx}$          | gauge length for meridional imperfections                 |
| $l_{g\theta}$     | gauge length for circumferential imperfections            |
| $l_{gw}$          | gauge length across welds                                 |

|               |  |
|---------------|--|
| $U_{0x}$      | local dimple parameters on meridians   |
| $U_{0\theta}$ | local dimple parameters on circumferences  |
| $U_{0w}$      | local dimple parameters on welds   |
| $a$           | construction quality coefficient   |
| $\theta_v$    | angle between tank wall and vertical direction                                   |
| $s$           | distance measured on a generator of tank   |
| $\delta_0$    | geometric imperfection amplitude   |
| $\theta$      | angular coordinate measured from the center of circumference                     |
| $l_b$         | imperfection wavelength  |
| $n$           | circumferential wavenumber<br>number of data points on a imperfection curve      |
| $N$           | total number of longitudinal stiffeners<br>harmonic number                       |
| $l_{ei}$      | elastic effective length   |
| $\lambda_i$   | half wavelength of meridional bending  |
| $D_i$         | shell flexural rigidity  |
| $M_i$         | bending moment per unit circumference between the ring and the $i$ th shell part |
| $Q_i$         | shear force per unit circumference between the ring and the $i$ th shell part    |
| $w_r$         | radial displacement at the centroid of ring stiffener                            |
| $\phi_r$      | rotation angle of ring stiffener about circumference                             |
| $O_i$         | origin of cylindrical coordinate system  |
| $d_i$         | height extent of sampling area   |

|                      |  |
|----------------------|--|
| $l_i$                | arc length of sampling area  |
| $h_i$                | Elevation of the center of sampling area                           |
| $\theta_k$           | angular coordinate of data point                                   |
| $\rho_k$             | radial coordinate of data point                                    |
| $z_k$                | vertical coordinate of data point                                  |
| $x_0$                | $x$ coordinate of ellipse center                                   |
| $y_0$                | $y$ coordinate of ellipse center                                   |
| $A$                  | length of semi-axis A  |
| $B$                  | length of semi-axis B  |
| $\theta'$            | angular coordinate on global cylindrical coordinate system         |
| $\rho'$              | radial coordinate on global cylindrical coordinate system          |
| $\rho_{nom}$         | radius of nominal circumference                                    |
| $\delta_p$           | perpendicular imperfections  |
| $\delta_r$           | radial deviation   |
| $\theta'$            | angular range of sampling  |
| $\delta(d, \theta)$  | discrete imperfection amplitude function at given circumference    |
| $\delta(\theta', L)$ | discrete imperfection amplitude function at given circumference    |
| $\eta_c$             | ratio of total difference between circumferential sampling results |
| $\eta_m$             | ratio of total difference between circumferential sampling results |
| $L$                  | meridional length  |

|                      |  |
|----------------------|--|
| $\Delta_x$           | translations along $x$ direction<br>deformation along $x$ direction                      |
| $\Delta_y$           | translations along $y$ direction<br>deformation along $y$ direction                      |
| $\Delta_z$           | translations along $z$ direction<br>deformation along $z$ direction                      |
| $\delta_x$           | translations along $x$ direction   |
| $\delta_y$           | translations along $y$ direction   |
| $\delta_z$           | translations along $z$ direction   |
| $\theta_x$           | rotations around $x$ axis  |
| $\theta_y$           | rotations around $y$ axis  |
| $\theta_z$           | rotations around $z$ axis  |
| $E$                  | Young's modulus  |
| $E_T$                | tangent modulus  |
| $\mu$                | Poisson's ratio  |
| $\sigma_{yt}$        | tensile yield strength   |
| $\sigma_{yc}$        | compressive yield strength   |
| $\sigma_u$           | ultimate strength  |
| $\varepsilon$        | engineering strain   |
| $g$                  | gravitational acceleration   |
| $H$                  | depth from the free surface of hydrostatic pressure<br>total height of the conical shell |
| $\Delta_{total}$     | total deformation  |
| $\Delta_{total,max}$ | maximum total deformation  |

|                  |   |
|------------------|---|
| $\sigma_{v,max}$ | maximum von Mises equivalent stress     |
| $P_{cr}$         | critical load factor                    |
| $R_{eq}$         | radius of the equivalent cylinder       |
| $H_{eq}$         | total height of the equivalent cylinder |
| $\Delta$         | deviation of radius from ovalization    |
| $\varphi$        | inclination angle of ellipse            |
| $l_m$            | meridional imperfection wavelength      |
| $l_c$            | circumferential imperfection wavelength |
| $\rho$           | fluid density                           |



# Chapter 1 Introduction

## 1.1 Background

Storage tanks are widely used as containers of mass materials for industrial and civilian use. As an essential kind of facility in disposing considerable amount of necessities, fabrication techniques and construction materials has been continuously evolving. Regardless of certain chemical contact tanks, where polymer like polyethylene is often employed for construction, steel and reinforced concrete tanks are two main options. The former takes most advantage of lower initial investment while the latter could be more cost effective when calculating life cycle expenses (leakage, deterioration, and recyclability, etc.). Steel tanks are often selected for water storage. Because of less need of precaution comparing to high-risk environment such as gas storage where the tanks are often built underground, water tanks are frequently designed in a high elevation to utilize gravity as a source of transmission pressure. Two types of structures are representative for such: liquid-filled cylindrical and conical tanks.

According to the steel water tank design standards published by the American Water Works Association (AWWA), loads from multiple sources are required to be considered in the design process of elevated steel tanks. Apart from situations where the structure is put into service, it is possible for additional structures to be added on top for the advantage of elevation. For example, an antenna might be supported on the roof of an elevated tank, where its self-weight is dispersed through the roof. The circumference of the roof is attached to the main vessel which usually has a cylindrical or conical shape. At the joint, the extra roof load is transferred to the vessel below causing additional meridional stresses to those developed due to hydrostatic pressure. These meridional stresses reach maximum value close to the base of the tank vessel where it is usually the most critical part susceptible to elastic or inelastic buckling of the shell. Consequently, any add-on structures should be considered as superimposed load to guide the design process or the retrofit after years of usage. The shape of tanks is also an essential factor for capacity. In cylindrical shells, meridional compressive stress is mostly contributed from roof loads, while in conical shells, another contribution is from hydrostatic pressure. This

makes it easier to buckle under excessive loads and is easily affected by the base radius and wall inclination in case of conical shape tanks.

The first event evoking attention to buckling problem on imperfect liquid-filled steel tanks occurred in Seneffe, Belgium in 1972. An elevated conical water tank of 1500 m<sup>3</sup> capacity collapsed suddenly when it was filled with water for the first time. The water surface was 1.74m below the overflow level when the failure was initiated by buckling at the bottom of the vessel. In 1977, a research group at Gent university started to investigate the mechanism of this failure. Vandepitte et al. (1982) employed hundreds of small-scale models made of various materials in buckling tests for hydrostatically loaded conical shells. A series of design equations was then proposed by Vandepitte et al. (1982) based on these experimental investigations and were adopted as references by The European Recommendations of Steel Construction (ECCS) for its third edition published in 1984. The influence of geometric imperfections was noticed in studies by Vandepitte et al. since experiments showed a significant impact on the buckling capacity of conical shells, especially for those close to the bottom of the cone, where it is the most critical location. Vandepitte et al. (1982) made a conservative assumption in their design approach considering axisymmetric sinusoidal imperfections along tank generators. Such type of geometric imperfection is considered as the most critical since it usually conforms the first buckling mode of a perfect conical tank.

Another important event happened in Dec 19<sup>th</sup>, 1990. A conical steel tank located in Fredericton, Canada, dramatically collapsed after being filled up to its capacity with water. Reports were soon been implemented after the incident (Korol 1991; Dawe et al. 1993). Vandepitte et al. (1992) also did the investigation following the request from International Specialized Risk Management (I.S.R.M.) Ltd. A series of tests was done by the laboratory at Ghent University as data support. In those experiments, numerical models were used to simulate the Fredericton's tank with geometrical imperfections. Similar to research of Belgium tank, axisymmetric imperfections in sine wave mode were employed as the assumed shape. Researchers managed to obtain the buckling capacity of imperfect tanks having various conditions by changing the amplitude and location of imperfections. The reason of collapse was attributed to the inadequate wall thickness near the bottom of the steel vessel. Vandepitte et al. (1992) found that the standard used for design (AWWA D100, 1984 edition) involved neither the concern of

shell buckling nor the limit of geometrical imperfections despite the recommendation in ECCS standard (1984 edition).

El Damatty et al. (1997) started a series of studies on the stability of hydrostatically loaded conical tanks, following research works done on the case of Fredericton tank. Tests on elastic stability were conducted by El Damatty et al. (1997) using finite element analysis where axisymmetric geometric imperfections are simulated following Vandepitte's (1982) assumption. The imperfection pattern along circumferences is assumed also as a harmonic wave superimposed on meridional imperfections. In another test on inelastic stability of the tank, El Damatty et al. (1998) employed a more complicated imperfection pattern referring to recorded measurements in an aerospace engineering data bank. Result of these works that geometrical imperfections have a large impact on buckling capacity of liquid-filled conical tanks (LFCT) and axisymmetric shape around the tank is found to be the most critical for meridian imperfections. El Damatty et al. (1999) proposed a simple design procedure involving conservative assumptions based on works above. This aimed at providing an alternative to the complex nonlinear analysis approach in the widely used AWWA D100 design standard (1984 edition). It was further extended by El Damatty et al. (2001) for designing new stiffened tanks or adding stiffeners to old ones as retrofit. The referenced work (El Damatty et al. 2001) on the behavior of stiffened LFCT presented a new assumption of circumferential imperfection pattern with evenly spaced longitudinal stiffeners, where it is specified as a harmonic wave with a half wavelength equals the space between stiffeners.

It is already known that this popular usage of a harmonic wave on simulating geometric imperfections will for sure be conservative in designing and analyzing LFCT (El Damatty et al. 1997). This simplicity and conservativeness are sometimes just the aim of researchers (El Damatty et al. 1997), while sometimes it results from the limit of technique (Vandepitte et al. 1991). As the development of computing and analyzing tools nowadays, it is possible to investigate the effect and details of true imperfections or make it clear how far it is from the assumptions. Geometric imperfections appear largely during constructions, differences in fabrication techniques makes the pattern irreplaceable for certain type of structures. However, few studies have been done to investigate detailed conditions in real cases and examined them with simplified assumptions. As one of the most related works, Hornung et al. (2002)

investigated the buckling phenomenon of imperfect cylindrical tanks with both real buckling tests and numerical finite element analysis (FEA). Measured imperfections are evaluated with design standards and compared with eigenmode-shape imperfections. Another important investigation was done by Rotter et al. (1992) on geometrical imperfections of a cylinder metal silo. The main work conducted by Rotter et al. (1992) is numerical investigation with Fourier analysis on measurements. A few features are found from the results and utilized in later research works (de Paor et al. 2012; Kameshwar et al. 2016) for simulating imperfections on cylindrical shells.

Given the existing investigations in the body of the literature, no study has been done on measured imperfections in case of LFCT. Most design standards and research works are still employing conservative assumptions of imperfection patterns. Due to the difference in shapes, working environments and fabrication processes, conclusions from previous works on cylindrical shells are not applicable. Hence, it is indispensable to have a study for the measured imperfection from real conical tanks.

## **1.2 Research objectives**

This study is mainly based on considering an existing imperfect stiffened steel tank, as a case study, where laser scan data and nonlinear buckling analysis have been utilized to achieve the main objectives listed later. As the first research on a real measurement of geometrical imperfections from an elevated steel conical tank, this paper aims to: 1) Compare the measured imperfection data with assumptions and criteria from design standards and previous studies available in the literature to evaluate the condition and quality of the tank 2) Acquire the impact of considering the effect of actual imperfections on the tank's buckling capacity and compare it with predictions from previous studies and design standards. Considering specifications of imperfection types and patterns in design standards, the raw data is processed in order to obtain the comparative imperfection components for evaluation.

In the nonlinear buckling analysis, using the finite element method (FEM), imperfections are simulated following simplified assumptions following design standards provisions, and real measurements from the studied tank. The comparison between results helps in assessing the

adequacy of classification and assumptions provided in design standards.

### **1.3 Outline of thesis**

This thesis has been prepared in an “Integrated-Article” format. There are four chapters in this thesis. The four chapters cover the required background information on this field of research, gaps in literature, the proposed methodology to address these gaps, main findings, conclusions, and future recommendations.

All tabulated data, mathematical derivations and computer codes utilized in the work will be presented as annexes at the end of this thesis.

#### **Chapter 2**

This chapter aims at numerical analysis on measured imperfection from a real case. A series of decomposition process has been done on the cloud data with reference to classification of geometrical imperfections in AWWA and ECCS design standards. Global & local imperfection components are extracted as with least-square fitting (LSQ) approach. The properties of each component are investigated and compared with multiple tolerances. Based on the results, evaluations of the tank condition in this case are presented and utilized for directions of following analysis.

#### **Chapter 3**

The objective of this chapter is to evaluate the conservativeness of the assumed simple geometric imperfection shape reported in literatures by utilizing nonlinear FEM analysis. Mesh quality in the model is determined from convergence analysis. The FEA technique utilized by the author is verified by similar results from a repeated representative experiment from a previous work. Plastic deformation is examined, and the effect of previous assumptions and measured imperfections are analyzed. Conclusions of this chapter are obtained based on comparison between results.

## 1.4 References

D100-84: AWWA Standard for Welded Carbon Steel Tanks for Water Storage. (1984). American Water Works Association, Denver, Colorado.

AWWA D100-11 Welded Carbon Steel Tanks for Water Storage. (2011). American Water Works Association, Denver, Colorado.

Dawe J. L., Seah C. K., Abdel-Zahr A. K. (1993). "Investigation of the Regent Street Water Tower Collapse." *Management & Operations, AWWA Journal*, 34-47.

de Paor C., Cronin K., Gleeson J. P., Kelliher D. (2012). "Statistical characterization and modelling of random geometric imperfections in cylindrical shells." *Thin-Walled Structures*, Volume 58, 9–17.

El Damatty A. A., Korol R. M., Mirza F. A. (1997a). "Stability of imperfect steel conical tanks under hydrostatic loading." *Journal of Structural Engineering*, Volume 123, Issue 6, 703–712.

El Damatty, A. A., El-Attar, M., and Korol, R. M. (1998). "Inelastic stability of conical tanks." *Thin-Walled Structures*, Volume 31, 343–359.

El Damatty, A. A., El-Attar, M., Korol, R. M. (1999). "Simple Design Procedure for Liquid-Filled Steel Conical Tanks." *Journal of Structural Engineering*, Volume 125, No. 8, 879-890.

El Damatty A. A., Marroquin E. G., El Attar M. (2001). "Behavior of stiffened liquid-filled conical tanks." *Thin-Walled Structures*, Volume 39, 353–373.

European Recommendations for Steel Construction: Buckling of Shells. (1984). European Convention for Constructional Steelwork, 3rd edition, Brussels.

Hornung U., Saal H. (2002). “Buckling loads of tank shells with imperfections.” *International Journal of Nonlinear Mechanics*, Volume 37, 605–621.

Kameshwar S., Padgett J. E. (2016). “Stochastic Modeling of Geometric Imperfections in Aboveground Storage Tanks for Probabilistic Buckling Capacity Estimation.” *ASCE-ASME Journal of Risk and Uncertainty in Engineering Systems, Part A: Civil Engineering*, Volume 2, Issue 2, C4015005.

Korol R. M. (1991). “An assessment of Fredericton’s regent steel tower reservoir failure. Technical Report.” McMaster University, Hamilton, Canada.

Teng J. G., Lin X., Rotter J. M., Ding X. L. (2005). “Analysis of geometric imperfections in full-scale welded steel silos.” *Engineering Structures*, Volume 27, Issue 6, 938-950.

Vandepitte D., Rathe J., Verhegghe B., Paridaens R., Verschaeve C. (1982). “Experimental investigation of hydrostatically loaded conical shells and practical evaluation of the buckling load.” In: Ramm E. (ed.) *Buckling of shells*, Springer-Verlag KG, Berlin, Germany, 375-399.

Vandepitte D. (1992). “Report about the failure of a water tower, Fredericton, New Brunswick.” *Technical Report*, Ghent University, Ghent, Belgium.

# Chapter 2 Analysis of Imperfections in Conical Tanks – A Case Study

## 2.1 Background information

### 2.1.1 Representative works

The measurement and analysis of geometric imperfections on shell structures has accumulated data records for more than 50 years. Early investigations put the focus on the area where highly precise tolerances are required, such as aerospace engineering. Arbocz et al. (1964, 1977) conducted several surveys of imperfections on cylindrical shells and helped collecting imperfection data bank in TU Delft. However, in the structural engineering field, few studies have been reported concerning the imperfection measurements on shell structures such as silos and liquid tanks. To the best of the author's knowledge, no investigations of imperfections on LFCT have been reported in the literature.

Hornung et al. (2002) presented a series of investigation of four cylindrical oil tanks with diameters ranging from 10 m to 70 m. Geometric imperfections are measured from the inside surface, and the result shows that some imperfections on the shell are far greater than the tolerance specified in European codes for shell structures: prENV1993-1-6 (1999) and prENV1993-4-2 (1999). Another important investigation was carried out by Rotter et al. (2005) who studied the geometrical imperfections of a cylinder metal silo in Port Kembla, Australia. In Rotter's work, a set of measured data points representing silo surface were fitted first with a perfect 'reference cylinder' where the geometric imperfection can be extracted more precisely. Rotter et al. utilized 2D Fourier series to simulate the data. Results showed that axisymmetric deviations and ovalization are still dominant in the extracted imperfections despite much effect from global deviation have been considered. This leads to a gathering of large-wavelength-and-high-amplitude components in the result of Fourier analysis. Also, a few components were found in the imperfections with the wavelength close to multiples of distances between weld joints and the panel size.

As to imperfection study on LFCT, Vandepitte et al. (1982) introduced an assumption of



axisymmetric sinewave meridional imperfections in his work. Based on imperfection amplitude, the tank quality is classified as ‘good cone’ or ‘poor cone’. Similar imperfection pattern was employed in later research works (El Damatty et al. 1997, 1998; Hafeez et al. 2010) and was extended by combining circumferential imperfection patterns on stiffened tanks. Up to now, applied geometric imperfection shapes on LFCT are all assumed as axisymmetric pattern in of design codes and literatures. A deep study of real imperfection in LFCT is essential.

### 2.1.2 Scopes

Laser scan cloud data are obtained from an existing LFCT in Ontario, Canada and provided to the present study. This provides an opportunity to evaluate the geometric imperfections of LCFT from the laser scan data and shed light on the magnitude of the imperfections in comparison to the imperfection tolerances prescribed in the design codes as well as recommended in the literature (Vandepitte et al. 1982; El Damatty et al. 1997, 2001). This is the objective of the study reported in Chapter 2. Section 2.2 introduces specifications of imperfection tolerance in several widely used design standards and previous studies reported in literatures. Section 2.3 describes the general information of the LFCT considered in the present study including the geometry of the LCFT and properties of the laser scan cloud data. Section 2.4 describes the analyses carried out to evaluate the geometric imperfections on the LFCT based on the laser scan data. The comparison between the extracted imperfection and those specified in the design standards is included in Section 2.5, followed by conclusions in Section 2.6.

## 2.2 Specifications from design standards and literatures

Geometric imperfections ( $\delta$ ) are generally considered as the combination of global imperfections ( $\delta_{global}$ ) and local imperfections ( $\delta_{local}$ ).

$$\delta = \delta_{global} + \delta_{local} \quad (2 - 1)$$

According to Eurocode 3 - Design of Steel Structures – Part 1-6: Strength and Stability for Shell Structures (EN 1993-1-6: 2007), geometric imperfections on shells should be within the tolerance for the limit state design for buckling. The same requirement is also applied in

Eurocode 3 - Design of Steel Structures – Part 4-2: Tanks (EN 1993-4-2: 2007) for design consideration. Three types of imperfection are considered: out of roundness as global imperfections, eccentricities (deviation from middle surfaces) and dimples as local imperfections. Parameters are calculated based on measured imperfections and evaluated according to the requirement in different fabrication quality class.

The out-of-roundness in EN 1993-1-6: 2007 is assessed by a coefficient  $U_r$ , which is calculated as a ratio of radius difference shown in Figure 2.1.

$$U_r = \frac{d_{\max} - d_{\min}}{d_{\text{nom}}} \quad (2 - 2)$$

Where:

$d_{\max}$  : maximum internal diameter.

$d_{\min}$  : minimum internal diameter.

$d_{\text{nom}}$  : nominal internal diameter.

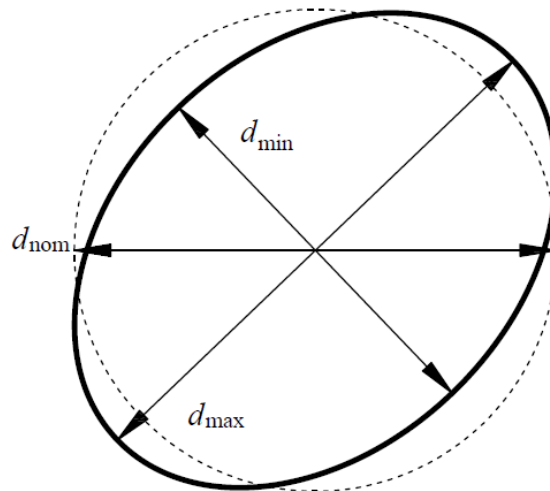


**Figure 0.1 Specified global imperfection in EN 1993-1-6: 2007**

Eccentricities are evaluated with parameters  $e_a$  and  $U_e$ . Parameters are illustrated in Figure 2.2.

$$e_a = e_{\text{tot}} - e_{\text{int}} \quad (2 - 3)$$

$$U_e = \frac{e_a}{t_{\text{av}}} \quad (2 - 4)$$

Where:

$e_{\text{tot}}$  : the eccentricity between middle surfaces of joined plates.

$e_{\text{int}}$  : intended offset between middle surfaces of joined plates.

$t_{\text{av}}$  : average thickness of plates at joint.

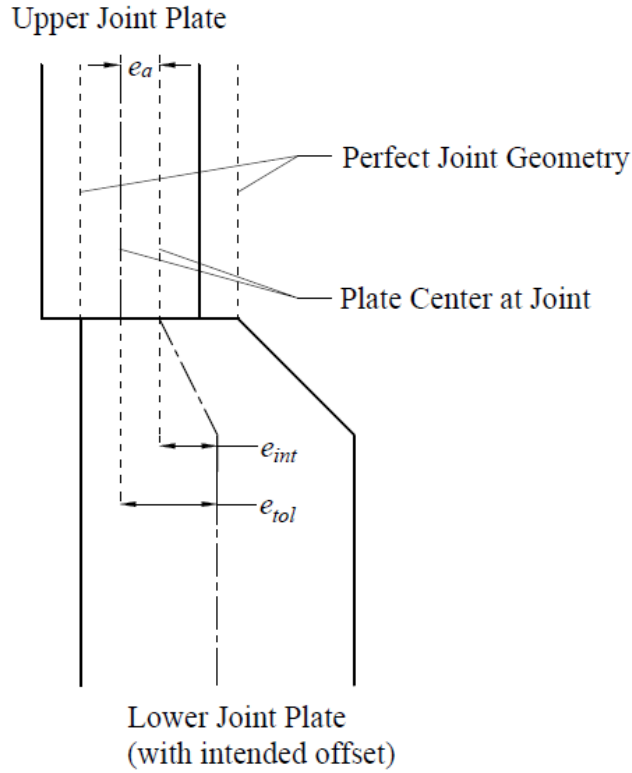


**Figure 0.2 Specified eccentricities in EN 1993-1-6: 2007 (elevation view)**

According to EN 1993-1-6: 2007, dimples are measured with a gauge and evaluated with parameter  $U_{0,max}$ . Parameters are shown in Figure 2.3.

$$U_{0,max} = (U_{0x}, U_{0\theta}, U_{0w})_{max} \quad (2-5)$$

$$l_{gx} = 4\sqrt{Rt} \quad (2-6)$$

$$l_{g\theta} = 2.3(l^2Rt)^{0.25} \leq R \quad (2-7)$$

$$l_{gw} = 25t_{min} \leq 500 \text{ mm} \quad (2-8)$$

$$U_{0x} = \frac{\delta}{l_{gx}} \quad (2-9)$$

$$U_{0\theta} = \frac{\delta}{l_{gx}} \quad (2-10)$$

$$U_{0w} = \frac{\delta}{l_{gx}} \quad (2-11)$$

Where:

$t$  : shell thickness.

$t_{\min}$  : minimum shell thickness at the weld.

$\delta$  : imperfection amplitude.

$R$  : tank radius.

$l$  : meridional length.

$l_{gx}$  : gauge length for meridional imperfections.

$l_{g\theta}$  : gauge length for circumferential imperfections.

$l_{gw}$  : gauge length across welds.

$U_{0x}, U_{0\theta}, U_{0w}$ : dimple parameters.

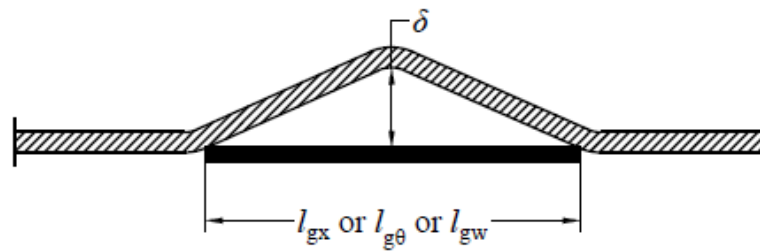


**Figure 0.3 Specified dimple in EN 1993-1-6: 2007**

**Table 0.1 Specified imperfection tolerance in EN 1993-1-6: 2007**

| Fabrication Quality Class | $U_r$ ( $d \geq 1.25m$ ) | $e_a$ | $U_e$ | $U_{0,max}$ |
|---------------------------|--------------------------|-------|-------|-------------|
| Class A (Excellent)       | 0.007                    | 2 mm  | 0.14  | 0.006       |
| Class B (High)            | 0.010                    | 3 mm  | 0.20  | 0.010       |
| Class C (Normal)          | 0.015                    | 4 mm  | 0.20  | 0.016       |

Eurocode 8 - Design of Structures for Earthquake Resistance - Part 4: Silos, Tanks and Pipelines (EN 1998-4: 2006) provides a further consideration for seismic design for tanks. To prevent the tank from elastic buckling, a tolerance is presented as the overall acceptable amplitude for geometric imperfections:

$$\frac{\delta}{t} = \frac{0.06}{a} \sqrt{\frac{R}{t}} \quad (2 - 12)$$

The imperfection amplitude  $\delta$  refers to a specification in the work by Priestley et al. (1986) on seismic design: ‘Radial errors in wall position’. Therefore, overall effects of global and local imperfections shall be included for evaluation.

The value of the coefficient  $a$  depends on the construction quality, as shown in Table 2.2:

**Table 0.2 Coefficient value for different construction quality in EN 1998-4: 2006**

| Construction Qualities         | $a$ |
|--------------------------------|-----|
| Normal Construction            | 1   |
| Quality Construction           | 1.5 |
| Very High-Quality Construction | 2.5 |

In the standards from American Water Works Association (AWWA D100-11), deviations from theoretical shapes are considered as two types: deviations from roundness (global imperfections) and deviations measured along meridians (local imperfections). The tolerance for the global imperfection is expressed as the tolerance for the tank radius measured at the elevation of 0.3 m as detailed in Table 2.3.

**Table 0.3 AWWA D100-11 global imperfection tolerance**

| Diameter Max (m) | Radius Tolerance (mm) |
|------------------|-----------------------|
| 12.2             | ±13                   |
| 45.7             | ±19                   |
| < 76.2           | ±25                   |
| ≥ 76.2           | ±32                   |

Limitations of local imperfections are involved in the most complex design approach for designing steel water tanks, where critical buckling stress is determined by either nonlinear buckling analysis or a set of design equations. Initial geometric imperfections are introduced in the model to acquire precise results. Considering local deviation from theoretical shape during tank assembly, a tolerance is given as:

$$\delta = 0.04\sqrt{Rt} \quad (2 - 13)$$

The shape of local imperfection is assumed to be sinusoidal with a wavelength of  $4\sqrt{Rt}$ . The value of the coefficient representing elastic buckling effect changes for various imperfection amplitudes. The calculated critical buckling stress decreases as a result of larger local deviations.

Several specifications on imperfection shape and amplitude have also been reported in literatures. Based on a series of analyses with small scale models, Vandepitte et al. (1982)

proposed an expression of buckling wavelength  $L_b$  of conical tank on meridians. In Vandepitte's assumption, the quality of tank can be classified into 'good cone' and 'poor cone', corresponding to local imperfection amplitude at 0.8% and 2% of half buckling wavelength.

$$L_b = 3.6 \sqrt{\frac{R_b t}{\cos \theta_v}} \quad (2 - 14)$$

Where:

$R_b$  : radius at the tank base.

$\theta_v$  : angle between tank wall and vertical direction.

El Damatty et al. (1997) proposed a description of geometrical imperfections as the superimposed pattern on Vandepitte's assumption in order to simulate complicated imperfection shape in real tanks:

$$\delta(s, \theta) = \delta_0 \sin\left(\frac{2\pi s}{l_b}\right) \cos(n\theta) \quad (2 - 15)$$

Where:

$\delta_0$  : imperfection amplitude.

$s$  : distance measured on a generator of tank.

$l_b$  : imperfection wavelength specified by Vandepitte et al. (1982).

$\theta$  : angular coordinate measured from the center of circumference.

$n$  : circumferential wavenumber.

As a consideration for conservative design, circumferential pattern is also determined as symmetrical to provide the most critical scenario. This description is further extended by El Damatty et al. (2001) for simulating geometrical imperfections in a stiffened tank. Longitudinal stiffeners can have a large influence on circumferential pattern. In the new specification (El Damatty et al. 2001), the wave number  $n$  in Eq. 2-15 is determined as half of the total number of evenly spaced longitudinal stiffeners  $N$ .

$$\delta(s, \theta) = \delta_0 \sin\left(\frac{2\pi s}{l_b}\right) \cos\left(\frac{N}{2}\theta\right) \quad (2 - 16)$$

Another specification was proposed by Chen et al. (2001) on the imperfections shape of cylindrical shell near the ring stiffeners (Figure 2.4).

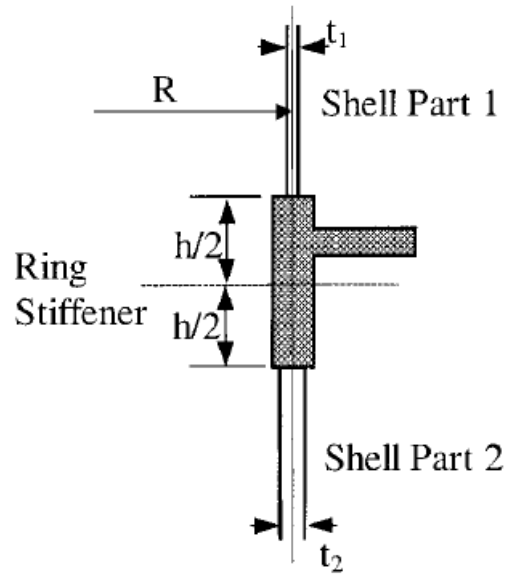


**Figure 0.4 Ring stiffener in cylindrical shell by Chen et al. (2001)**

The imperfection amplitude  $\delta$  for  $i^{\text{th}}$  shell part along the distance  $z_i$  can be calculated with stress resultants between ring pieces shown in Figure 2.5:

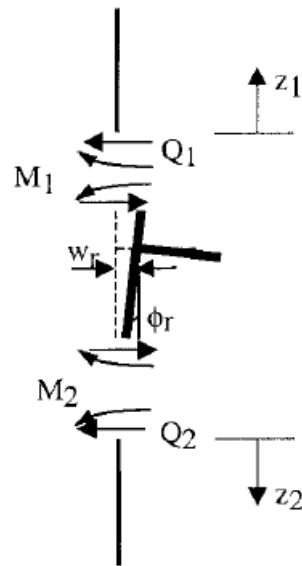


**Figure 0.5 Stress resultants between ring pieces by Chen et al. (2001)**

$$\delta_i(z_i) = \frac{l_{ei}^3}{2D_i} \left[ Q_i \cos \frac{z_i}{l_{ei}} - \frac{M_i}{l_{ei}} \left( \cos \frac{z_i}{l_{ei}} - \sin \frac{z_i}{l_{ei}} \right) \right] e^{-\frac{z_i}{l_{ei}}} \quad (2-17)$$

$$M_i = \frac{2D_i}{l_{ei}^2} \left[ w_r + (2i-3)\phi_r \left( \frac{h}{2} + l_{ei} \right) \right] \quad (2-18)$$

$$Q_i = -\frac{2D_i}{l_{ei}^3} [2w_r + (2i-3)\phi_r(h + l_{ei})] \quad (2-19)$$

$$l_{ei} = \frac{\lambda_i}{\pi} \quad (2-20)$$

$$\lambda_i = \frac{\pi \sqrt{Rt_i}}{[3(1-\nu^2)]^{\frac{1}{4}}} \quad (2-21)$$

$$D_i = \frac{Et_i^3}{12(1-\nu^2)} \quad (2-22)$$

Where:

$l_{ei}$  : elastic effective length.

$\lambda_i$  : half wavelength of meridional bending.

$D_i$  : shell flexural rigidity.

$M_i$  : bending moment per unit circumference between the ring and the  $i$ th shell part.

$Q_i$  : shear force per unit circumference between the ring and the  $i$ th shell part.

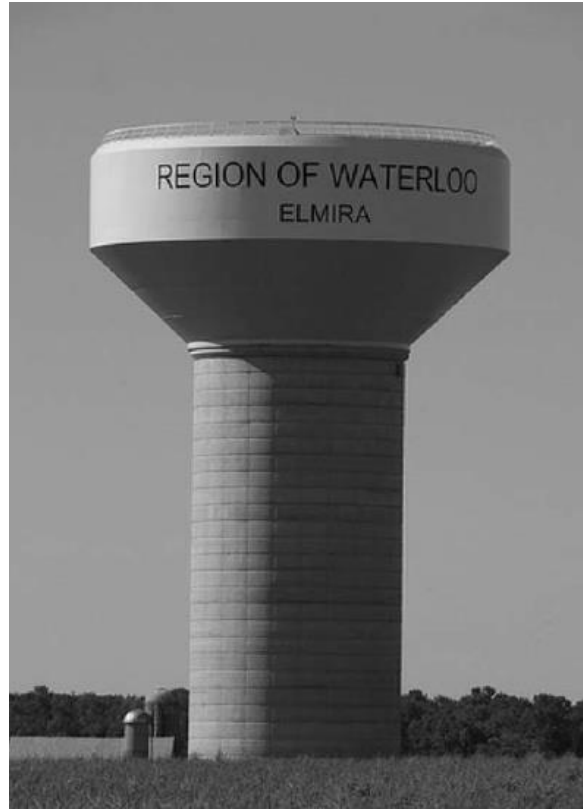
$w_r$  : radial displacement at the centroid of ring stiffener.

$\phi_r$  : rotation angle of ring stiffener about circumference.

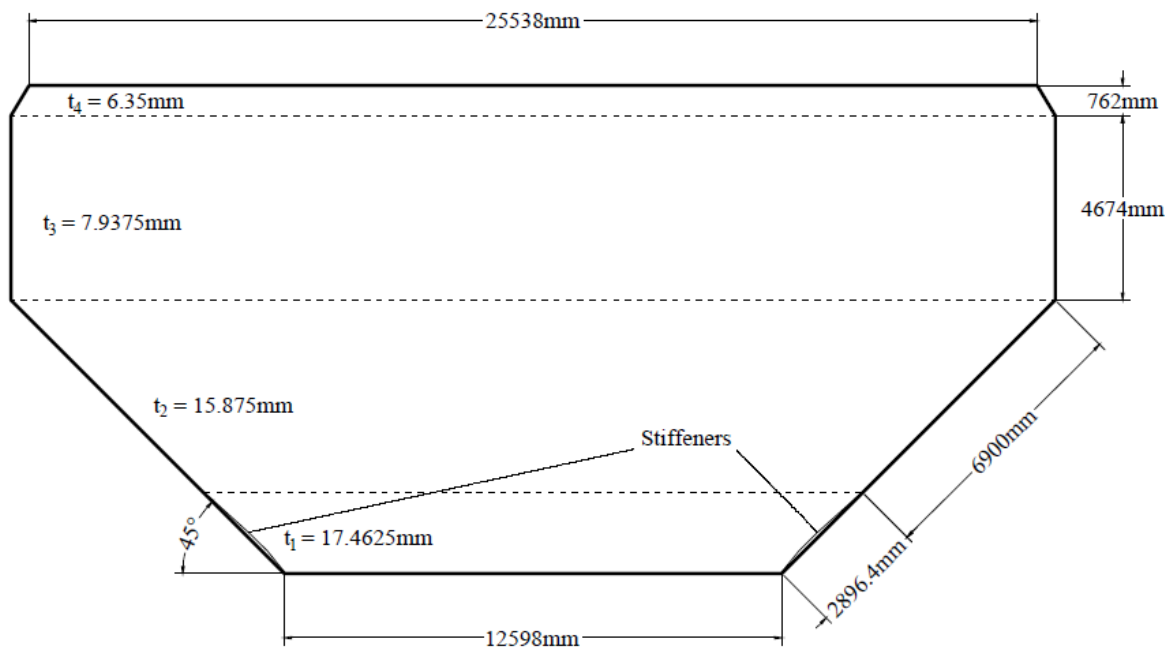
### 2.3 Introduction of the LFCT in case study

Figure 2.6 shows the appearance of a real elevated conical tank. In this study, a stiffened liquid-filled steel conical tank has been considered as a case. The nominal geometry is shown in Figure 2.7, 2.8 and 2.9. This elevated water tank has been in service for many years. It is combined with a conical bottom sitting on the concrete shaft (not shown in Figure 2.7) and a cylinder cap. A total of 48 stiffeners are distributed evenly around the tank circumference at the lower section of the cone, where the shell thickness  $t_1 = 17.4625$  mm.





**Figure 0.6 Photo of a typical elevated combined conical tank in Canada**



**Figure 0.7 Elevation view of the studied conical tank**

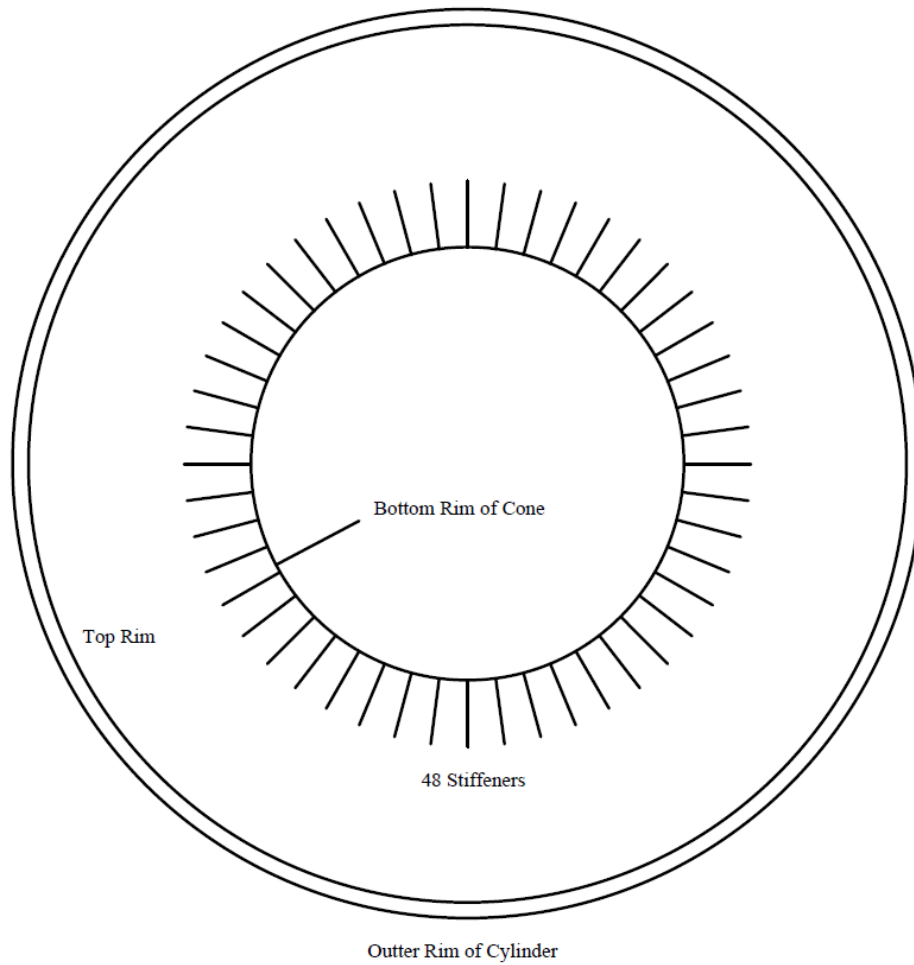


**Figure 0.8 Stiffeners configuration of the studied conical tank (top view)**

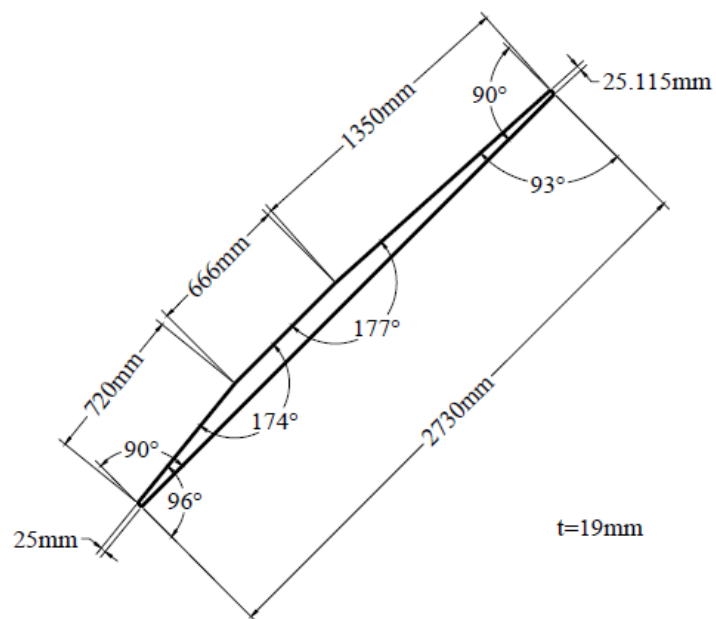


**Figure 0.9 Geometry of stiffeners (elevation view)**

To measure the imperfection of this shell structure, a laser scan was conducted on the exterior surface of the tank when it is empty. Since the conical part is the most critical component of the tank for buckling failure, the cloud points of the conical vessel were extracted from the laser scan data to be considered in the analysis.

The extracted cloud data (shown in Figure 2.10 and 2.11) of the conical vessel contains 3,250,386 scan points in the Cartesian coordinate system. The conical vessel surface has been scanned with an extremely high resolution (0.1mm along the elevation). The dimension of the scan data ranges from -13.2356 m to 13.2664 m in the  $x$ -direction, -13.1835 m to 13.2016 m in the  $y$ -direction and 0 m to 6.9066 m in the  $z$ -direction. Data points on the plane  $z = 0$  m is aligned to horizontal level of the cone bottom.

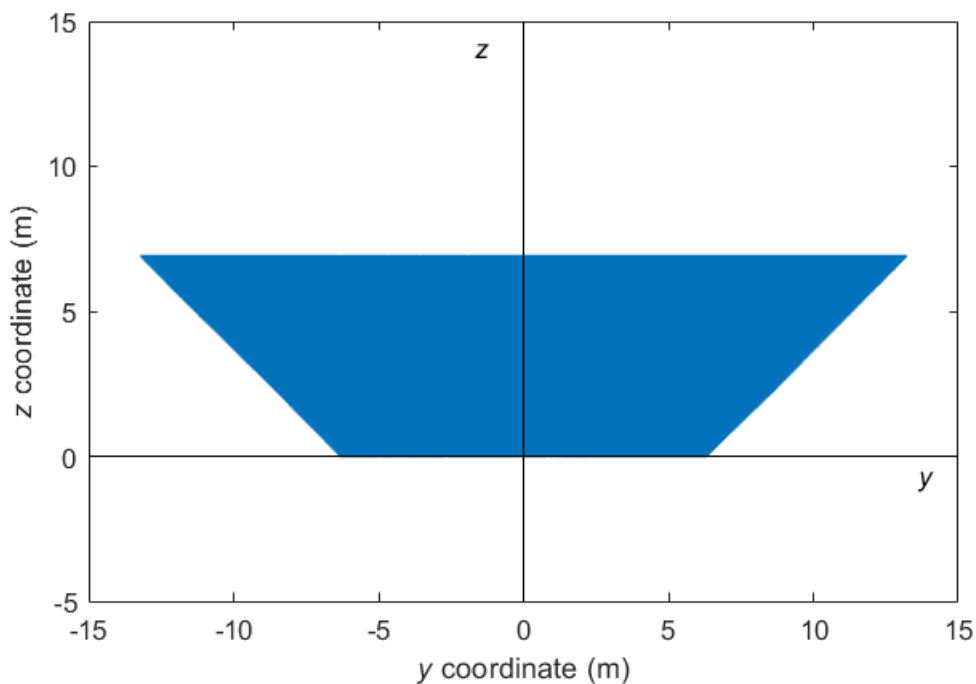


**Figure 0.10 Side view of laser scan cloud data ( $y$ - $z$  plane)**

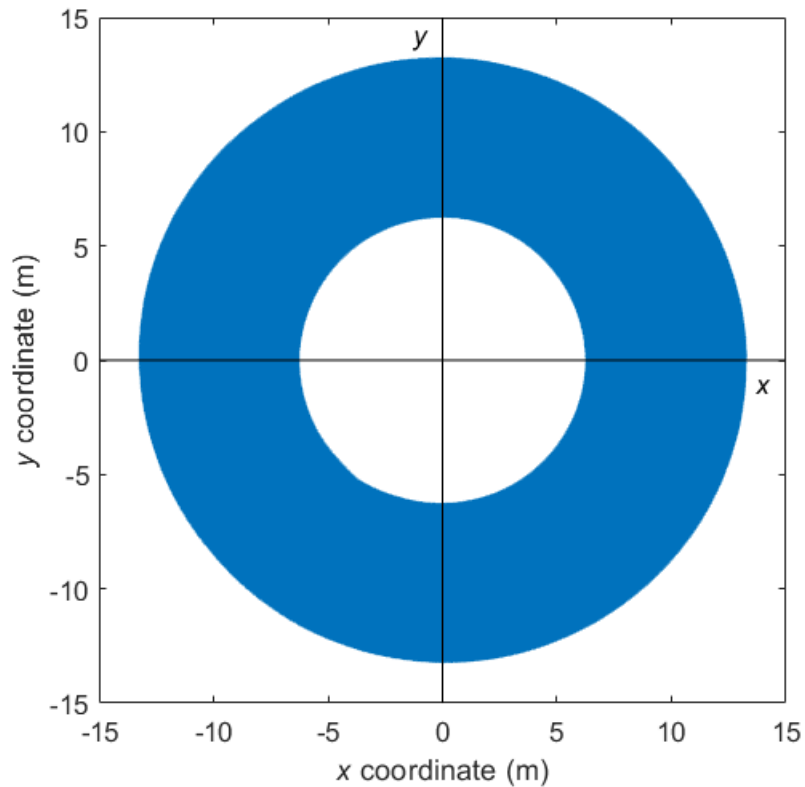


**Figure 0.11 Plan view of laser scan cloud data (x-y plane)**

## **2.4 Data processing**

### 2.4.1 Down-sampling of imperfection data

#### *2.4.1.1 Methodology and parameters*

Because of the extremely high resolution of the scan data, a sampling process is carried out to reduce the number of data points employed in the imperfection analysis to improve the computational efficiency. This process also extracts circumferential and meridional imperfection shapes for the comparison with tolerances mentioned in section 2.2.

Rotter et al. (2005) reported that the central axis of the tank may vary at different elevations and that there is ovalization for imperfect shell structures. In order to get an accurate result, it is assumed that the central axis of the case study tank is varying slightly along the elevation and hence distort the shape of meridian, which is shown in Figure 2.12.

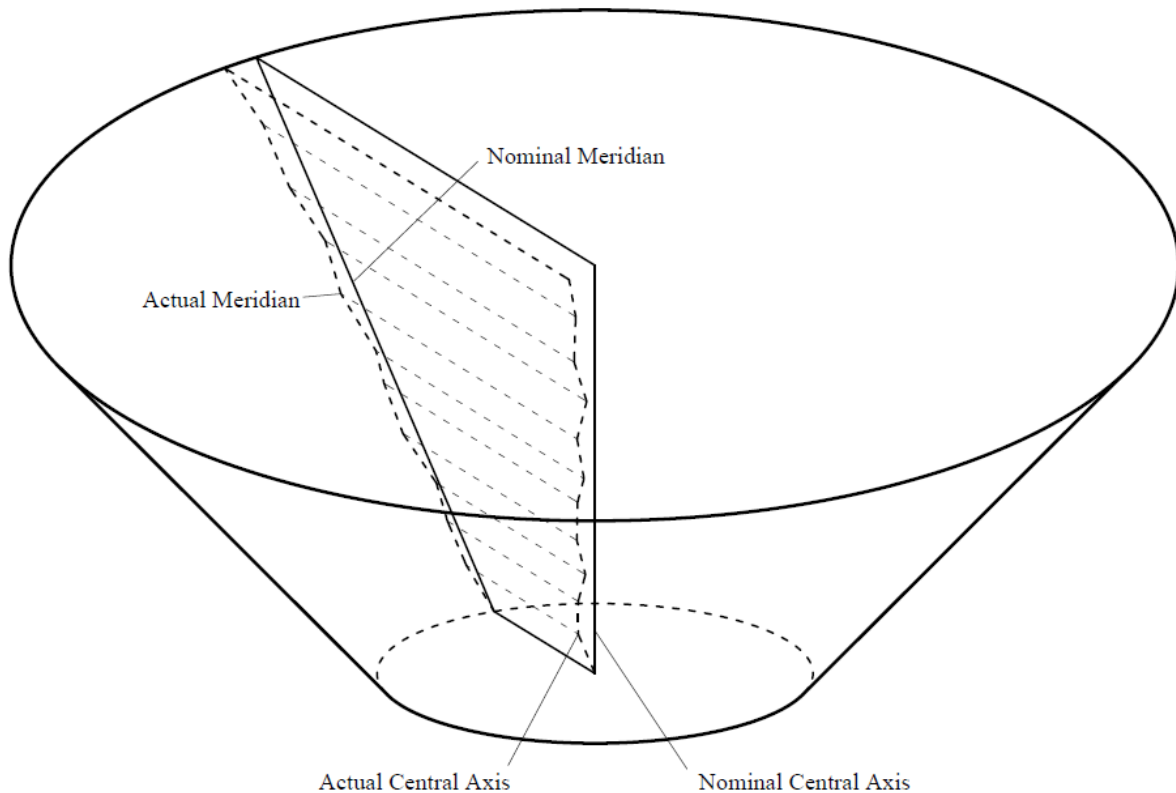


**Figure 0.12 Assumed distorted central axis & meridians**

For each point on the varying central axis, a set of data points are located on the tank wall which are toward the specific angle and at the same elevation. A distorted meridian is delineated by collecting these sample points with the same angle. Likewise, circumferences are collected with sample points at the same elevation.

In this analysis, sampling procedure involves first dividing the tank surface into a series of contiguous small areas along aimed meridians and circumferences (shown in Figure 2.13). These are defined with a height extent  $d_i$  and the arc length  $l_i$  corresponding to a radius angle  $\theta_i$ . A cylindrical coordinate system is referenced where the  $\theta$ - $\rho$  plane is translated from the original coordinate system of the cloud data. The origin  $O_i$ , which is on the central axis at the same elevation as the center of focused small area. Each sampling point within an area is defined by the cylindrical coordinates  $(\theta, \rho, z)$ . The average value of the measurements is then calculated which is associated with the sampling points within each of the areas. The computed average value is then assigned to the center of the area and used in the subsequent analysis to extract the imperfections on the tank. For an area with  $n$  data points, the average values of  $\theta$ ,  $\rho$  and  $z$  are defined as follows:

$$\theta = \frac{1}{n} \sum_{k=1}^n \theta_k \quad (2-23)$$

$$\rho = \frac{1}{n} \sum_{k=1}^n \rho_k \quad (2-24)$$

$$z = \frac{1}{n} \sum_{k=1}^n z_k \quad (2-25)$$

Where  $\theta_k$ ,  $\rho_k$  and  $z_k$  are the coordinates for the  $k$ th data points ( $k = 1, 2, \dots, n$ ).

At any certain elevation  $z_i$ , the center  $O_i$  is obtained by using an ellipse function to fit data points within  $d_i/2$  height range over and below  $h_i$ . Details are shown in Figure 2.13:

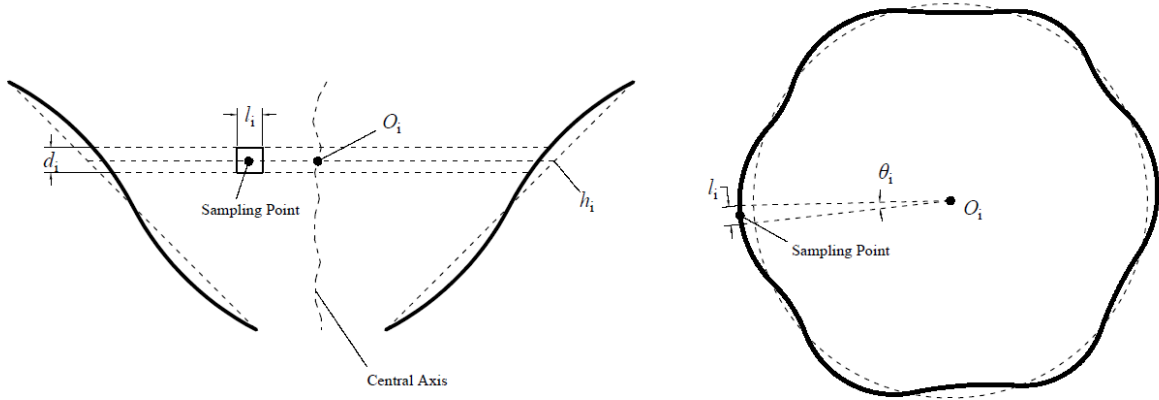


**Figure 0.13 Side view & plan view of sampling parameters**

#### 2.4.1.2 LSQ fitting with Ellipse

The fluctuating central axis can be generated by obtaining center locations in required elevations. In order to get a good result, it should satisfy that data points with any  $z$  value can be allocated to the center point at the same elevation. This procedure is initiated by calculating a large number of center points by fitting process using a type of ellipse function showed in Figure 2.14:

$$\left[ \frac{(x - x_0) \cos \theta + (y - y_0) \sin \theta}{A} \right]^2 + \left[ \frac{(y - y_0) \cos \theta - (x - x_0) \sin \theta}{B} \right]^2 = 1 \quad (2-26)$$

Where:

$x_0, y_0$  : plane coordinates of center  $O_i$ .

$\theta$  : inclination angle of ellipse.

$A, B$  : The length of semi-axis.

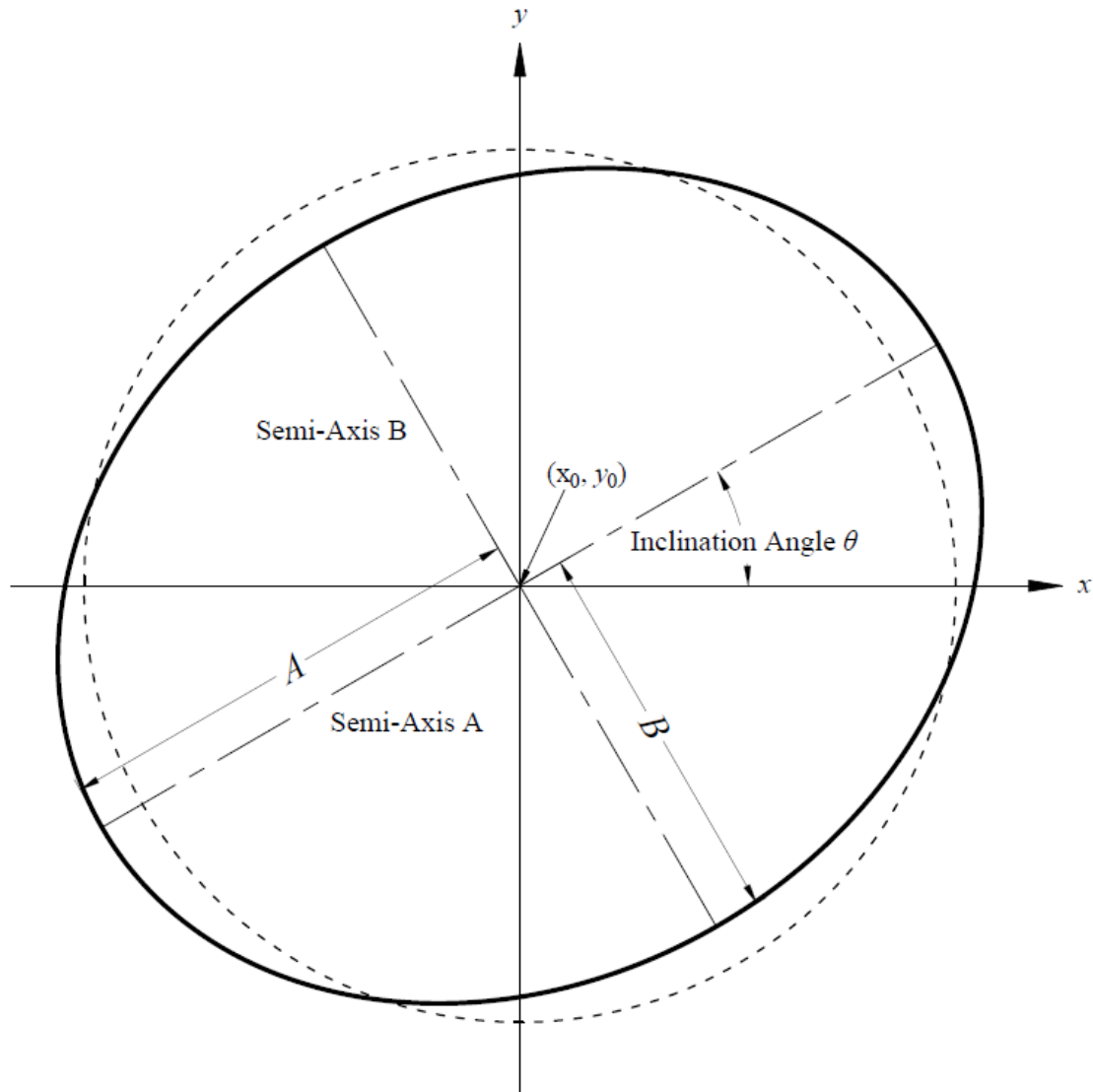


**Figure 0.14 Ellipse for LSQ fitting**

The resolution of cloud data along the  $z$ -axis is 0.0001 m, data points utilized for each fitting shall be collected within a wide range to get accurate results. As a trade-off between including enough scan points for each fitting ellipse and generating enough ellipses to from the varying central axis, the height range is selected as 0.0017 m, corresponding to 4063 fitting ellipses between  $z = 0$  to  $z = 6.9066$  m. The center location of each data group  $(x_0, y_0, z_0)$  is deemed as the center of the ellipse.

The method used in the fitting process is the nonlinear least-square (LSQ) method with the Levenberg-Marquardt algorithm (Levenberg 1944; Marquardt 1963). An iteration is used for continuous computation in different  $z$  values. In the first loop at  $z = 0$  m, initial values for LSQ

method are input as the estimation of geometry at the base of tank.

$$\begin{Bmatrix} x_0 \\ y_0 \\ A \\ B \\ \theta \end{Bmatrix} = \begin{Bmatrix} 0 \\ 0 \\ 6 \\ 6 \\ 0 \end{Bmatrix} \quad (2 - 27)$$

At the start of the next loop, initial values are replaced by computation results of the previous loop. Considering similar geometry between adjacent elevations, this helps in achieving accurate results. This process is conducted using a MATLAB R2019a built in-house code. Obtained results include central axes, length of semi-axes and inclination angle which are shown in Figures 2.15, 2.16, 2.17 and 2.18.

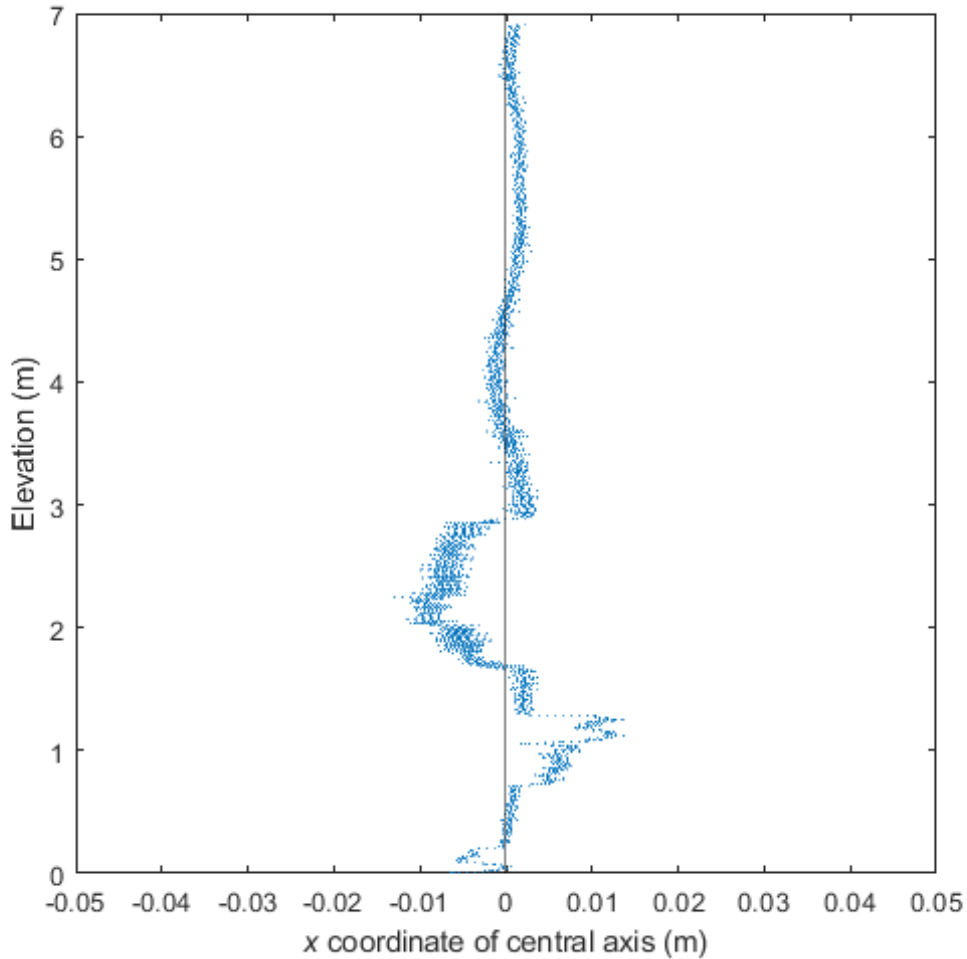


**Figure 0.15 Calculated x coordinate of deviated central axis**



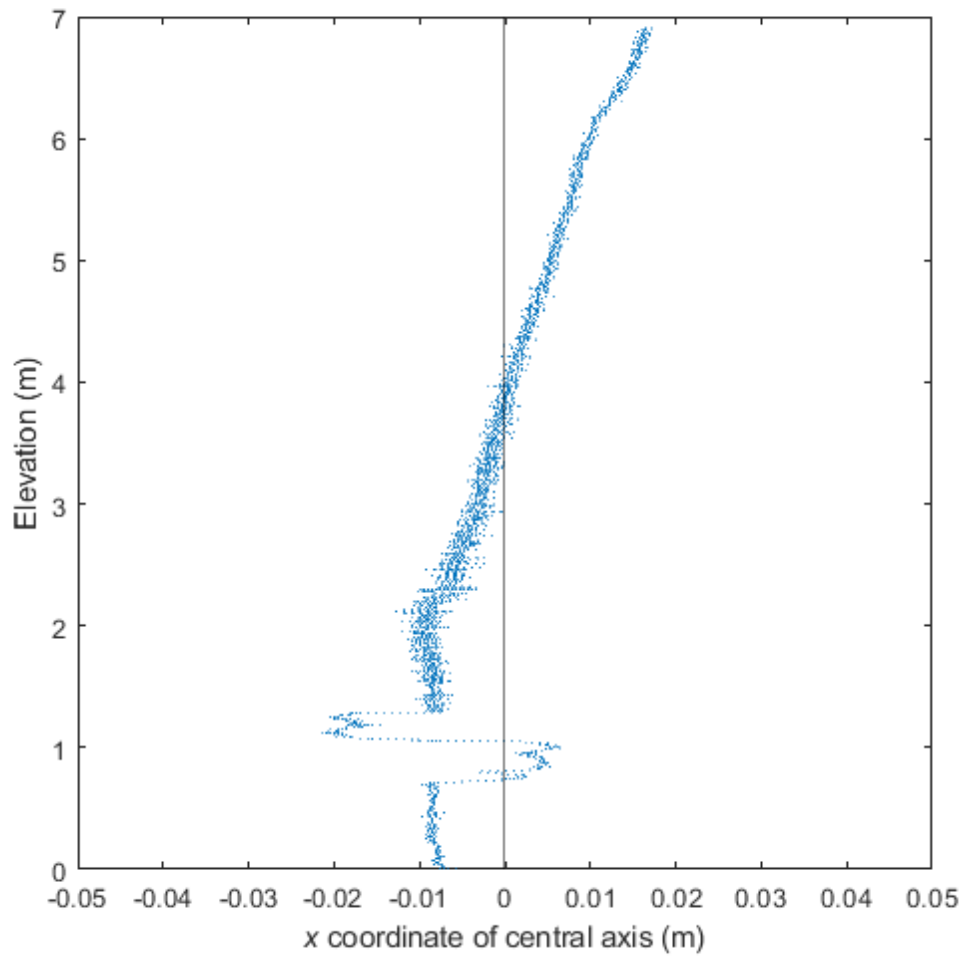


**Figure 0.16** Calculated y coordinate of deviated central axis

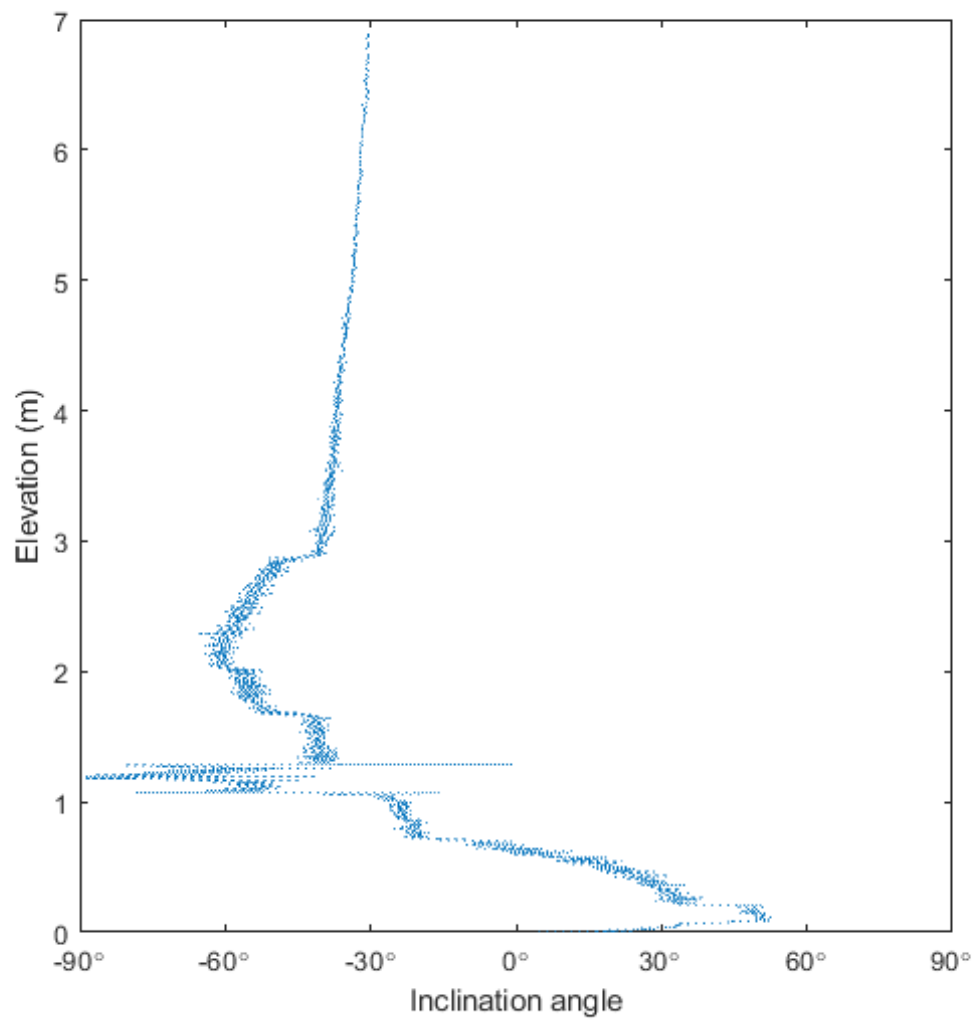


**Figure 0.17** Calculated inclination angle of fitting ellipses

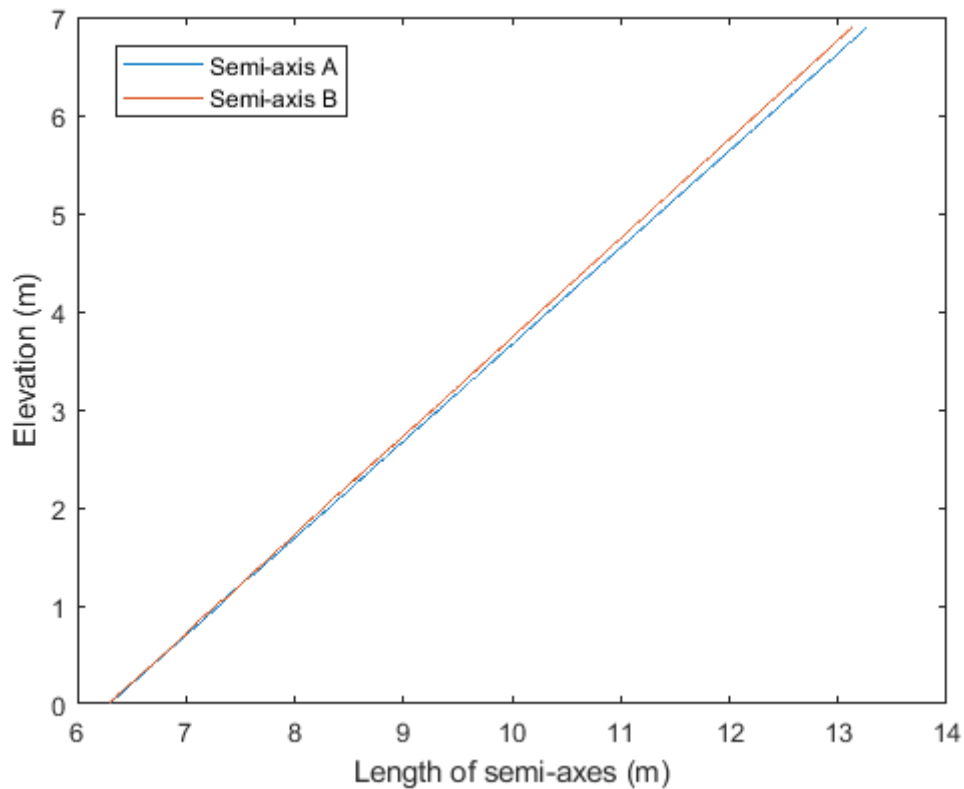


**Figure 0.18 Calculated semi-axes length of fitting ellipses**

It is clearly shown in Figure 2.15 and Figure 2.16 that large fluctuations occur in the lower third of the tank at elevation  $z = 1$  m in  $y$ -direction and  $z = 2$  m in  $x$ -direction. Stiffeners are installed at the bottom of the tank with the top edge at the elevation close to  $z = 2$  m; therefore, it is likely that relatively large imperfections are caused during the process of welding these stiffeners to the tank wall. Also, large variation can be found in the inclination angle below  $z = 3$  m. Figure 2.18 shows the difference between the lengths of the semi-major and semi-minor axes increasing with the elevation. These indicate complicated imperfection shapes which is discussed in the following sections.

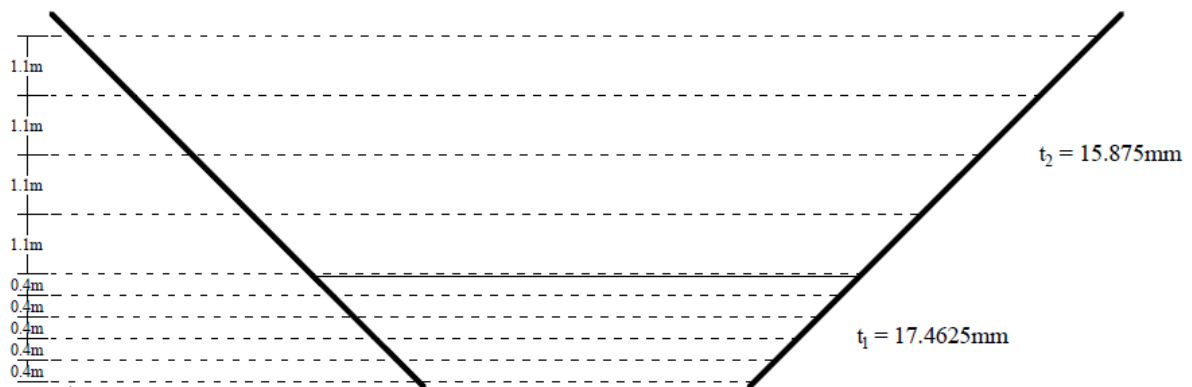
Each profile consists of result data points calculated from 4063 fitting ellipses and is further refined with Cubic Spline Interpolation and extended to the same volume with cloud data. In this way, results from fitting ellipse are assigned to entire cloud data where corresponding value can be obtained given any  $z$  value of data point.

### 2.4.1.3 Imperfection analysis

In this analysis, imperfections at 12 meridians and 10 circumferences are extracted from the cloud data with the sampling procedure.

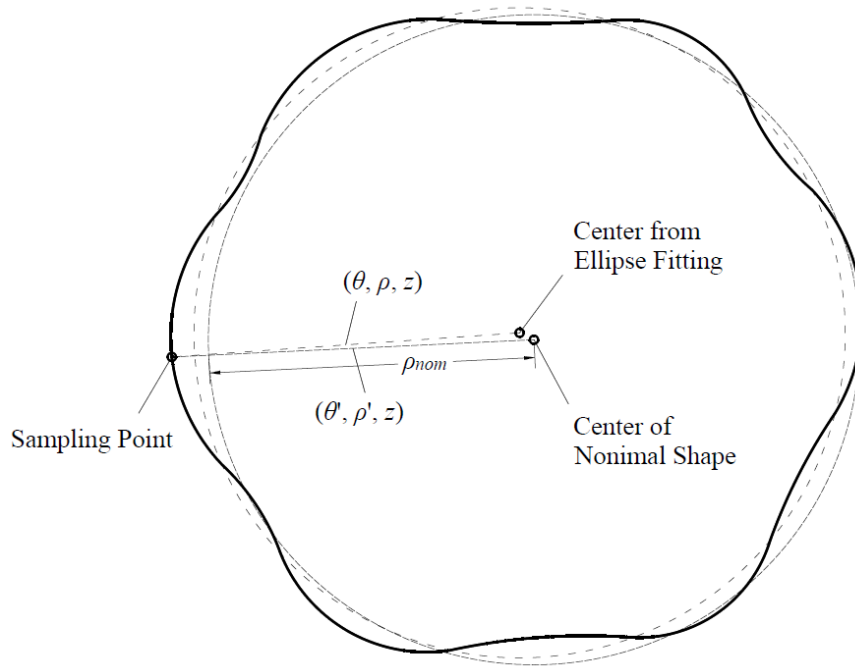
Meridional imperfections are at: 15°, 45°, 75°, 105°, 135°, 165°, 195°, 225°, 255°, 285°, 315°, 345°.

Circumferential imperfections are at: 0.1 m, 0.5 m, 0.9 m, 1.3 m, 1.7 m, 2.1 m, 3.2 m, 4.3 m, 5.4 m, 6.5 m. More circumferences are collected at the bottom of the tank because the imperfections at the bottom area are usually the most critical to the buckling capacity. The layout of selected circumferences is shown in Figure 2.19.



**Figure 0.19 Selected circumferences layout**

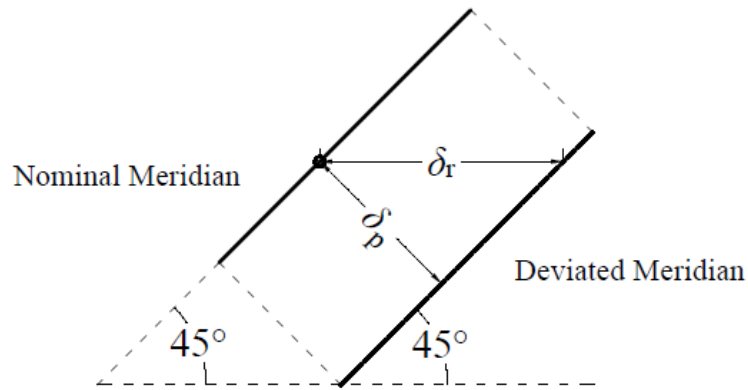
The location at the sampling points  $(\theta, \rho, z)$  is generated from the LSQ fitting process and is recorded in the coordinate system attached to a varying central axis (described in section 2.4.1.1). Imperfection calculation requires the sampling point to be associated with a new cylindrical coordinate system  $(\theta', \rho', z)$  based on a fixed central axis of the nominal tank shape, as shown in Figure 2.20.



**Figure 0.20 Coordinate systems employed for sampling procedure & imperfection calculation**

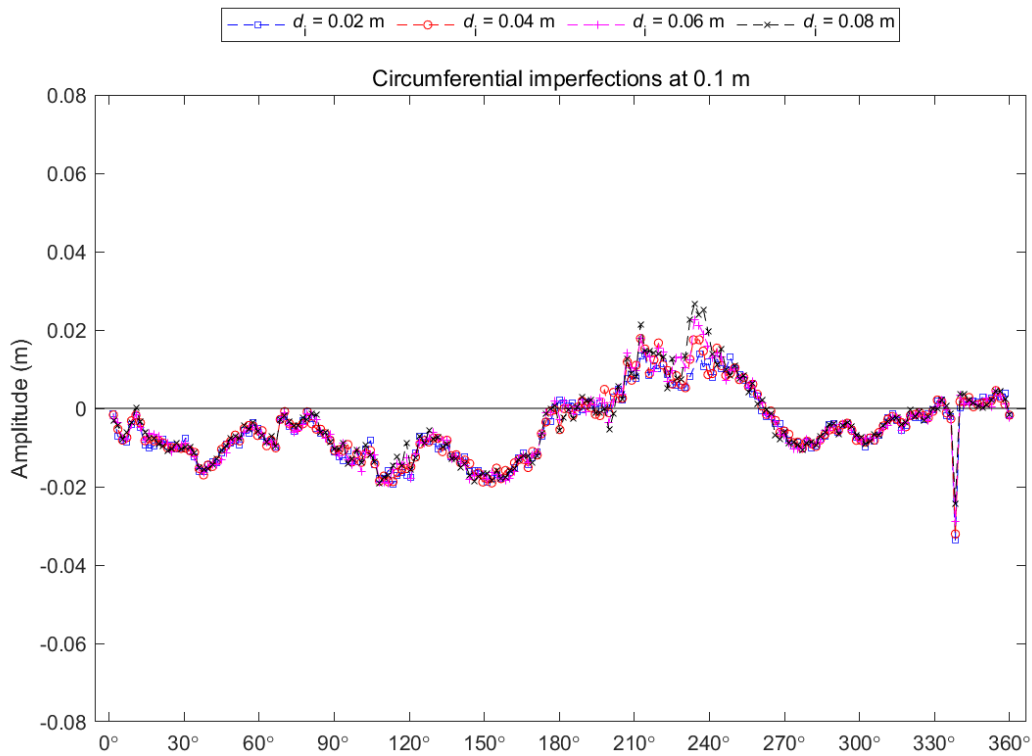
In this way, the radial deviation between sampling points and the perfect tank is acquired as  $\rho - \rho_{nom}$  (radius of nominal circumference at given location). However, both in design standards (AWWA, ECCS) and previous investigations (Hornung et al. 2002; Rotter et al. 2005), the direction of imperfections is defined perpendicular to the tank wall. In order to calculate perpendicular imperfections, a geometrical approximation is introduced. In AWWA D100-11, the imperfection amplitude is assumed to be less than 1/100 of the wavelength. Also, the case study of cylindrical shells by Rotter et al. (2005) shows that despite many harmonic components can be found in the 1D Fourier analysis results of meridional imperfections, the shortest wavelength of main components (3000 mm) is still huge, compared to the imperfection amplitude among selected meridians (less than 28 mm). Therefore, it is assumed that given any small section on a meridian of the perfect shell, its corresponding part on the deviated meridian is still approximately parallel to it. In this way, the relationship between the perpendicular imperfections  $\delta_p$  and the radial deviation  $\delta_r$  can be expressed as shown in Eq. 2-28 and Figure 2.21.

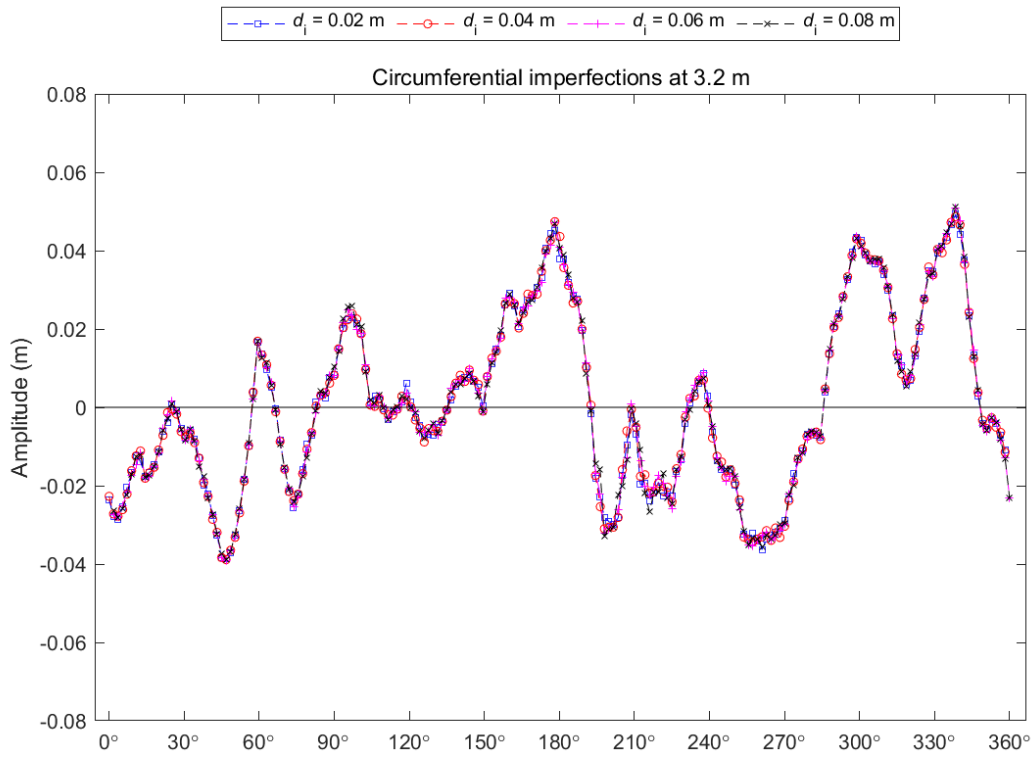
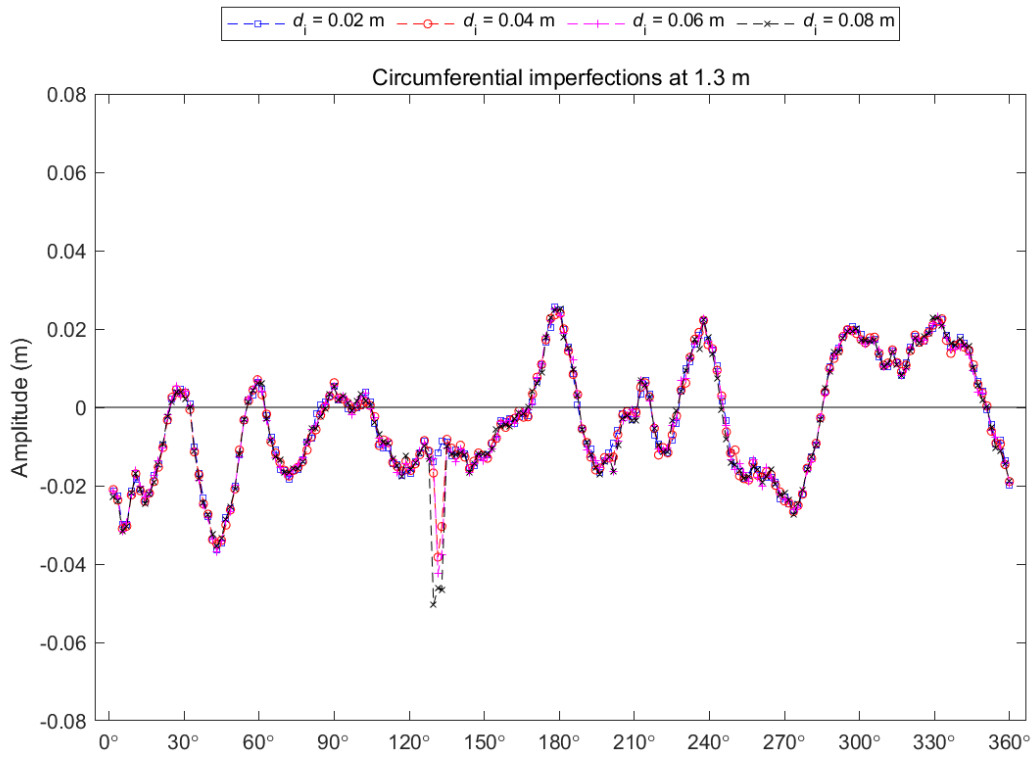
$$\delta_p = \frac{\sqrt{2}}{2} \delta_r \quad (2 - 28)$$

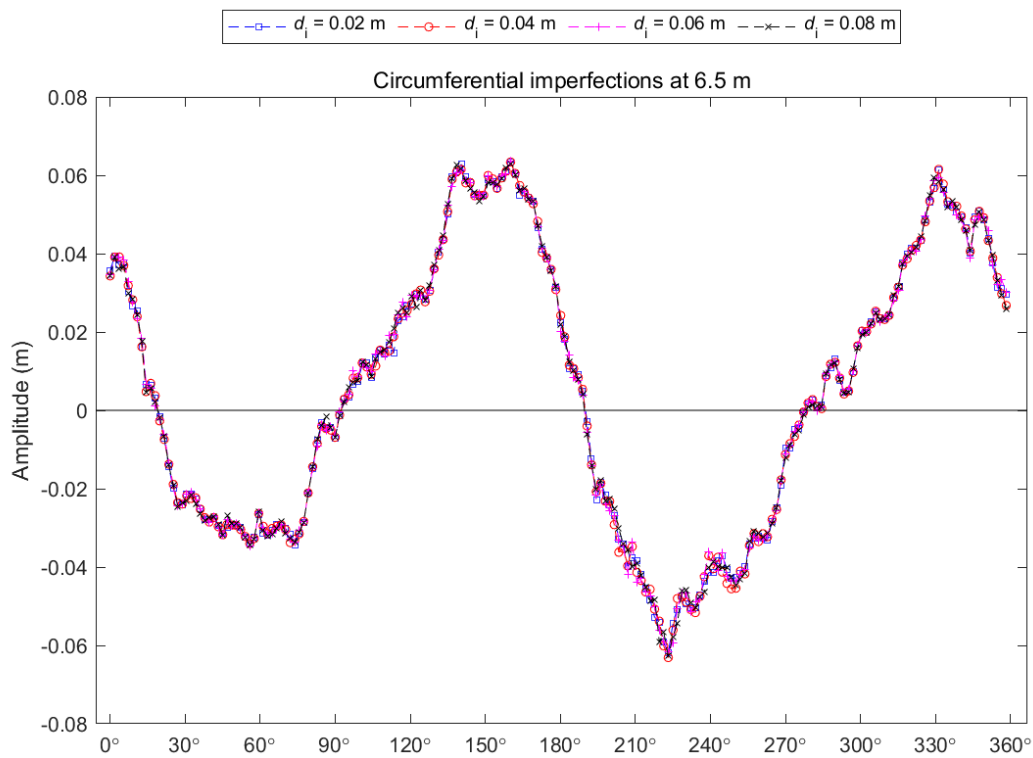


**Figure 0.21 Radial deviation & perpendicular deviation (geometric imperfections)**

To investigate the impact of the size of the small area for sampling on the extracted imperfections, circumferential imperfections are checked with  $d_i$  among 0.02 m, 0.04 m, 0.06 m and 0.08 m, while meridional imperfections are checked with  $\theta_i$  among  $0.36^\circ$ ,  $0.72^\circ$ ,  $1.08^\circ$  and  $1.44^\circ$ . This process is conducted in MATLAB R2019a. Examples of the results of circumferential imperfections are shown in Figure 2.22. Other results are shown in appendix Figure A.1.



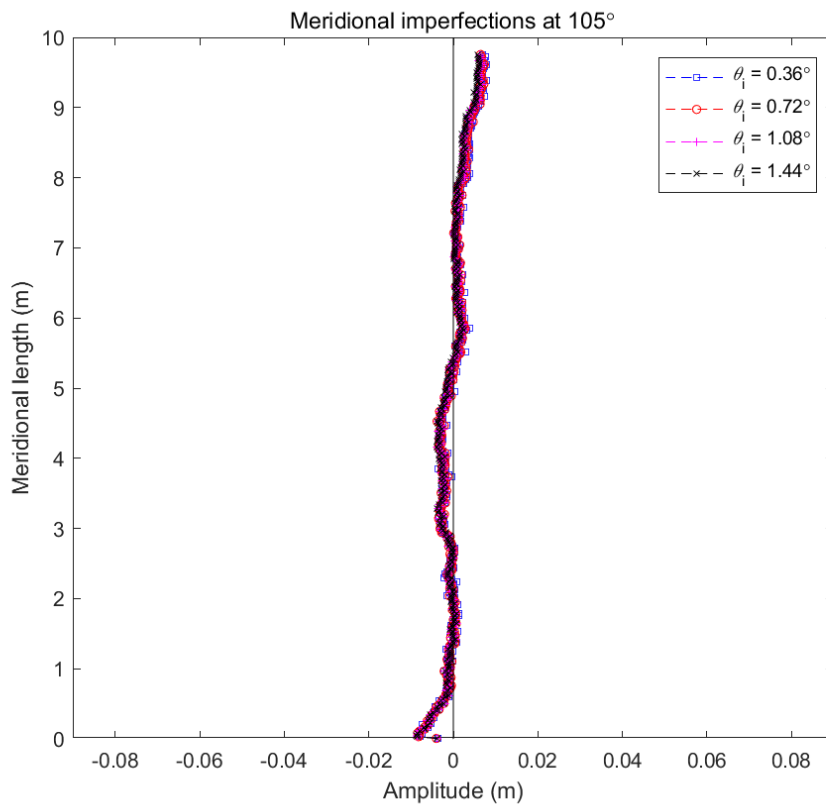
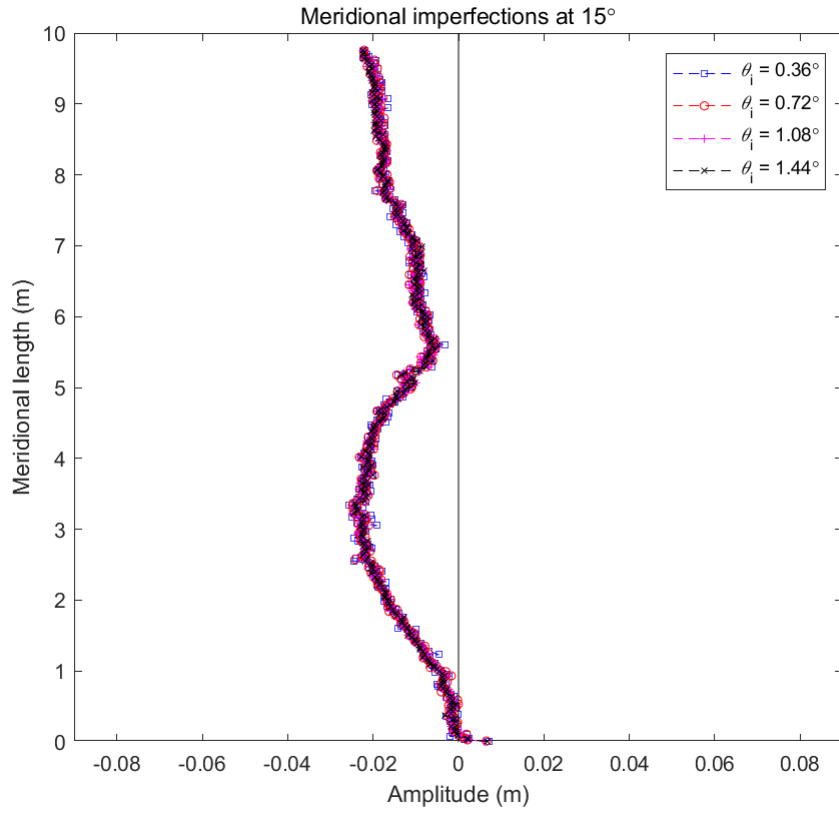


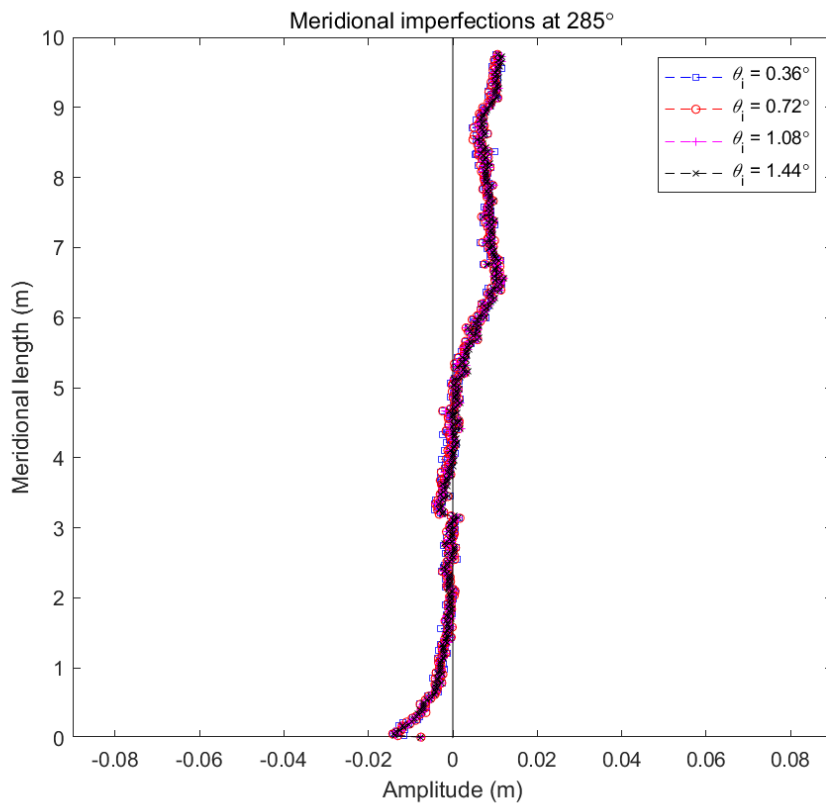
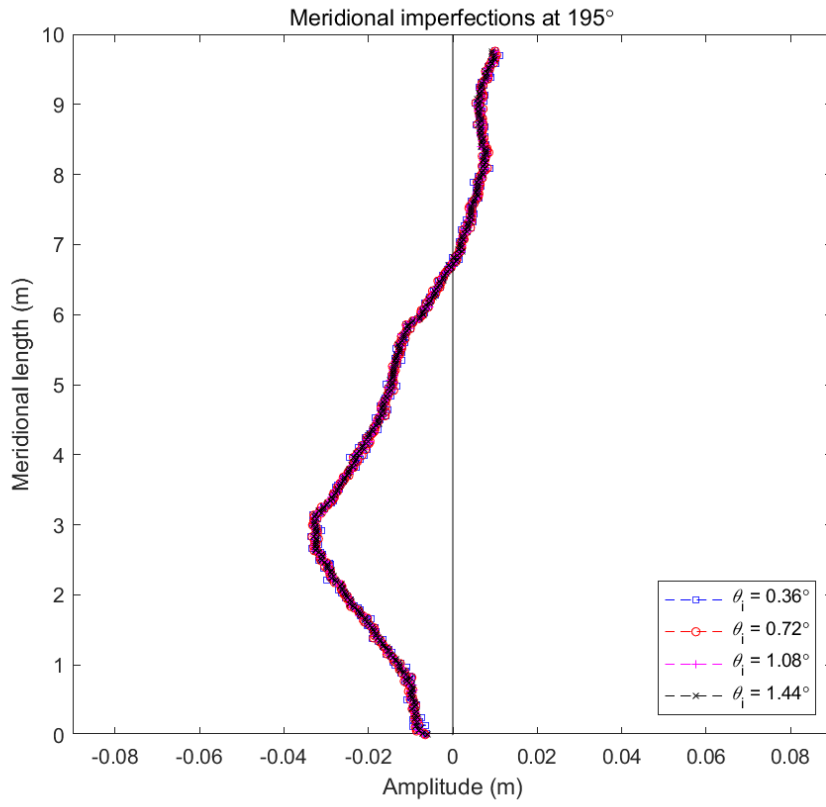


**Figure 0.22 Calculated circumferential imperfections with  $d_i$  of 0.02 - 0.05 m**

It is clearly shown that the obtained circumferential imperfections are highly similar to each other when the sampling height range lies between 0.02 – 0.05 m. Divergence is found only in few circumferential sections ( $z = 0.1$  m,  $30^\circ \leq \theta \leq 60^\circ$ ;  $z = 1.3$  m,  $300^\circ \leq \theta \leq 330^\circ$ ). Examples of the results of meridional imperfections under narrow angular range are shown in Figure 2.23. Other results are shown in appendix Figure A.2.







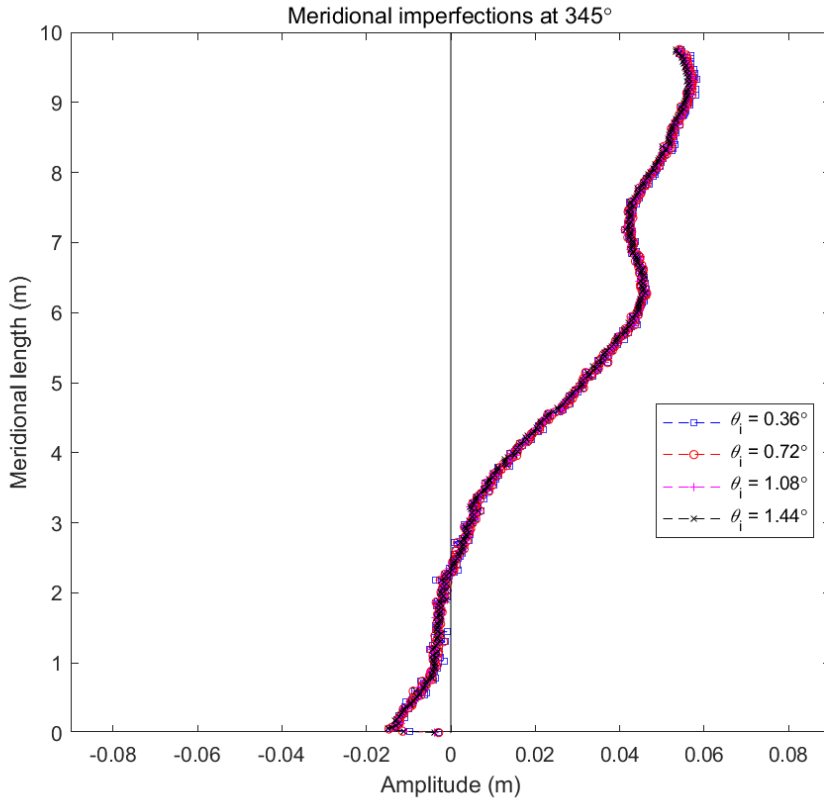


**Figure 0.23** Calculated meridional imperfections with  $\theta_i$  of  $0.36^\circ$  -  $1.44^\circ$

Meridional results are still close to each other with different resolution. It is noticed that imperfection amplitude at the bottom is comparatively smaller in most meridians. Maximum amplitudes usually occur in the middle part at meridional length equal to 3 m. Top of the meridian is also a place where largest imperfection happens.

Clearly, any imperfection at given circumference can be located with a sampling height range  $d$  and angle  $\theta$ . Hence, it can be expressed as  $\delta(d, \theta)$ . Similarly, any imperfection at given meridian can be located with a sampling angular range  $\theta'$  and meridional length  $L$ . Hence, it can be expressed as  $\delta(\theta', L)$ . This helps to measure the sensitivity in a quantitative way, where a parameter  $\eta$  can be defined here to describe the average deviation ratio between two curves with different sampling resolutions. For circumferential imperfections, it is determined as:

$$\eta_c(d_1, d_2) = \frac{\sum_{i=1}^n |\delta(d_1, \theta_i) - \delta(d_2, \theta_i)|}{\sum_{i=1}^n |\delta(d_1, \theta_i)|} \quad (2 - 29)$$

Where:

$\eta_c$ : ratio of total difference between sampling with  $d_1$  (base) and sampling with  $d_2$  (deviated), to the total amplitude of sampling with  $d_1$  (base).

$d_1$  : sampling resolution (height range) of the base curve.

$d_2$  : sampling resolution (height range) of the deviated curve.

$\theta$  : the angular coordinate of data points on a circumferential imperfection curve.

$n$  : number of data points on a circumferential imperfection curve.

$\delta$  : imperfection amplitude.

For meridional imperfections, it is determined as:

$$\eta_m(\theta'_1, \theta'_2) = \frac{\sum_{i=1}^n |\delta(\theta'_1, L_i) - \delta(\theta'_2, L_i)|}{\sum_{i=1}^n |\delta(\theta'_1, L_i)|} \quad (2 - 30)$$

Where:

$\eta_m$  : ratio of total difference between sampling with  $\theta_1'$  (base) and sampling with  $\theta_2'$  (deviated), to the total amplitude of sampling with  $\theta_1'$  (base).

$\theta_1'$  : sampling resolution (angular range) of the base curve.

$\theta_2'$  : sampling resolution (angular range) of the deviated curve.

$L$  : the length coordinate of data points on a meridional imperfection curve.

$n$  : number of data points on a meridional imperfection curve.

Calculated results are shown in Figure 2.24.

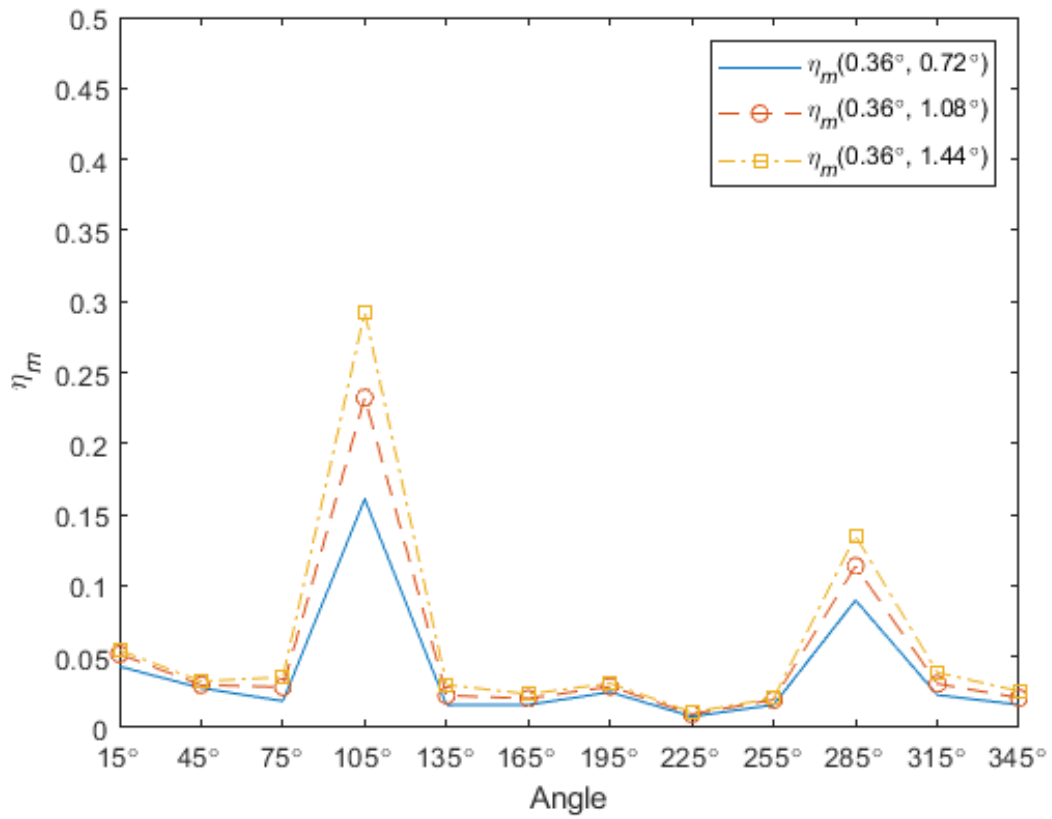
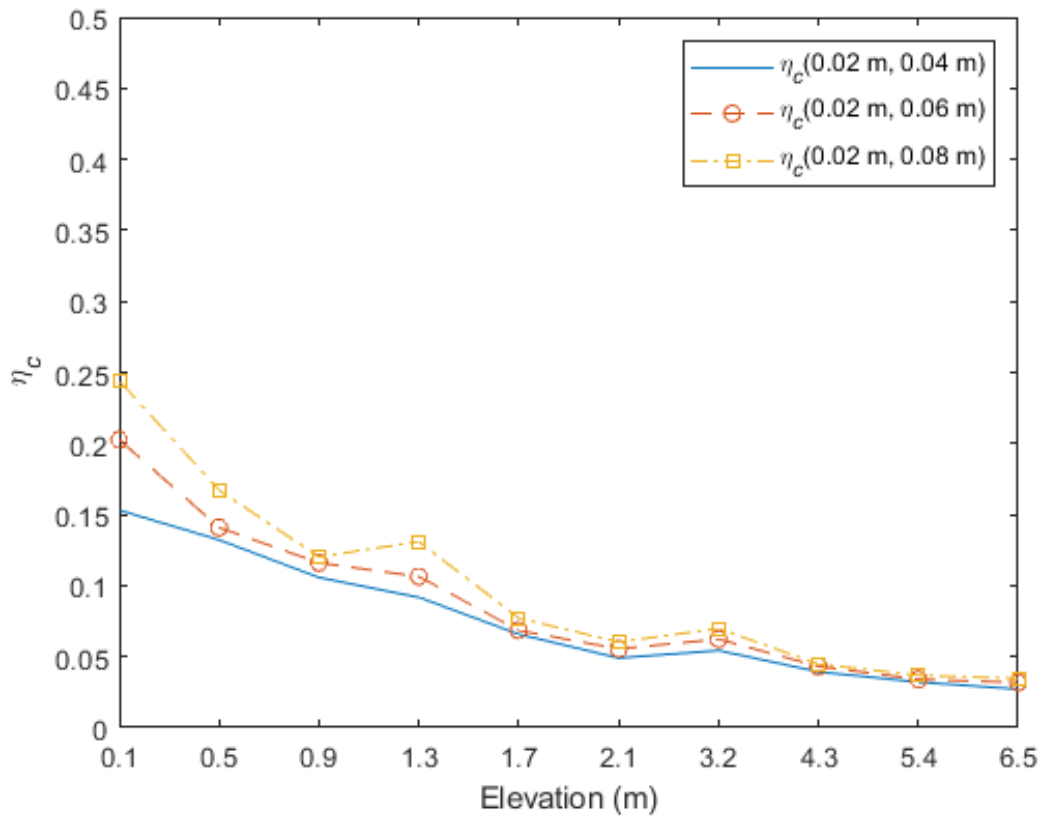
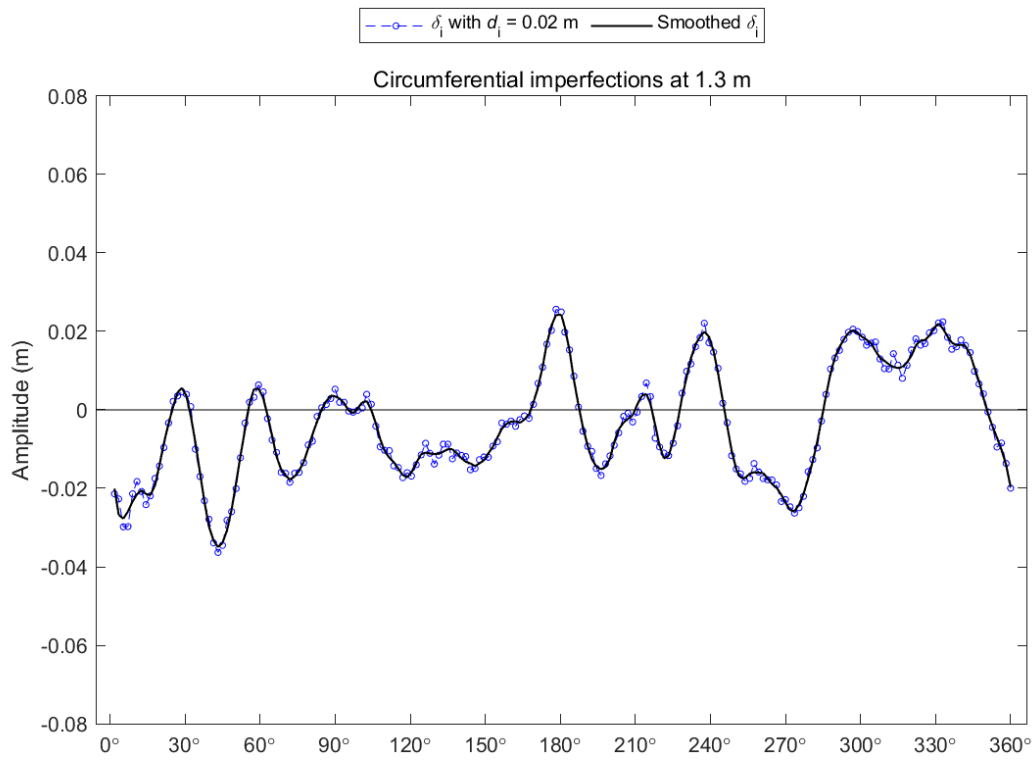
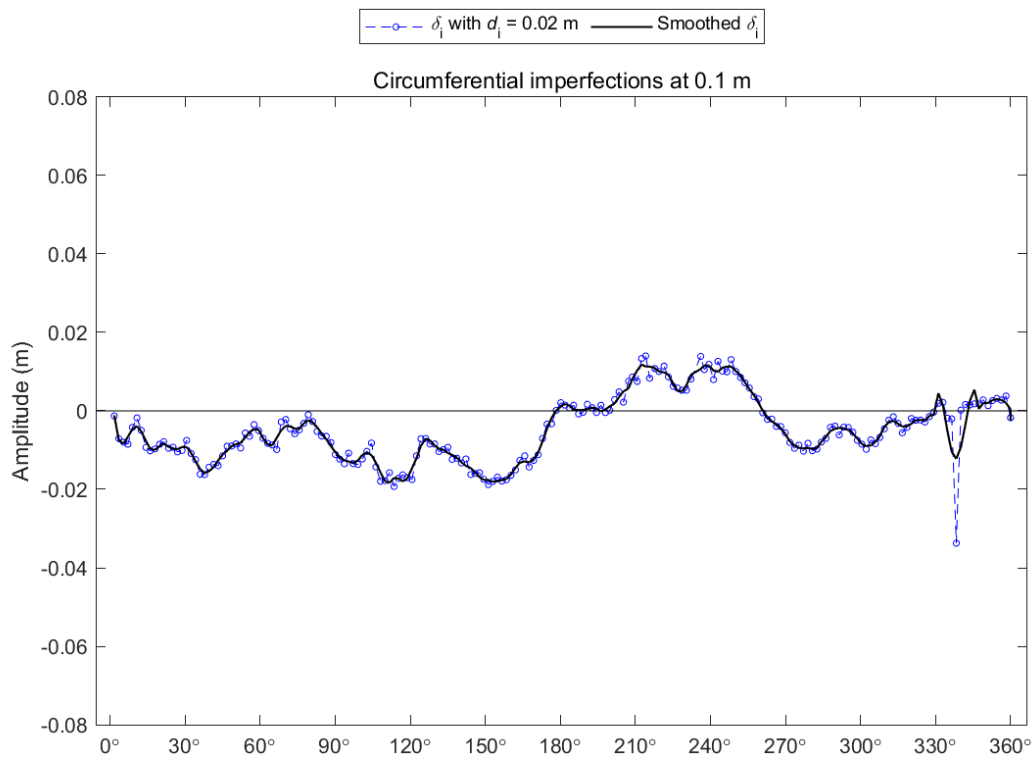


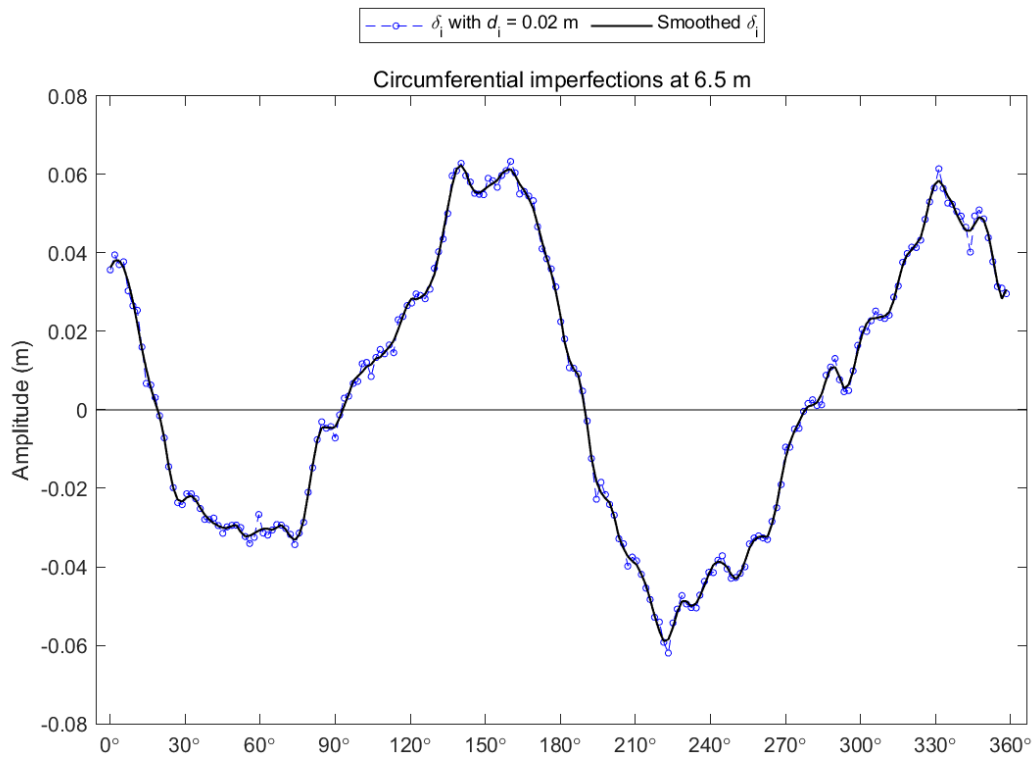
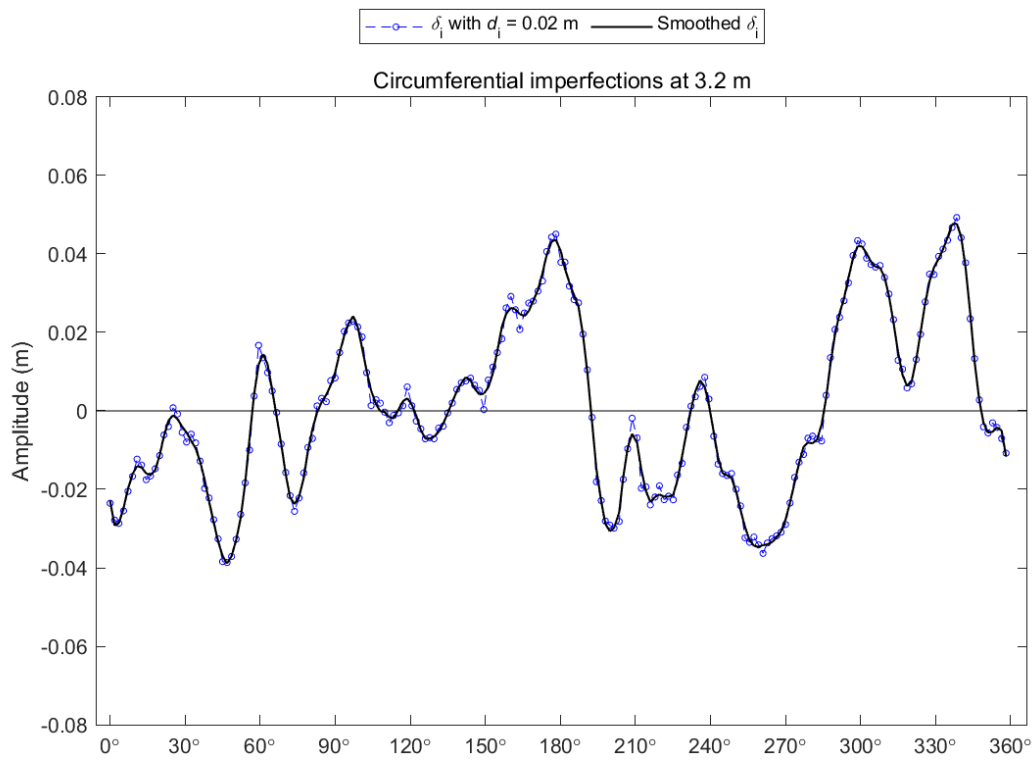
**Figure 0.24** Difference between sampling results with various resolution

Generally, a few observations can be drawn from these results. Sensitivity in this case is different along various directions. It is shown that circumferential imperfection has the highest sensitivity close to the bottom. The differences between sampling results diverge quickly with different  $d_i$ , from 20% to 30%, while they are relatively small at the top (around 5%). Meridional sensitivity varies among different meridians. The differences in most meridians are below 5% but increases to 30% at  $105^\circ$  location. The main reason of high sensitivity (from 10% to 30%) in certain regions (circumferences below 1.7 m and meridians around  $105^\circ$  and  $285^\circ$ ) is their low imperfection amplitudes, which makes the difference between sampling results occupy a relatively larger proportion. Based on the result, we can see change of results are still less than 25% even when sampling resolution is quadrupled. However, in order to get the most accurate result, parameter range for sampling procedure is determined as 0.02 m height range for circumferences and  $0.36^\circ$  angular range for meridians, which is the smallest number. This is employed in the following analysis.

#### *2.4.1.4 Imperfection smoothing*

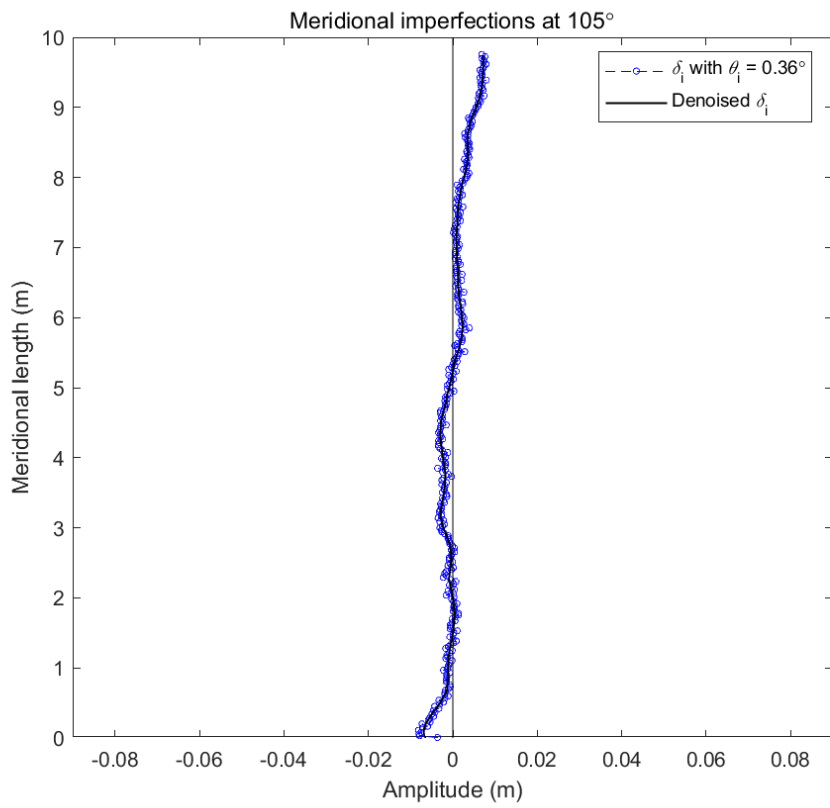
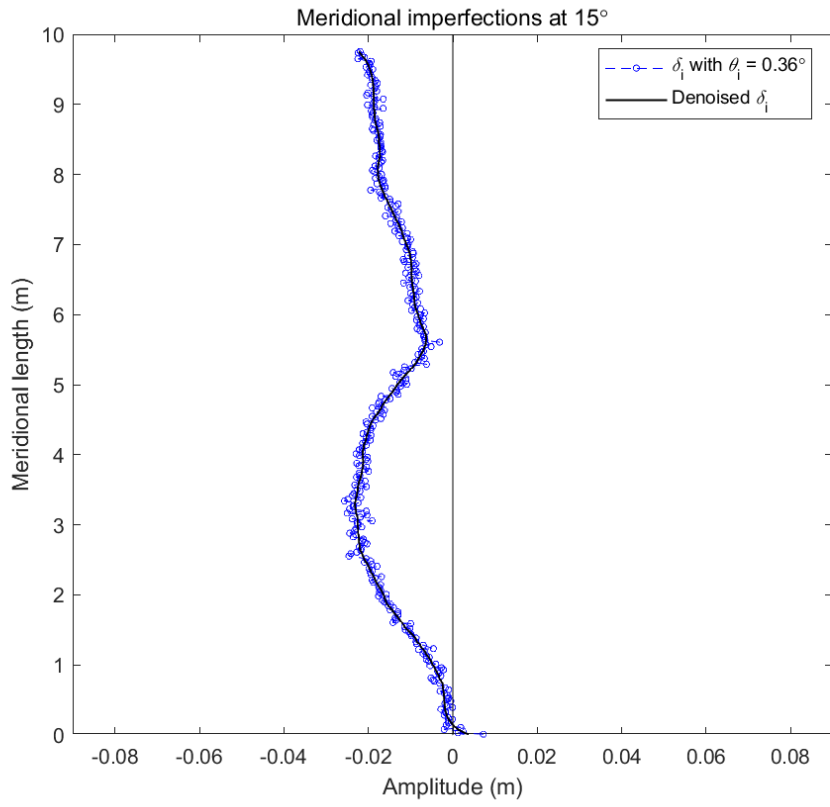
A series of imperfection patterns have been collected along meridians and circumferences. Multiple harmonic components can be found in the results and those with long wavelength are usually the focus of study. Previous investigations and design standards have proposed several assumptions to simulate effects of main imperfection components in an approximate way. In this case, those counterparts should be extracted from data sets to compare with existing theoretical assumptions. Therefore, a denoising procedure is employed on  $\delta_p$  (imperfections perpendicular to the tank wall) resulting from the sampling procedure with the Savitzky-Golay filter (Savitzky et al. 1964). Parameter values utilized in sampling procedure are  $d_i = 0.02$  m,  $\theta_i = 0.36^\circ$ . Examples of smoothed curves are shown in Figures 2.25 and 2.26. Other results are shown in appendices Figure A.3 and Figure A.4. These smoothed imperfection shapes will be utilized in the following analysis where global & local imperfection components are extracted on these meridians and circumferences.

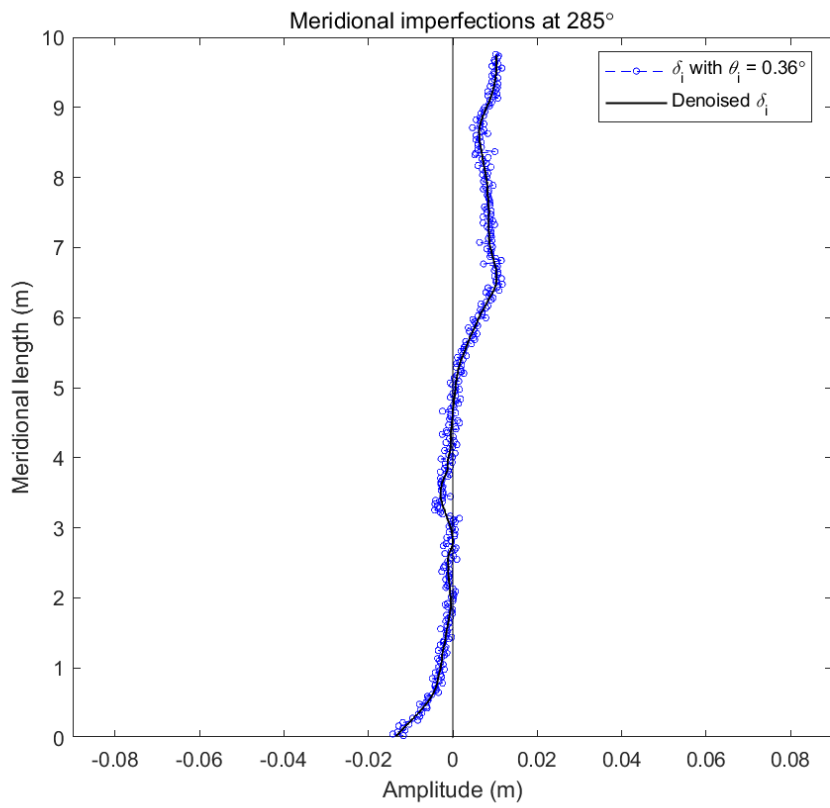
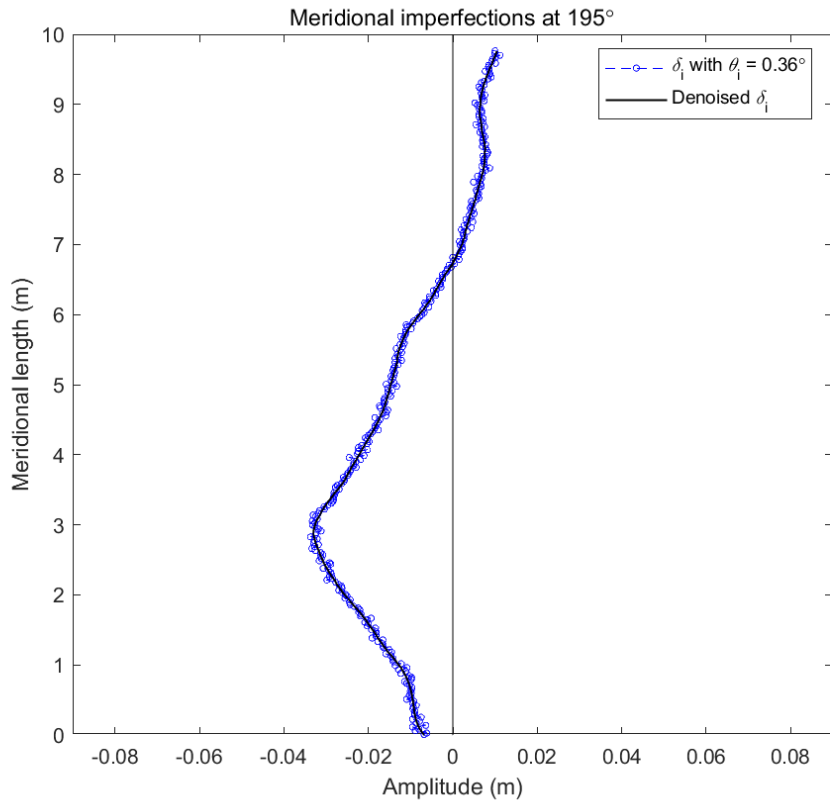




**Figure 0.25 Denoised circumferential imperfections**







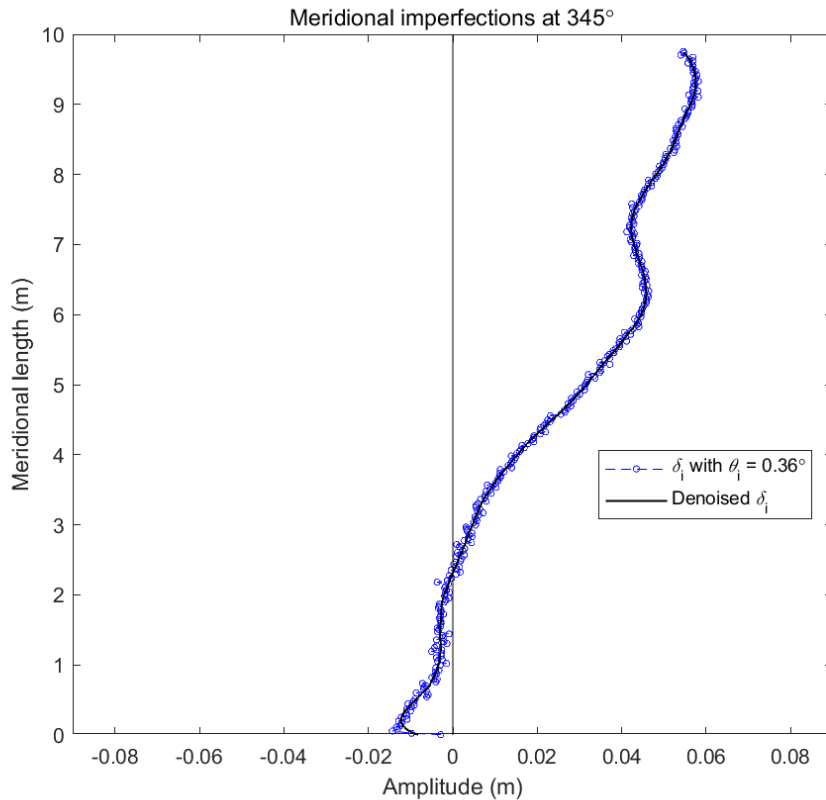


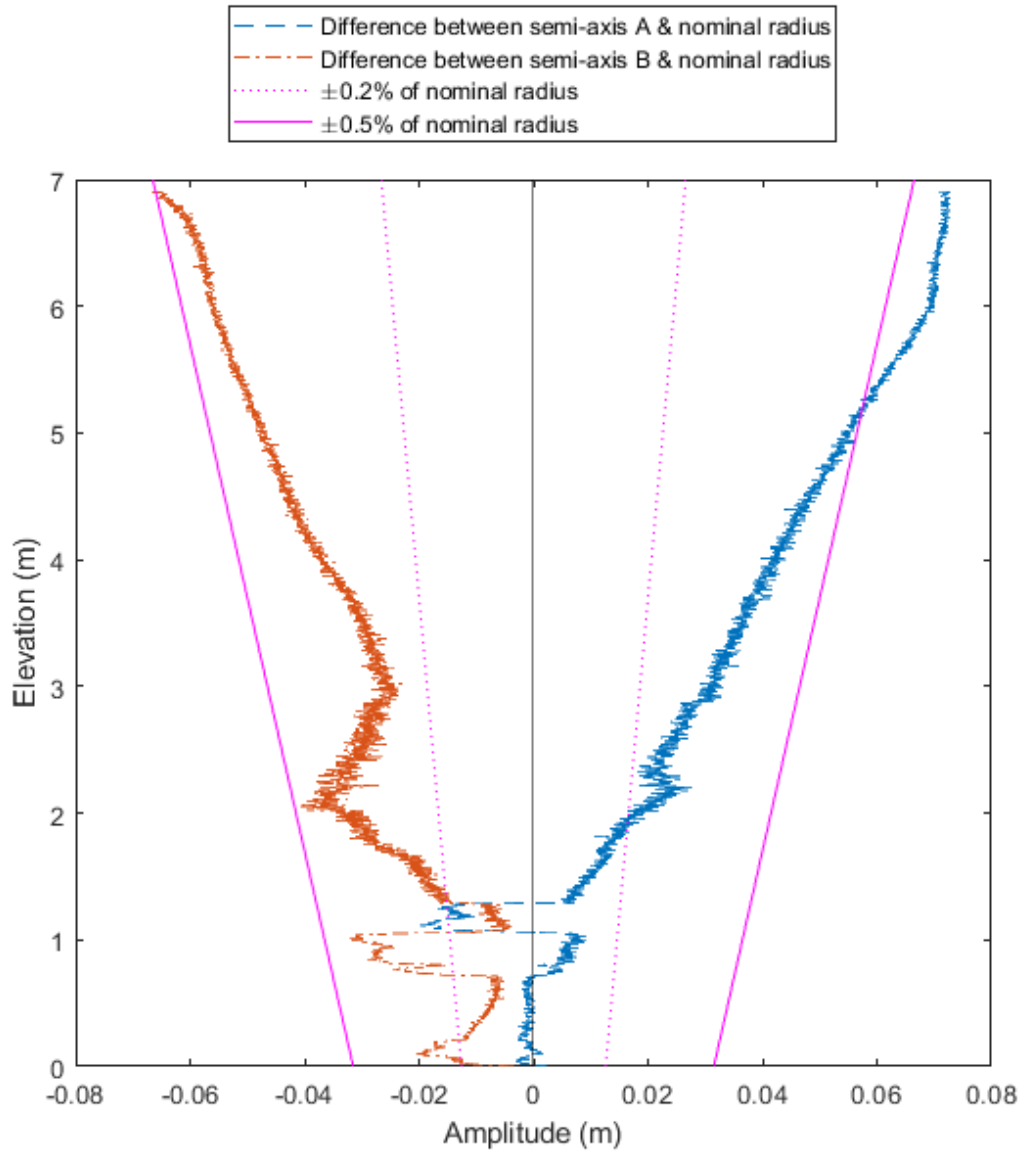
**Figure 0.26 Denoised meridional imperfections**

### 2.4.3 Global imperfection

In the AWWA D100-11 and EN 1993-1-6: 2007 design codes, imperfections are generally classified as global imperfections and local imperfections. Generally, global imperfections are deemed as out-of-roundness or ovalization. An LSQ fitting process is introduced in section 2.4.1.1 and 2.4.1.2 where the profiles of semi-axes length and inclination angle of fitting ellipse (Eq. 2-26) are generated. These help to depict the ovalization effect varying along the elevation. Apart from this, central deviation shall be deemed as an additional component of global imperfection. The ovalization effect (out-of-roundness) in design standards is usually measured on the contralateral positions of the tank, where deviations of the central location do not leave influence. However, the local imperfection is always measured unilaterally, where central deviation will certainly apply large impacts on the profile and change the amplitude of local imperfections.

Figures 2.15, 2.16, 2.17 and 2.18 have shown results calculated from LSQ ellipse fitting.

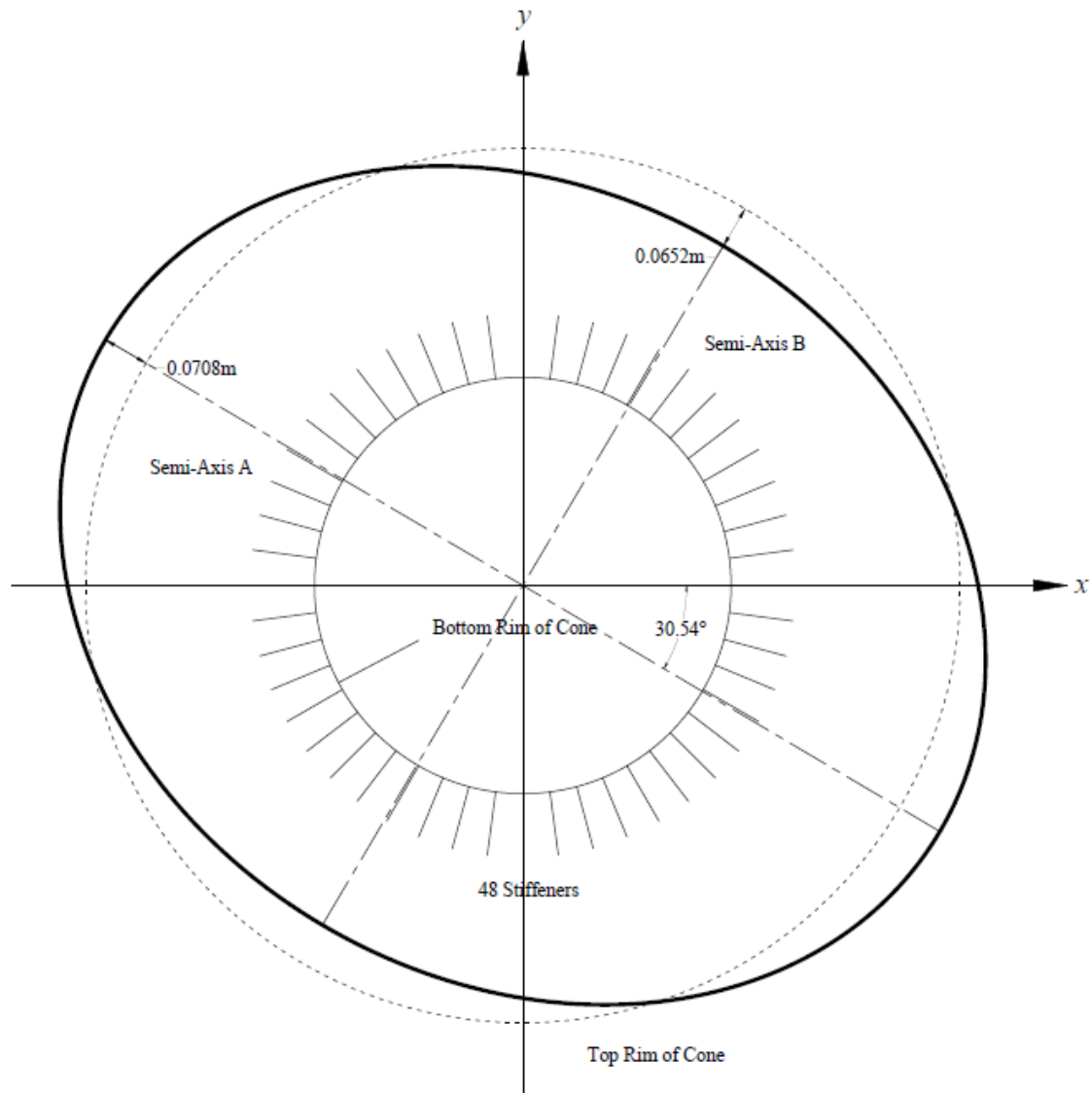
Ovalization amplitude can be measured by the difference between nominal radius and semi-axes, which is shown in Figure 2.27.



**Figure 0.27 Difference between nominal radius and calculated semi-axes of fitting ellipse**

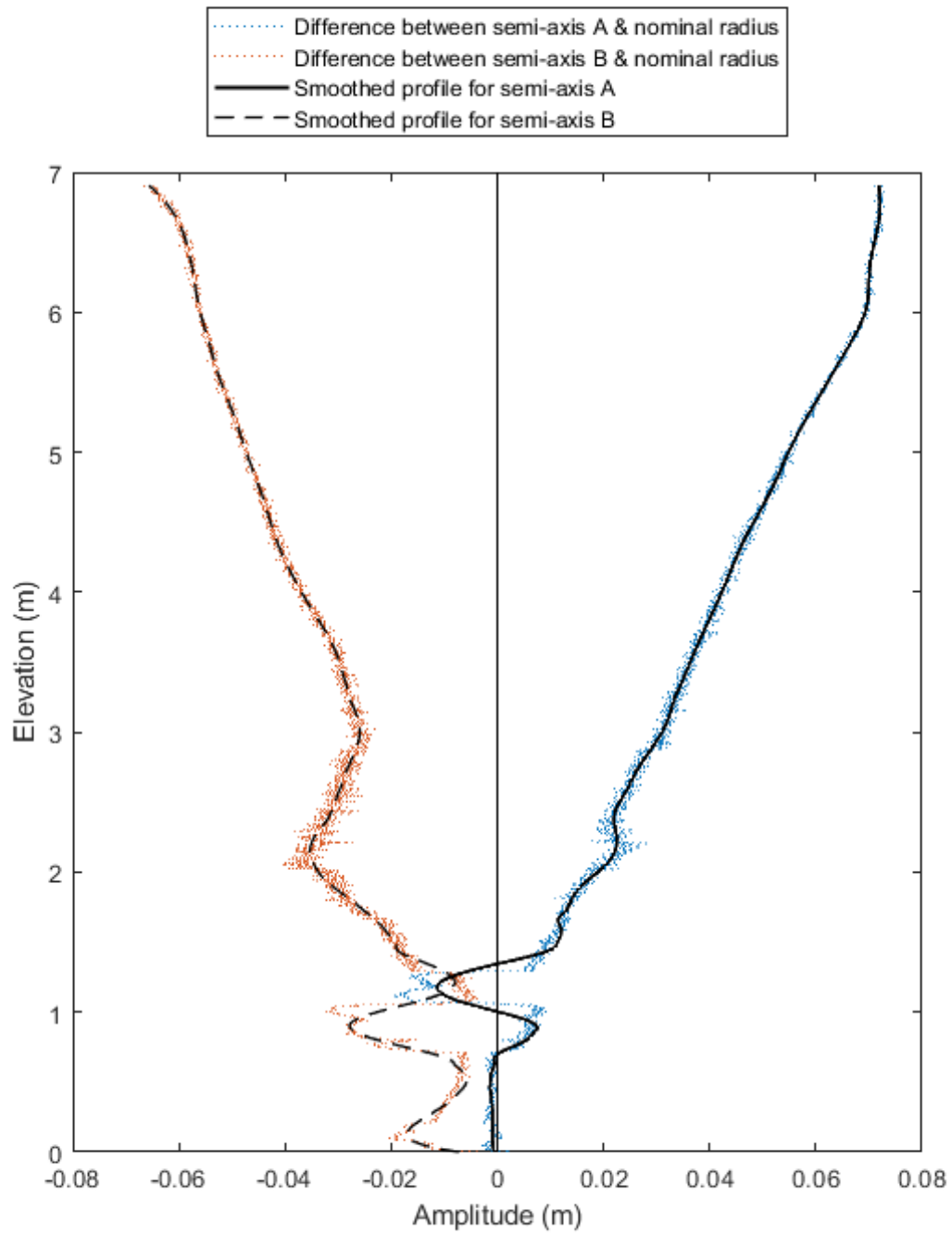
It is clearly demonstrated that most difference between 2 semi-axes lies between 0.2% and 0.5% of the nominal length. Large differences between the two semi-axes occur between  $z = 0.5$  m – 2.5 m, which is around the top edge of longitudinal stiffeners. The inclination angle also fluctuates markedly below  $z = 3$  m but becomes stable at the top. Ovalization effect is close to linear in upper part of the tank. Inclination angle  $\theta$  reaches  $-30.54^\circ$  at the top of the cone. The

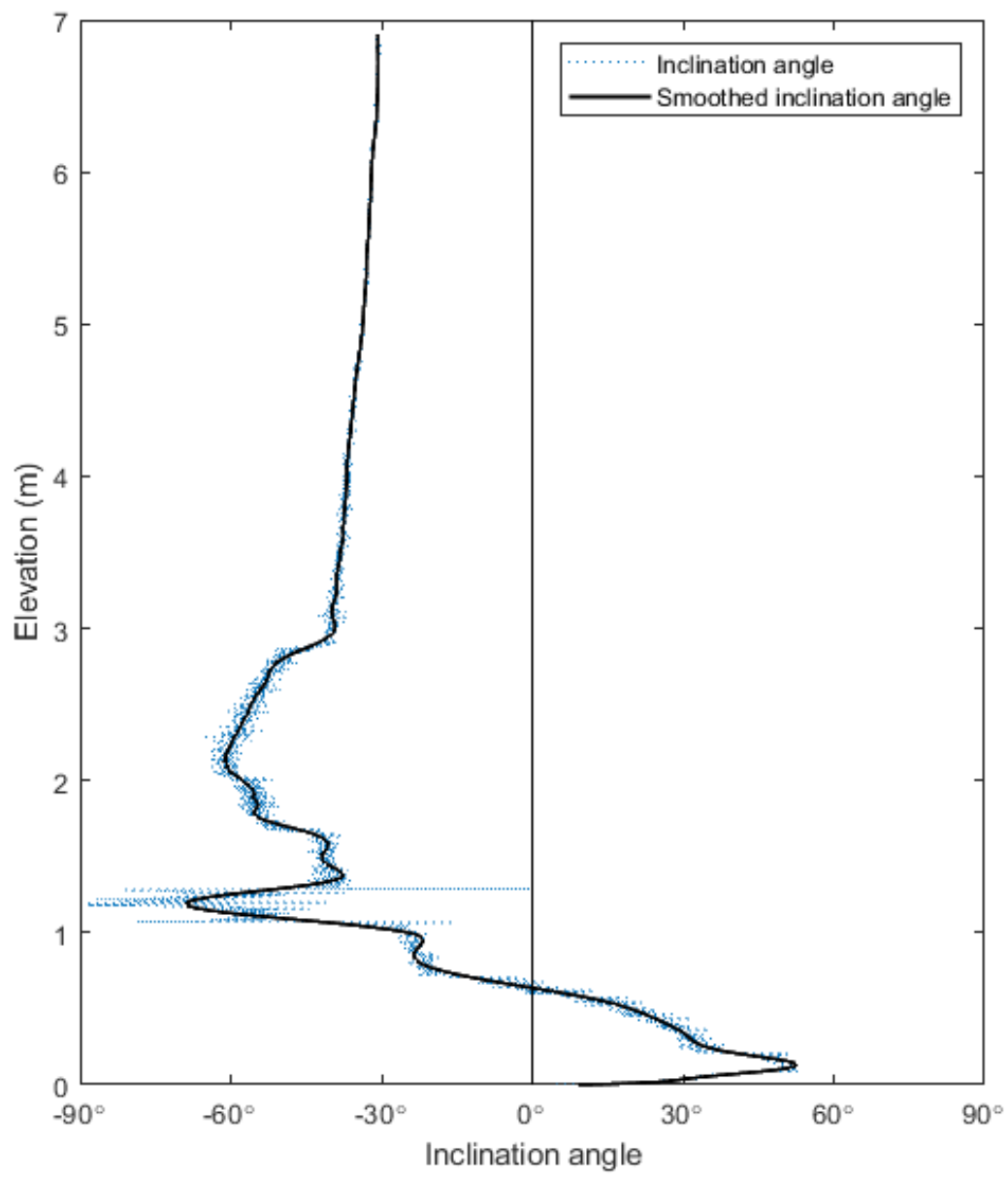
difference between semi-axis A and nominal radius is 0.0708 m at the top. This value is 0.0652 m for semi-axis B. According to the geometry relationship shown in Figure 2.21, the actual global imperfection (perpendicular to the wall) is between -0.349% - 0.379% of nominal radius length at the top of cone. This proportion rapidly drops to a negligible value at the base. The Ovalization effect at the top is illustrated in Figure 2.28.

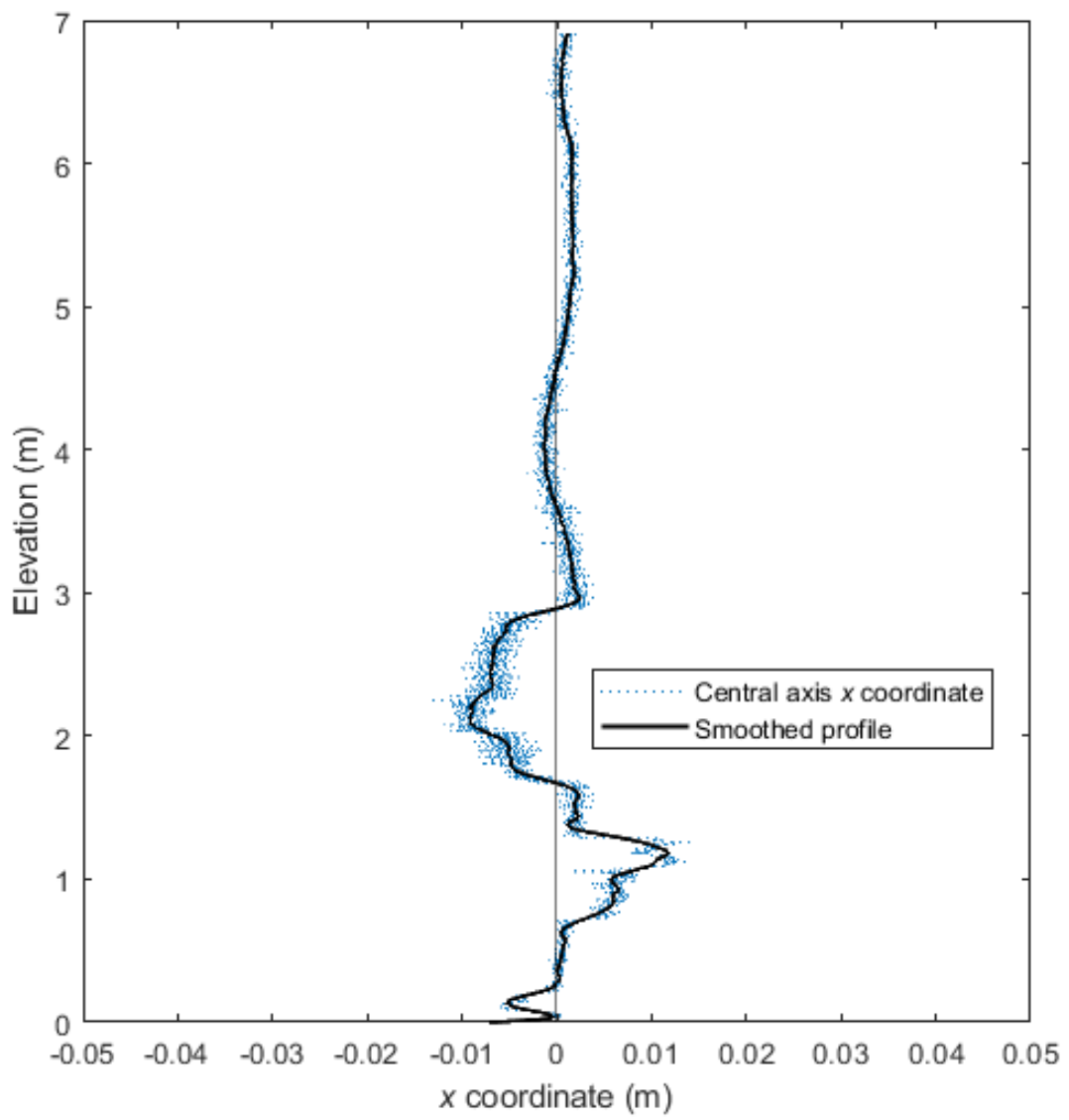


**Figure 0.28 Plan view of ovalization effect on the top of cone (20 times scaled)**

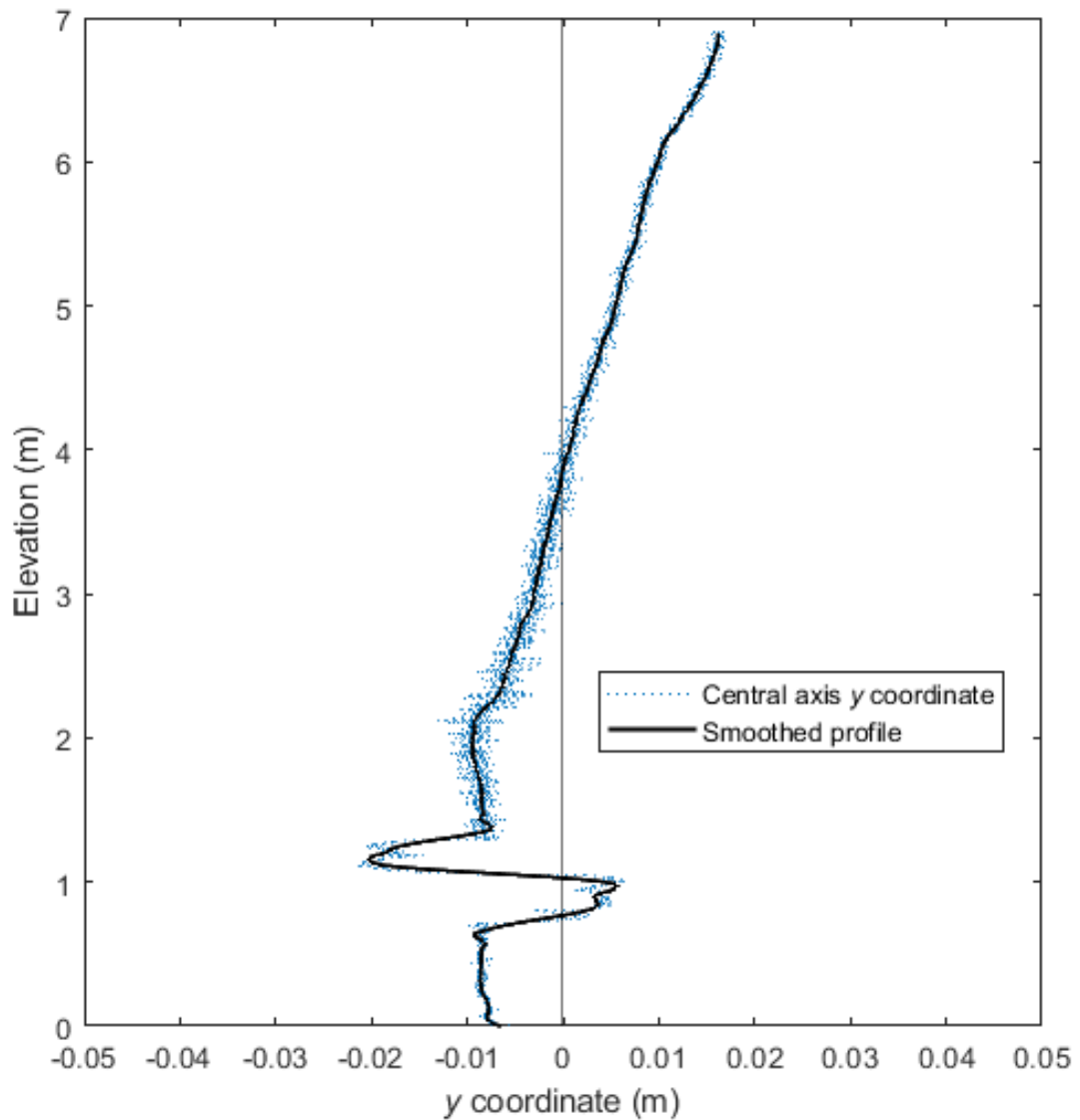
To get a characteristic pattern and eliminate influence from noise, smoothed profiles of shifting semi-axis length, inclination angle, central deviation along  $x$ -axis and  $y$ -axis are generated with the Savitzky-Golay filter and will be employed as global imperfections in later analyzing procedures (shown in Figure 2.29).





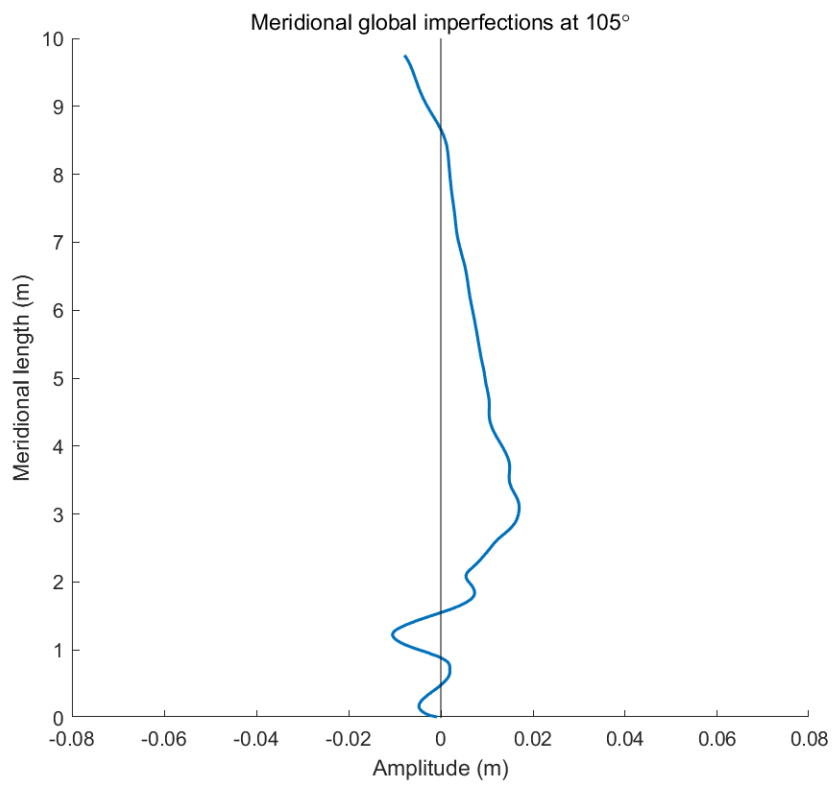
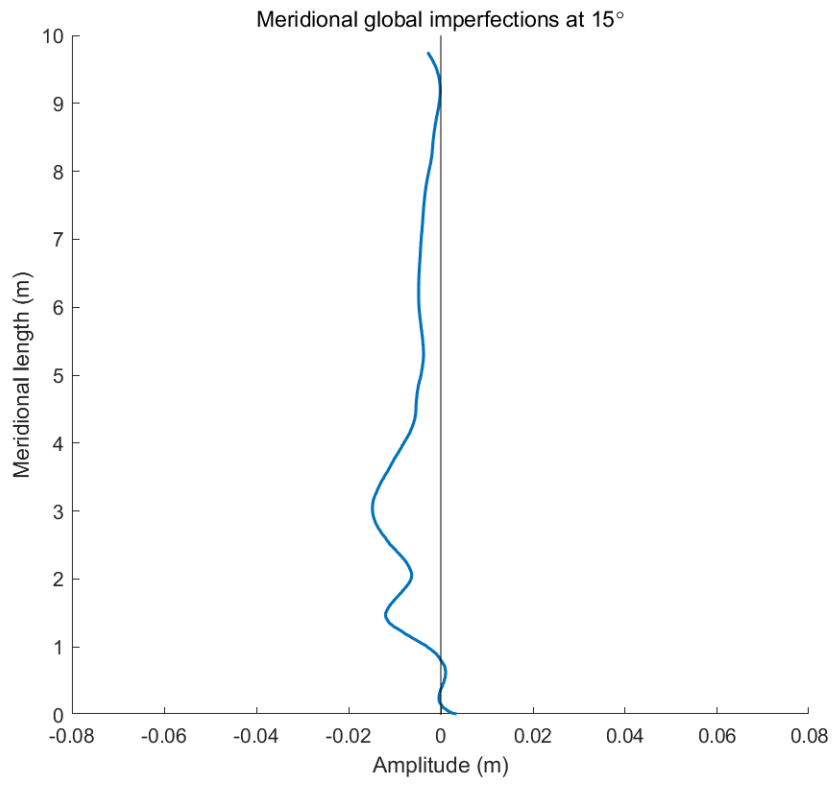


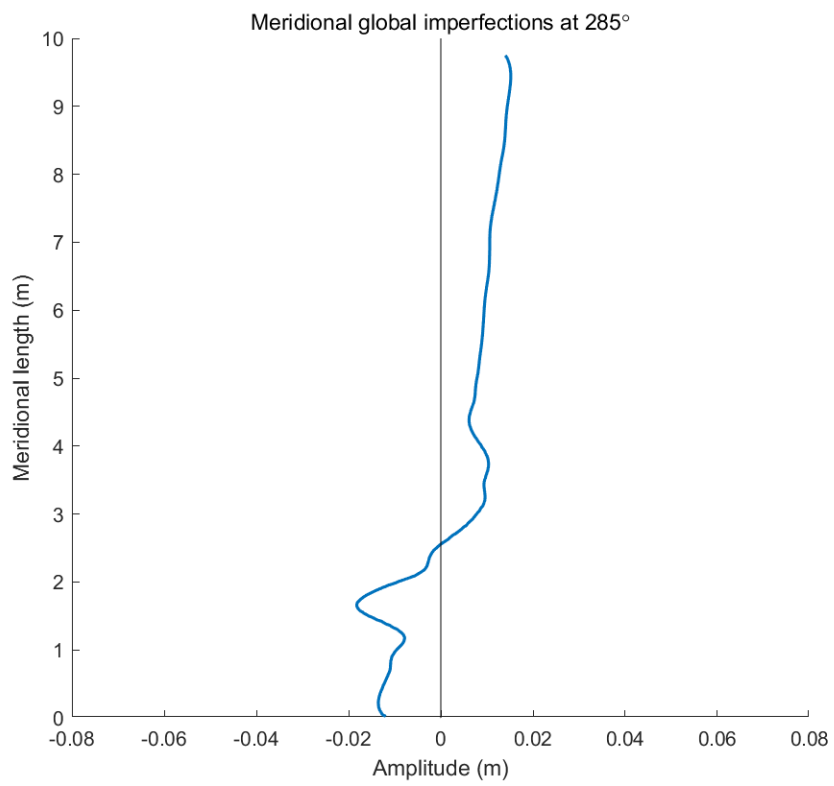
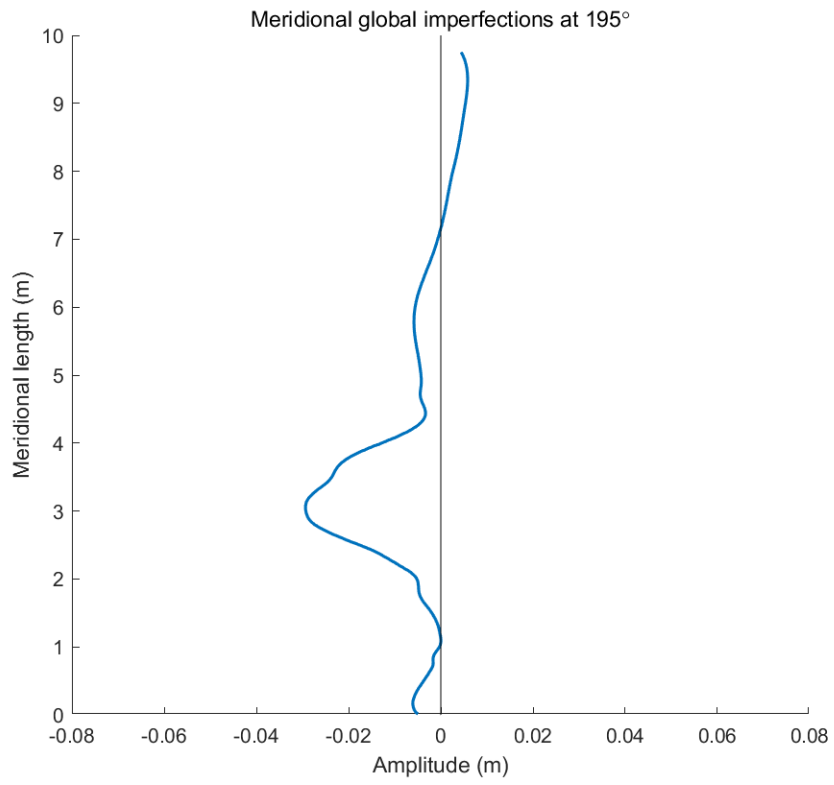




**Figure 0.29 Smoothed profile of global imperfection parameters**

Examples of smoothed global imperfections are depicted along several meridians and circumferences shown in Figure 2.30 and 2.31. Other results are shown in appendices Figure A.5 and Figure A.6.





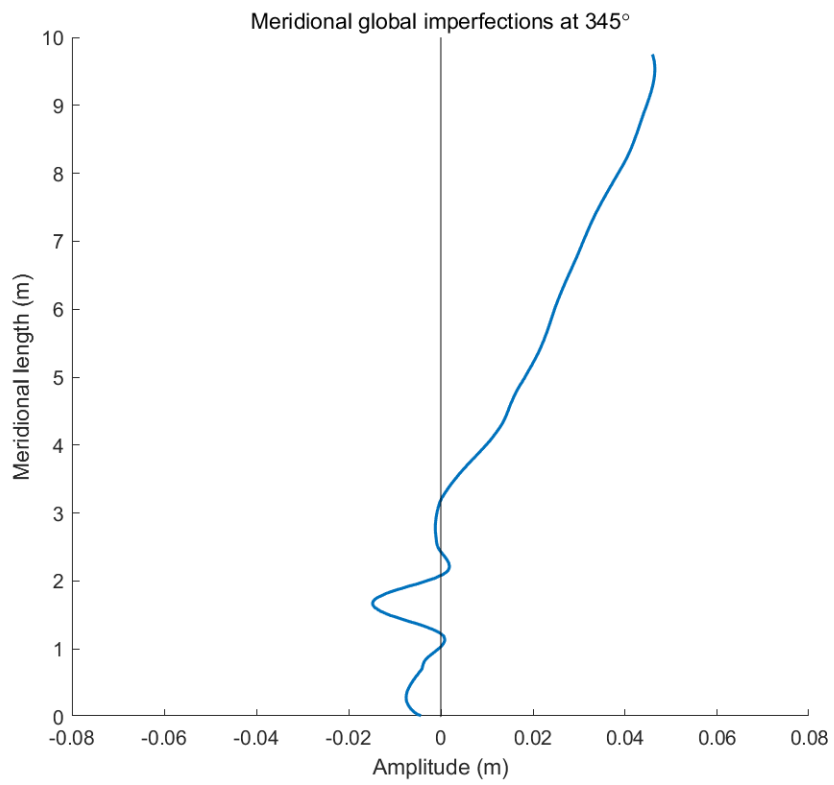
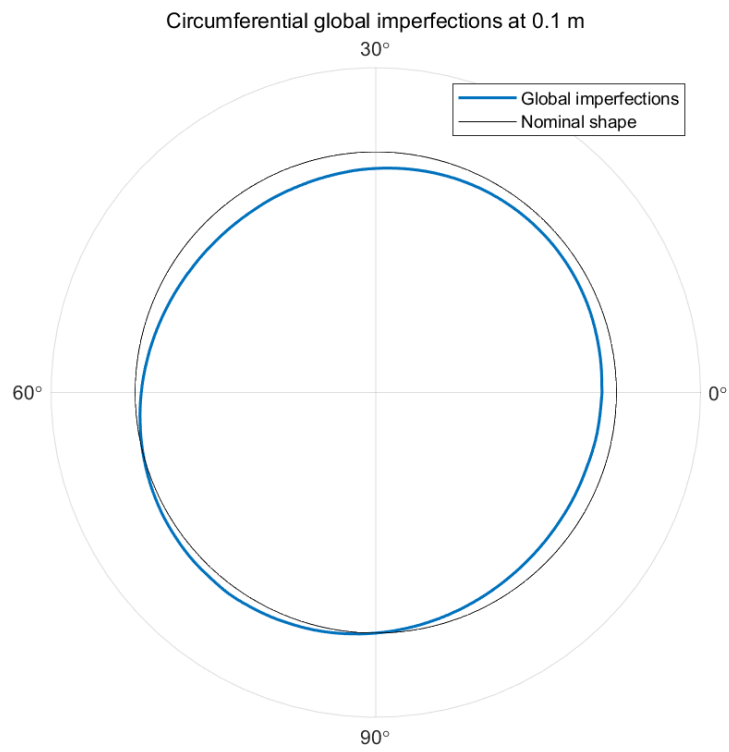
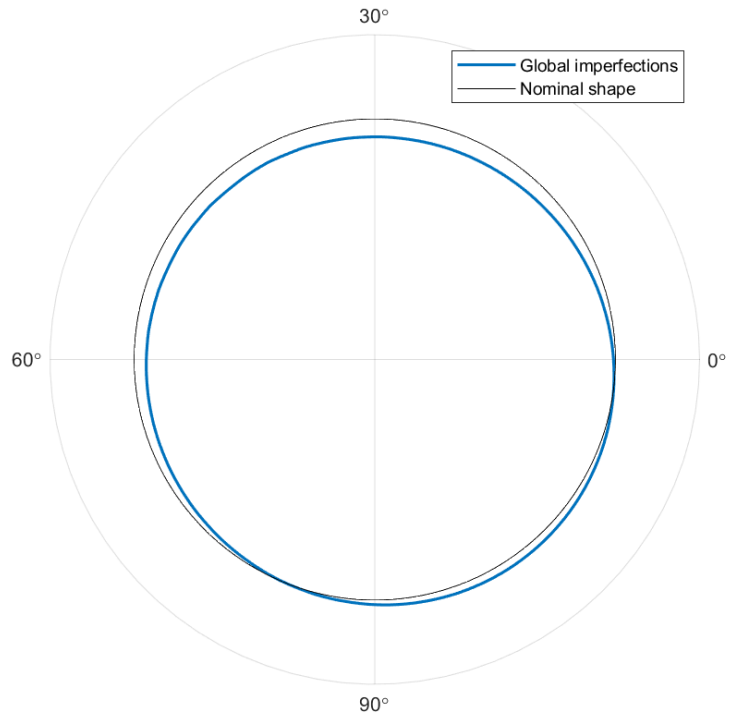


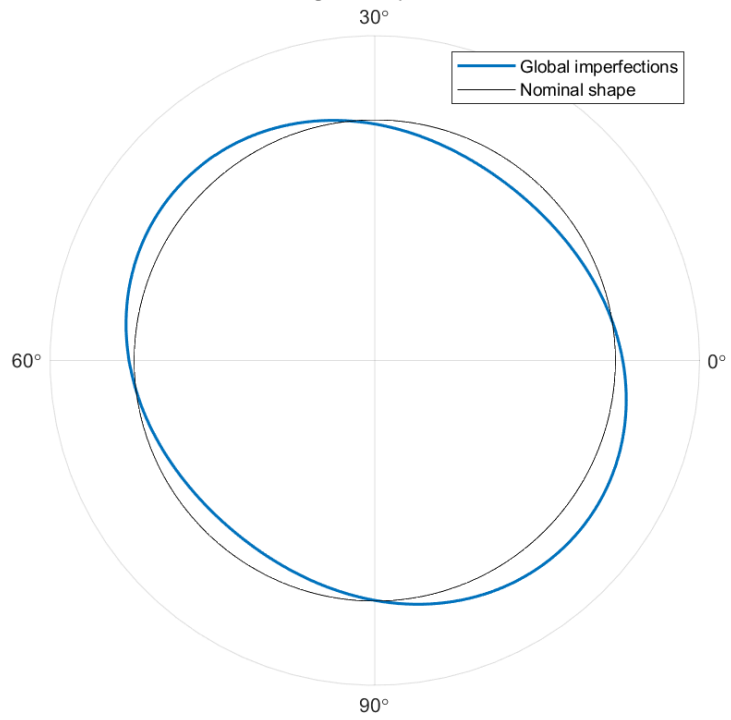
**Figure 0.30 Meridional global imperfections**



Circumferential global imperfections at 1.3 m



Circumferential global imperfections at 3.2 m



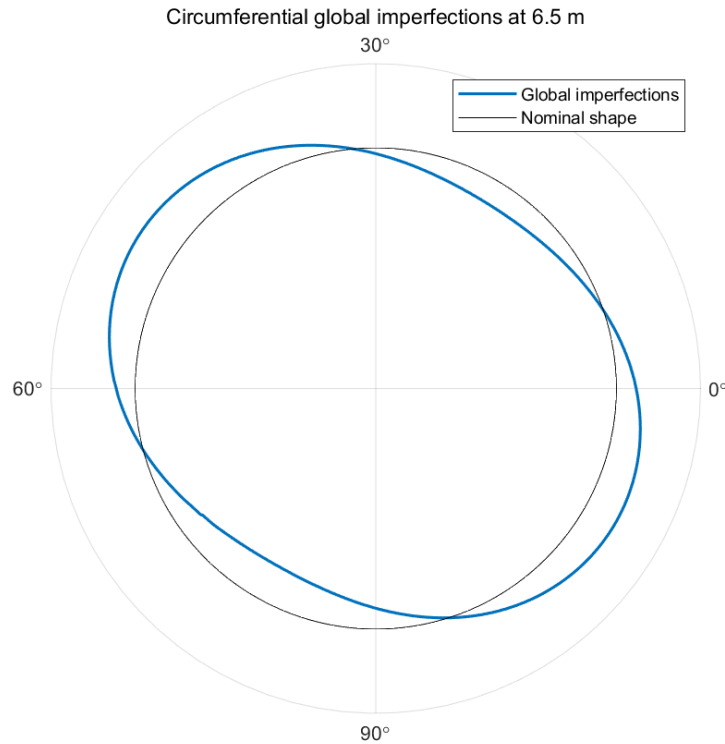


**Figure 0.31 Circumferential global imperfections (40 times scaled)**

## 2.5 Comparison & evaluation

### 2.5.1 Equivalent cylinder

Steel tank design approaches in many standards including AWWA D100 and EN 1993-1-6: 2007 provide consideration for tanks of various shapes. When designing conical tanks, the equivalent cylinder method (ECM) is a commonly used approach. A conical tank will be transformed into a cylinder after several steps and the generated geometry can be used as an approximation. This simplifies the process in analysis, computation and comparison by making analogy to a unified simplest shape. The case in this section has focused on imperfections in conical part of a steel tank while assuming perfect shapes for other parts. Therefore, ECM is conducted on the imperfect cone in order to make comparison with other works and standards. EN 1993-1-6: 2007 provides multiple approaches to calculate the equivalent cylinder according to different sources for the membrane stress. Assuming the meridional compression as the main effect of the membrane stress, dimensions of the equivalent cylinder can be calculated with the

following equations:

$$L_{eq} = L \quad (2 - 31)$$

$$R_{eq} = \frac{R}{\cos \theta} \quad (2 - 32)$$

$$t_{eq} = t \quad (2 - 33)$$

Where:

$L$  : meridional length of the cone.

$L_{eq}$  : meridional length of equivalent cylinder.

$R$  : bottom radius of the cone.

$R_{eq}$  : bottom radius of equivalent cylinder.

$t$  : shell thickness of the cone.

$t_{eq}$  : shell thickness of equivalent cylinder.

According to configuration of loads applied on FEM model in section 2.3.2, where the load condition in real case is simulated, it can be clearly observed that roof loads applied on the outer rim of the tank will be transmitted as a uniform line pressure on the top rim of cone where large meridional compression will result from component force. The effect of hydrostatic pressure on the membrane is complex, especially for stiffened conical tanks. Methods commonly used for evaluation are PCA-CCTWP (1993) simplified methods or finite-element analysis. Previous investigations (Azabi et al. 2016) show that linearly varying hydrostatic pressure exerts hoop tension force and meridional moment on the wall. Inclination of conical shell results in additional meridional compression as the part of membrane stress. Since the hoop tensile stress is unlikely to contribute to buckling failure in steel conical tanks. It is reasonable to assume meridional compression as the main type of membrane stress. The stress effect is shown in Figure 2.32.

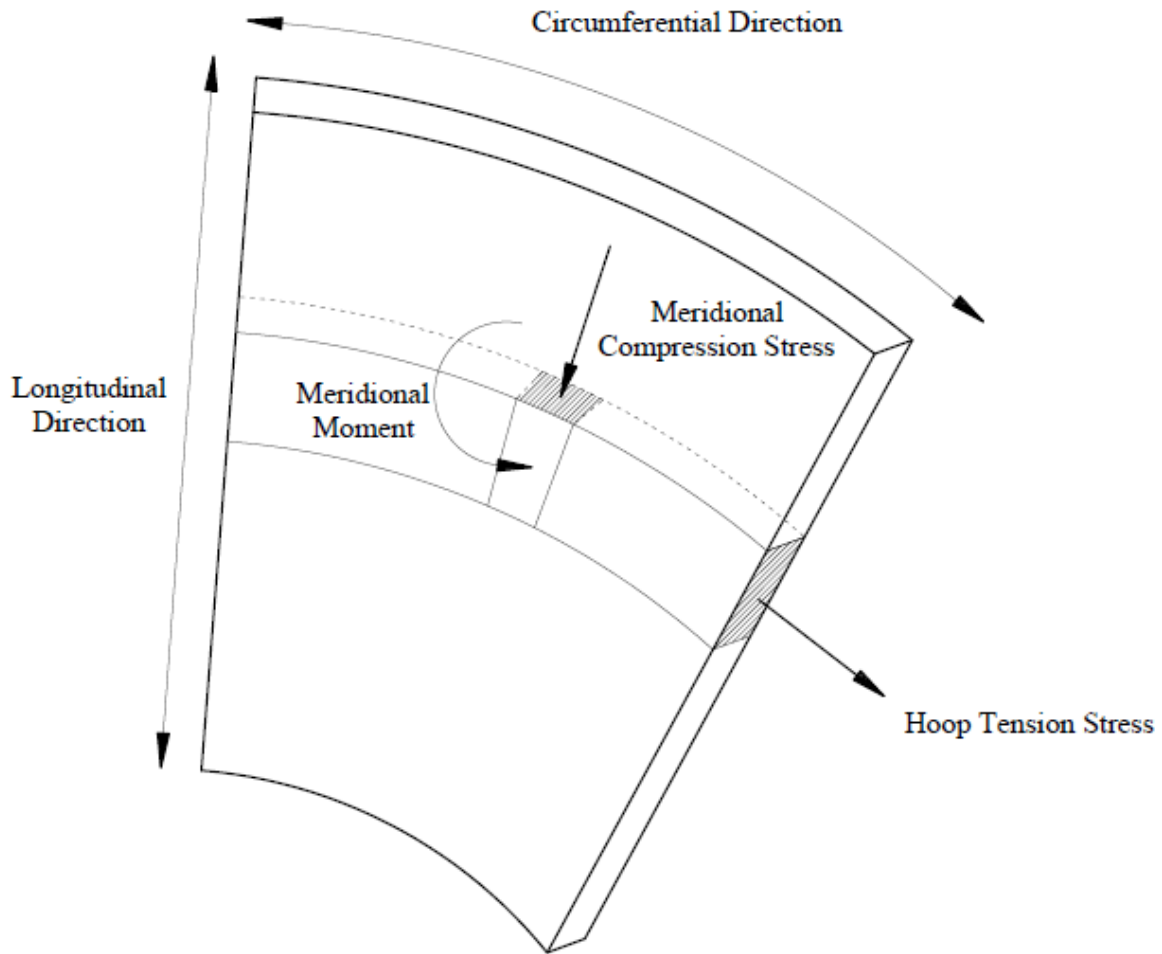


**Figure 0.32 Contribution of hydrostatic pressure to membrane stress**

Due to different shell thickness in two parts of the cone, the calculated equivalent cylinder consists of 2 parts. Both parts share the same radius of 8.908 m. The meridional length is the same height in equivalent cylinder. In the lower part, Height and shell thickness is 2.896 m and 17.4625 mm. In the upper part, Height and shell thickness is 6.9 m and 15.875 mm. This result shown in Figure 2.33(a) will be utilized in comparison to EN 1993-1-6: 2007 and EN 1998-4: 2006 standards.

Many recommendations have been provided in AWWA D100-11 for ECM in the design procedure. El Damatty et al. (2012) provide a few equations to generate the dimensions of equivalent cylinder, which give a good approximation in seismic design and analysis:

$$H_{eq} = \frac{H}{\cos \theta} \quad (2 - 34)$$

$$R_{eq} = \frac{2R + H \tan \theta}{2 \cos \theta} \quad (2 - 35)$$

$$t_{eq} = t \quad (2 - 36)$$



Where:

$H$  : total height of the cone.

$R_{eq}$  : radius of the equivalent cylinder.

$H_{eq}$  : total height of the equivalent cylinder.

This calculated equivalent cylinder also consists of 2 parts. Both parts share the same radius of 13.806 m. Height and shell thickness of the lower part is 2.896 m and 17.4625 mm. Height and shell thickness of the upper part is 6.9 m and 15.875 mm. This result shown in Figure 2.33(b) will be utilized in comparison with AWWA D100 standard.

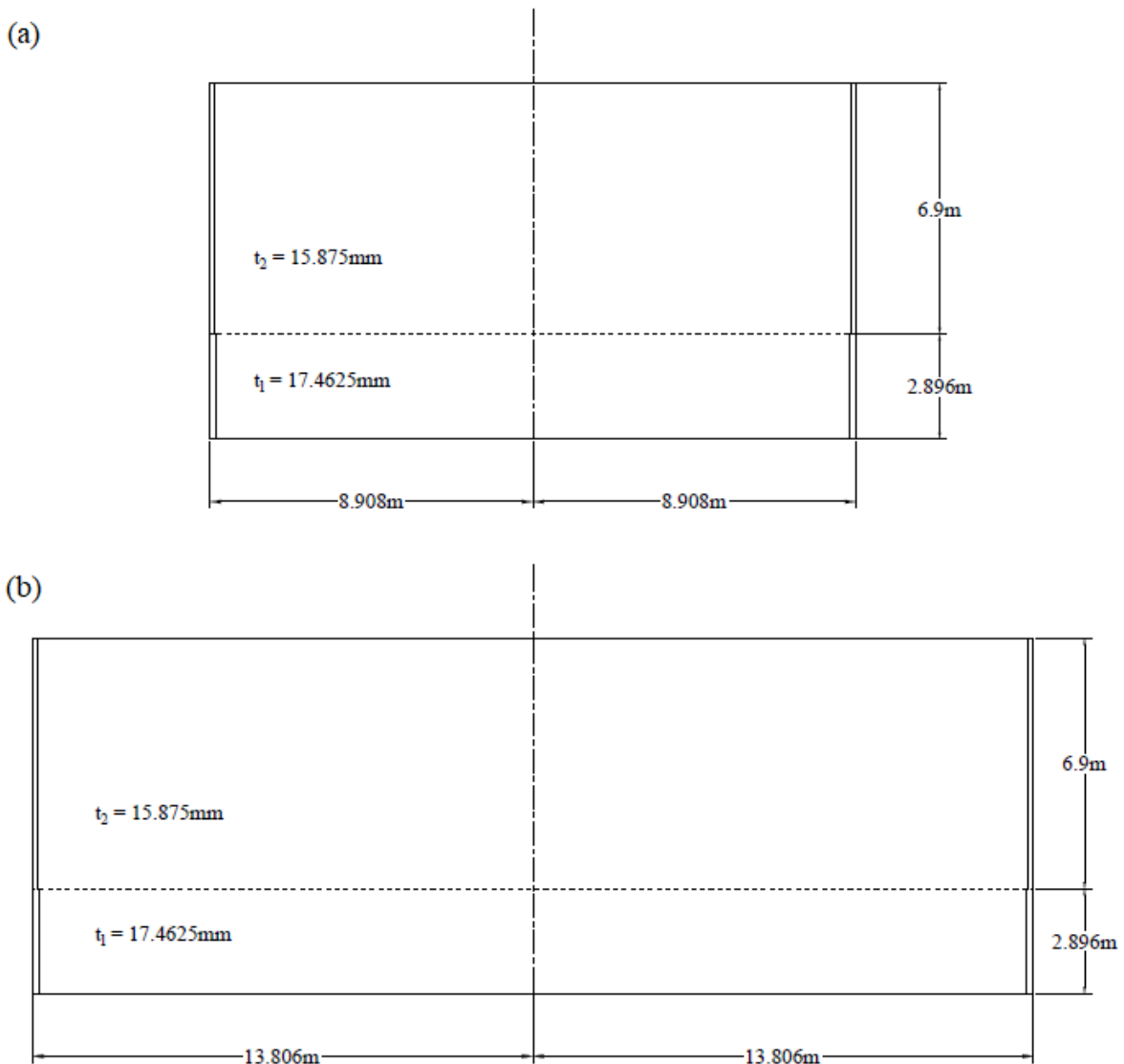


**Figure 0.33 Equivalent cylinders in (a) EN 1993-1-6: 2007; (b) AWWA D100-11 standards**

## 2.5.2 Evaluation of meridional & circumferential imperfections

### 2.5.2.1 Evaluation with specification in AWWA D100-11

In this case, the global imperfection (described in section 2.4.3) mainly results from linearly increased ovalization effect on a cone. Therefore, equivalent cylinder is employed for comparison. The maximum deviation of major & minor axis in the cone is 0.536% and 0.494%. According to section 2.1.2, maximum global imperfections at 0.3 m shall be compared with criteria. The upper and lower bound are chosen from smoothed curve of semi-axes, which are 1.3 mm – 10.5 mm. The radius of equivalent cylinder is 27.612 m. Therefore, the radius tolerance in AWWA standard is  $\pm 13$  mm -  $\pm 19$  mm. The tank in the case study satisfies the global imperfection criteria. The local imperfection tolerance is calculated under the assumption of imperfection wavelength. For the upper part, imperfection amplitude and wavelength are given as:

$$L_m = 4\sqrt{Rt} = 4 \times \sqrt{13.806 \times 15.875 \times 10^{-3}} = 1.8726 \text{ m}$$

$$\delta = 0.01L_m = 0.01 \times 1.8726 = 0.018726 \text{ m}$$

For the lower part, these values are calculated as:

$$L_m = 4\sqrt{Rt} = 4 \times \sqrt{13.806 \times 17.4625 \times 10^{-3}} = 1.964 \text{ m}$$

$$\delta = 0.01L_m = 0.01 \times 1.964 = 0.01964 \text{ m}$$

Given any angle  $\theta$  on an inclined ellipse, the difference between oval radius from a perfect circle radius is given as:

$$\Delta = \left| A \cos \left[ \arctan \left( \frac{A}{B} \tan(\theta - \varphi) \right) \right] \right| \times \sqrt{1 + \tan^2(\theta - \varphi)} - R \quad (2 - 37)$$

Where:

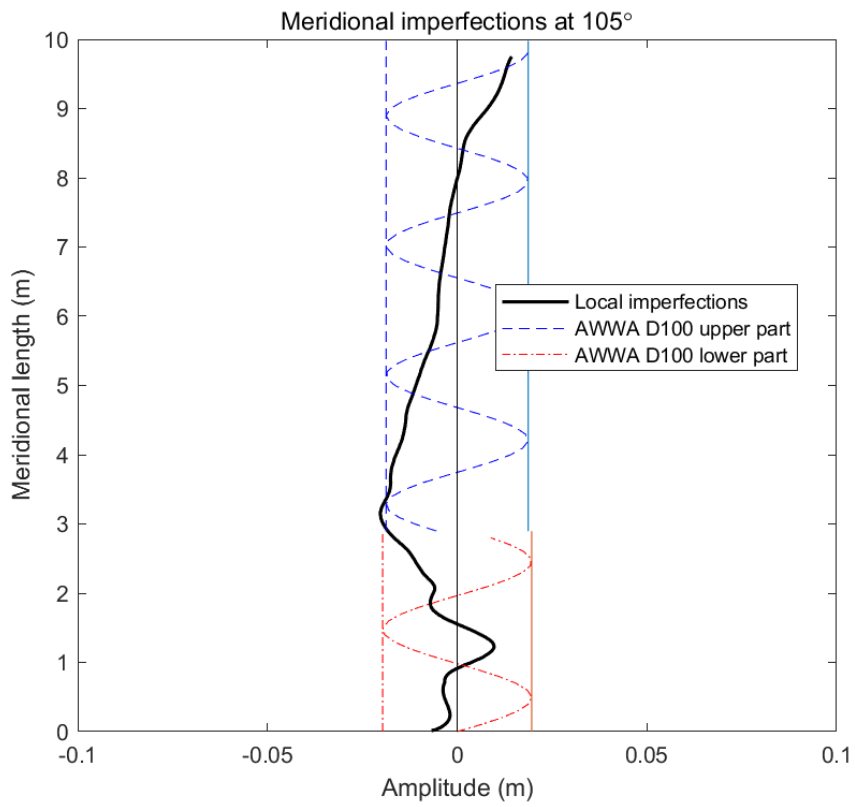
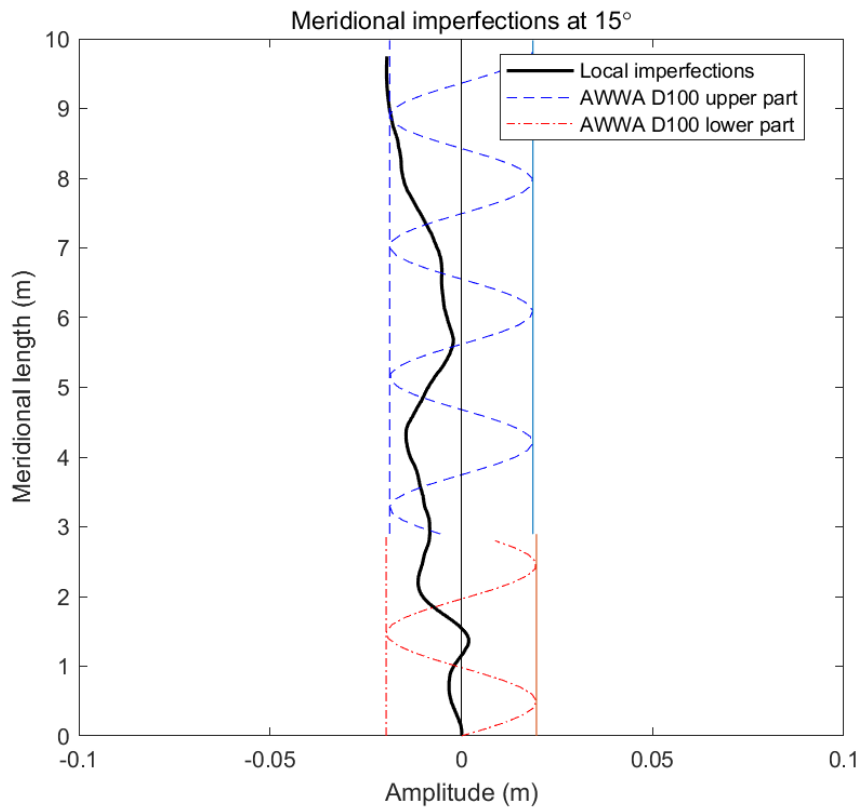
$A, B$  : semi-major/semi-minor axis of the ellipse.

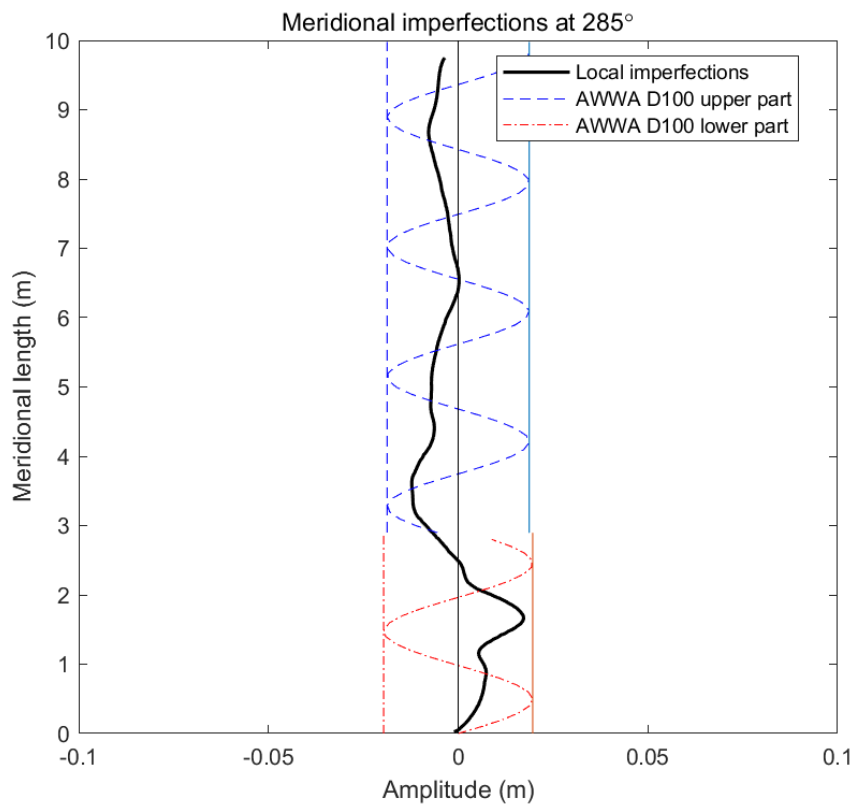
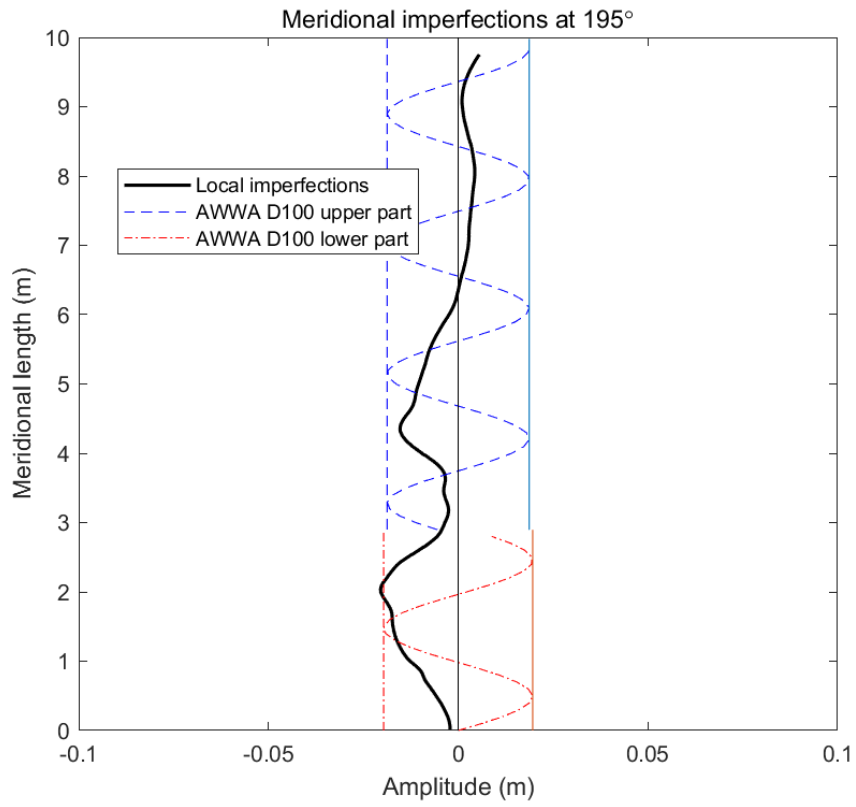
$R$  : radius of perfect circle.

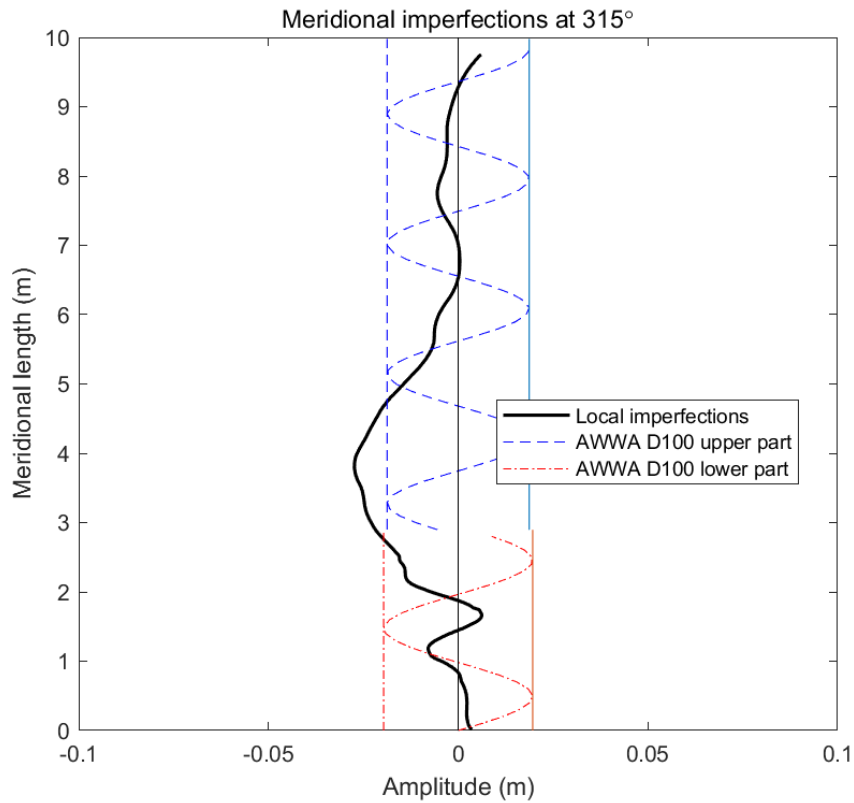
$\varphi$  : inclination angle of ellipse.

In this way, local imperfections are generated by removing ovalization effects from multiple meridional imperfections. Results are collected for the following comparison and evaluation based on criteria and assumptions in design codes. Examples of the comparison is shown in

Figure 2.34. Other results are shown in appendix Figure A.7.



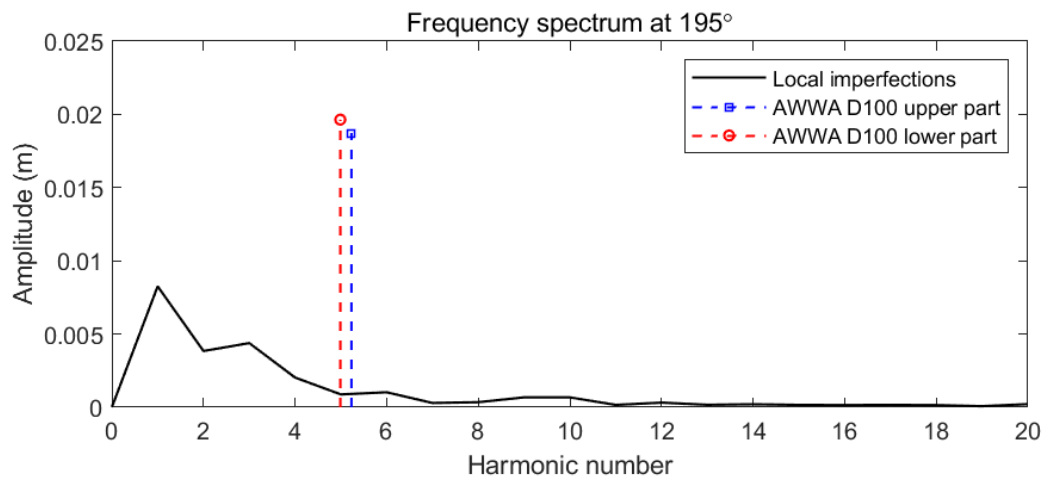
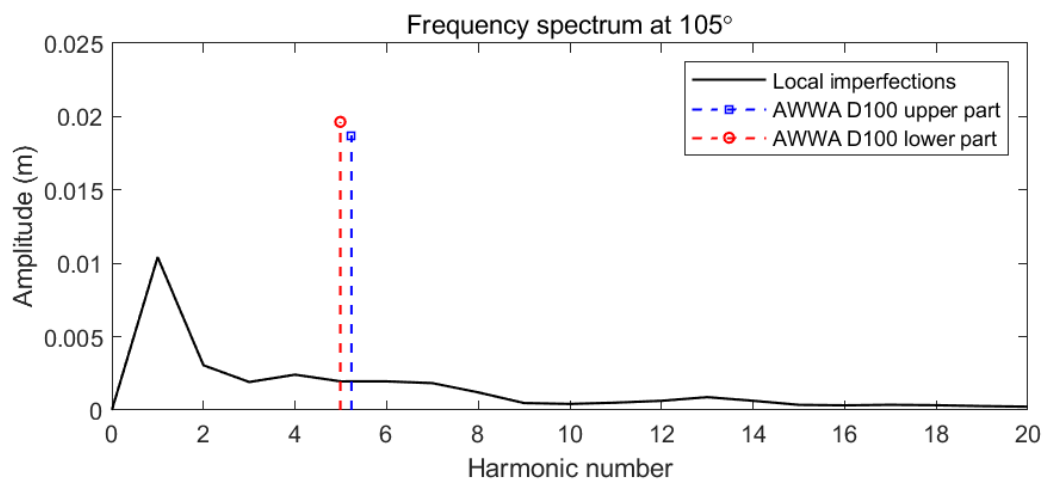
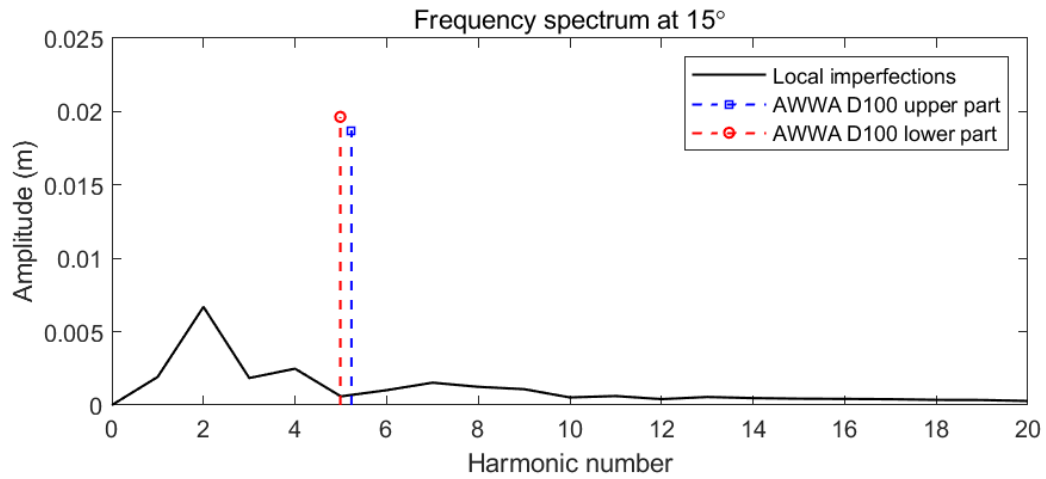




**Figure 0.34 Evaluation of local imperfection amplitude with specifications in AWWA D100-11**

It can be observed in the result that imperfection amplitude varies markedly among meridians. For most meridians, local imperfections do not exceed the criteria or only exceed a little. However, some meridians contain large imperfections compared with the tolerance. In several meridians around 75°, 105°, 165°, 225°, 255°, 315°, very large imperfections occur between elevations 2 m - 4 m.

The assumption of sinusoid wave of local imperfections does not fit the real case for most meridians: few parts have shown the imperfection in such a pattern. In order to make an accurate evaluation, 1D Fourier transform is conducted on meridians and examples of results of first 20 harmonic numbers are shown in Figure 2.35. Other results are shown in appendix Figure A.8.



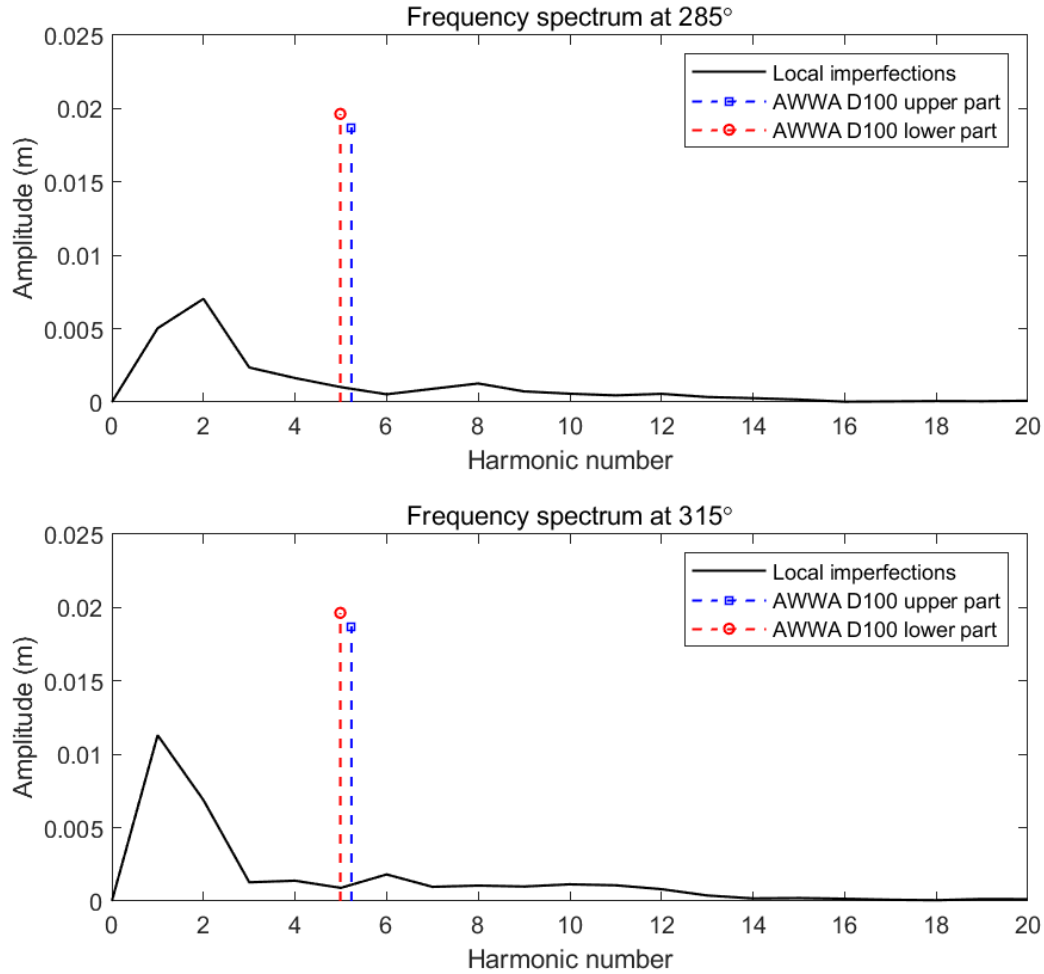


**Figure 0.35 Evaluation of local imperfection wavelength with specifications in AWWA D100-11**

Wavelength of each harmonic number  $l_m$  can be calculated as:

$$l_m = \frac{L}{N} \quad (2 - 38)$$

Where:

$l_m$  : wavelength of each harmonic number.

$L$  : meridian length.

$N$  : harmonic number.

Figure 2.35 indicates clearly that most harmonic components accumulate at the low frequency part. The wavelength of largest component is close to meridional length, which is much higher than AWWA D100-11 assumptions. The wavelength of the 2<sup>nd</sup> peak on several meridians is close to one-third of the meridian length. Still, main components at the 3<sup>rd</sup> - 6<sup>th</sup> peaks gather around the assumed wavelength with comparably small amplitudes. Therefore, the specified

imperfection shape in AWWA D100-11 has a little effect this case. The assumed wavelength is much shorter than the main wavelength of measured meridional imperfection.

### 2.5.2.2 Evaluation with specification in EN 1993-1-6: 2007

Meridional imperfections in EN 1993-1-6: 2007 is also classified into global and local components. Furthermore, local components are classified into meridional eccentricity and small dimples. Different from the AWWA D100-11 standard, no assumptions of imperfection shape have been mentioned, let alone assumptions on wavelength. According to section 2.1.2, the parameter  $U_r$  can be calculated using difference between major & minor axis of the equivalent cylinder:

$$d_{\max} = (1 + 0.536\%) \times 2 \times (8.908 - 15.875 \times 10^{-3}) = 17.8796 \text{ m}$$

$$d_{\min} = (1 - 0.494\%) \times 2 \times (8.908 - 15.875 \times 10^{-3}) = 17.6964 \text{ m}$$

Where the deviation of diameter at the top is 0.494% - 0.536%. nominal radius of interior tank wall at the top is calculated as  $8.908 - 15.875 \times 10^{-3} = 8.8922 \text{ m}$ .

$$U_r = \frac{17.8796 - 17.6964}{(8.908 - 15.875 \times 10^{-3}) \times 2} = 0.0103 < 0.015$$

Since the diameter of the equivalent cylinder is over 1.25 m, we can see from comparison that global imperfections in this case satisfy class C, which means the tank has a normal fabrication quality.

For the evaluation of local imperfections, the ovalization effect is removed to extract local components. Since the scan data records geometrical information on the exterior surface, no eccentricity is checked in this case. Based on the criteria, local dimples are evaluated only in meridional and circumferential directions since no information of welds has been collected. Parameters are calculated with geometry of equivalent cylinder.

For the upper part with thin shells:

$$l_{gx} = 4 \times \sqrt{8.908 \times 15.875 \times 10^{-3}} = 1.5042 \text{ m}$$

$$l_{g\theta} = 2.3 \times (9.796^2 \times 8.908 \times 15.875 \times 10^{-3})^{0.25} = 4.4144 \text{ m} \leq 8.908 \text{ m}$$

For the lower part with thick shells:

$$l_{gx} = 4 \times \sqrt{8.908 \times 17.4625 \times 10^{-3}} = 1.5776 \text{ m}$$



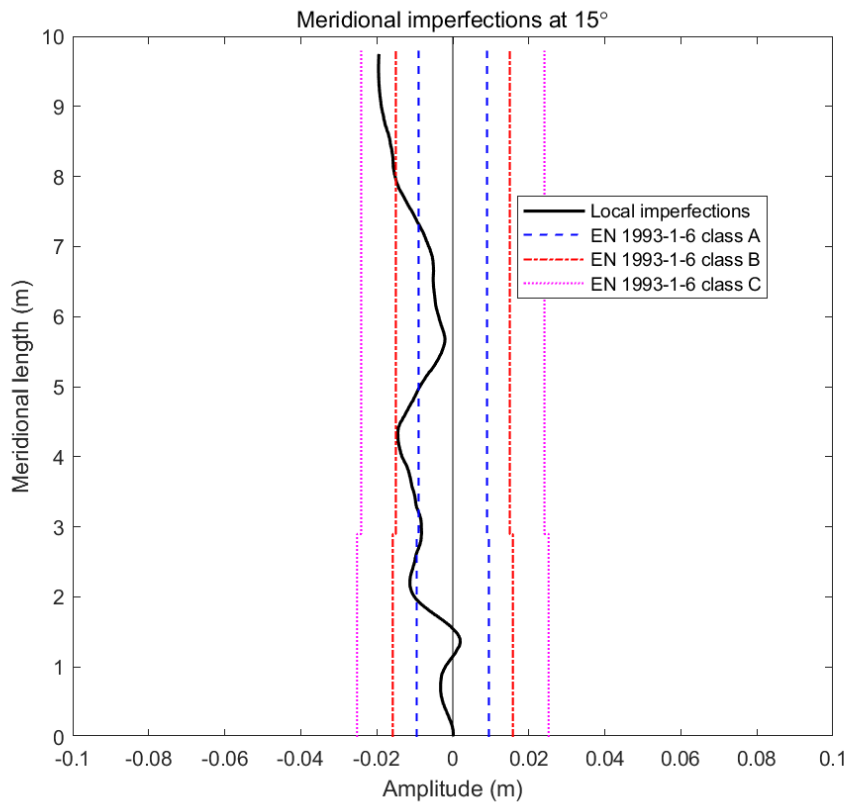
$$l_{g\theta} = 2.3 \times (9.796^2 \times 8.908 \times 17.4625 \times 10^{-3})^{0.25} = 4.5209 \text{ m} \leq 8.908 \text{ m}$$

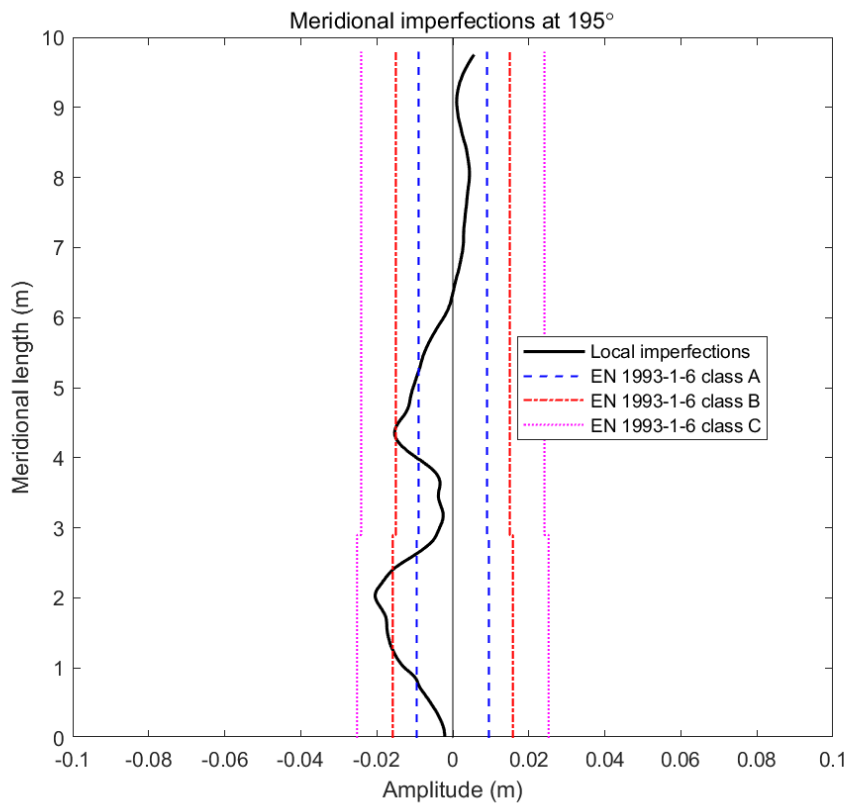
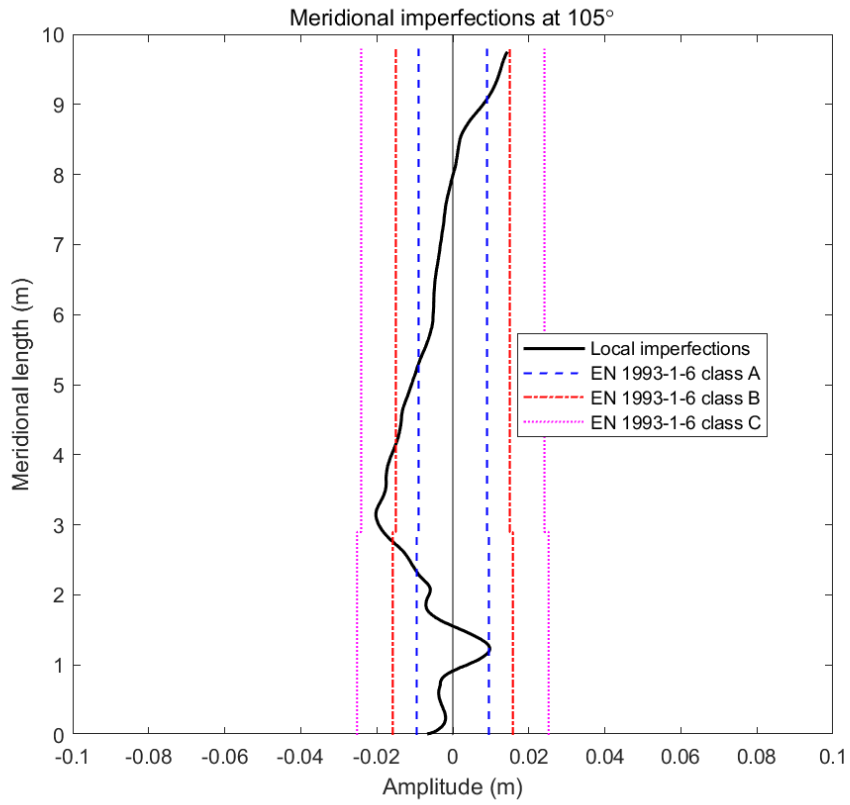
The limitations on local imperfection amplitude are computed based on tolerance of each quality class calculated in Table 2.4.

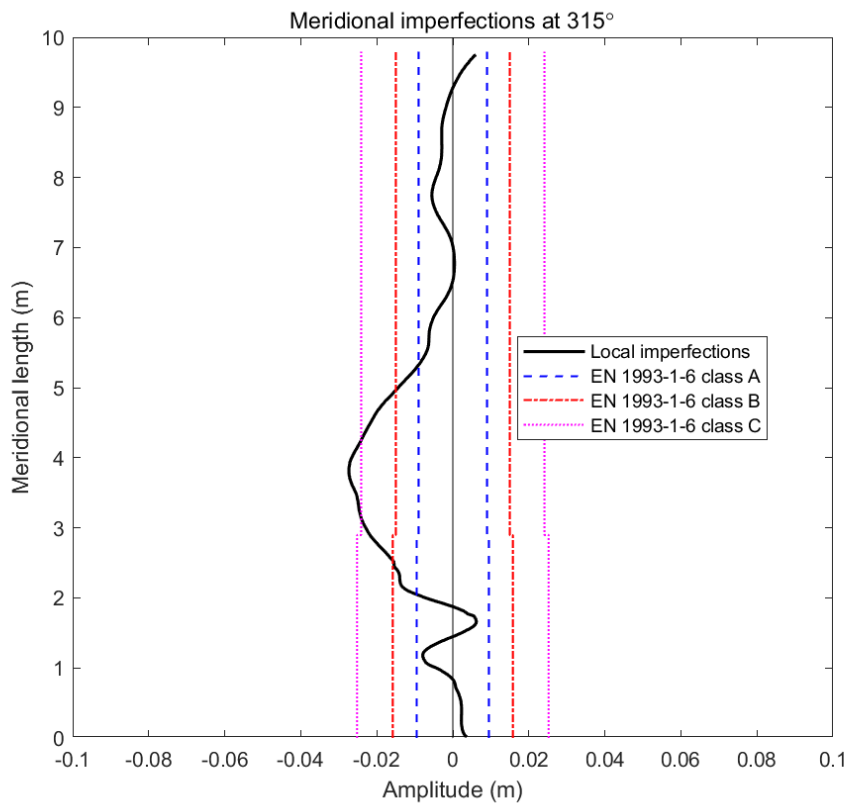
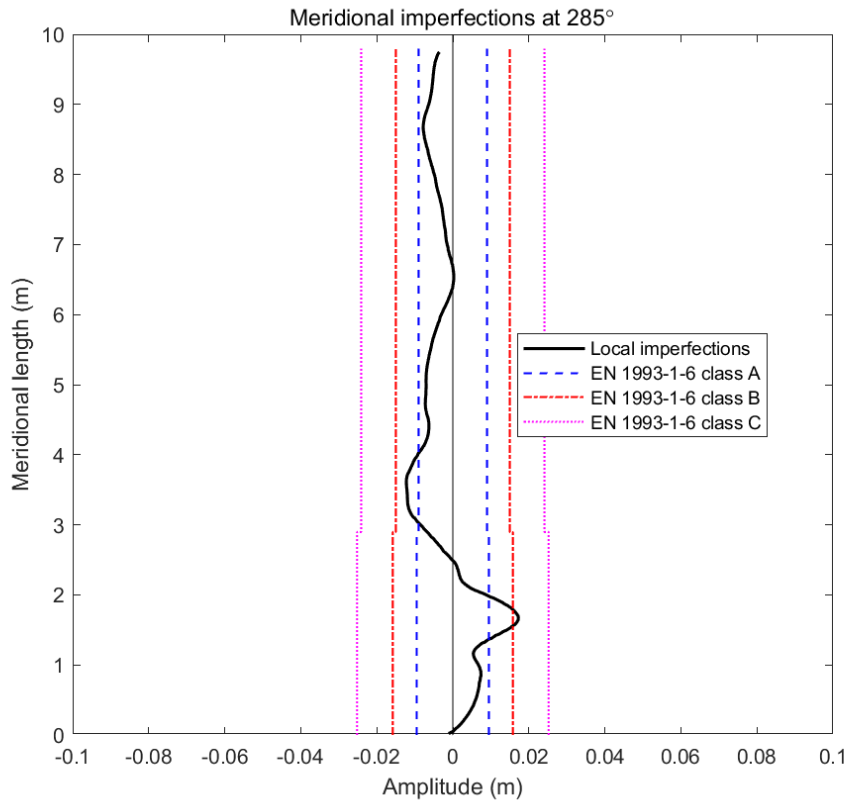
**Table 0.4 Local imperfection amplitude tolerance in EN 1993-1-6: 2007**

| Fabrication Quality<br>Class | Upper Part<br>( $t_1 = 15.875 \text{ mm}$ ) |                 | Lower Part<br>( $t_2 = 17.4625 \text{ mm}$ ) |                 |
|------------------------------|---|-----------------|--|-----------------|
|                              | Meridional                                  | Circumferential | Meridional                                   | Circumferential |
|                              | Class A (Excellent)                         | 0.009 m         | 0.0265 m                                     | 0.0095 m        |
| Class B (High)               | 0.015 m                                     | 0.0441 m        | 0.0158 m                                     | 0.0452 m        |
| Class C (Normal)             | 0.0241 m                                    | 0.0706 m        | 0.0252 m                                     | 0.0723 m        |

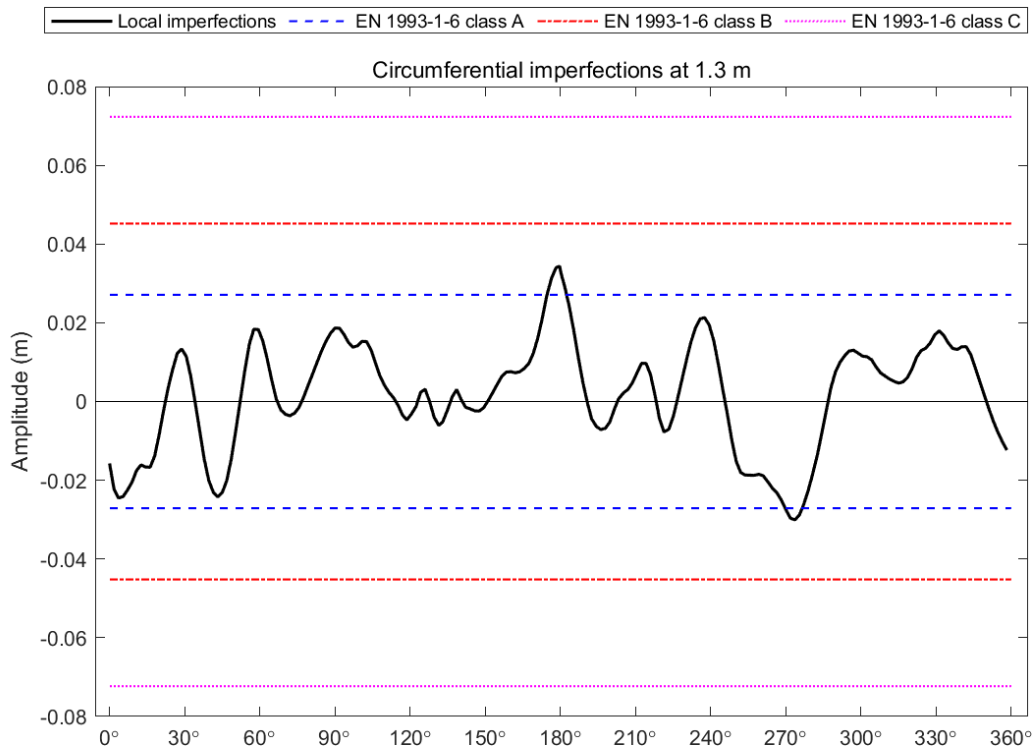
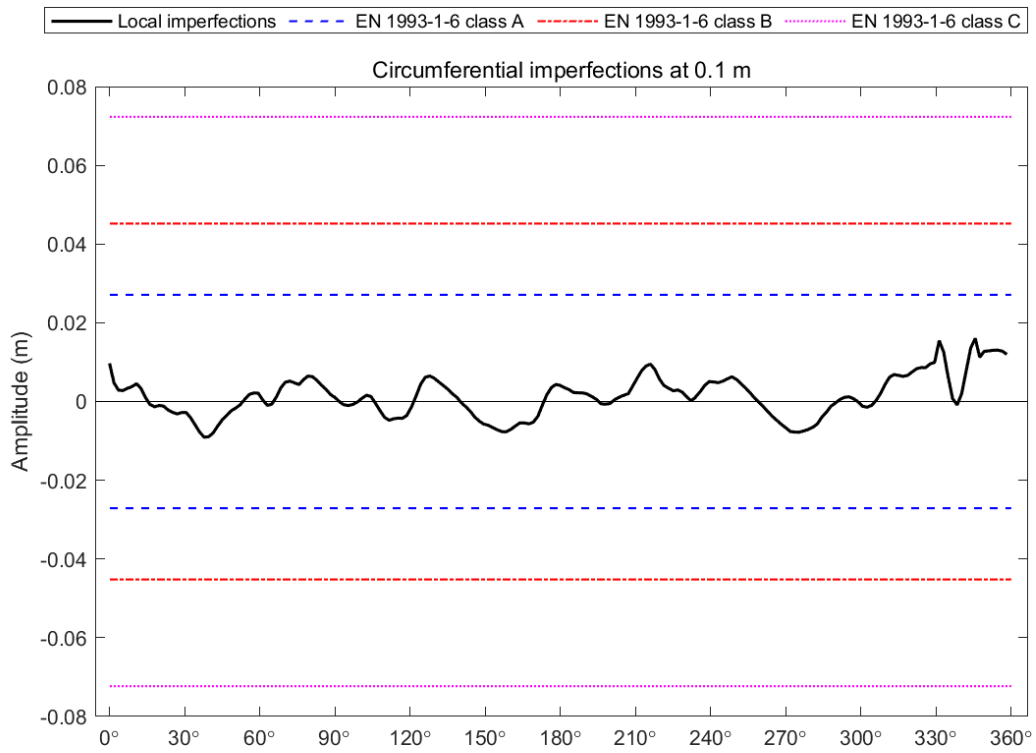
Examples of comparison of meridional imperfections are shown in Figure 2.36. Examples of circumferential results are shown in Figure 2.37. Other results are shown in appendices Figure A.9 and Figure A.10.







**Figure 0.36 Evaluation of meridional local imperfection amplitude with specifications in EN 1993-1-6: 2007**



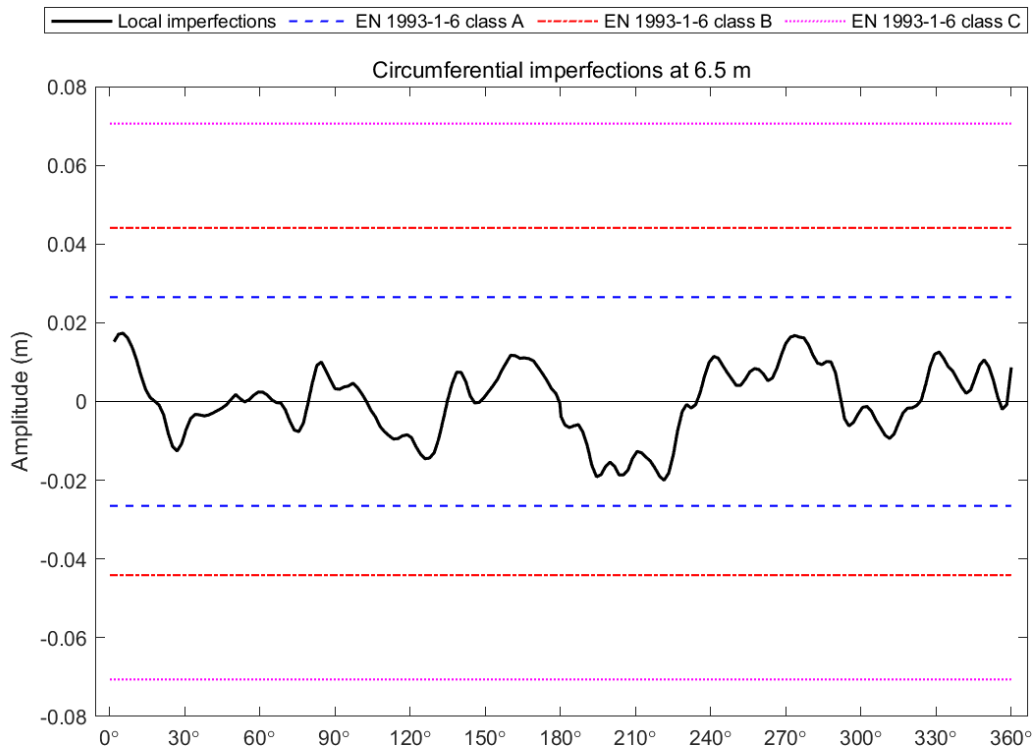
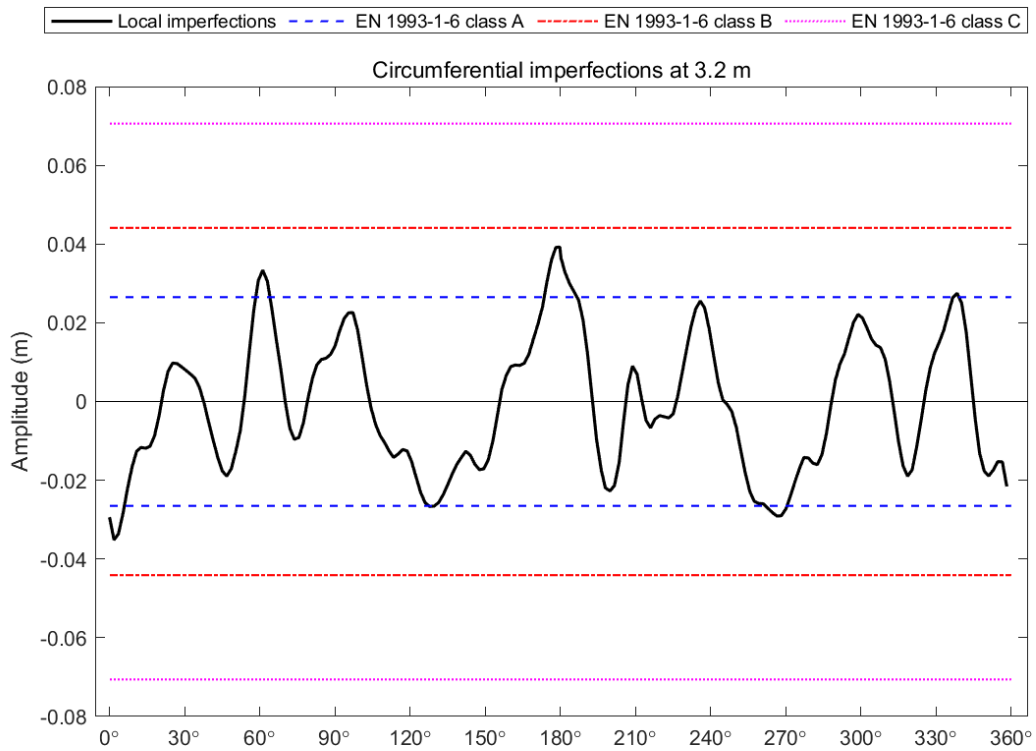


**Figure 0.37 Evaluation of circumferential local imperfection amplitude with specifications in EN 1993-1-6: 2007**

For EN-1993-1-6: 2007 standard, imperfections on meridians around 135° satisfy class B. Most meridians satisfy class C. Imperfections in the meridian at 315° slightly exceed the Class C tolerance. Imperfections around 75° exceed markedly the Class C tolerance between 2 m – 4 m.

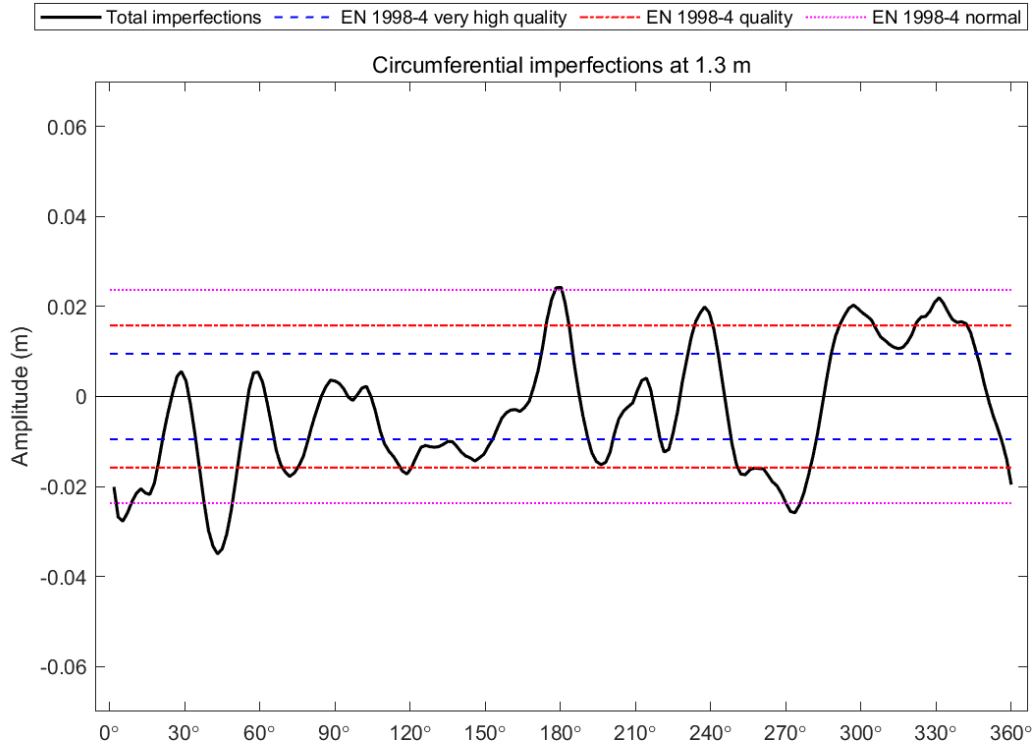
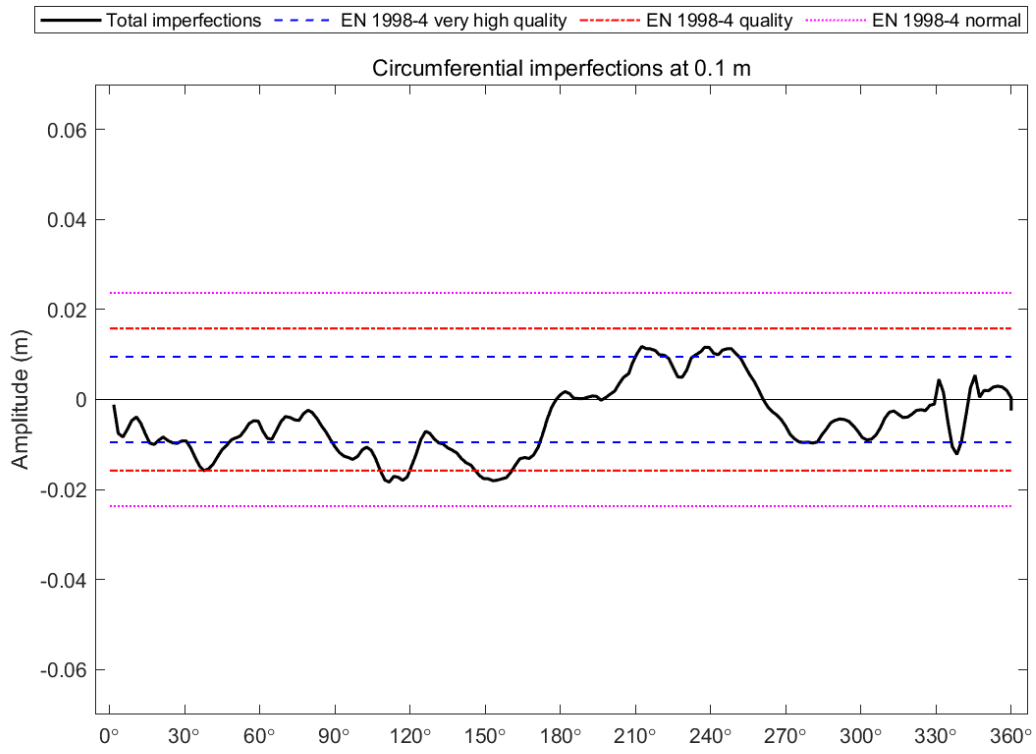
In circumferential results, imperfections around 0.1 m, 0.5 m and 6.5 m satisfy class A. Class B is satisfied by circumferences around 0.9 m, 1.3 m, 1.7 m, 3.2 m, 4.3 m, 5.4 m. Circumferences at 2.1 m still satisfy class C. It can be generally concluded that due to the violation in meridional direction. This case does not satisfy local imperfection criteria in EN-1993-1-6: 2007.

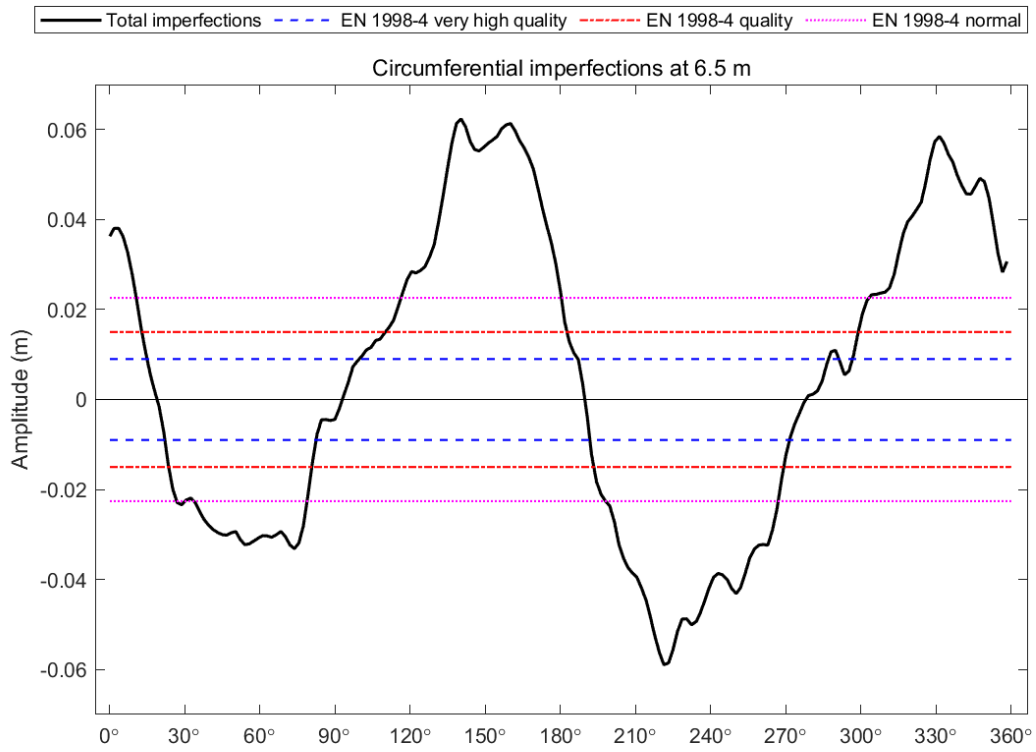
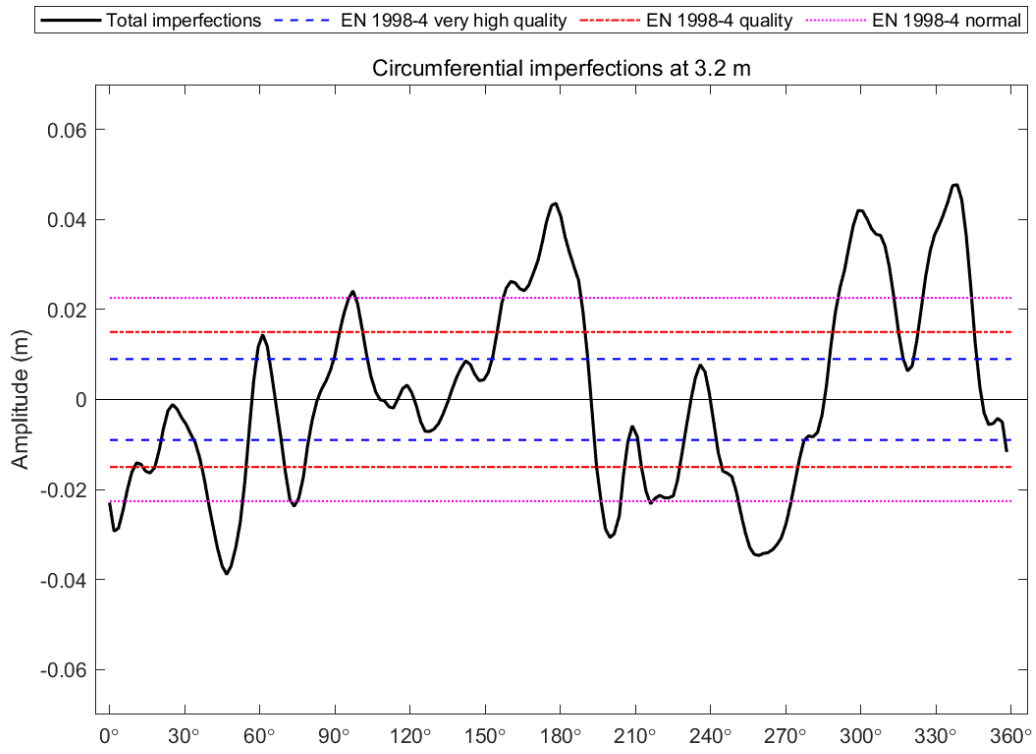
#### 2.5.2.3 Evaluation with specification in EN 1998-4: 2006

According to Eq. 2-12 and Table 2.2, the total imperfection amplitude shall satisfy seismic design. Calculated imperfection tolerances are shown in Table 2.5. Examples of the comparison between total imperfections and EN 1998-4 design criteria are shown in Figure 2.38. Other results are shown in appendix Figure A.11.

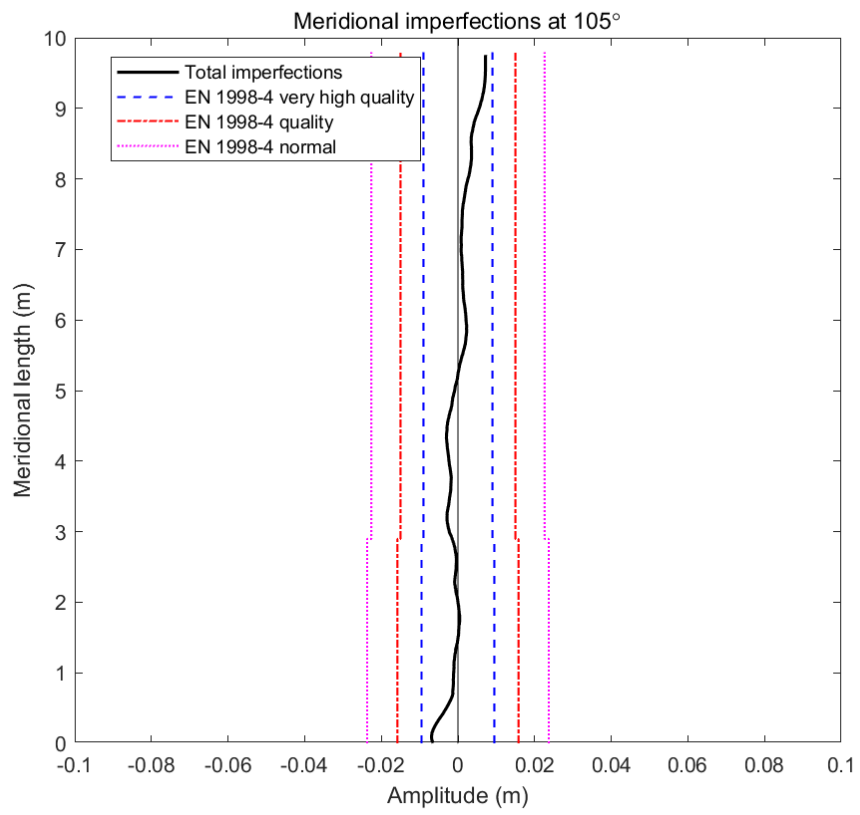
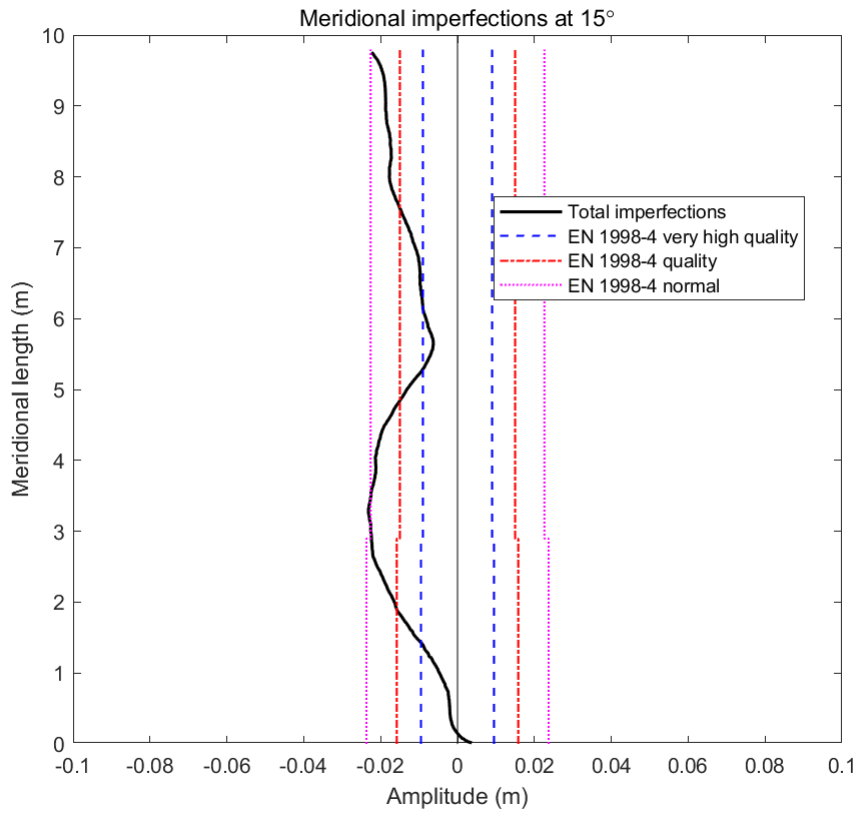
**Table 0.5 Imperfection tolerance for EN 1998-4 seismic design**

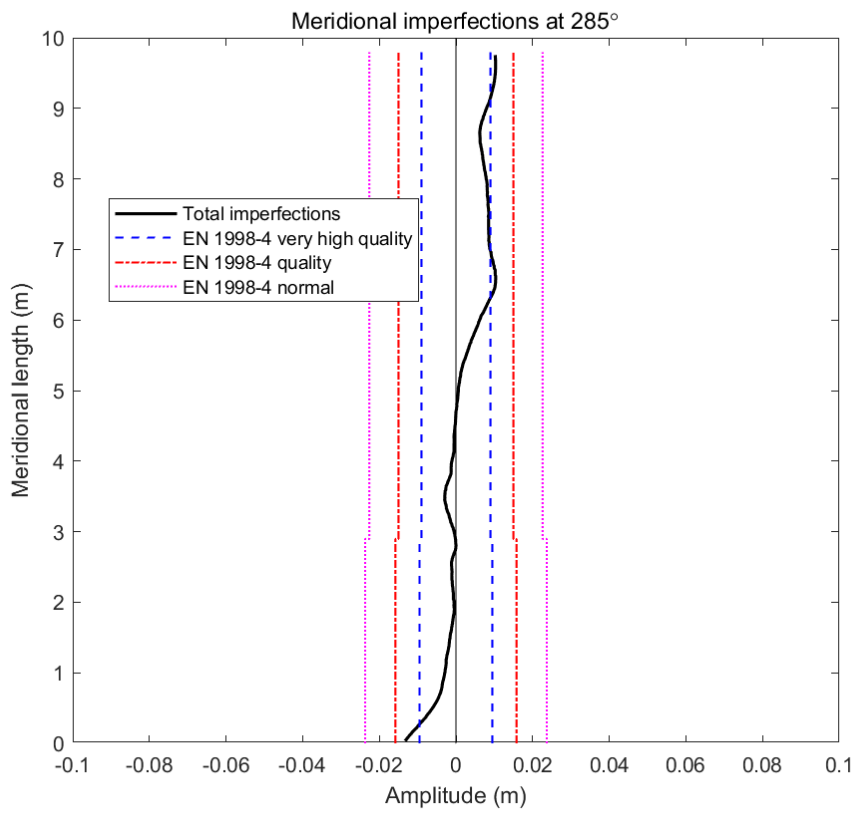
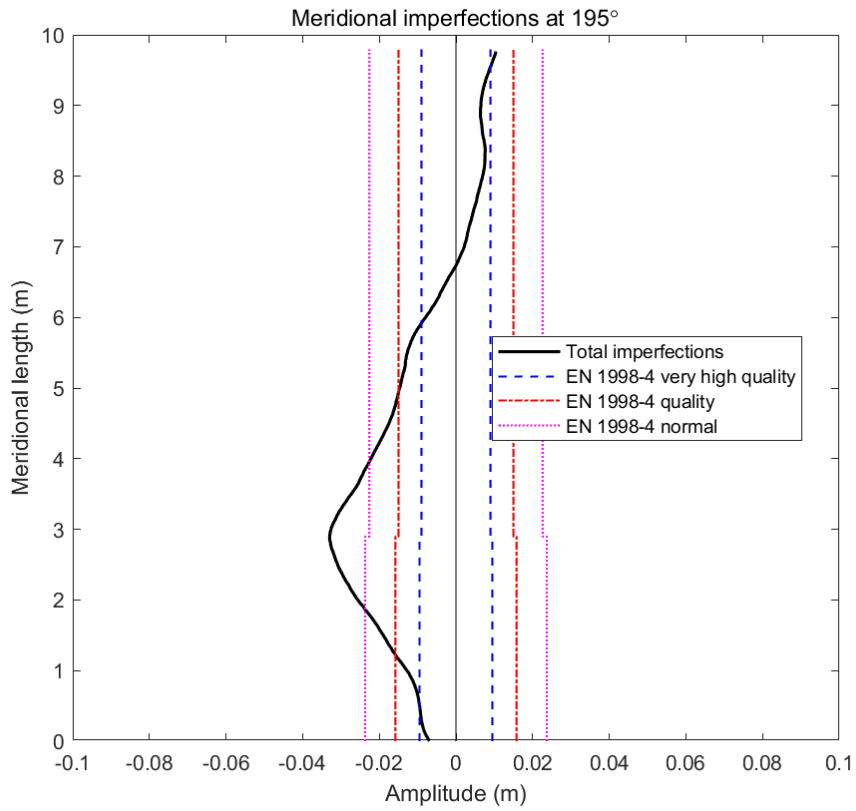
| Quality Class                  | Upper Part<br>( $t_1 = 15.875 \text{ mm}$ ) | Lower Part<br>( $t_2 = 17.4625 \text{ mm}$ ) |
|--------------------------------|---|--|
| Normal Construction            | 0.0226 m                                    | 0.0237 m                                     |
| Quality Construction           | 0.015 m                                     | 0.0158 m                                     |
| Very High Quality Construction | 0.009 m                                     | 0.0095 m                                     |











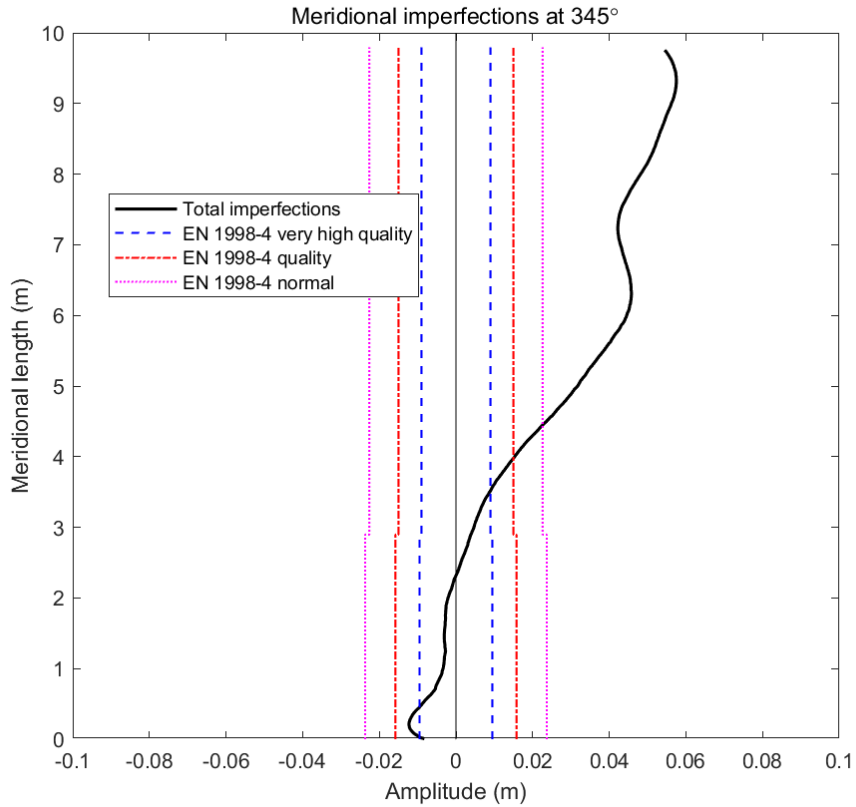


**Figure 0.38 Evaluation of total imperfection amplitude with specifications in EN 1998-4: 2006**

Figure 2.38 indicates that on both circumferential and meridional directions, imperfection amplitude is in general larger than the tolerance. The imperfection amplitude is below the limits only in few locations. The meridian at 105° satisfies very high quality limit. Circumferences at  $z = 0.1 \text{ m}$  &  $0.5 \text{ m}$  and the meridian at 285° satisfies quality limit.

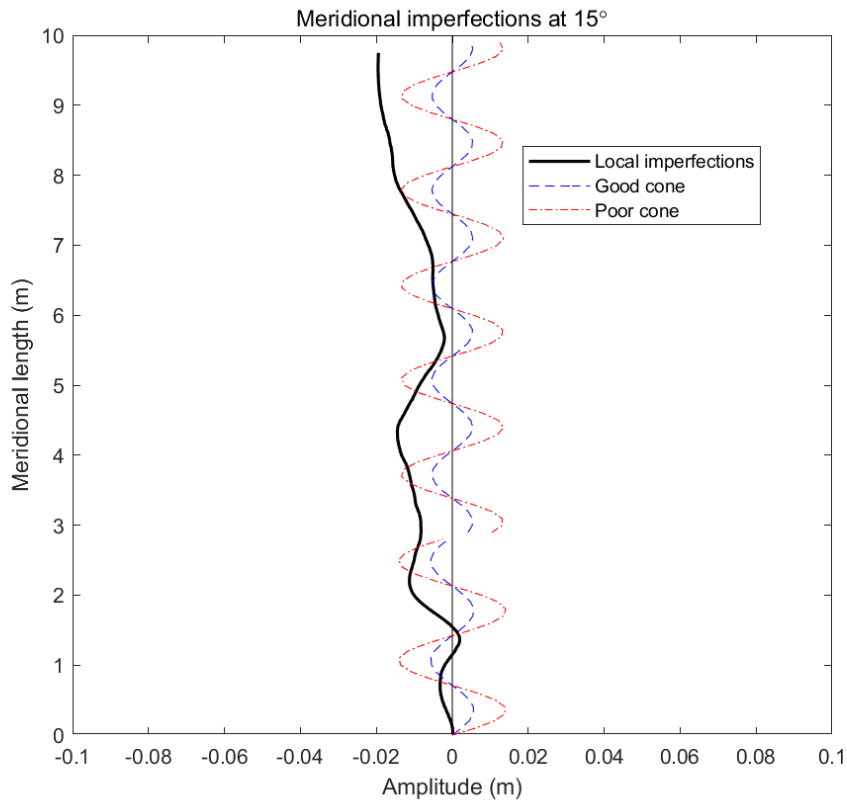
2.5.2.4 Evaluation with specification by Vandepitte et al. (1982)

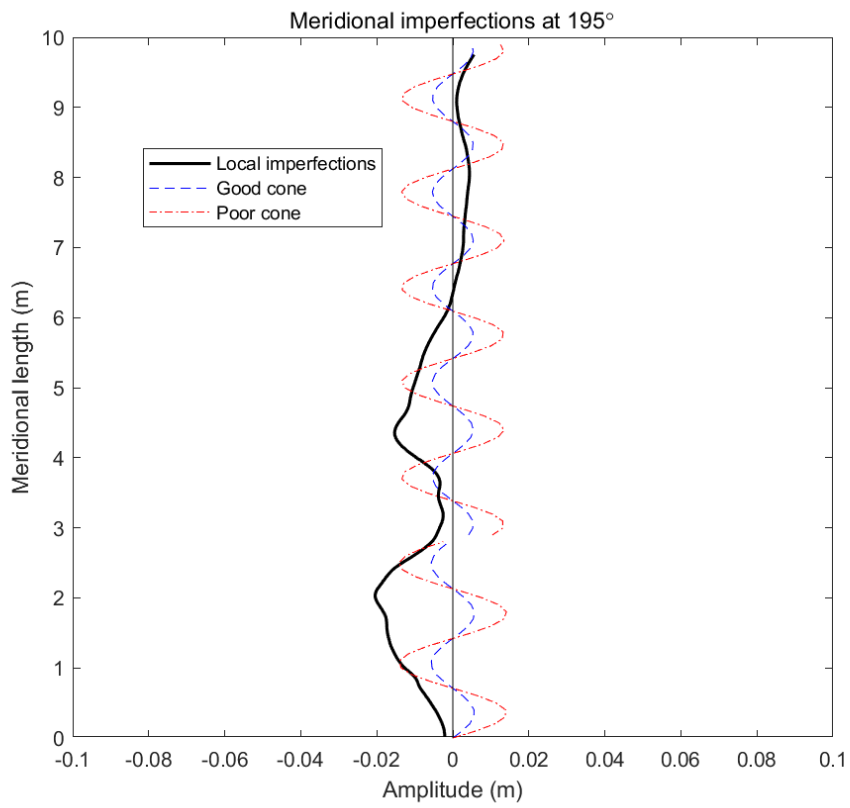
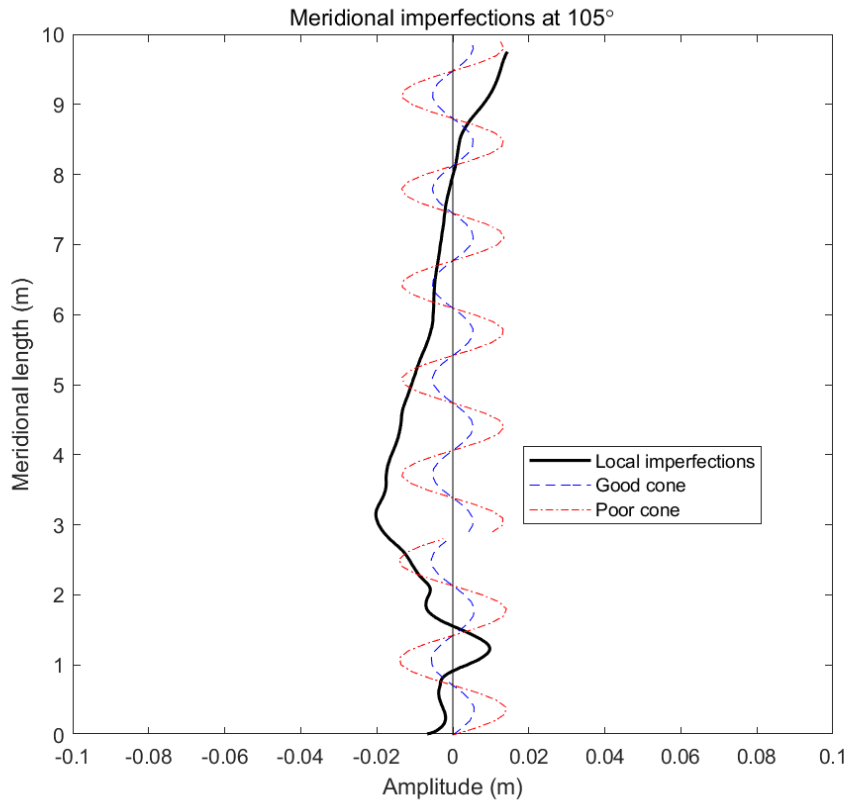
The imperfection shape assumed by Vandepitte et al. (1982) is mentioned in section 2.2.4. In this case, the wavelength and amplitude for all scenarios is calculated in Table 2.6.

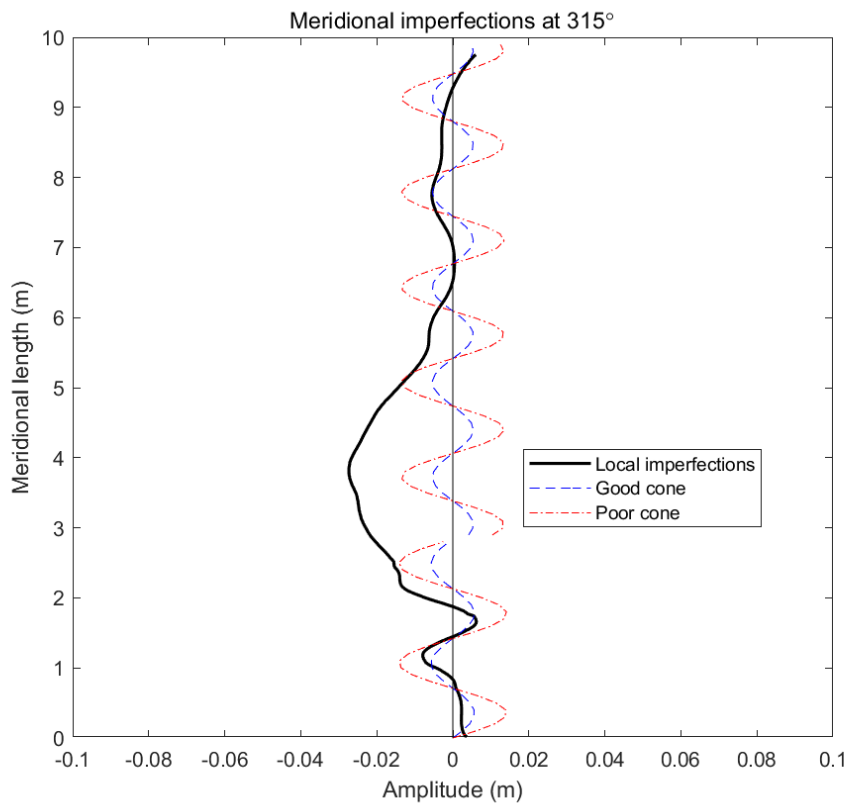
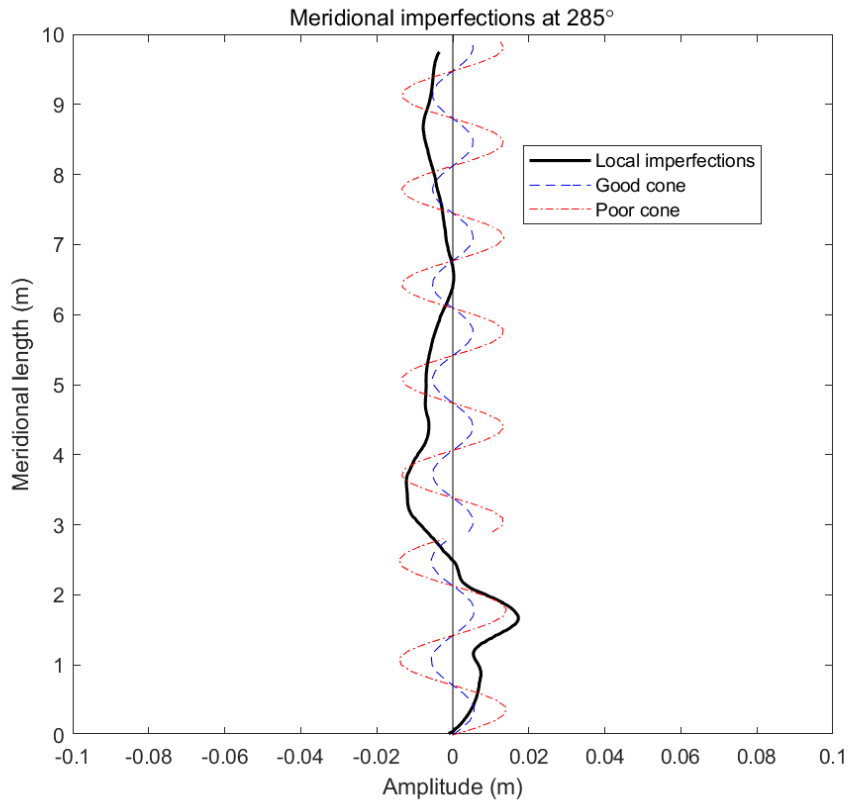
**Table 0.6 Tolerance and assumption by Vandepitte et al. (1982)**

| Quality Class | Upper Part<br>( $t_1 = 15.875$ mm) |           | Lower Part<br>( $t_2 = 17.4625$ mm) |           |
|---------------|------------------------------------|-----------|-------------------------------------|-----------|
|               | Wavelength                         | Amplitude | Wavelength                          | Amplitude |
| Good Cone     | 1.3538 m                           | 0.0054 m  | 1.4199 m                            | 0.0057 m  |
| Poor Cone     |                                    | 0.0135 m  |                                     | 0.0142 m  |

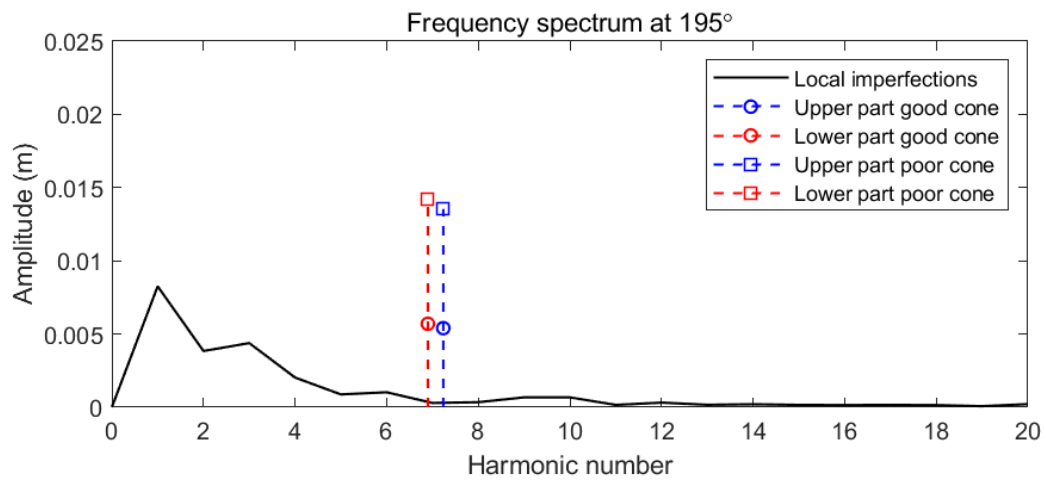
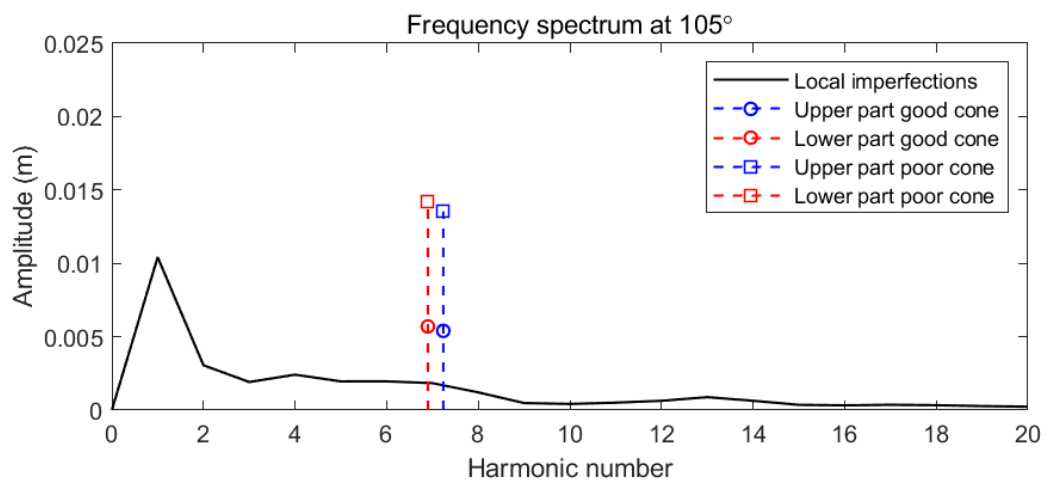
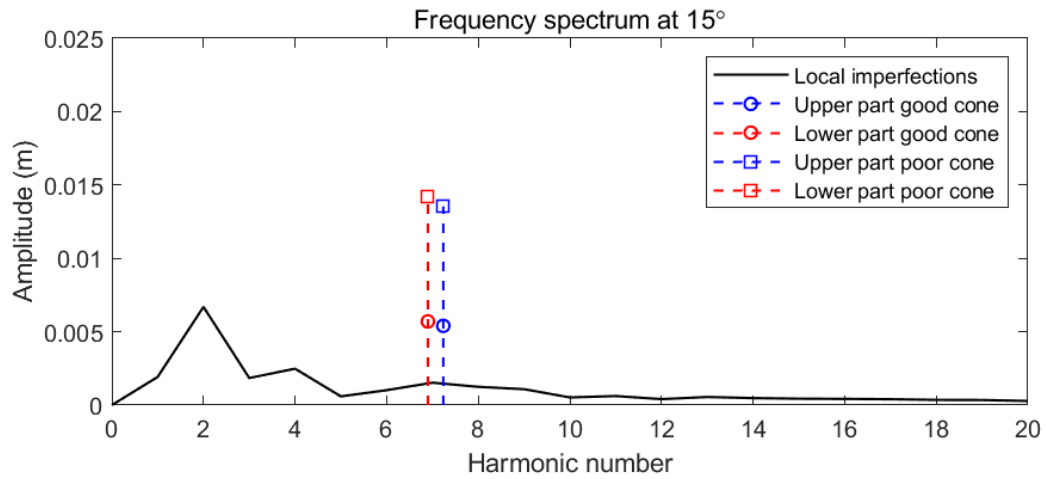
Examples of comparison between Vandepitte’s assumptions and meridional local imperfections are shown in Figure 2.39. Examples of Fourier transform results are shown in Figure 2.40. Other results are shown in appendices Figure A.12 and Figure A.13.







**Figure 0.39 Evaluation of meridional local imperfection amplitude with specifications by Vandepitte et al. (1982)**



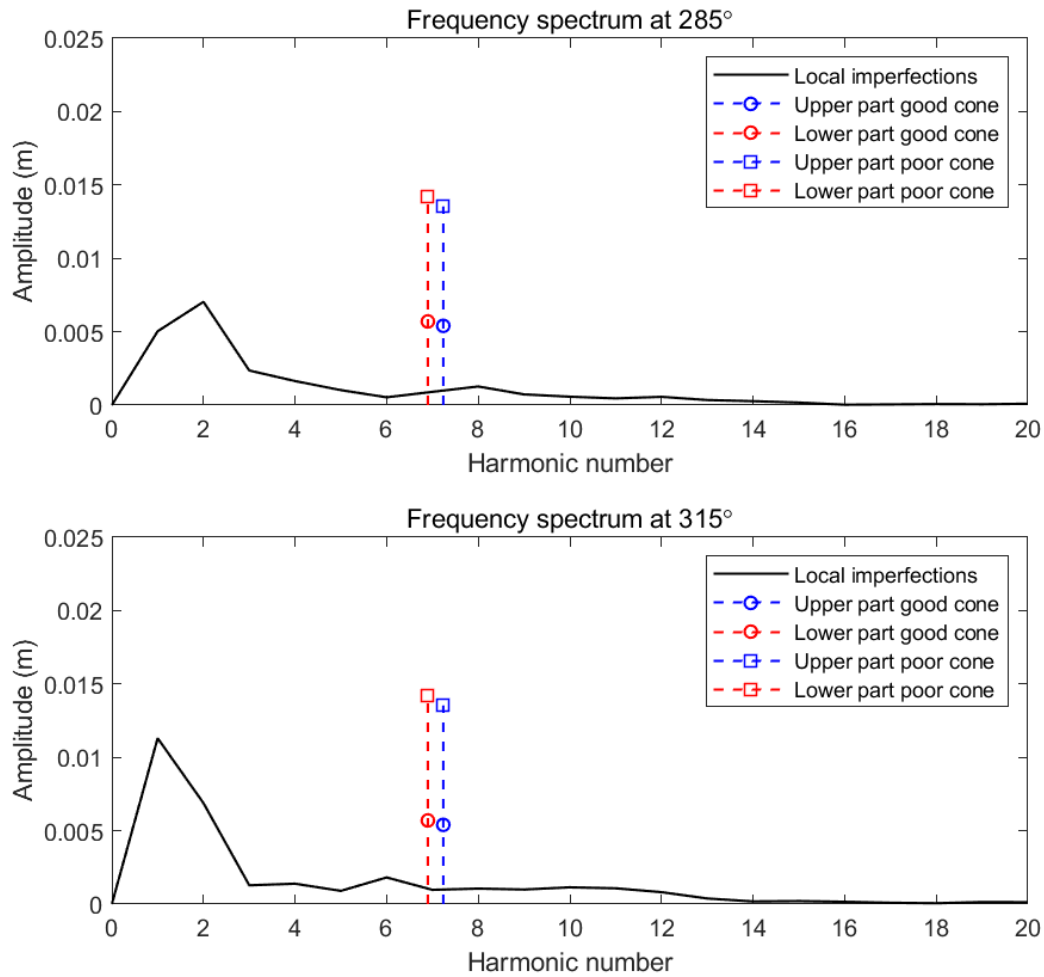


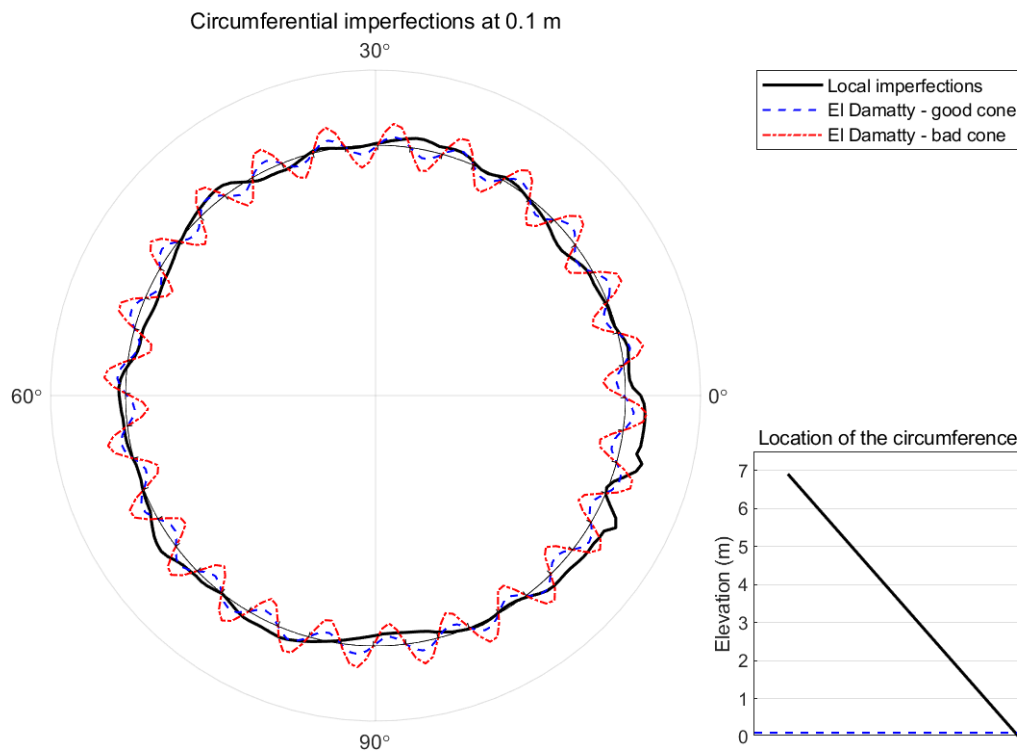
**Figure 0.40 Evaluation of meridional local imperfection wavelength with specifications by Vandepitte et al. (1982)**

Comparing with Vandepitte’s assumption, only the imperfection on the meridian around 135° satisfies Vandepitte’s criteria for the poor cone. The overall imperfections in the case exceed the tolerance markedly. In the Fourier transform result, the wavelength of Vandepitte’s assumption is even smaller than that from the AWWA D100 standard, which is markedly shorter than the main components of local imperfections in this case.

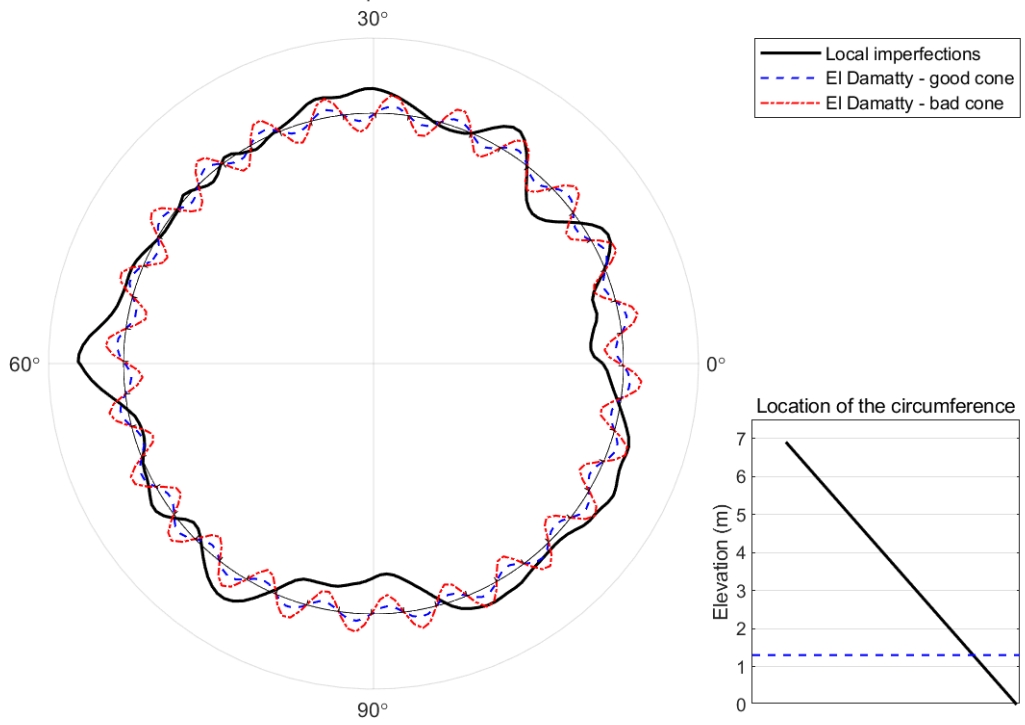


### 2.5.2.5 Evaluation with specification by El Damatty et al. (2001)

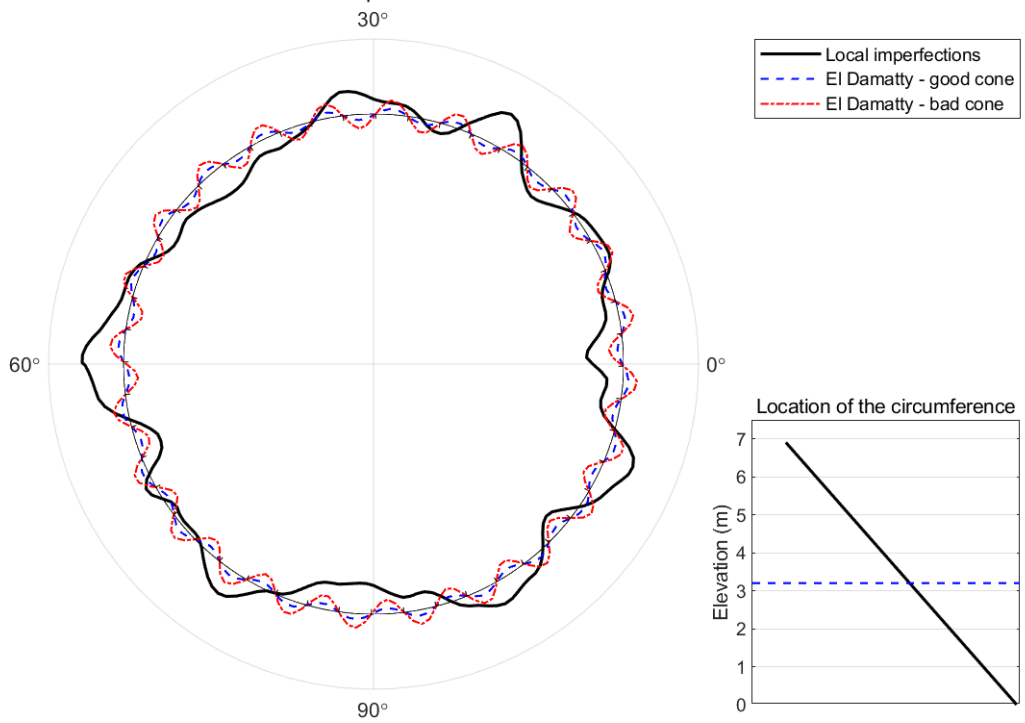
A specification by El Damatty et al. (2001) (described in section 2.2.5) provides the assumed sinusoid circumference pattern which is related to evenly distributed longitudinal stiffeners. Comparison results from the above show that the real case is far from Vandepitte's assumptions on meridional imperfections. However, Circumferential imperfection shapes still need to be checked with El Damatty's assumption. Examples of comparisons are shown in Figure 2.41. Examples of Fourier transform results are shown in Figure 2.42. Other results are shown in appendices Figure A.14 and Figure A.15.

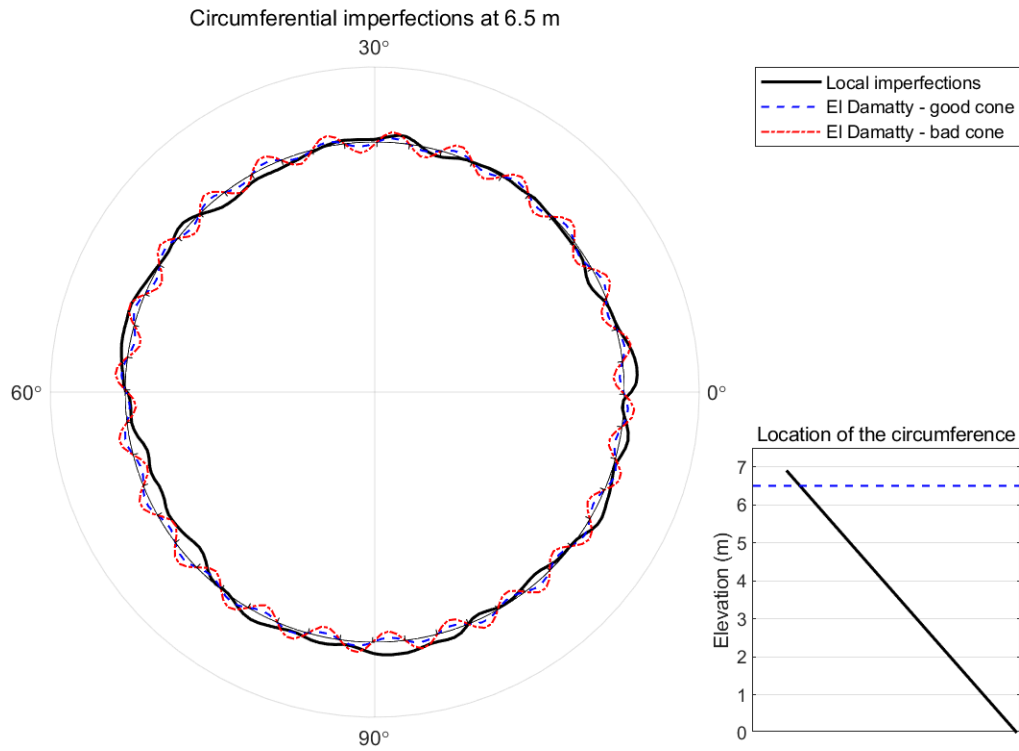


Circumferential imperfections at 1.3 m

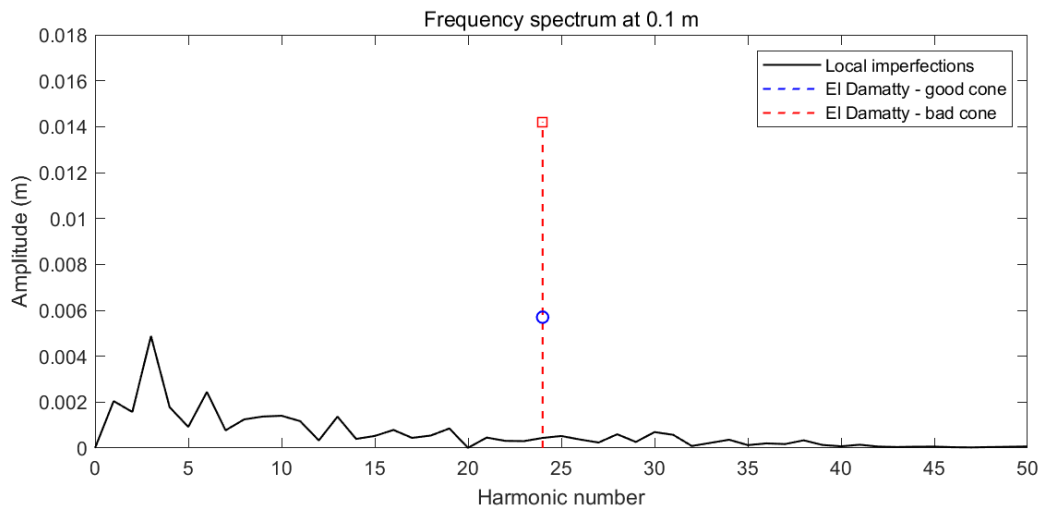


Circumferential imperfections at 3.2 m





**Figure 0.41 Comparison of circumferential local imperfections with specifications by El Damatty et al. (2001) (40 times scaled)**



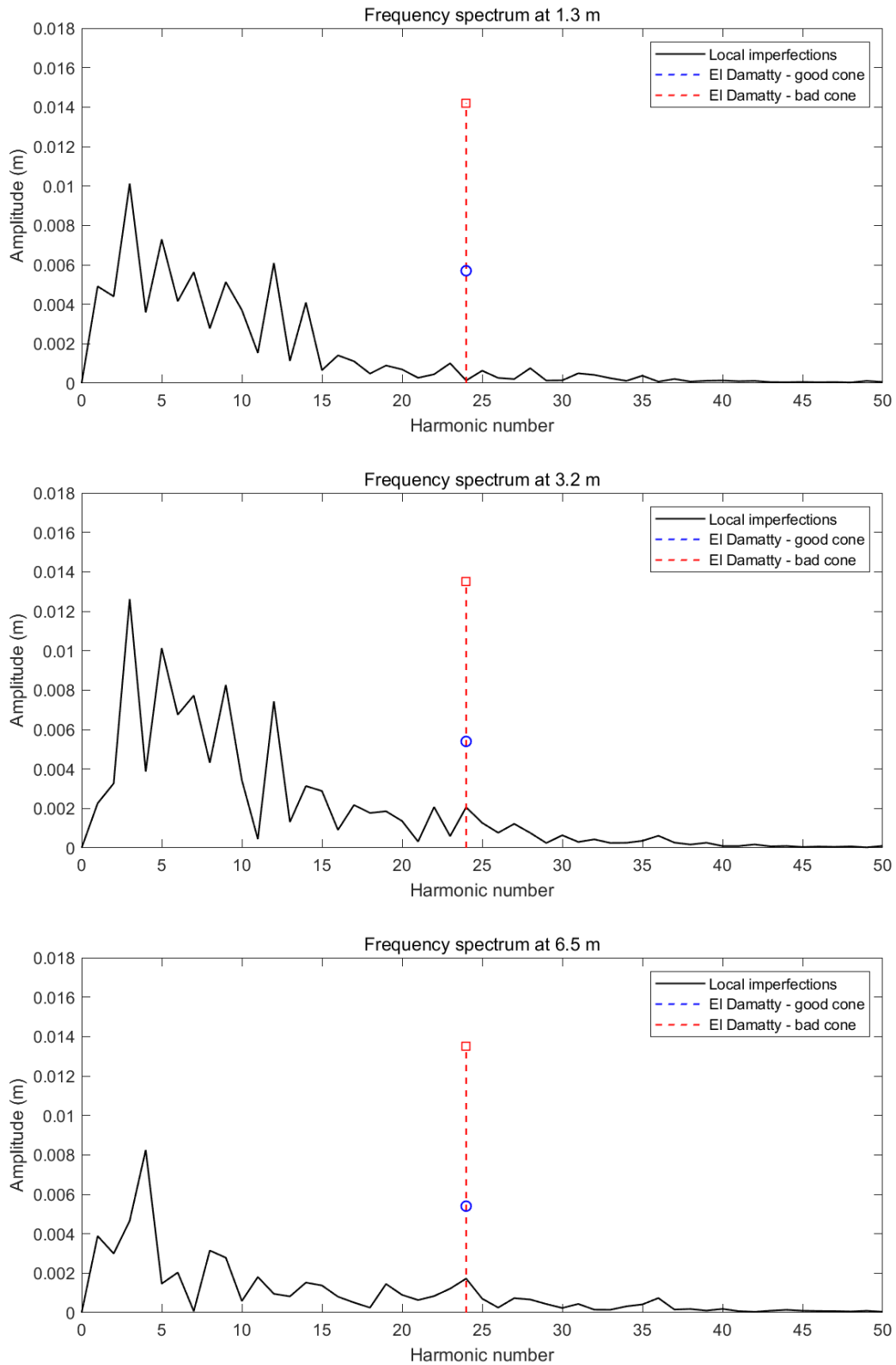


**Figure 0.42 Evaluation of circumferential local imperfection wavelength with specifications by Vandepitte et al. (1982)**

The wavelength  $l_c$  (m) of each harmonic number  $N$  can be calculated as:

$$l_c = \frac{2\pi R}{N}$$

A few patterns similar to the assumption can be observed in several sections. However, real imperfections in this case show more complicated shapes and larger wavelength, especially in the middle part of the cone. The Fourier transform result shows that main components of the imperfection are in the low frequency regions with the wavelength below 1/15 of parameters. Only for circumferences in upper part of the cone (3.2 m - 6.5 m), a small peak can be observed with the same wavelength as assumptions in the work by El Damatty et al. (2001). Generally, the imperfections along the tank circumference obtained in the case study are associated with much larger wavelengths than the assumed pattern longitudinally stiffened cones.

## 2.6 Conclusion

In this chapter, geometric imperfections on a decommissioned LFCT are extracted from a set of high-resolution laser scan cloud data. Analyses are carried out to homogenize the cloud data and evaluate the imperfection profiles on the meridians around the tank circumference and circumferences at different elevations. Global & local imperfections are evaluated by applying a LSQ fitting process. Several tolerances from design standards and specifications in literatures are introduced and employed to evaluate geometric imperfections in this case. Conclusions can be drawn from results and analysis:

- 1) Real case shows the complexity of imperfection shapes on a LFCT. The global imperfection consists of deviation of the central axis of the tank from the nominal position and nonlinear ovalization effect with the varying inclination angle of the ellipse.
- 2) The tolerance of global imperfections (out-of-roundness) in AWWA D100-11 and EN 1993-1-6: 2007 are satisfied in this case. However, the tolerance of local imperfections and total imperfections in codes and specifications are all exceeded. The local imperfections exceed the tolerances mostly in the middle and lower section of the cone (2 m to 5 m on the meridian from the base). The imperfection is more than 150% of the tolerance at most. Total imperfection tolerances in EN 1998-4: 2006 are also violated on the top of cone with the imperfection amplitude more than 200% of the tolerance.

3) Assumptions of local imperfection wavelength are introduced by the AWWA D100-11 standard, Vandepitte et al. (1982) and El Damatty et al. (1997, 2001). Fourier analysis results show that wavelength of the main harmonic components of the imperfections along the meridians and circumferences are much larger than those recommended in AWWA D100-11 and by Vandepitte et al. (1982) and El Damatty et al (2001). Wavelength of the 1<sup>st</sup> components is close to the meridional length, 2<sup>nd</sup> – 4<sup>th</sup> components have the wavelength close to 1/2 – 1/4 of the meridional length. Wavelength of circumferential imperfections are mostly around 1/2 – 1/15 of the circumferential length. This may be affected by global imperfections since the local imperfections are collected as residual component when global imperfection is extracted as ovalization, while actual global imperfection shape might be more complicated than the ellipse.

## 2.7 References

AWWA D100-11 Welded Carbon Steel Tanks for Water Storage. (2011). American Water Works Association, Denver, Colorado.

*Ansys® Academic Research Mechanical, Release 16.1*, ANSYS, Inc.

Árbocz J., Babcock C.D. Jr. (1964). “The Effect of General Imperfections on the Buckling of Cylindrical shells.” *Journal of Structural Engineering*, Volume 36, Issue 1, 879-890.

Árbocz J., Williams J. G., (1977). “Imperfection Surveys on a 10-ft-Diameter Shell Structure.” *AIAA Journal*, Volume 15, Issue 7, 949-956.

Azabi T. M., El Ansary A. M., El Damatty A. A. (2016). “Analysis and Design of Elevated Liquid-Filled Reinforced Concrete Conical Tanks.” *Advances in Structural Engineering*, Volume 19, Issue 6, 995-1008.

Chen J. F., Yu S. K., Ooi J. Y., Rotter J. M. (2001). “Finite-Element Modeling of Filling Pressures in A Full-Scale Silo.” *Journal of Engineering Mechanics*, Volume 127, Issue 10, 1058–1066.

Circular Concrete Tanks without Prestressing. (1993). Portland Cement Association (PCA-CCTWP), Skokie, Illinois.

El Damatty A. A., Korol R. M., Mirza F. A. (1997a). “Stability of Imperfect Steel Conical Tanks under Hydrostatic Loading.” *Journal of Structural Engineering*, Volume 123, Issue 6, 703–712.

El Damatty, A. A., El-Attar, M., and Korol, R. M. (1998). “Inelastic Stability of Conical Tanks.” *Thin-Walled Structures*, Volume 31, 343–359.

El Damatty A. A., Marroquin E. G., El Attar M. (2001). “Behavior of Stiffened Liquid-Filled Conical Tanks.” *Thin-Walled Structures*, Volume 39, 353–373.

EN 1993-1-6: Eurocode 3 - Design of Steel Structures – Part 1-6: Strength and Stability for Shell Structures. (2007). European Committee for Standardization, Brussels, Belgium.

EN 1993-4-2: Eurocode 3 - Design of Steel Structures – Part 4-2: Tanks. (2007). European Committee for Standardization, Brussels, Belgium.

EN 1998-4: Eurocode 8 - Design of Structures for Earthquake Resistance - Part 4: Silos, Tanks and Pipelines. (2006). European Committee for Standardization, Brussels, Belgium.

Hafeez G., El Ansary A. M., El Damatty, A. A. (2010). “Stability of Combined Imperfect Conical Tanks under Hydrostatic Loading.” *Journal of Constructional Steel Research*, Volume 66, Issue 11, 1387-1397.

Hornung U., Saal H. (2002). “Buckling Loads of Tank Shells with Imperfections.” *International Journal of Nonlinear Mechanics*, Volume 37, 605–621.

Levenberg K. (1944). “A Method for the Solution of Certain Non-Linear Problems in Least Squares.” *Quarterly of Applied Mathematics*, Volume 2, Issue 2, 164-168.

Marquardt D. (1963). “An Algorithm for Least-Squares Estimation of Nonlinear Parameters.” *SIAM Journal on Applied Mathematics*, Volume 11, Issue 2, 431-441.

MATLAB. (2019). *9.6.0.1072779 (R2019a)*. Natick, Massachusetts: The MathWorks Inc.

National Building Code of Canada. (2015). Ottawa: Associate Committee on the National Building Code, National Research Council.



Riks E. (1979). "An Incremental Approach to the Solution of Snapping and Buckling Problems." *International Journal of Solids and Structures*, Volume 15, Issue 7, 529-551.

Savitzky A., Golay M. J. E. (1964). "Smoothing and Differentiation of Data by Simplified Least Squares Procedures." *Analytical Chemistry*, Volume 36, Issue 8, 1627-1639.

Teng J. G., Lin X., Rotter J. M., Ding X. L. (2005). "Analysis of geometric imperfections in full-scale welded steel silos." *Engineering Structures*, Volume 27, Issue 6, 938-950.

Vandepitte D., Rathe J., Verhegghe B., Paridaens R., Verschaeve C. (1982). "Experimental investigation of hydrostatically loaded conical shells and practical evaluation of the buckling load." In: Ramm E. (ed.) *Buckling of shells*, Springer-Verlag KG, Berlin, Germany, 375-399.

# Chapter 3 Nonlinear Buckling analysis of Stiffened Conical Tanks Considering Various Imperfection Patterns

## 3.1 Introduction

Geometric imperfections are usually inevitable factors introduced during fabrication which have large impacts on the buckling capacity of sensitive structures such as shells. Early studies have concentrated on shells which require high level of quality control (Arbocz et al. 1964). This later was extended to other fields (e.g., in the construction field) with lower level of quality control due to the difference in fabrication techniques and limitation of having a controlled environment. As a representative investigation, Hornung et al. (2002) carried out buckling tests of pressurized cylindrical tanks on both real structures and model simulation. They observed that, despite having imperfection amplitudes from real measurements much larger than those assumed by design standards, the capacity of the studied pressurized cylinders was higher when such real measurements were considered compared to the case of considering design standards amplitudes. Hornung et al. (2002) simulated buckling test with FEM model and made comparisons to real tests results, only those models of complete tank shell and measured imperfections from real tanks agreed with observation from buckling tests. Those models with specified imperfections from design codes did not buckle under the same loads.

However, investigations of liquid-filled-conical-tanks (LFCT), which are widely used for liquid storage, have not been reported extensively in the literature. Research focus on this type of shell structure was evoked by a tragic collapse of a tank in Belgium in 1972. Vandepitte et al. (1982) introduced a classification of conical tank quality under the assumption of axisymmetric sinewave imperfections along meridians. The tank is classified as 'good cone' or 'poor cone' based on a specific imperfection amplitude which can be estimated as a function of the buckling wavelength. Another tank collapse incident happened in Canada Fredericton in 1990 started a new series of study. Vandepitte et al. (1991) studied the Fredericton tank by simulating tests with assumed axisymmetric imperfections. Results showed that the buckling capacity of the tank vessel under hydrostatic loading decreased to 72% - 80% when imperfection amplitude rose to 0.8% of half of the buckling wavelength and further reached

53% - 61% with imperfection amplitude of 2% of half of the buckling wavelength. El Damatty et al. (1997) provided another study on imperfect LFCT. The Fredericton tank was also analyzed in this study with similar axisymmetric imperfection and Vandepitte's classification of 'good cone' and 'poor cone'. The tank capacity reduced to around 76% for 'good cone' (imperfection amplitude: 0.4% of the buckling wavelength) and 52% for 'poor cone' (imperfection amplitude: 1% of the wavelength), which provides a comparable result to Vandepitte's work. Similar methods are employed by El Damatty et al. (2001) to a further study on stiffened LFCT. Following a similar analyzing approach, Hafeez et al. (2010) checked the stability of combined conical tanks where a cylindrical cap was added at the top, showing that 'good cone' has around 80% buckling capacity and 'poor cone' has around 60% capacity.

It can be observed from existing studies that most results lie in similar ranges. However, in full-scale tanks, imperfection configuration assumed by Vandepitte et al. based on scaled experimental studies might not lead to the most critical case. Moreover, no study about the impact of real imperfections on the capacity of LFCT has been reported in the literature.

In the current study, geometric imperfections are measured from an existing LFCT and utilized to conduct nonlinear finite element analysis (FEA) to quantitatively evaluate the impact of these imperfections on the buckling capacity of the studied tank. Furthermore, comparisons with other imperfection patterns available in the literature and from different design standards are carried out. The next section describes specified imperfection shapes in literature. Information of the studied conical tank is provided in section 3.3. Section 3.4 presents the validation of the FEM approach by comparing it with simulation techniques from previous studies in the literature. The analysis of plastic deformation effect is provided in Section 3.5. Section 3.6 provides convergence and sensitivity analyses to determine the meshing resolution of the model and describes the FEA procedure of LFCT with different imperfection patterns. A comparison between buckling capacities associated with the assumed patterns and with previous studies is also shown in this section. Finally, conclusions and recommendation that can be drawn from this study are provided in Section 3.7.

### 3.2 Imperfection shape specifications

Vandepitte et al. (1982) assumed sinewave meridional imperfections (shown in Figure 3.1) on conical tanks based on experiments on scaled models. This pattern is identical to first buckling mode of a perfect tank where the half buckling wavelength  $L_b$  is calculated as follows:

$$L_b = 3.6 \sqrt{\frac{R_b t}{\cos \theta_v}} \quad (3 - 1)$$

Where:

$R_b$  : radius at the tank base.

$\theta_v$  : angle between tank wall and vertical direction.

Vandepitte et al. (1982) also proposed a classification of tank quality based on local imperfection amplitude. The ‘good cone’ and ‘poor cone’ corresponding to 0.8% and 1% of half buckling wavelength.

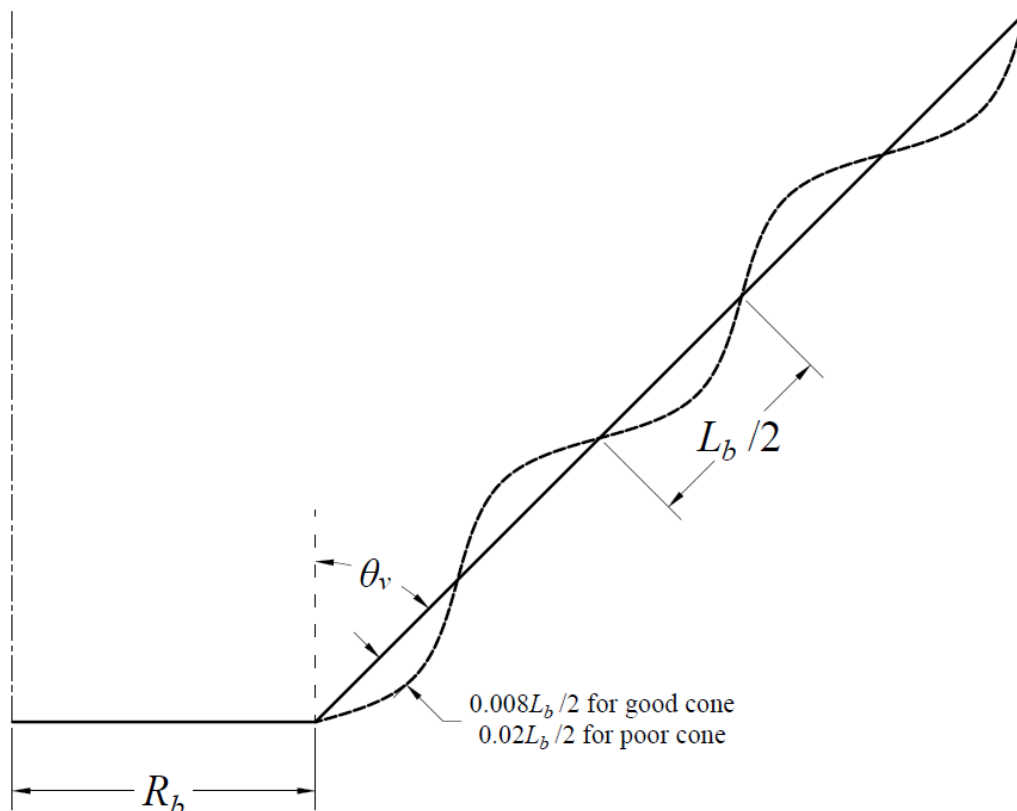


**Figure 0.1 Imperfection specification by Vandepitte et al. (1982)**

El Damatty et al. (1997) superimposed a circumferential imperfection wave on the axisymmetric one proposed by Vandepitte et al. (1982) for unstiffened shells:

$$\delta(s, \theta) = \delta_0 \sin\left(\frac{2\pi s}{l_b}\right) \cos(n\theta) \quad (3 - 2)$$

Where:

$\delta_0$  : imperfection amplitude.

$s$  : distance measured on a generator of tank.

$l_b$  : imperfection wavelength specified by Vandepitte et al. (1982).

$\theta$  : angular coordinate measured from the center of circumference.

$n$  : circumferential wavenumber.

El Damatty et al. (2001) further extended this to stiffened tanks (Figure 3.2), where the circumferential wave number  $n$  can be calculated as half of the total number of evenly spaced longitudinal stiffeners  $N$  and the amplitude of the imperfection delta is given by,

$$\delta(s, \theta) = \delta_0 \sin\left(\frac{2\pi s}{l_b}\right) \cos\left(\frac{N}{2}\theta\right) \quad (3 - 3)$$

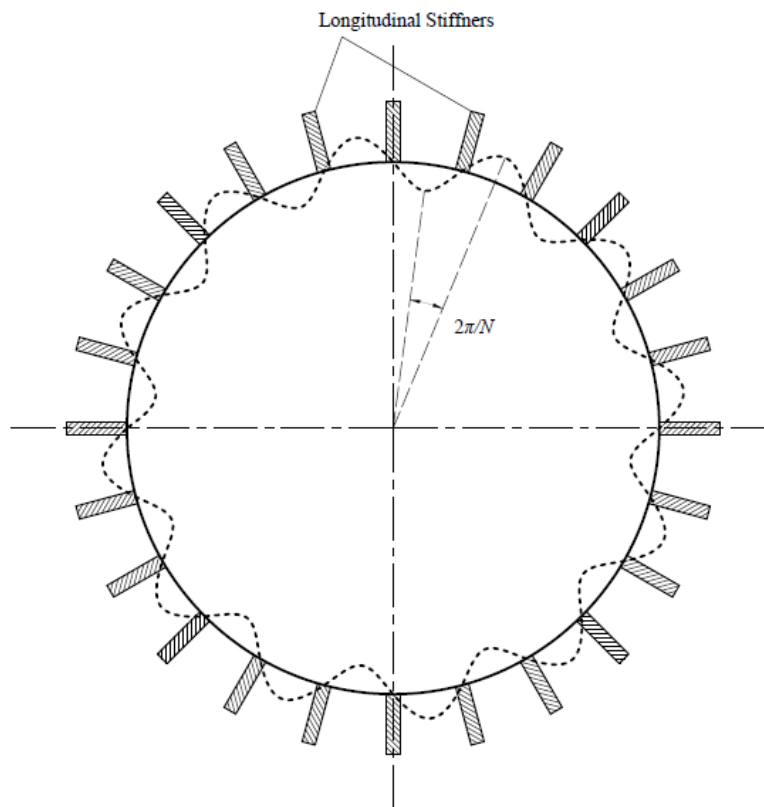


**Figure 0.2 Circumferential imperfection patterns by El Damatty et al. (2001)**

### 3.3 Introduction of the case

Laser scan data was carried out on a stiffened LFCT to gather the geometric imperfection which is processed and analyzed in Chapter 2. Geometry of the tank is shown in Figures 3.3, 3.4 and 3.5. The elevated water tank investigated in this study is a combined stiffened conical tank where the tank vessel that consists of a conical shell at the lower part sitting on a concrete shaft (not shown in Figure 3.3) and a cylindrical cap at the upper part. A total of 48 stiffeners are distributed evenly around the tank circumference at the lower section of the cone, where the shell thickness  $t_1 = 17.4625$  mm. Examples of imperfection shapes extracted from laser scan data on several meridians and circumferences are illustrated in Figures 3.6 and 3.7. Other results are shown in appendices Figure A.16 and Figure A.17.

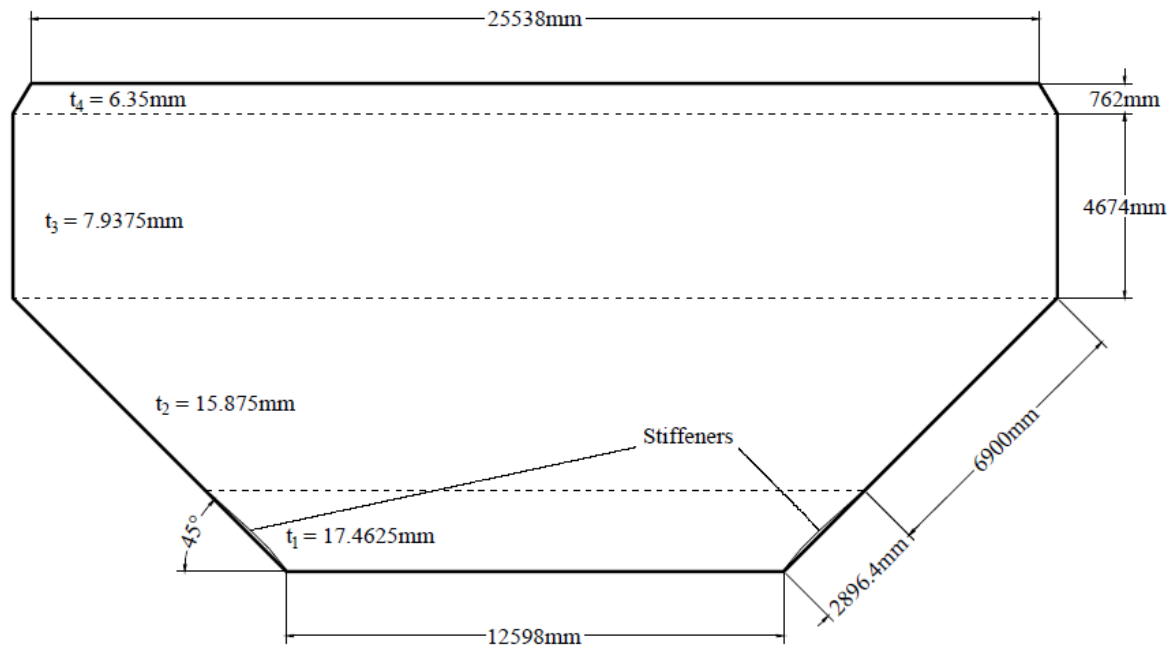


**Figure 0.3 Elevation view of the tank**

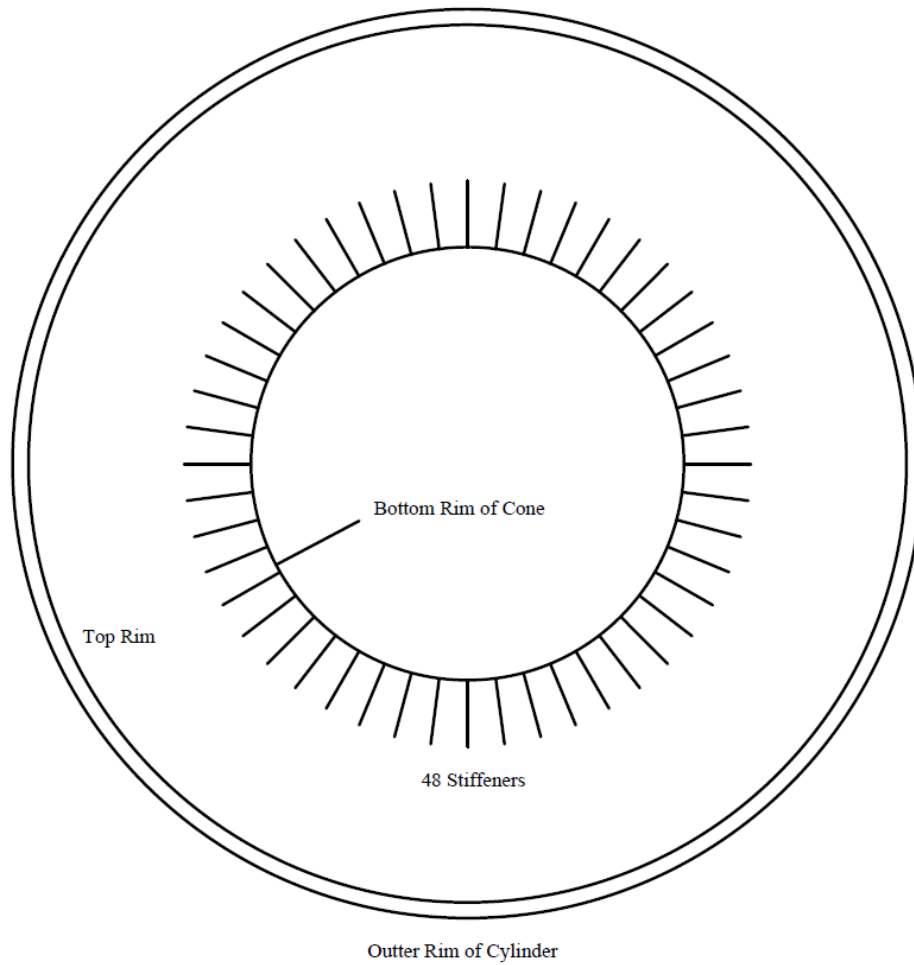


**Figure 0.4 Stiffeners configuration of the tank (top view)**

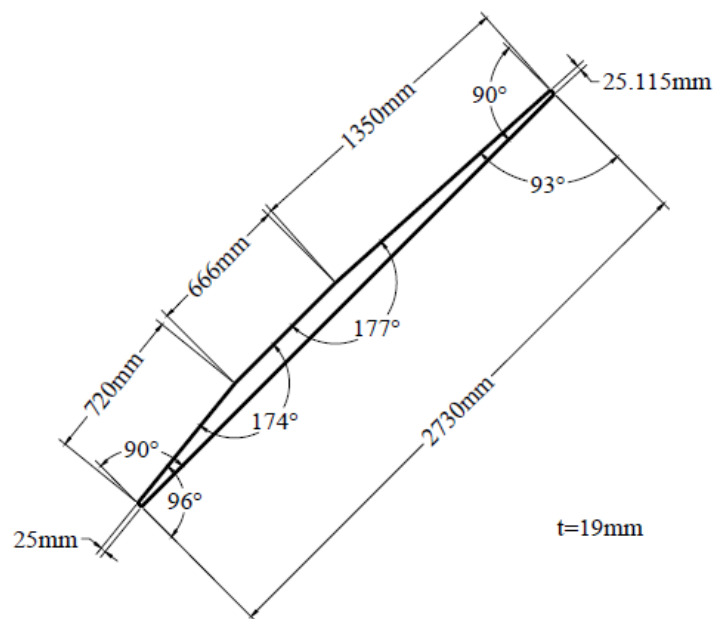
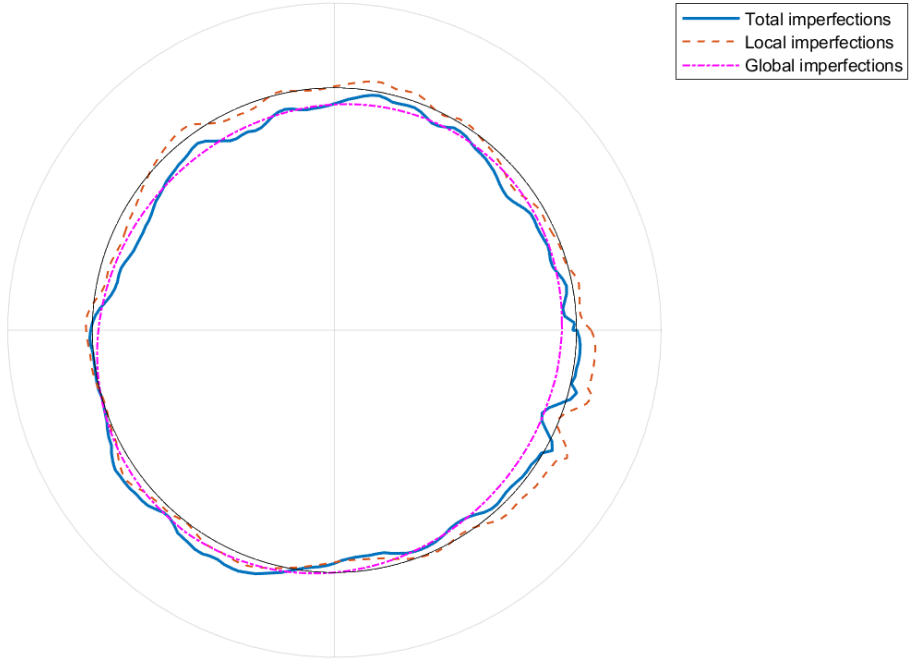
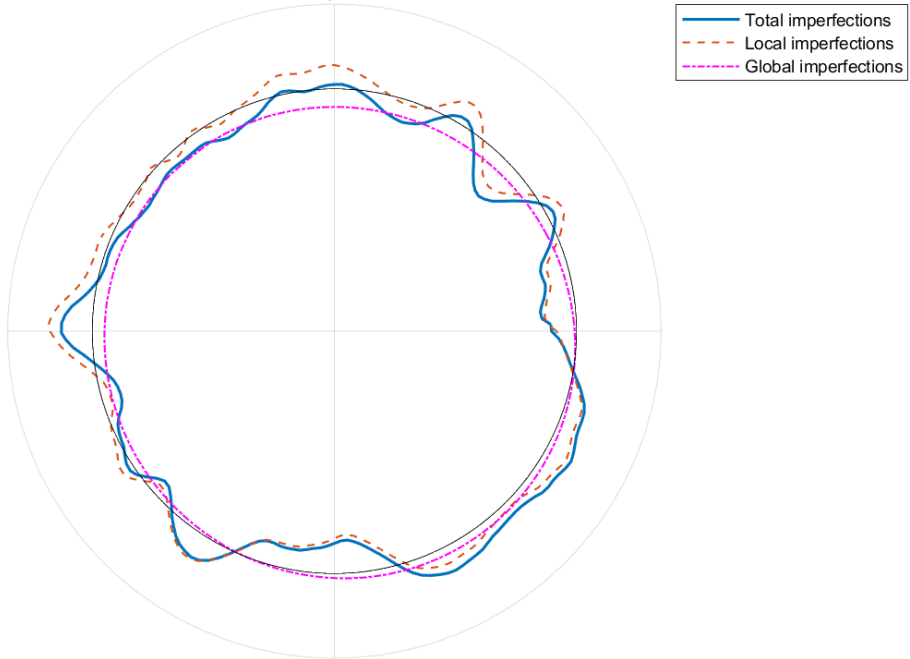


**Figure 0.5 Stiffener geometry (elevation view)**

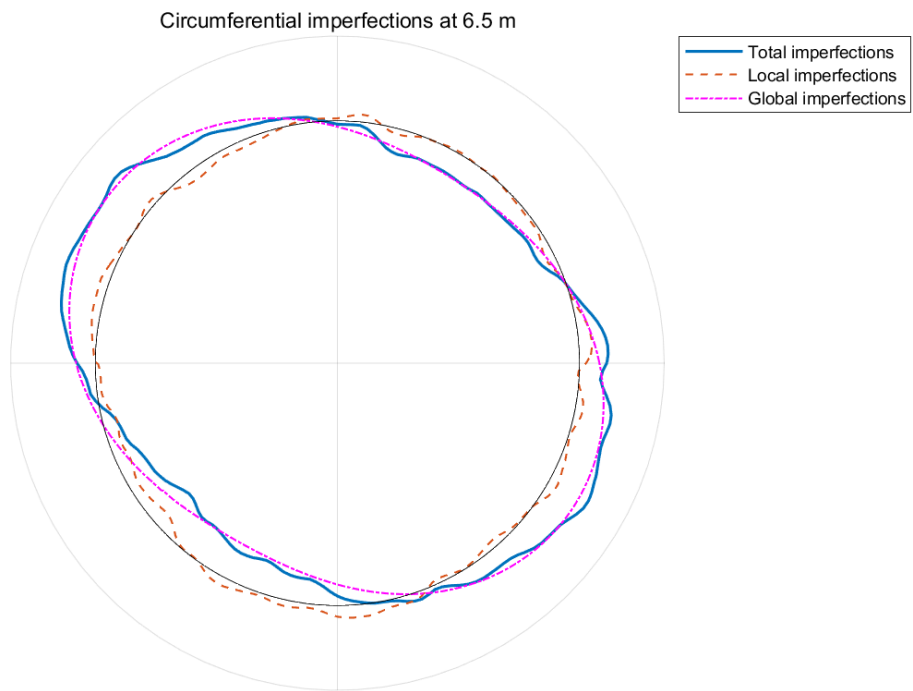
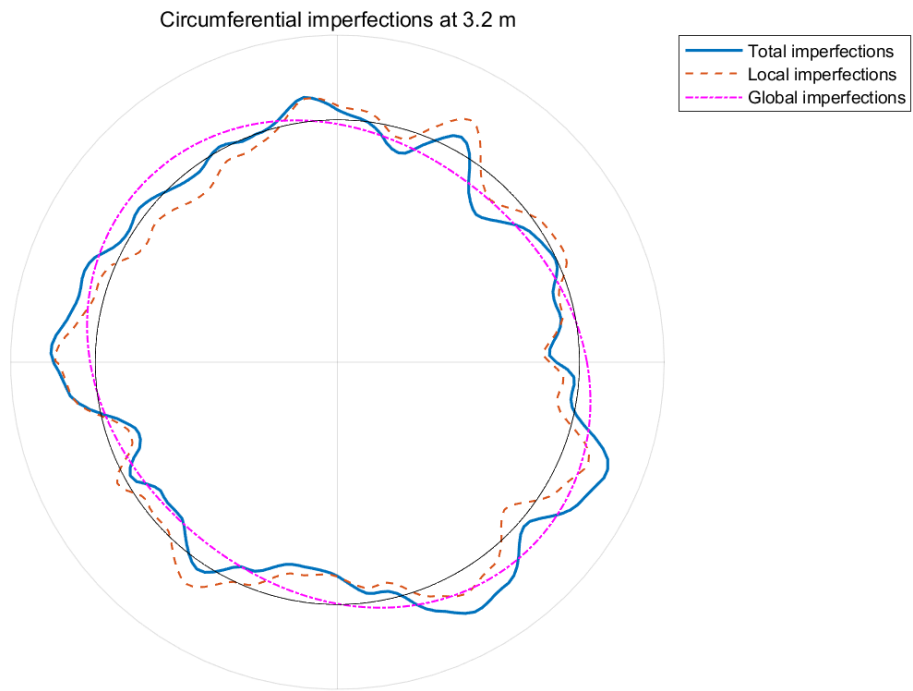
Circumferential imperfections at 0.1 m



Circumferential imperfections at 1.3 m

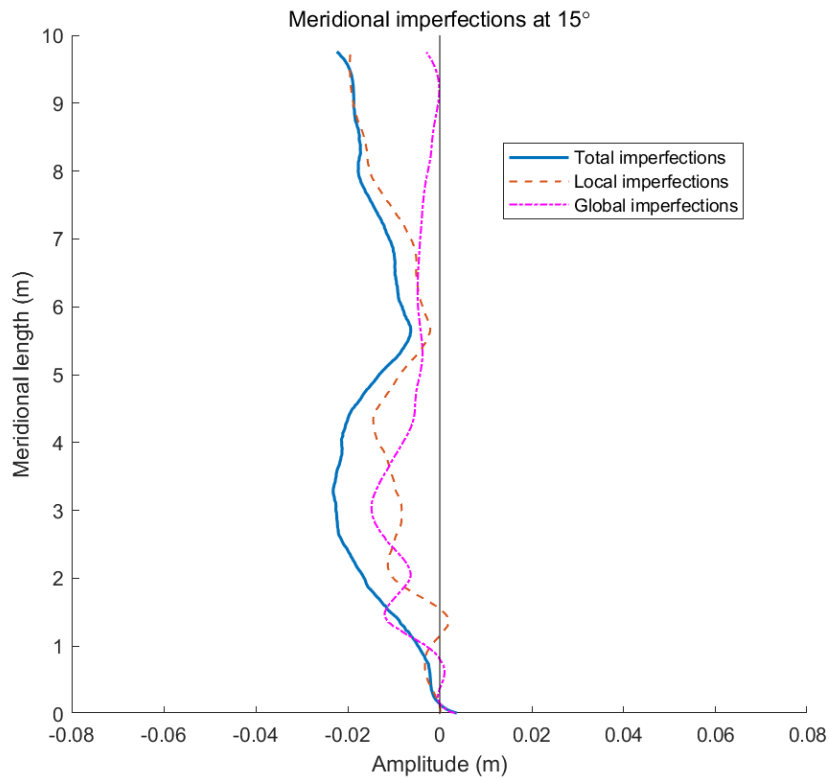


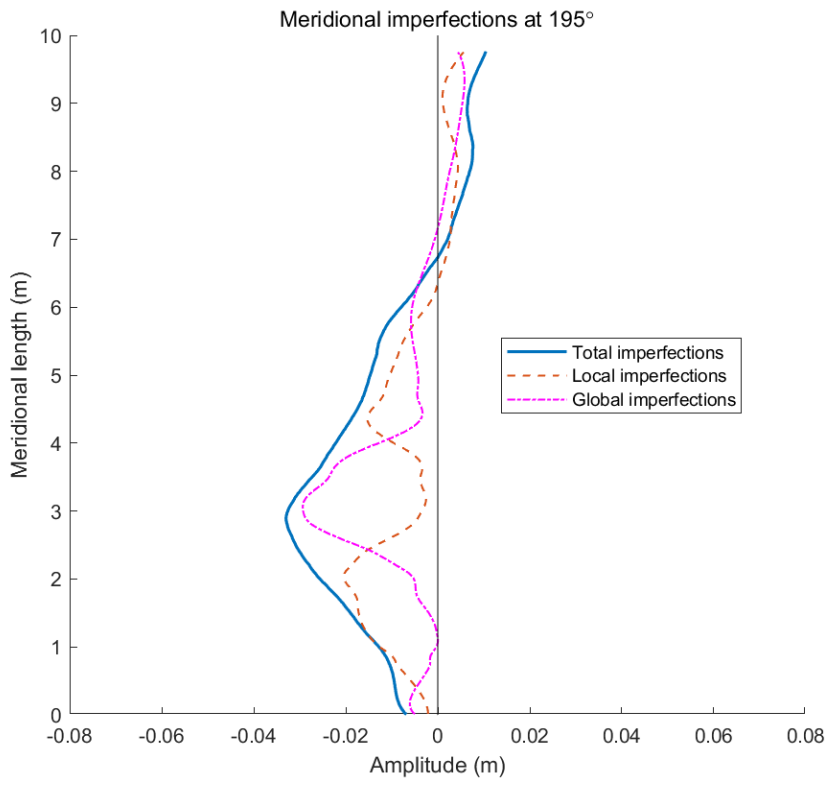
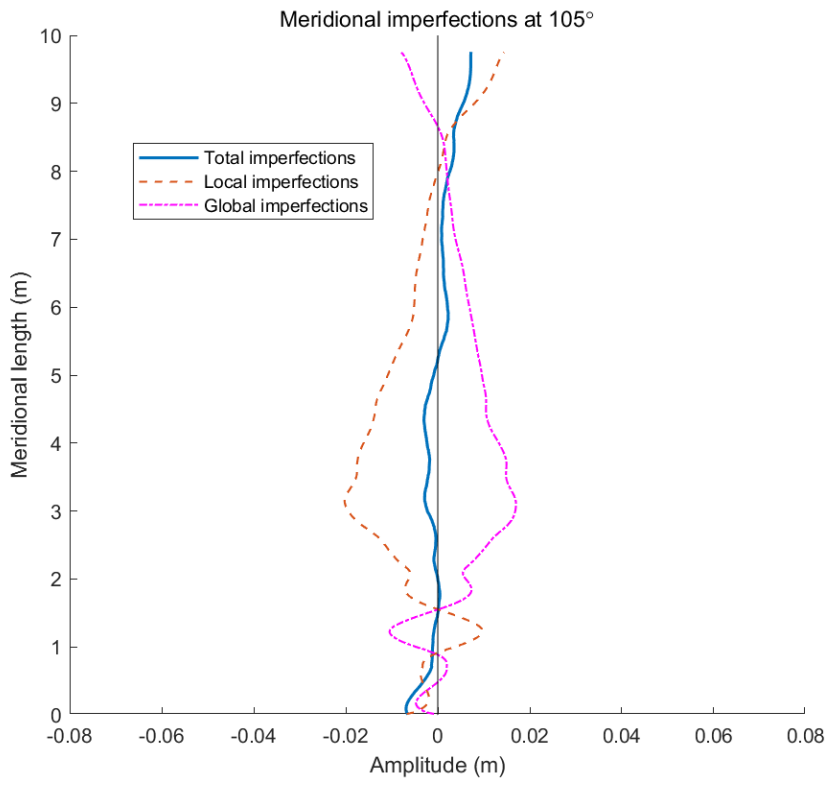




**Figure 0.6 Circumferential imperfections from cloud data (40 times scaled)**

It is shown that in circumferences at lower part of the tank ( $z = 0.1$  m and  $0.5$  m), both global & local imperfections have small amplitudes compared to the size of circumference. Local imperfections are dominant in the shape of total imperfections since it provides high frequency fluctuations around the slightly ovalized circumference. In the middle part (from  $z = 0.9$  m to  $z = 4.3$  m), the pattern of local imperfections becomes obvious, shown as a series of harmonic waves around the circumferences. The local component is still dominant since it has a larger range of deviation than the global one. Also, the amplitude of local imperfections are generally larger than the global imperfections. Global imperfections become dominant when reaching the top part ( $z = 5.4$  m to  $6.5$  m). It shows a larger amplitude and make the total imperfection shape close to ovalization.





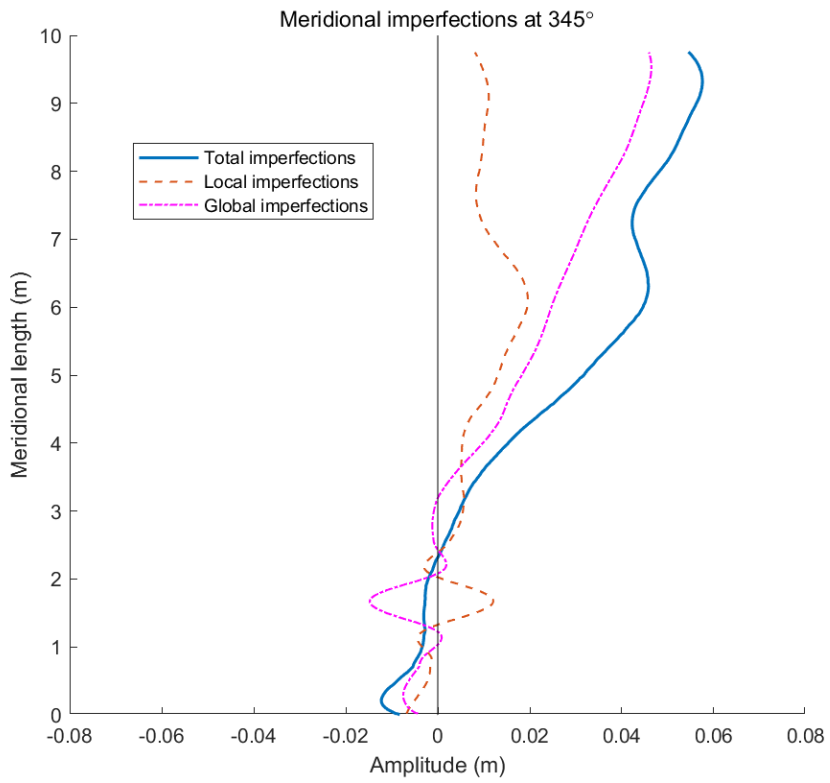
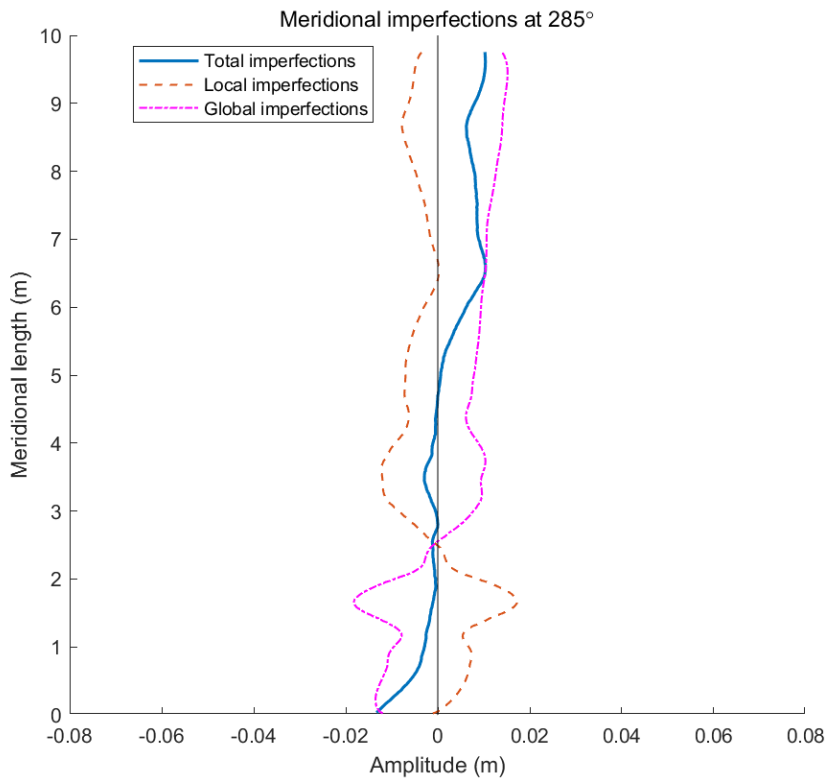


**Figure 0.7 Meridional imperfections from cloud data**

Compared with circumferential patterns, meridional imperfections show much more complicated patterns and fewer noticeable trends. It is seen that the maximum amplitude in local imperfections usually happens in the lower middle part of the meridian (from  $z = 2$  m to  $z = 4$  m), while the maximum amplitude in global imperfections usually happens at the top part and governs the position of maximum amplitude in total imperfections. A few similar shapes are noticed between global & local imperfections at the lower part of meridians (from  $z = 0$  m to  $z = 2$  m), which resemble harmonic waves with small wavelength. Global & local imperfections are in opposite directions to each other lead to smoother shapes of total imperfections shown in meridians.

### **3.4 FEM verification**

#### 3.4.1 Introduction

Both imperfections measured from real LFCT and recommended in the literature (Vandepitte et al. 1982; El Damatty et al. 1997, 2001) are employed in FEM implemented using the commercial software package ANSYS 16.1. This accuracy of the FEM developed in this study is first verified by repeating a series of experiments on a tank located in Fredericton, Canada. It was reported by Vandepitte et al. (1992) as a part of the investigation on the collapse incident. This tank is located at the top of a water tower and is an axisymmetric structure made of steel. Vandepitte et al. made assumption in the experiment that the wall thickness is varying at the lower conical part but constant at the top cylindrical part. Geometry of the tank is illustrated in Figure 3.8.

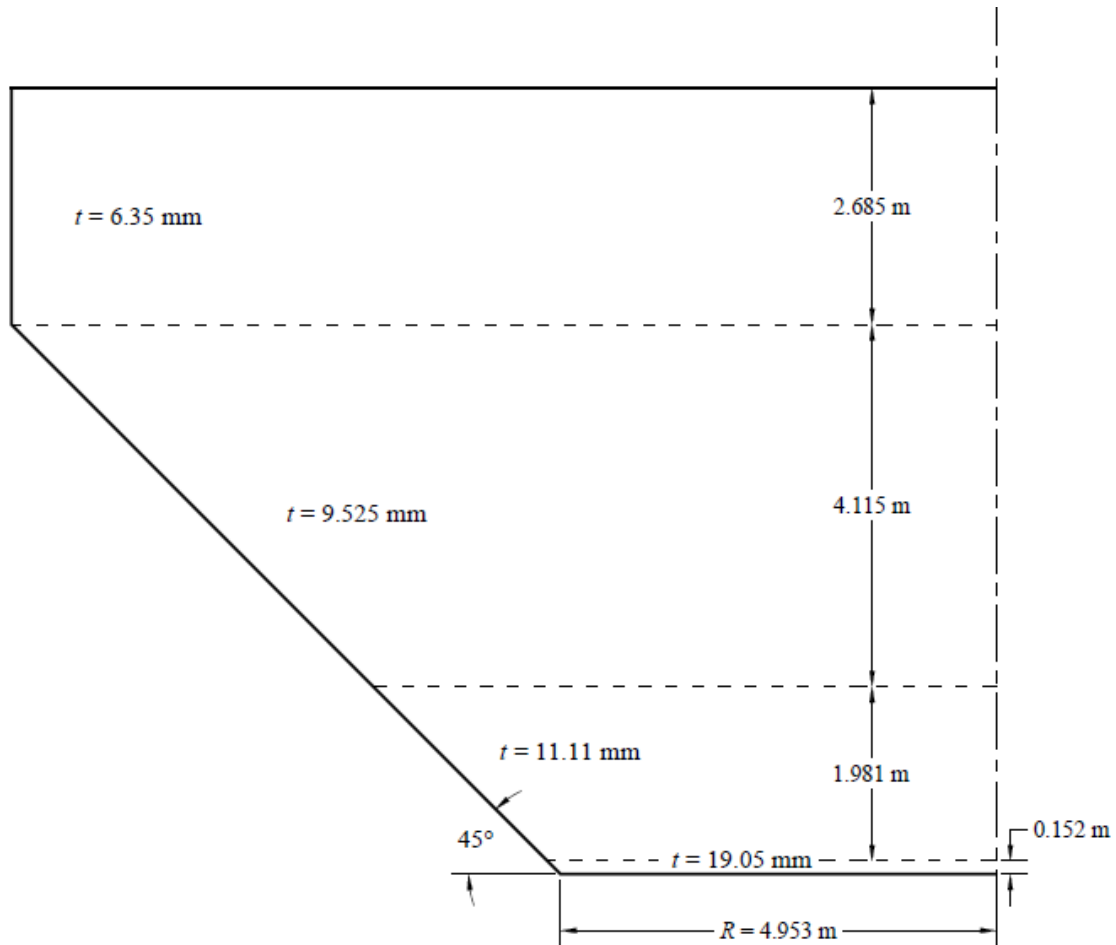


**Figure 0.8 Geometry of the Fredericton tank**

Finite element model was established and calculated in the experiment by an FEM program ‘F04B08’, which was developed by a group in Ghent university. In this verification analysis, the same geometry is modelled in ANSYS 16.0 using SHELL181 element available in the ANSYS library. It is a four-node or three-node element (Figure 3.9) with 6 degrees of freedom at each node: Translations  $\Delta_x$ ,  $\Delta_y$  and  $\Delta_z$ ; Rotations  $\theta_x$ ,  $\theta_y$  and  $\theta_z$ .

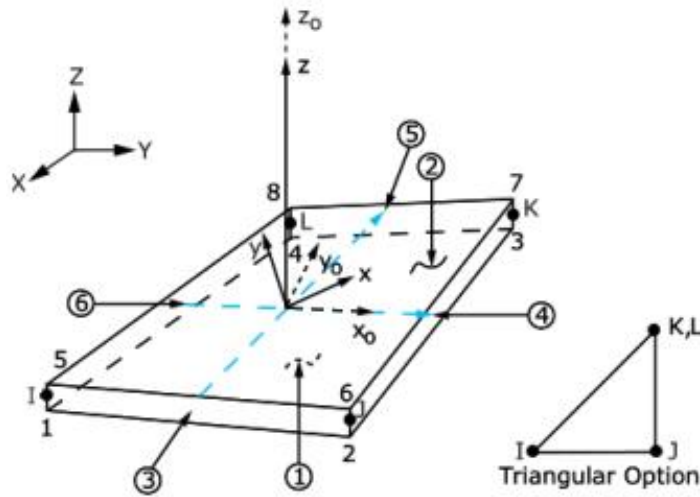


**Figure 0.9 Geometry of SHELL181 element**

Uniform material properties employed by Vandepitte et al. are shown in Table 3.1. The same values are applied in the verification model.

**Table 0.1 Material properties in verification**

| Name   | Value               |
|--|---------------------|
| Young's Modulus ( $E$ )                      | $2 \times 10^5$ MPa |
| Poisson's Ratio ( $\mu$ )                    | 0.3                 |
| Tensile Yield Strength ( $\sigma_{yt}$ )     | 250 MPa             |
| Compressive Yield Strength ( $\sigma_{yc}$ ) | 250 MPa             |

It was assumed that the top edge of Fredericton tank is free to move. Vandepitte et al. applied the boundary condition on the lower edge of the tank to restrain translations along and perpendicular to the generatrix. Only rotations about the tangent of lower rim are allowed. This is simulated by applying simply supported edge in the verification model (shown in Figure 3.10).

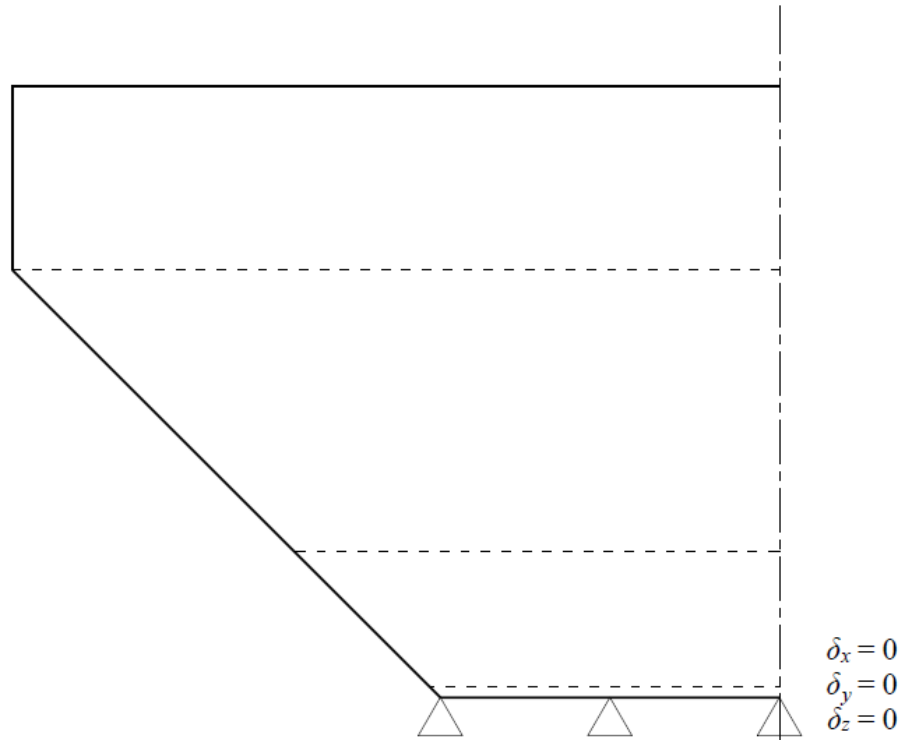


**Figure 0.10 Boundary conditions of verification model**

Two types of loads are assumed on the Fredericton tank as shown in Table 3.2: Water load is determined as water weight of  $9.81 \text{ m/s}^2$  (hydrostatic acceleration)  $\times 1000 \text{ N/m}^3$  (fluid density). Free surface is set to the top of tank.

**Table 0.2 Loads on Fredericton tank**

| Type                 | Amplitude                          | Location  | Direction         |
|----------------------|------------------------------------|---|-------------------|
| Hydrostatic Pressure | $\rho g H$                         | Interior Surface of Shell, with $z = 8.933 \text{ m}$ as Free Surface | Normal to Surface |
| Line Load            | $9.236 \times 10^{-3} \text{ N/m}$ | Top Rim of Cylinder   | Downward          |

Where:

$\rho$  : fluid density, equals to  $1000 \text{ kg/m}^3$ .

$g$  : hydrostatic acceleration, equals to  $9.81 \text{ m/s}^2$ .

$H$  : vertical distance from free surface.

It is assumed that the main part of line load is due to the roof structure. The other part is assumed as the substitution of self-weight. Due to the limitation of program utilized by Vandepitte et al.,



it is impossible to introduce body force on the model. The same types of loads are simulated on the verification model with the removal of self-weight in ANSYS 16.1.

Residual stress due to fabrication and welding process is not included in this study. El Damatty et al. (1997) justified that axial residual stress due to longitudinal welds do not influence the tank capacity. The effect of hoop residual stresses due to circumferential welds on the buckling capacity is found as between 10-15% by Hafeez et al. (2010).

Vandepitte et al. (1992) also introduced sine-wave geometric imperfections on the model to evaluate the effect of initial imperfections. It is shown in Figure 3.11 that Vandepitte et al. modelled 2 entire imperfection waves in the lower part of the conical shell where the thickness equals to 11.11 mm. Three types of model were established corresponding to different quality levels of the tank:

- 1) Perfect cone with no initial imperfections.
- 2) Imperfect, but 'good' shell with imperfection amplitude as 8.16 mm
- 3) 'Mediocre' shell with imperfection amplitude as 20.4 mm.

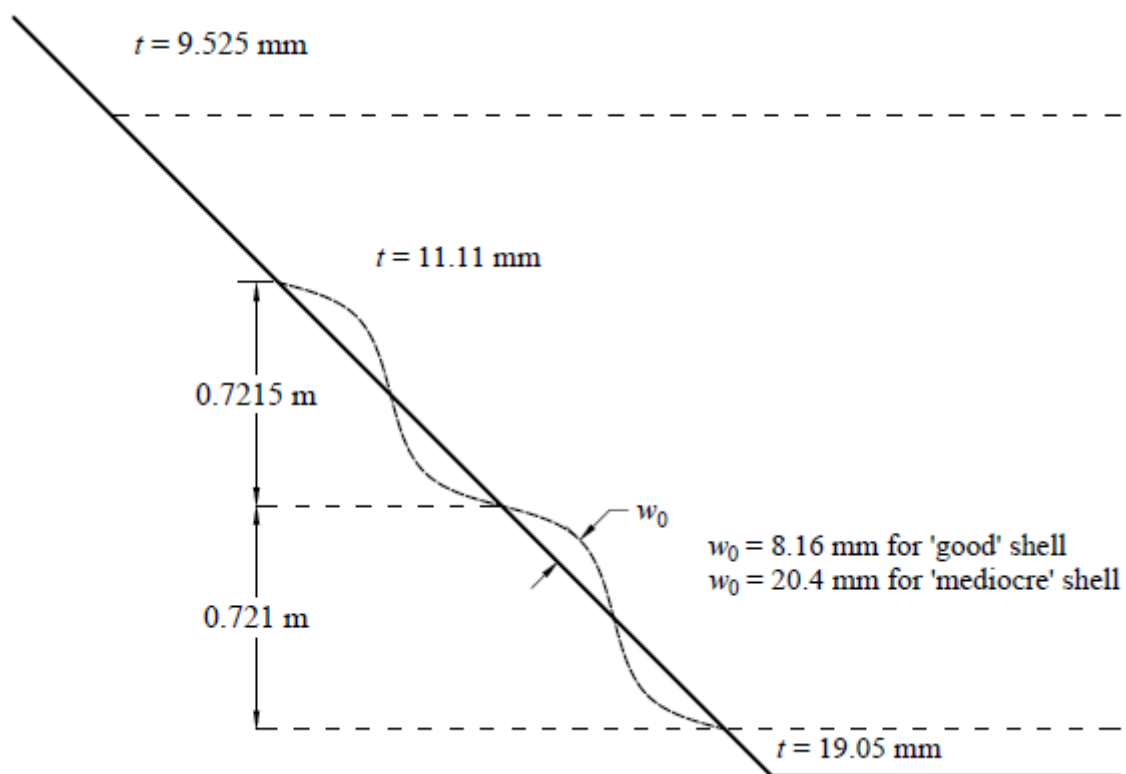
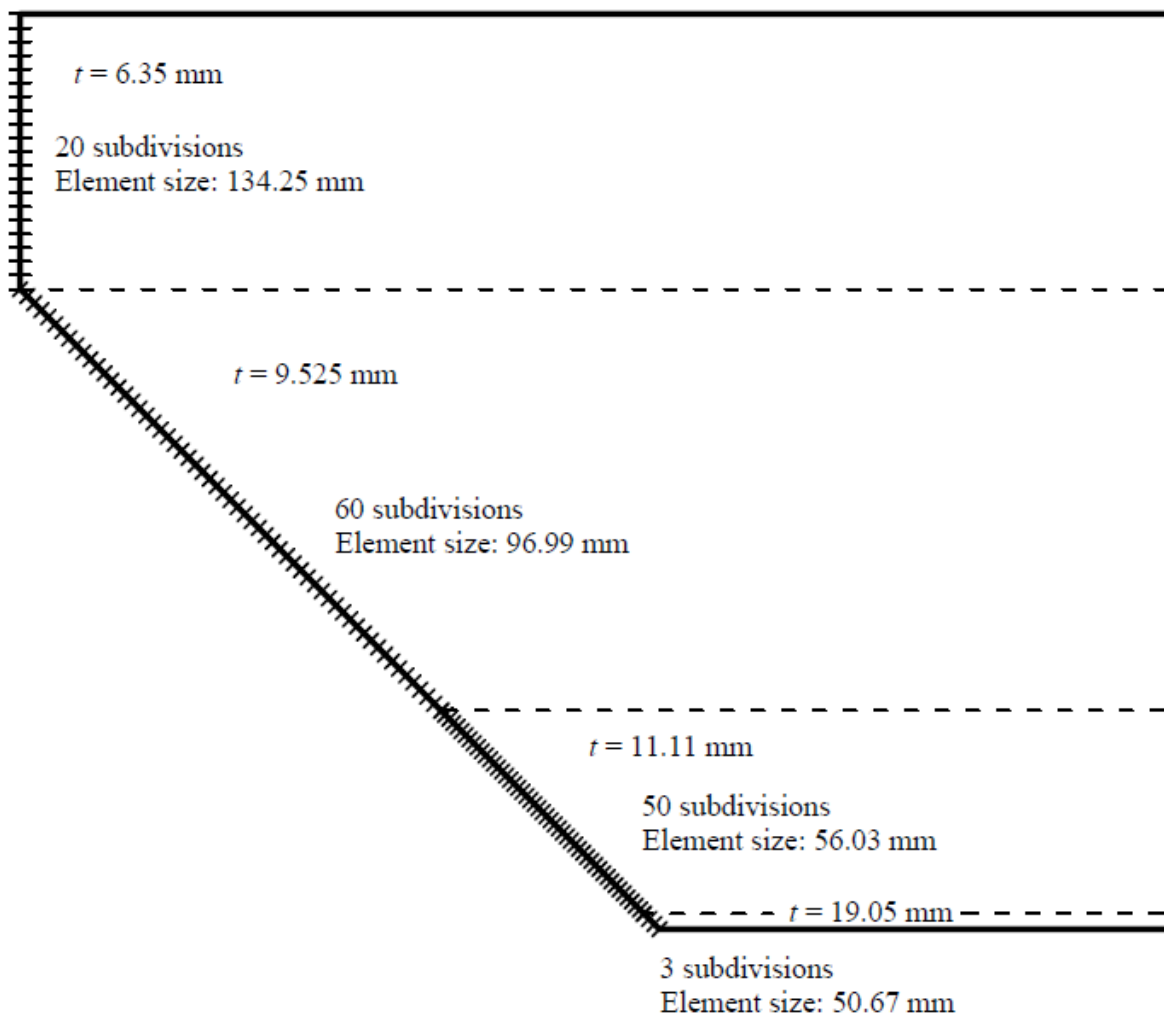


Figure 0.11 Geometric imperfections on Fredericton tank

### 3.4.2 Mesh sensitivity

Vandepitte et al. (1992) employed a fine mesh in the experiment to achieve accurate results as illustrated in Figure 3.12 and 3.13. Elements of large sizes are utilized in the cylindrical part and the top of conical part. Smaller elements are utilized in the lower part of the shell, which is the critical location to achieve a better prediction of buckling behavior. In the lower part of imperfect tank, the mesh is further refined to provide a better simulation of imperfections.



**Figure 0.12 Mesh of perfect Fredericton tank**

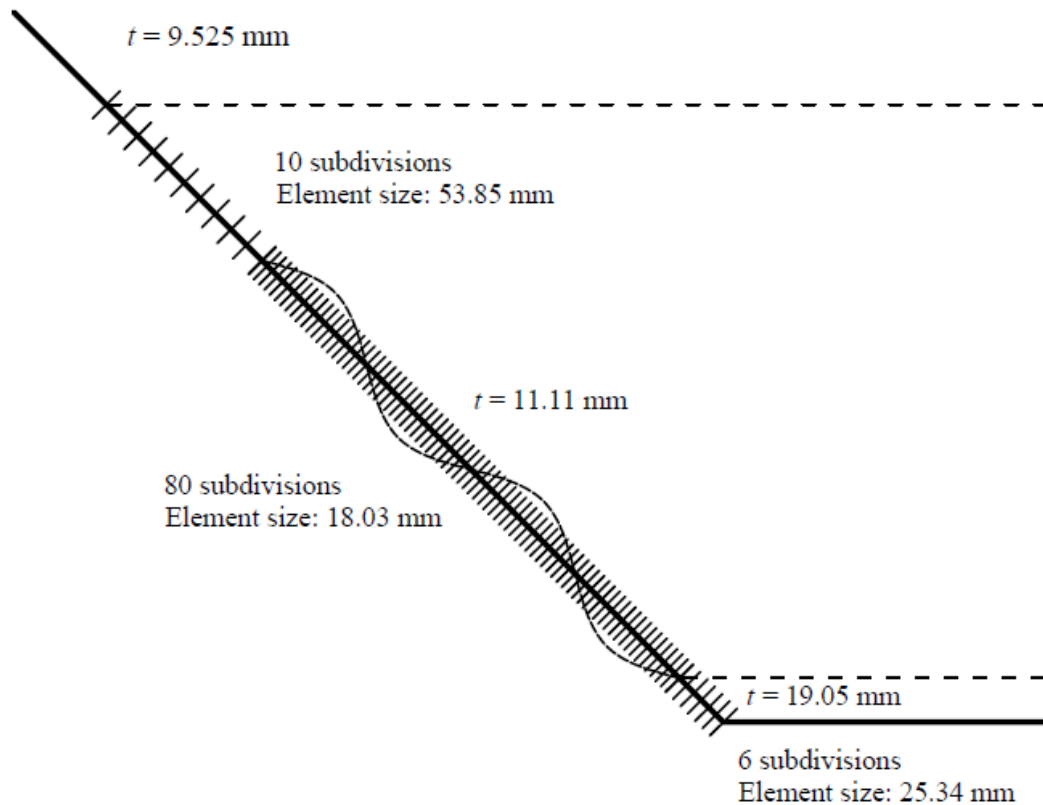


**Figure 0.13 Mesh of imperfect Fredericton tank**

The quality of mesh also has a large influence on analyzing results of verification model. Therefore, the mesh sensitivity is checked with multiple runs until a convergence in the result has been reached. The model is initially assigned with a coarse mesh defined by the local minimum element size at each section with gradings included to provide smooth transitions between sections with different mesh quality. The top cylinder was assigned with a minimum element size of 0.6 m. The top part of cone where  $t = 9.525$  mm has a minimum element size of 0.4 m. It decreases to 0.2 m at the bottom part where  $t = 11.11$  mm and 19.05 mm for a more accurate prediction of buckling behavior. Triangular shell elements have been used for the entire model and the size is decreased by 20% in each run. The local minimum element size and number of elements and nodes in each run are shown in Table 3.3. Examples of generated mesh for iteration steps are shown in Figures 3.14, 3.15 and 3.16.

**Table 0.3 Configurations of model in each step**

| Step Number     | Local Minimum Element Size (m) |                    |                    | Number of Nodes | Number of Elements |
|-----------------|--------------------------------|--------------------|--------------------|-----------------|--------------------|
|                 | Cylinder                       | Upper Part of Cone | Lower Part of Cone |                 |                    |
| 1 <sup>st</sup> | 0.6                            | 0.4                | 0.2                | 5406            | 10540              |
| 2 <sup>nd</sup> | 0.48                           | 0.32               | 0.16               | 8607            | 16872              |
| 3 <sup>rd</sup> | 0.384                          | 0.256              | 0.128              | 12872           | 25319              |
| 4 <sup>th</sup> | 0.307                          | 0.205              | 0.102              | 20744           | 40957              |
| 5 <sup>th</sup> | 0.246                          | 0.164              | 0.082              | 32476           | 64284              |
| 6 <sup>th</sup> | 0.197                          | 0.131              | 0.066              | 50174           | 99520              |
| 7 <sup>th</sup> | 0.157                          | 0.105              | 0.052              | 76328           | 151611             |

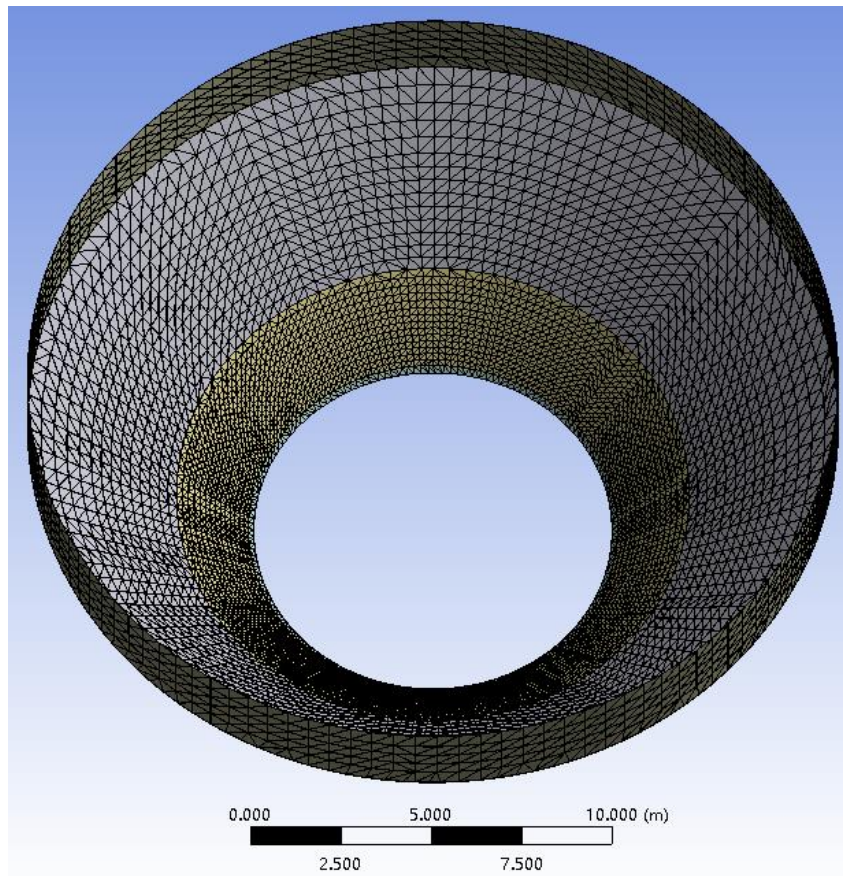


**Figure 0.14 Generated mesh for the 1<sup>st</sup> step**

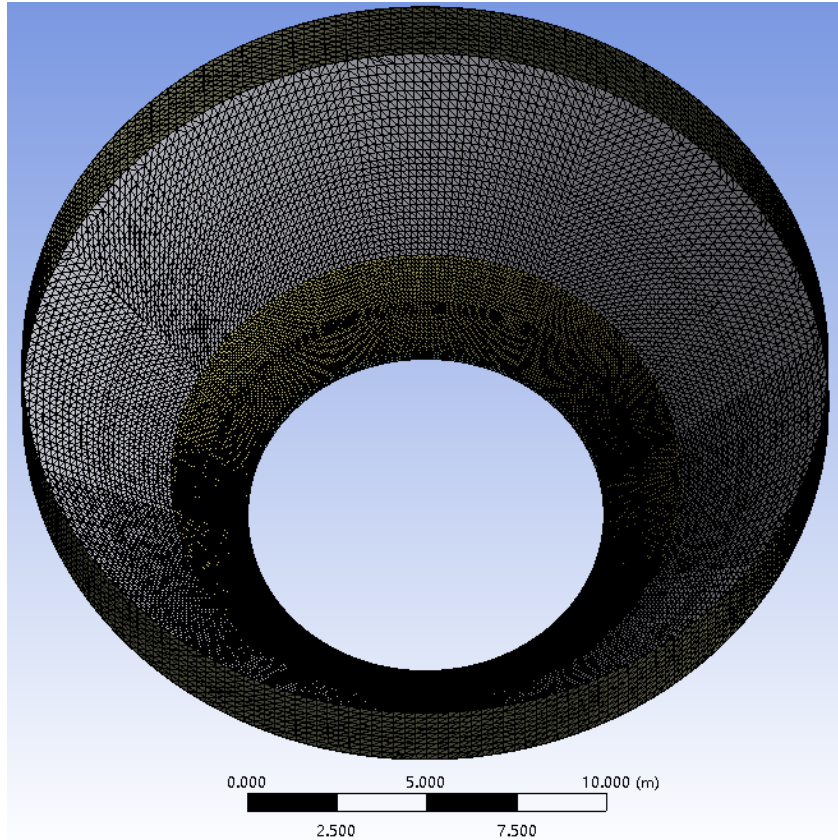


**Figure 0.15** Generated mesh for the 4<sup>th</sup> step

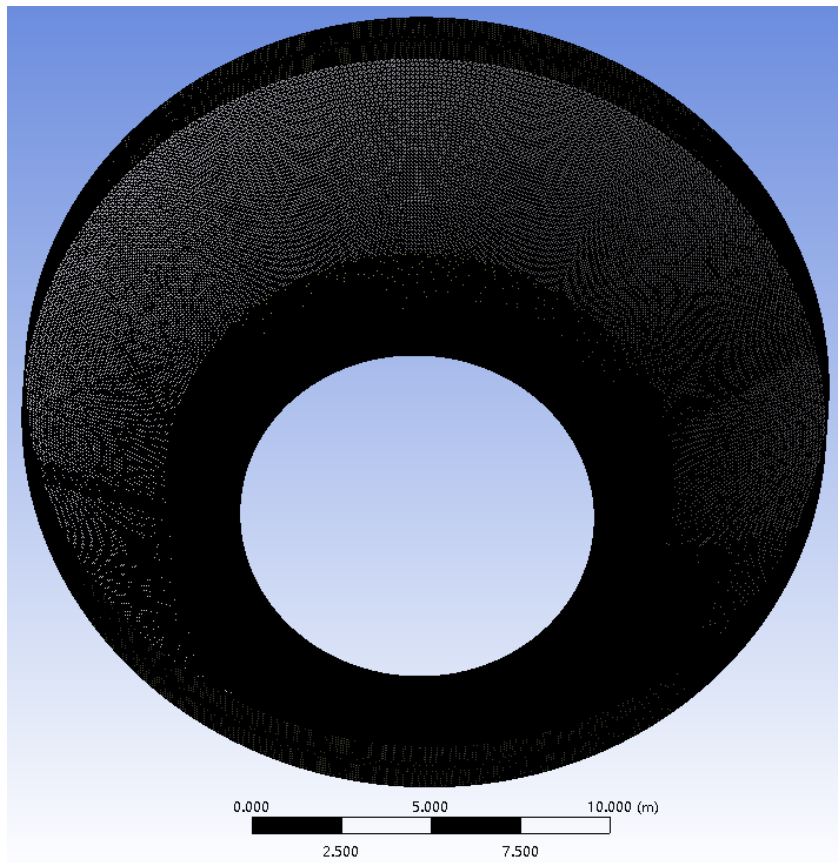


**Figure 0.16** Generated mesh for the 7<sup>th</sup> step

The von Mises yield criterion and isotropic hardening rule are adopted in the analysis. Since large deformation may occur during the analysis, the finite-strain configuration is employed to account for the geometric nonlinearity. To predict an accurate buckling capacity, the arc-length method (Riks 1979) is employed, and the buckling capacity is set to be at the first limit point where the stiffness matrix becomes singular.

Two cases in the report by Vandepitte et al. (1992) are simulated in the varication analysis: ‘good’ shell and ‘mediocre’ shell. The critical load factor ( $P_{cr}$ ) and the maximum von Mises equivalent stress ( $\sigma_{v,max}$ ) at buckling are collected to evaluate convergence, where  $P_{cr} = 1$  means a tank capacity that can just withstand the load levels specified in Table 3.2. Results are shown in Tables 3.4 and 3.5 and illustrated in Figures 3.17 and 3.18. Load-deflection curves are shown in Figures 3.19 and 3.20, indicating the limit point where the tank buckles in this analysis.

**Table 0.4 Verification analysis results for ‘good’ shell**

| Step Number     | $P_{cr}$ | Difference from last run | $\sigma_{v,max}$<br>(MPa) | Difference from last run |
|-----------------|----------|--------------------------|---------------------------|--------------------------|
| 1 <sup>st</sup> | 2.444    | -                        | 778.07                    | -                        |
| 2 <sup>nd</sup> | 2.098    | 14.161%                  | 649.36                    | 16.542%                  |
| 3 <sup>rd</sup> | 1.931    | 7.923%                   | 603.73                    | 7.027%                   |
| 4 <sup>th</sup> | 1.789    | 7.367%                   | 577.23                    | 4.389%                   |
| 5 <sup>th</sup> | 1.766    | 1.279%                   | 594.82                    | 3.047%                   |
| 6 <sup>th</sup> | 1.710    | 3.177%                   | 571.11                    | 3.986%                   |
| 7 <sup>th</sup> | 1.705    | 0.302%                   | 578.12                    | 1.227%                   |

**Table 0.5 Verification analysis results for ‘mediocre’ shell**

| Step Number     | $P_{cr}$ | Difference from last run | $\sigma_{v,max}$<br>(MPa) | Difference from last run |
|-----------------|----------|--------------------------|---------------------------|--------------------------|
| 1 <sup>st</sup> | 1.715    | -                        | 753.57                    | -                        |
| 2 <sup>nd</sup> | 1.431    | 16.509%                  | 700.71                    | 7.015%                   |
| 3 <sup>rd</sup> | 1.344    | 6.116%                   | 690.03                    | 1.524%                   |
| 4 <sup>th</sup> | 1.263    | 6.056%                   | 663.11                    | 3.901%                   |
| 5 <sup>th</sup> | 1.249    | 1.110%                   | 684.29                    | 3.194%                   |
| 6 <sup>th</sup> | 1.187    | 4.968%                   | 635.63                    | 7.111%                   |
| 7 <sup>th</sup> | 1.184    | 0.238%                   | 641.80                    | 0.971%                   |

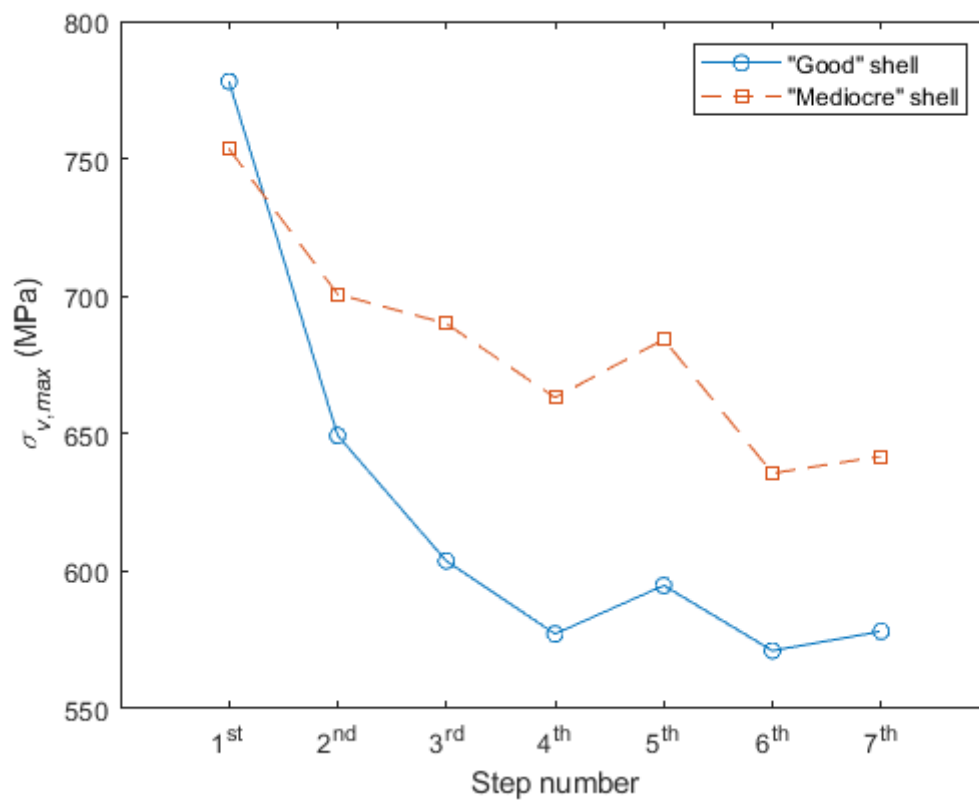
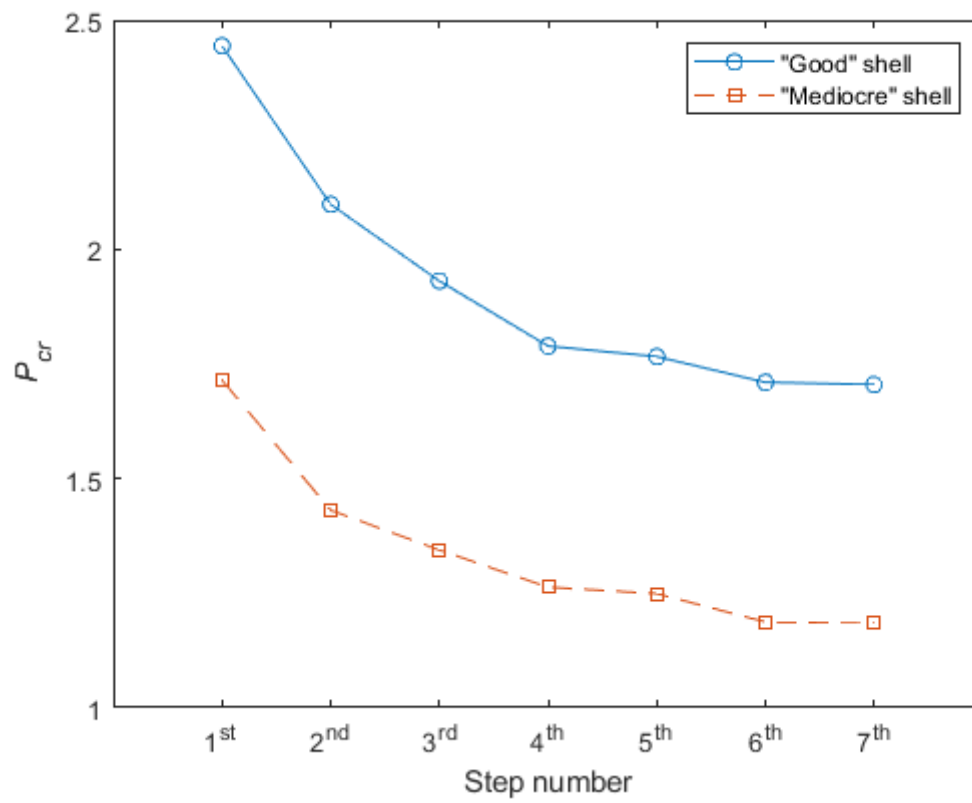


**Figure 0.17** Verification analysis results  $P_{cr}$  and  $\sigma_{v,max}$



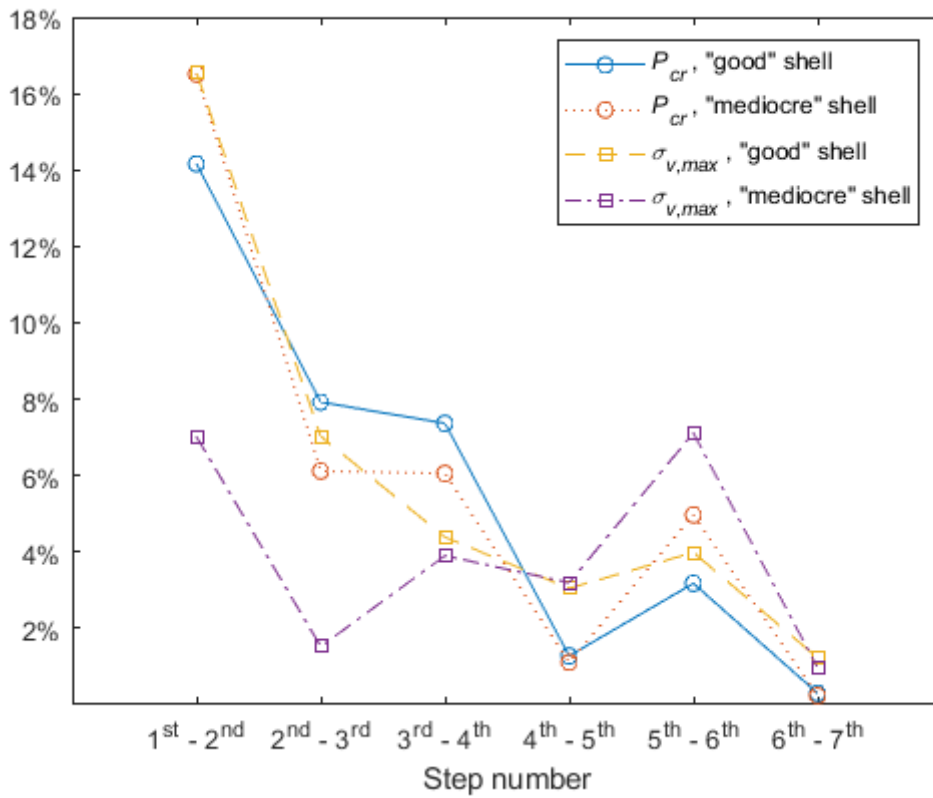


Figure 0.18 Difference between steps

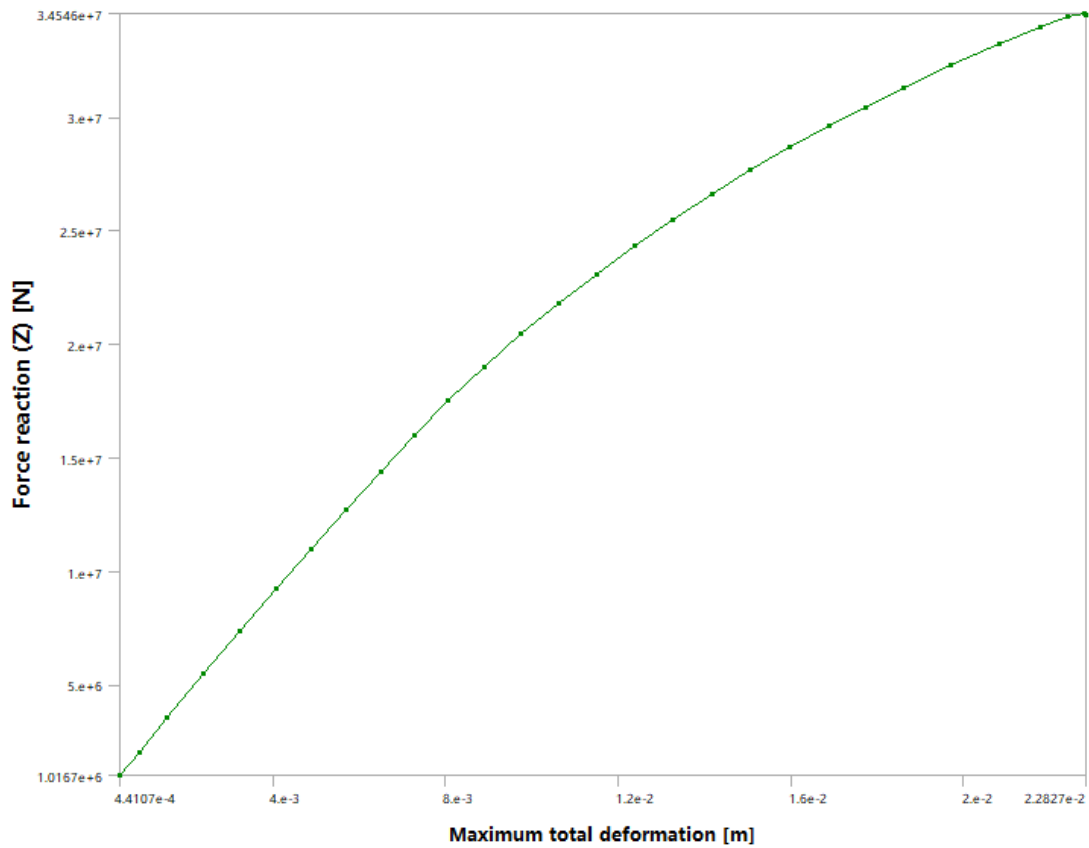
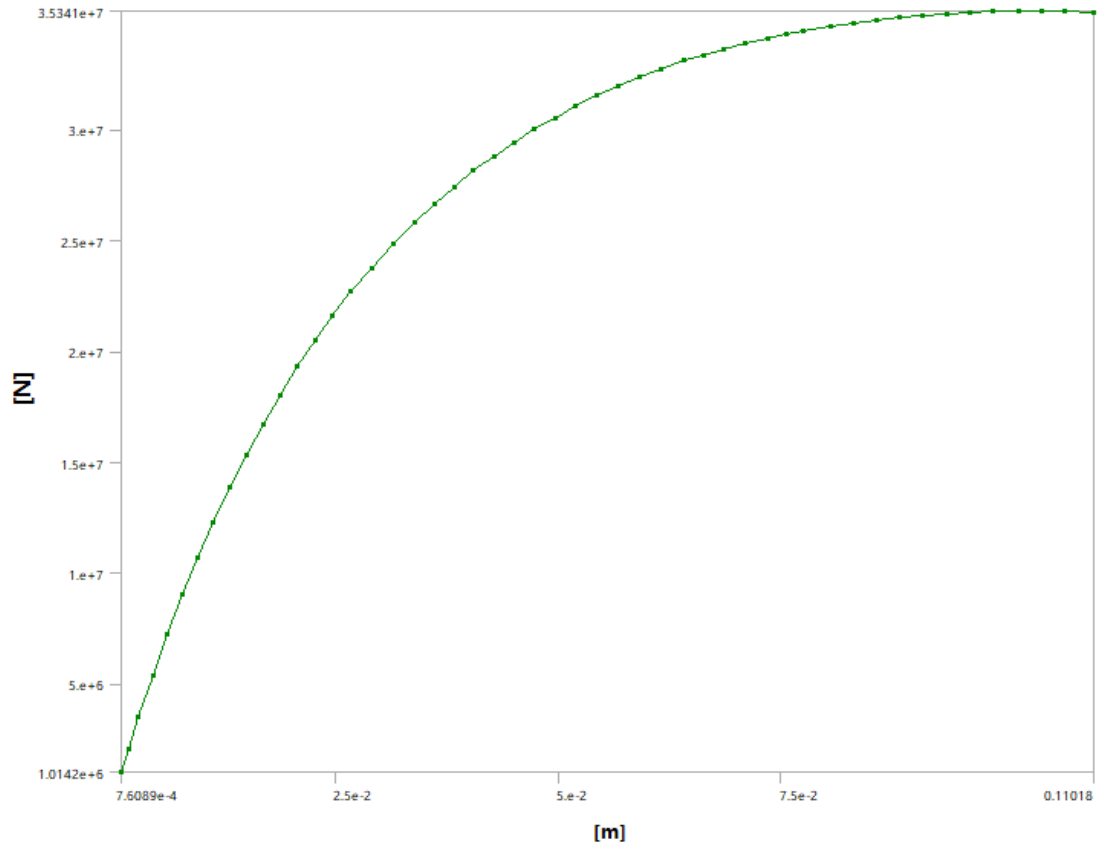


Figure 0.19 Load-deflection curve of 'good' shell (7<sup>th</sup> step)



**Figure 0.20 Load-deflection curve of ‘mediocre’ shell (7<sup>th</sup> step)**

It is clearly seen that both results of  $P_{cr}$  and  $\sigma_{v,max}$  have converged at the 6<sup>th</sup> step, their differences between the 6<sup>th</sup> step and the 7<sup>th</sup> step are very small (0.238% - 1.227%).

The  $P_{cr}$  value reported by Vandepitte et al. (1992) is 1.44 for ‘good’ shell and 1.10 for ‘mediocre’ shell. The result from this verification analysis (at the 7<sup>th</sup> step) is 1.705 for ‘good’ shell and 1.184 for ‘mediocre’ shell, which is 18.403% and 7.636% larger than Vandepitte’s result, respectively. The possible reason of the large difference in ‘good’ is the sensitivity of the tank to imperfection amplitude, where the tank modelled with low imperfections in ANSYS 16.1 can be more rigid compared to Vandepitte’s work.

### 3.5 Plastic deformation analysis

#### 3.5.1 Introduction

In this case study, the laser scan data can describe the exterior surface of a stiffened conical steel tank. Given the background information of this tank, the plastic deformation of the tank sustained during its service life may impact on the imperfections extracted from the cloud data.

That is, the deviation amplitude recorded by data points consists of two components: initial imperfections produced during the fabrication of the tank and plastic deformation from the hydrostatic load and additional external loads such as snow and live loads during the service life of the tank.

The effect of the plastic deformation is estimated in this section by using the finite element analysis (FEA). A finite element model (FEM) is established by using the FEA package ANSYS 16.1 to simulate the tank. The SHELL181 element is employed to construct the model. The material properties considered in the FEM are shown in Table 3.6.

**Table 0.6 Material properties of FEM model**

| Name   | Value                  |
|--|------------------------|
| Density                                      | 7850 kg/m <sup>3</sup> |
| Young's Modulus ( $E$ )                      | $2 \times 10^5$ MPa    |
| Poisson's Ratio ( $\mu$ )                    | 0.3                    |
| Tensile Yield Strength ( $\sigma_{yt}$ )     | 270 MPa                |
| Compressive Yield Strength ( $\sigma_{yc}$ ) | 270 MPa                |
| Ultimate Strength ( $\sigma_u$ )             | 400 MPa                |

The von Mises yield criterion and isotropic hardening rule are adopted in the analysis. A bilinear stress-strain relationship as shown in Figure 3.21 is considered in the model. The slope of the elastoplastic portion of the stress-strain curve is assumed to be 6000 MPa (El Damatty et al. 1997).

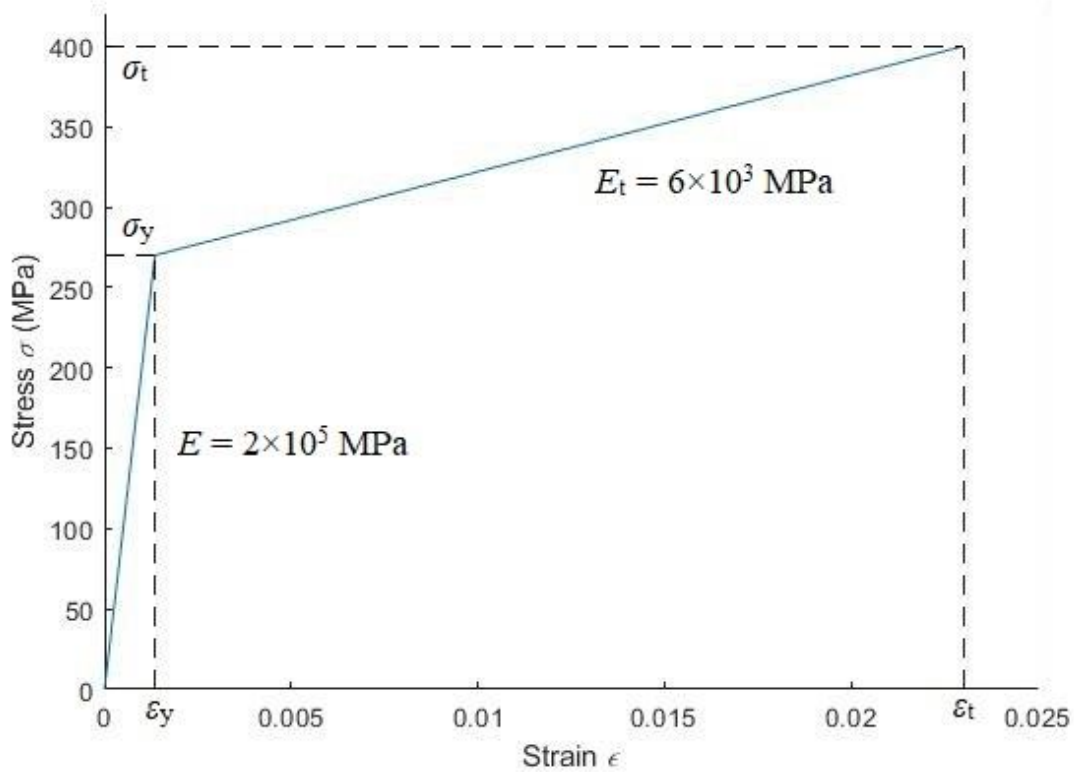


**Figure 0.21 Bilinear isotropic hardening**

Physical constraints of this tank from connected structures are simulated as boundary conditions. The bottom of the tank wall and stiffeners are welded to a plate on the top of the concrete shaft. Furthermore, there is a telecommunication tower installed on the top of this tank, where it is restrained to a cover plate. This allows the boundary conditions of the FEM to be determined as shown in Figure 3.22. This studied tank is designed with longitudinal stiffeners, bottom edge of conical shell and stiffeners are welded to a steel plate which is anchored to the concrete shaft. Pinned support is introduced in the model to simulate such physical constraints expected as “partially fixed”. While a fully fixed support will lead to conservative results. Also, horizontal movement of the top of model is restrained, which means it only has a vertical degree of freedom.

The design water load shown in Table 3.7 follows the requirements of AWWA D100-11 design criteria, which is factored by multiplying fluid density as  $1.25/0.9 \times 1000 \approx 1400 \text{ kg/m}^3$  (considered as dead load), where 1.25 and 0.9 are the partial safety factors for the dead load and steel yield strength, respectively (NBCC 2015, AWWA D100-11).

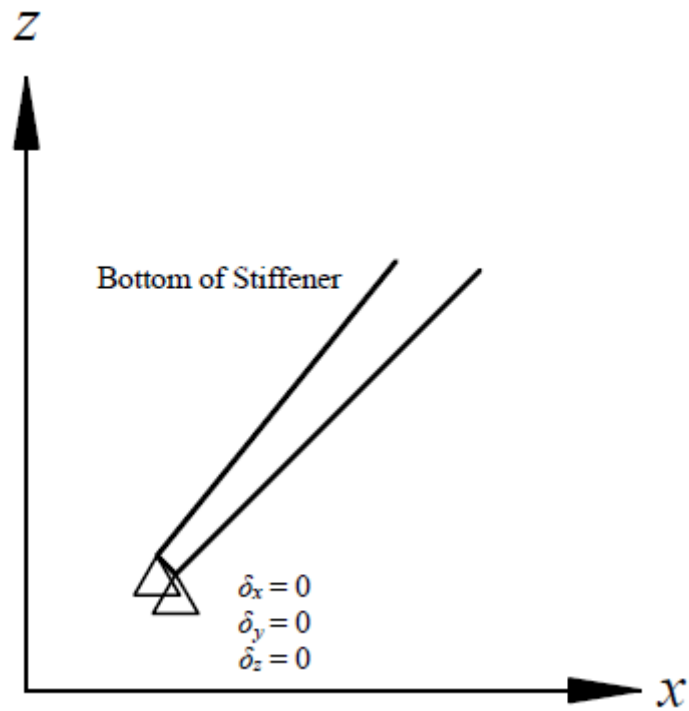
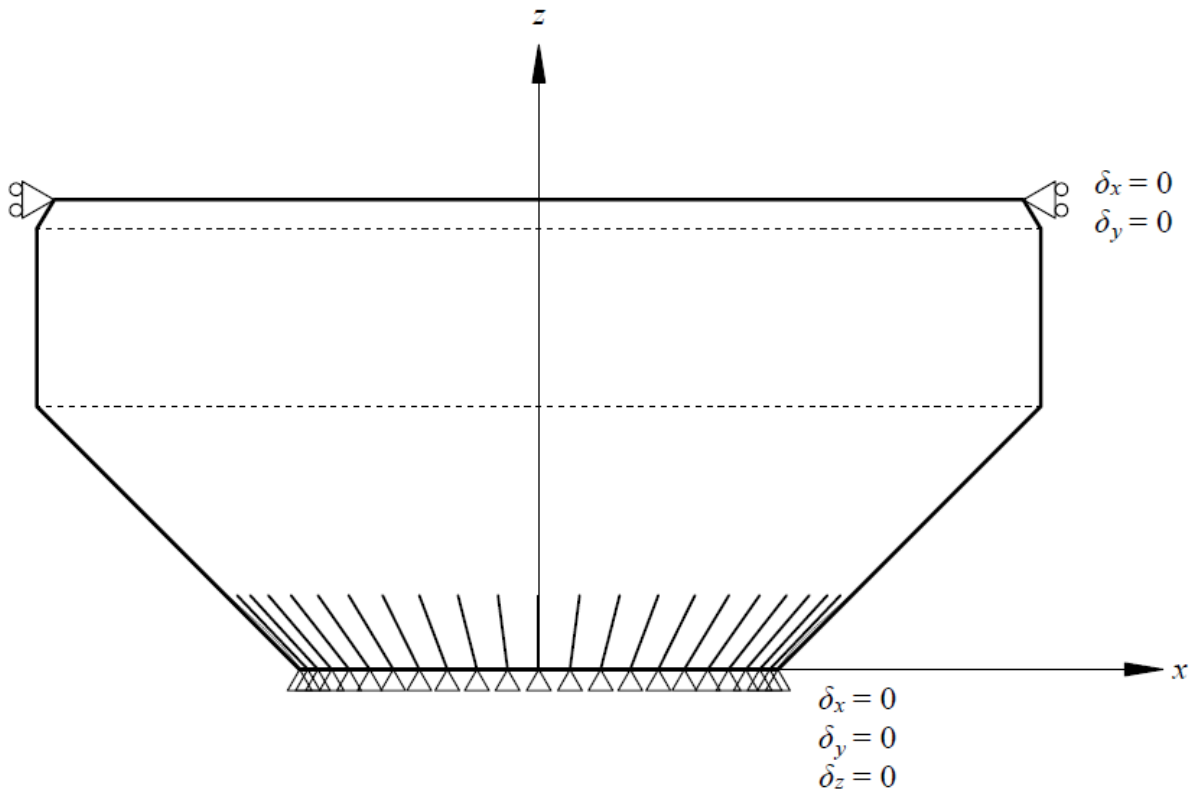


**Figure 0.22 Boundary conditions**

**Table 0.7 Water load applied on FEM model**

| Name                 | Amplitude   | Location   |
|----------------------|-------------|--|
| Hydrostatic Pressure | $1400gH$ Pa | Conical Shell and Part of Cylindrical Shell<br>with $z = 12.1$ m as Free Surface |

Where:

$g$  : gravitational acceleration, equal to  $9.81\text{m/s}^2$ .

$H$  : depth from the free surface.

Two load steps, loading and unloading, are carried out in this analysis. In the first step, 3 types of loads will be gradually applied to full scale on the FEM model to simulate the working condition. In the second step, the load amplitude gradually decreases to zero, which corresponds to the unloading process. Newton-Raphson method is utilized in searching for solution. Because the large deformation may happen in the process, the finite-strain configuration is employed to account for the geometric nonlinearity. Each load step is divided into substeps controlled by the program. 50 substeps are set initially, minimum number is set to 25 and maximum number is set to 100.

Total deformation ( $\Delta_{total}$ ) generated after the second step is collected as plastic deformation and will be compared with laser scan data. This result is calculated by ANSYS 16.1 FEA package as follows:

$$\Delta_{total} = \sqrt{\Delta_x^2 + \Delta_y^2 + \Delta_z^2} \quad (3 - 4)$$

Where:

$\Delta_x, \Delta_y, \Delta_z$  : Calculated deformation in  $x, y, z$  directions.

### 3.5.2 Mesh sensitivity

Results of FEA are easily affected by the element size in model. A mesh sensitivity analysis is introduced to determine a mesh quality where the solution is converged. The model is initially assigned with a coarse mesh. Mesh grading is considered by varying elements size from coarse mesh with a minimum element size of 0.6 m at the top cylindrical part to a finer mesh at the upper part of the conical vessel with minimum element size of 0.4 m. The most refined mesh is applied to the bottom part of conical vessel with minimum element size of 0.3 m. Triangular shell elements has been used to enable the mesh grading. Finer mesh used in the lower part of the conical vessel to yield towards more accurate prediction of the buckling capacity of the tank.

Multiple runs are employed for the analysis to reach a converged result, where element size is decreased by 20% by each step. Local minimum element size and number of elements and nodes for each step is shown in Table 3.8. Examples of generated mesh for each step is shown in Figures 3.23, 3.24 and 3.25.

**Table 0.8 Configurations of model in each step**

| Step Number     | Local Minimum Element Size (m) |                    |                                 | Number of Nodes | Number of Elements |
|-----------------|--------------------------------|--------------------|---------------------------------|-----------------|--------------------|
|                 | Cylindrical Cap                | Upper Part of Cone | Lower Part of Cone & Stiffeners |                 |                    |
| 1 <sup>st</sup> | 0.6                            | 0.4                | 0.3                             | 8026            | 15632              |
| 2 <sup>nd</sup> | 0.48                           | 0.32               | 0.24                            | 12002           | 23553              |
| 3 <sup>rd</sup> | 0.384                          | 0.256              | 0.192                           | 17819           | 35141              |
| 4 <sup>th</sup> | 0.307                          | 0.205              | 0.154                           | 24523           | 48500              |
| 5 <sup>th</sup> | 0.246                          | 0.164              | 0.123                           | 27831           | 55056              |

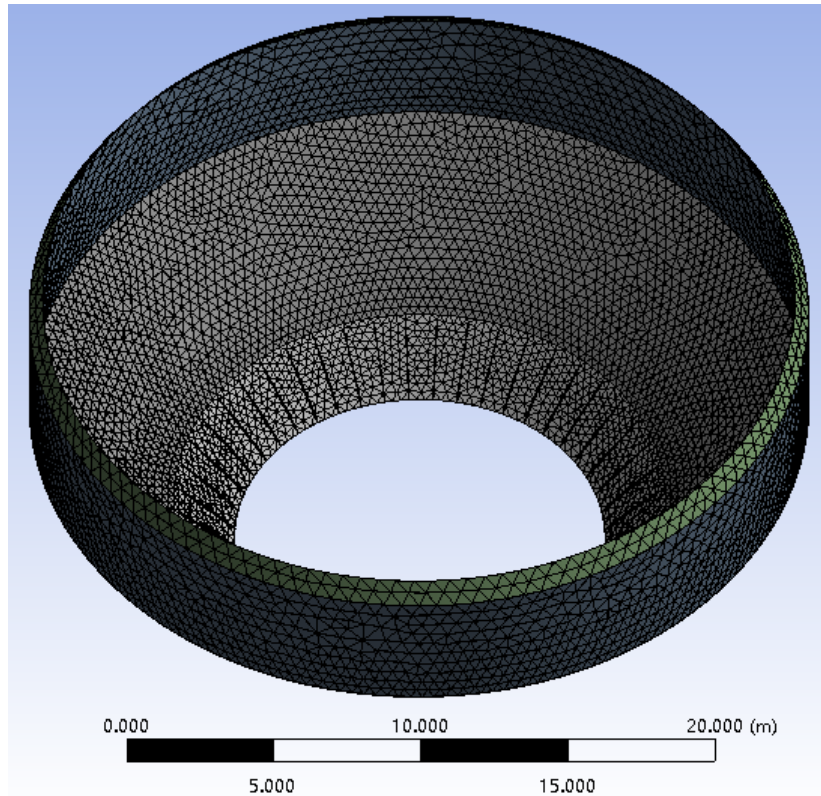


**Figure 0.23** Generated mesh for sensitivity analysis (1<sup>st</sup> step)

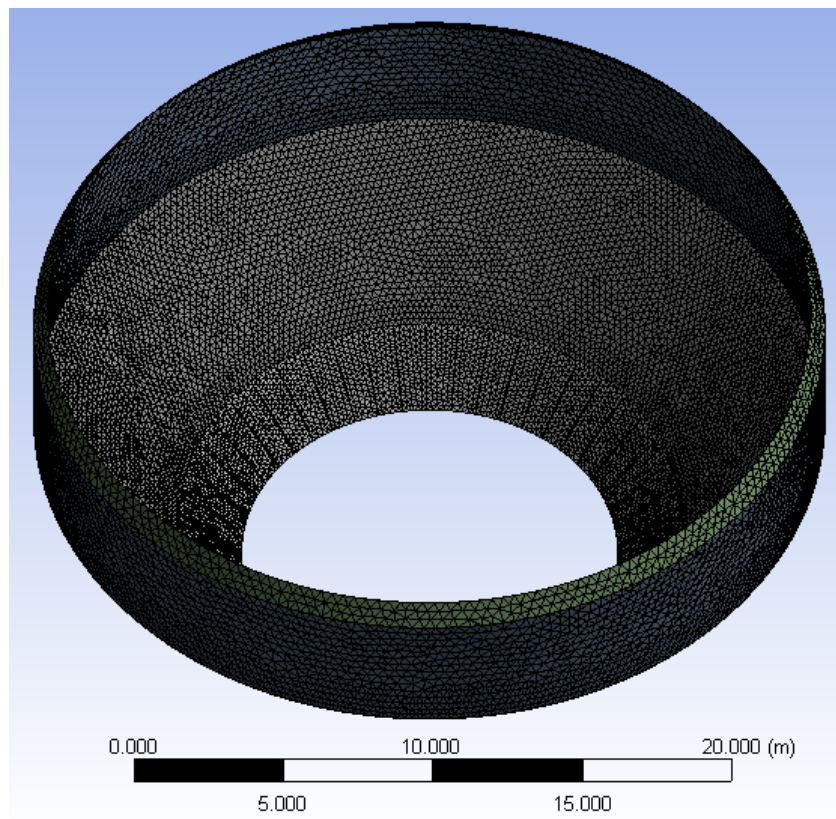


**Figure 0.24** Generated mesh for sensitivity analysis (3<sup>rd</sup> step)



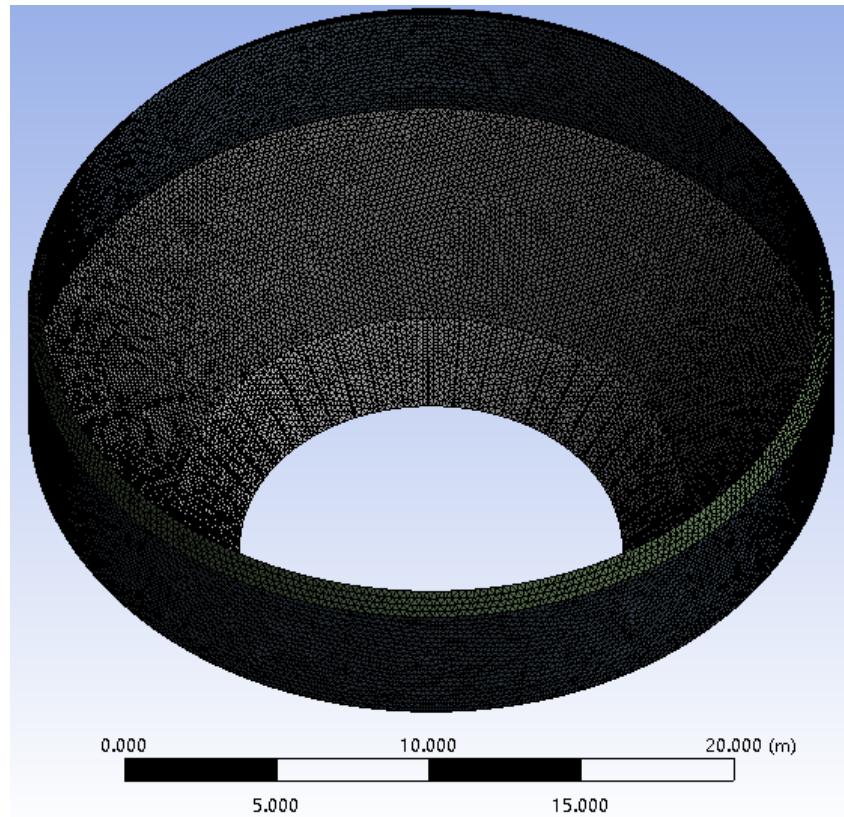


**Figure 0.25 Generated mesh for sensitivity analysis (5<sup>th</sup> step)**

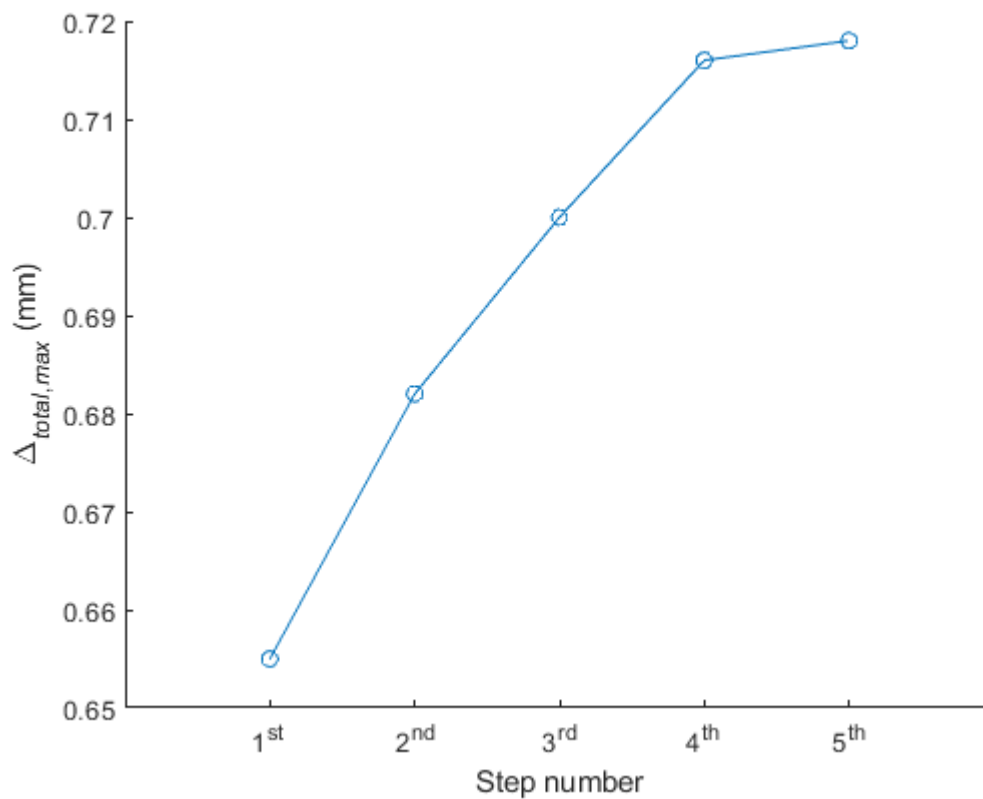
Since the plastic deformation is formed on an imperfect tank, the effect of initial geometric imperfections shall be included. This is done by generating distort mesh to simulate imperfection shape. The introduced imperfection pattern is specified by El Damatty et al. (2001) and is described in section 2.2.5. The amplitude is set to  $0.01L_b$ , corresponding to tank quality classified as ‘poor cone’ (Vandepitte et al. 1982).

Maximum total deflection ( $\Delta_{total,max}$ ) and maximum residual von Mises equivalent stress ( $\sigma_{v,max}$ ) at the end of unloading step are obtained to evaluate the convergence. (residual stress is distributed at the bottom rim of tank, which has negligible influence on the total deflection.)

Results of analysis and convergence situation are shown in Table 3.9 , Figure 3.26 and Figure 3.27.

**Table 0.9 Sensitivity analysis results**

| Step Number     | $\Delta_{total,max}$<br>(mm) | Difference from last step | $\sigma_{v,max}$<br>(MPa) | Difference from last step |
|-----------------|------------------------------|---------------------------|---------------------------|---------------------------|
| 1 <sup>st</sup> | 0.655                        | -                         | 293.32                    | -                         |
| 2 <sup>nd</sup> | 0.682                        | 4.122%                    | 296.04                    | 0.927%                    |
| 3 <sup>rd</sup> | 0.700                        | 2.639%                    | 303.91                    | 2.658%                    |
| 4 <sup>th</sup> | 0.716                        | 2.286%                    | 304.19                    | 0.092%                    |
| 5 <sup>th</sup> | 0.718                        | 0.279%                    | 303.92                    | 0.089%                    |



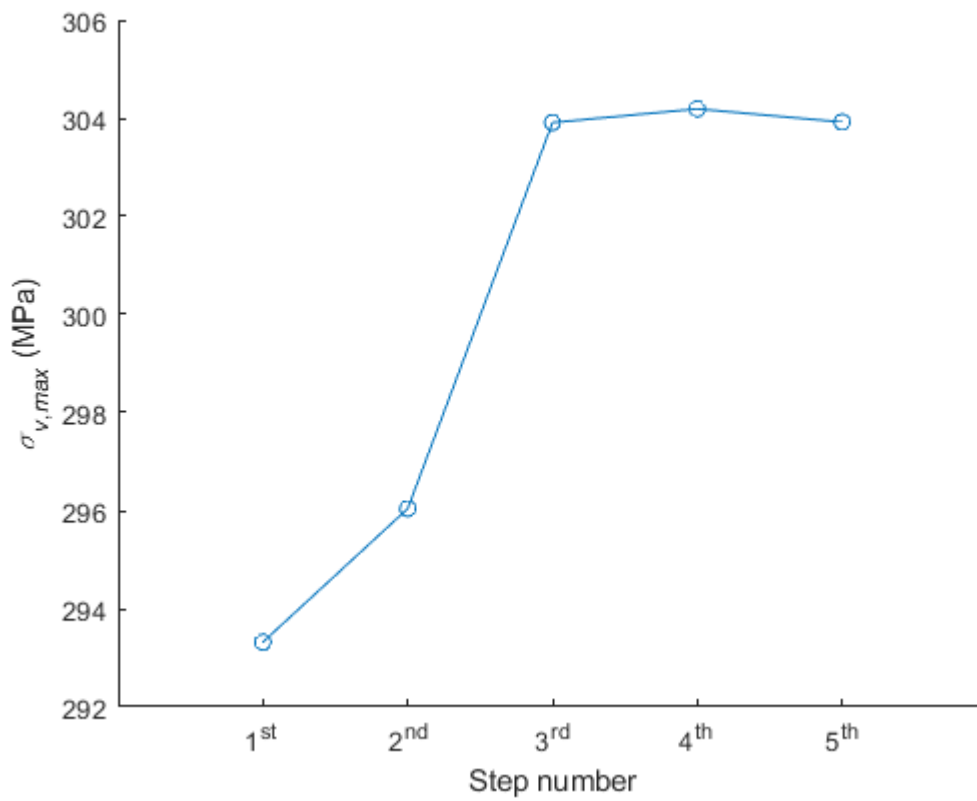


**Figure 0.26 Iterative analysis results**

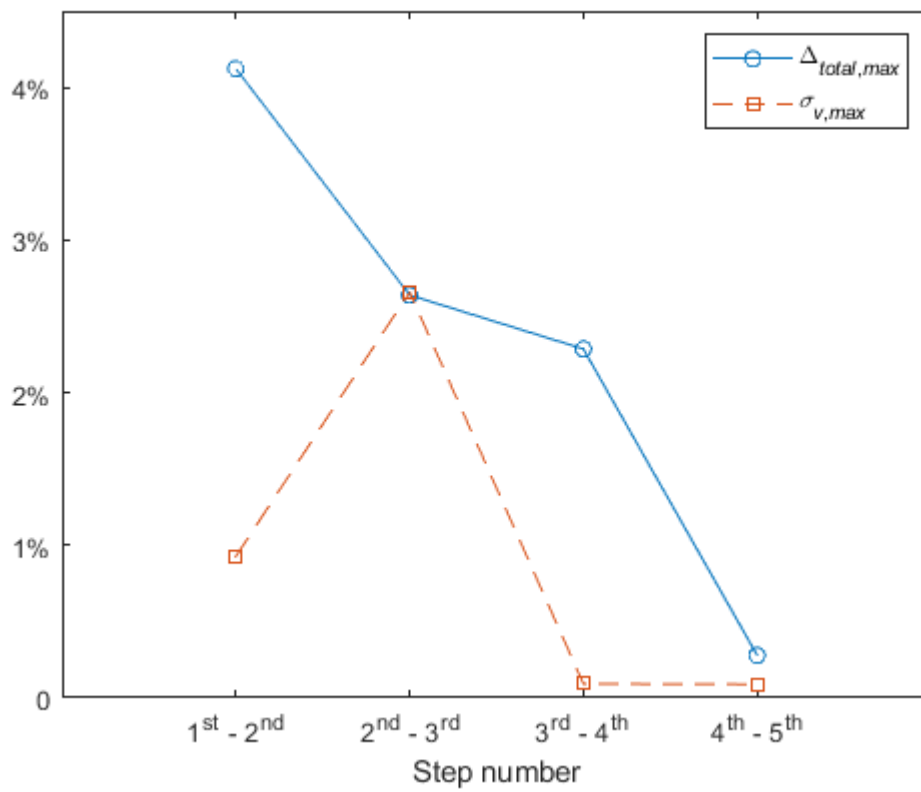


**Figure 0.27 Differences between iterative steps**

It is clearly shown that both  $P_{cr}$  and  $\sigma_{v,max}$  reaches convergence at the 4<sup>th</sup> step since the difference between 4<sup>th</sup> and 5<sup>th</sup> steps are extremely small (less than 0.1%). Hence, the mesh quality generated in the 4<sup>th</sup> step is employed for the following analysis.

Two sets of analysis are carried out involving different imperfection shapes. Considering the influence from the amplitude of initial imperfections, each set is allocated with a relatively lower amplitude and a higher one. This leads to four individual imperfections which are applied in total to obtain a critical effect of plastic deformation:

- 1) The assumed shape by El Damatty et al. (2001) (described in section 2.2.4 and 2.2.5). Imperfection amplitude is set to  $0.004L_b$  and  $0.01L_b$ , corresponding to the ‘good cone’ and the ‘poor cone’ classification specified by Vandepitte et al. (1982).
- 2) Geometric imperfections measured in cloud data (described in section 2.3). Imperfection amplitude is set to 100% and 40% from measurements (corresponding to the same proportion of amplitude from ‘good cone’ and ‘poor cone’ in the assumption).

In this study, all geometric imperfections are introduced into the FEM model with the aid of a in-house MATLAB code built by author, where the location of nodes in FEM model is recalculated with deviations to form a distorted mesh.

The total deformation (Eq. 3-4) calculated at the end of unloading procedure is collected as residual plastic deformation of the imperfect tank. Analysis results are shown in Figures 3.28, 3.29, 3.30 and 3.31.

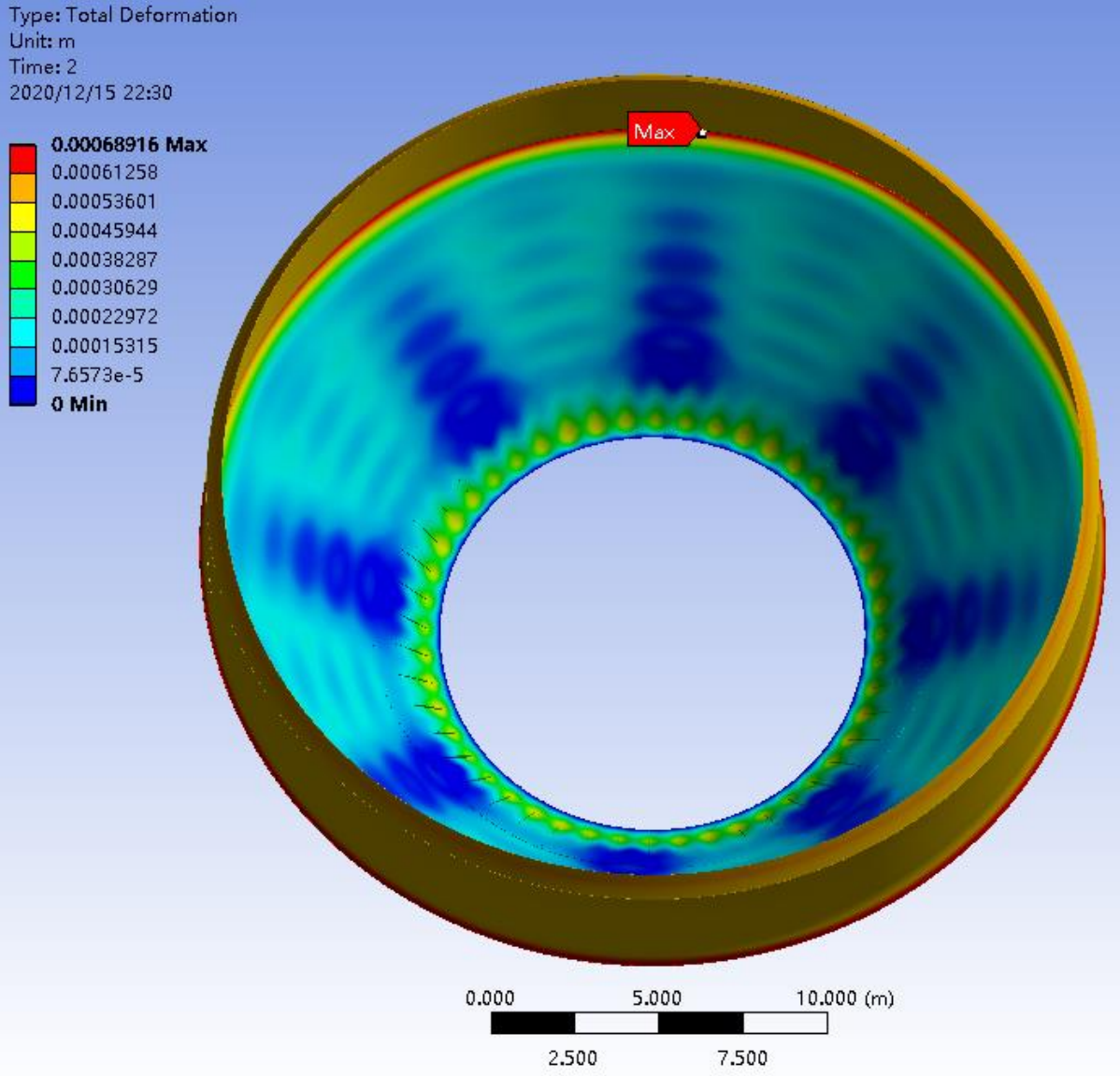


**Figure 0.28 Residual deformation of El Damatty et al. (2001) ‘good cone’  
(500 times scaled)**

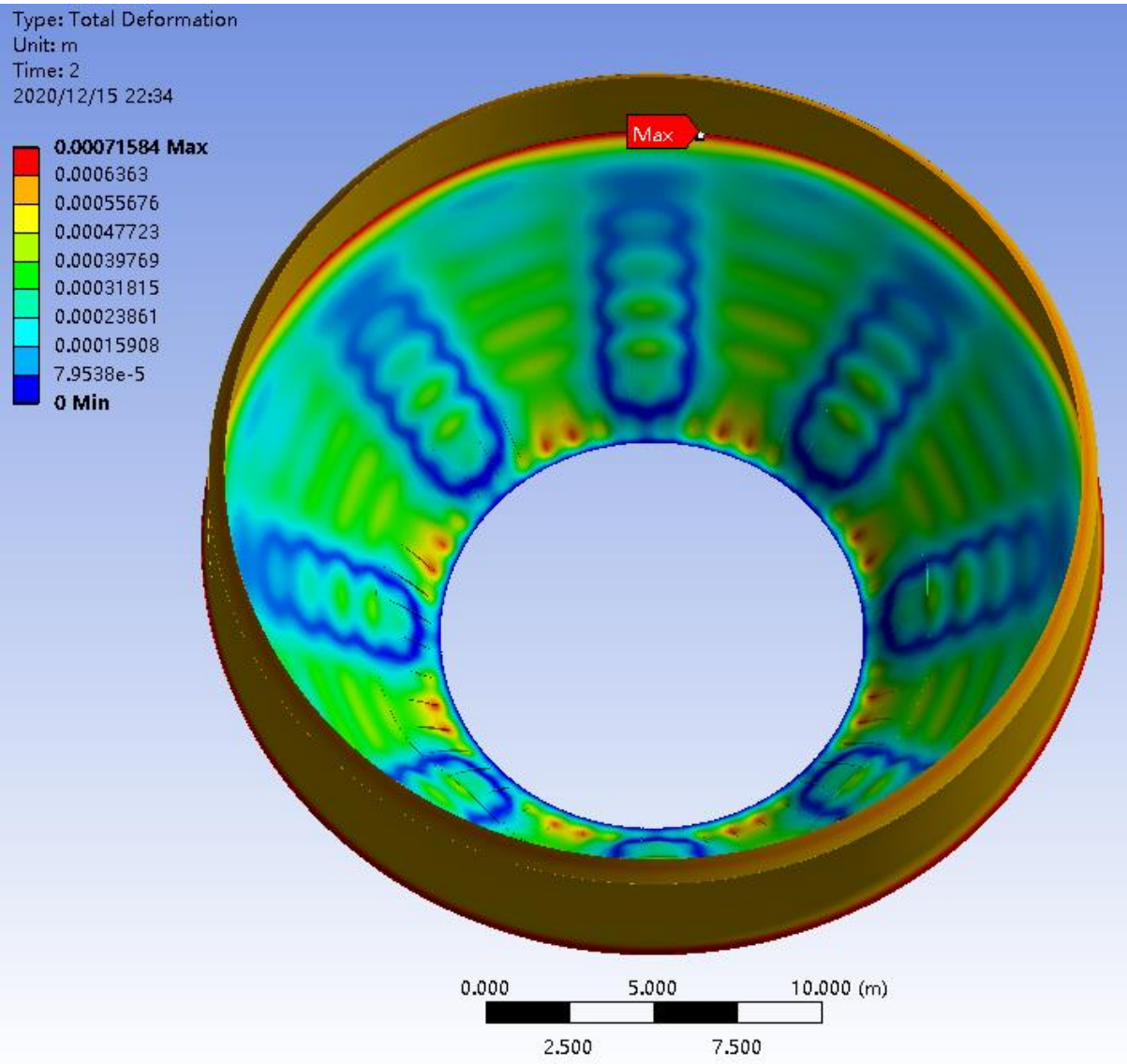


**Figure 0.29 Residual deformation of El Damatty et al. (2001) ‘poor cone’  
(500 times scaled)**

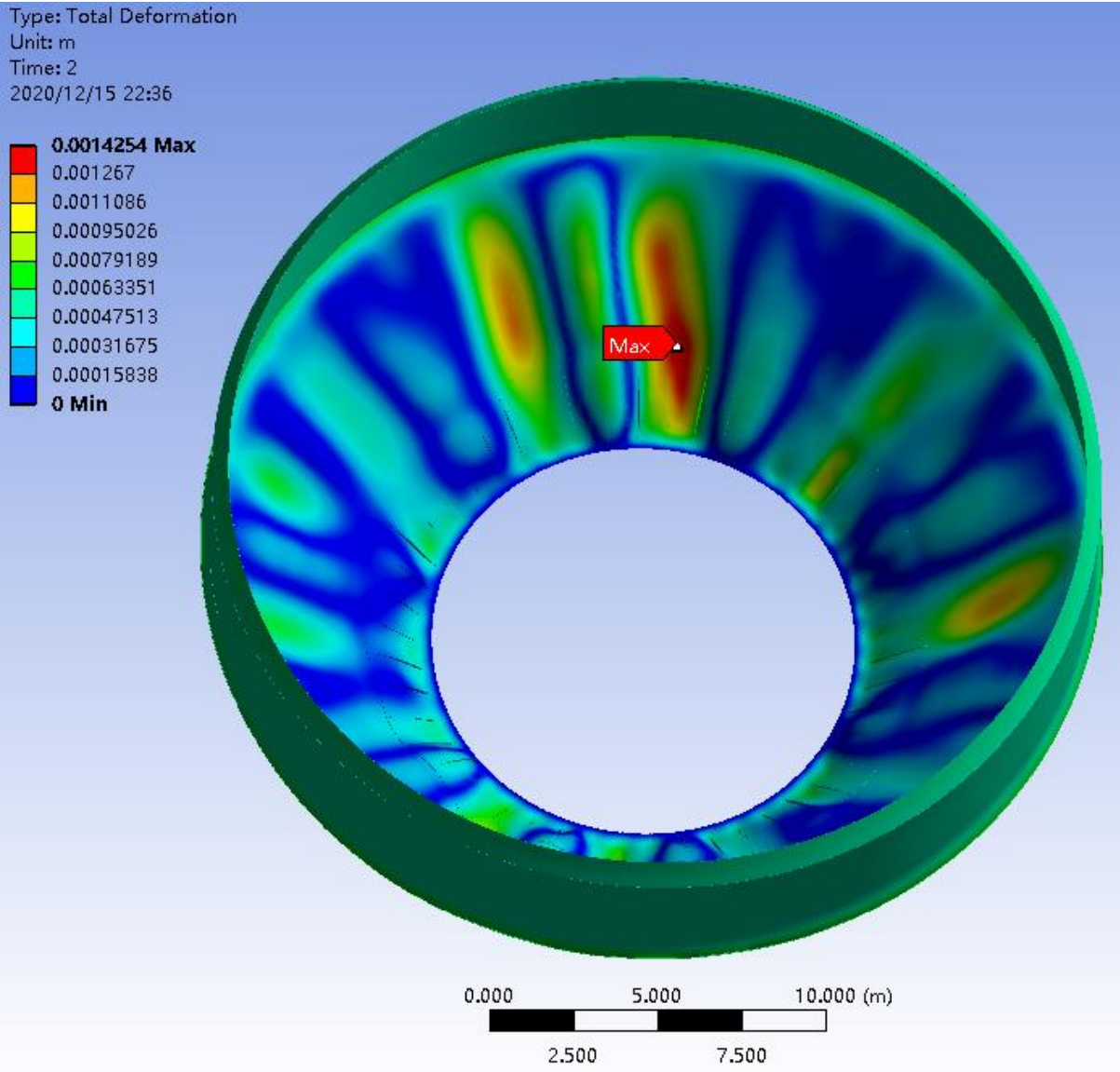


**Figure 0.30 Residual deformation of 100% measured imperfection (500 times scaled)**



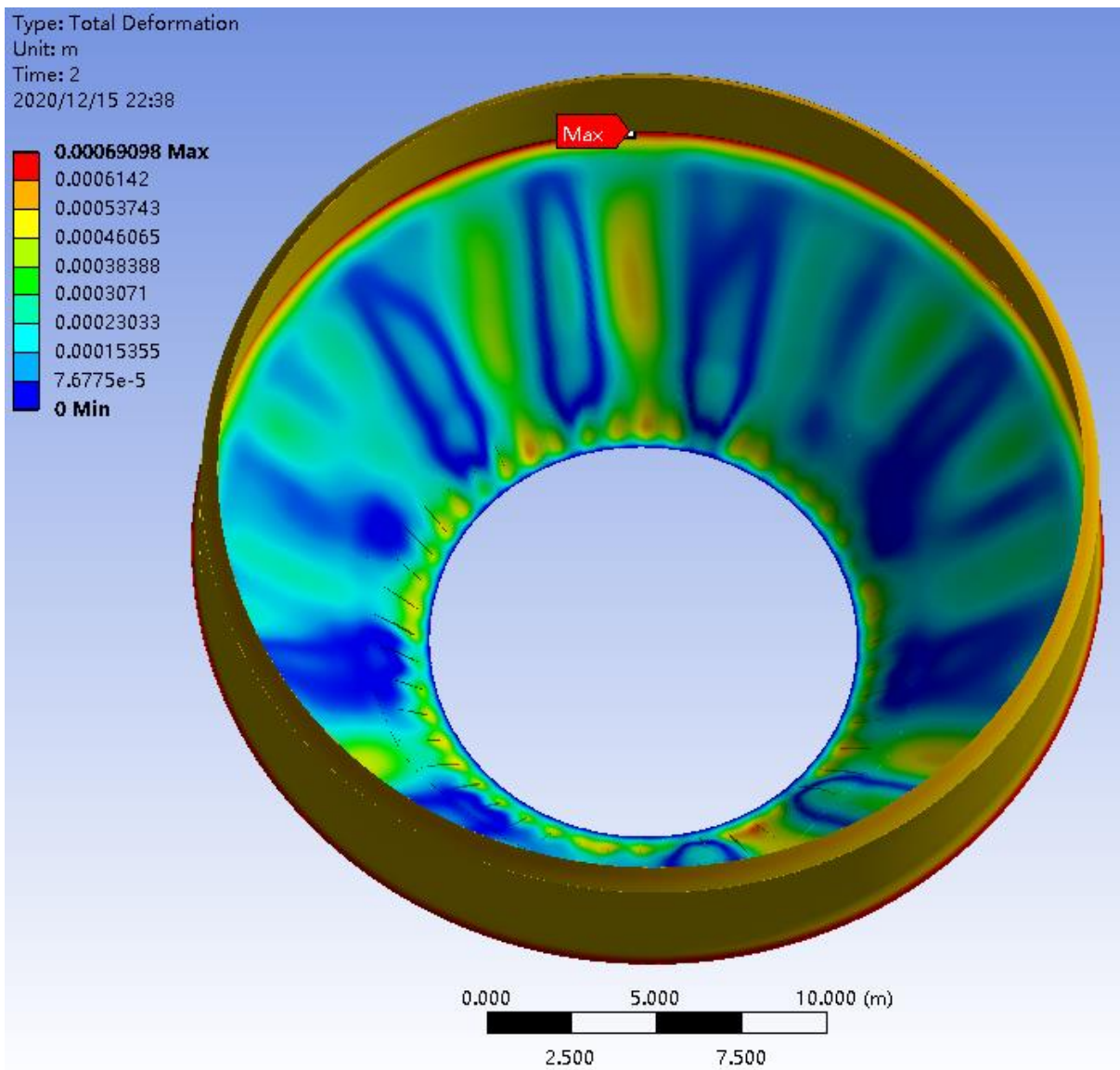


**Figure 0.31 Residual deformation of 40% measured imperfection (500 times scaled)**

It can be clearly seen from the result that the critical location varies a lot in different cases. The maximum deviation from nominal shape recorded in cloud data is around 0.05 m in the middle and 0.07 m at the top. The calculated maximum plastic deformation is less than 3% of the total amplitude. Even in the worst case (100% measured initial imperfection), the maximum plastic deformation only reaches 2.85% of the maximum deviation recorded in the cloud data. Therefore, the effect of plastic deformation is negligible in this case.



### 3.6 Imperfection Analysis

#### 3.6.1 Introduction

In this section, several imperfection shapes are considered in the analysis to evaluate their impact on the buckling capacity of the LFCT introduced in section 3.3. Comparison is made between imperfection shapes suggested by El Damatty et al. (2001) and the real imperfection measured from this tank (Figures 3.6 and 3.7).

The tank is modelled in ANSYS 16.0 using SHELL181 element available in the ANSYS library (Figure 3.9). Material properties of the model are shown in Table 3.10. Tangent modulus of bilinear strain hardening is assumed as 3% of Young's modulus (El Damatty et al. 1997).

**Table 0.10 Material properties of FEM model**

|  |                        |
|--|------------------------|
| Density                                      | 7850 kg/m <sup>3</sup> |
| Young's Modulus ( $E$ )                      | $2 \times 10^5$ MPa    |
| Tangent Modulus ( $E_T$ )                    | 6000 MPa               |
| Poisson's Ratio ( $\mu$ )                    | 0.3                    |
| Tensile Yield Strength ( $\sigma_{yt}$ )     | 270 MPa                |
| Compressive Yield Strength ( $\sigma_{yc}$ ) | 270 MPa                |
| Ultimate Strength ( $\sigma_u$ )             | 400 MPa                |

The top of this tank is welded to a steel plate to support roof structures are located and the bottom edge of this tank is restrained to the top of concrete shaft. The physical constraints of this structure are simulated by boundary conditions in the finite element model shown in Figure 3.32. Bottom edges of stiffeners and conical part are simply supported where only rotations are allowed. Restrictions of translation along  $x$  and  $y$  directions are applied on the top rim of the cone.

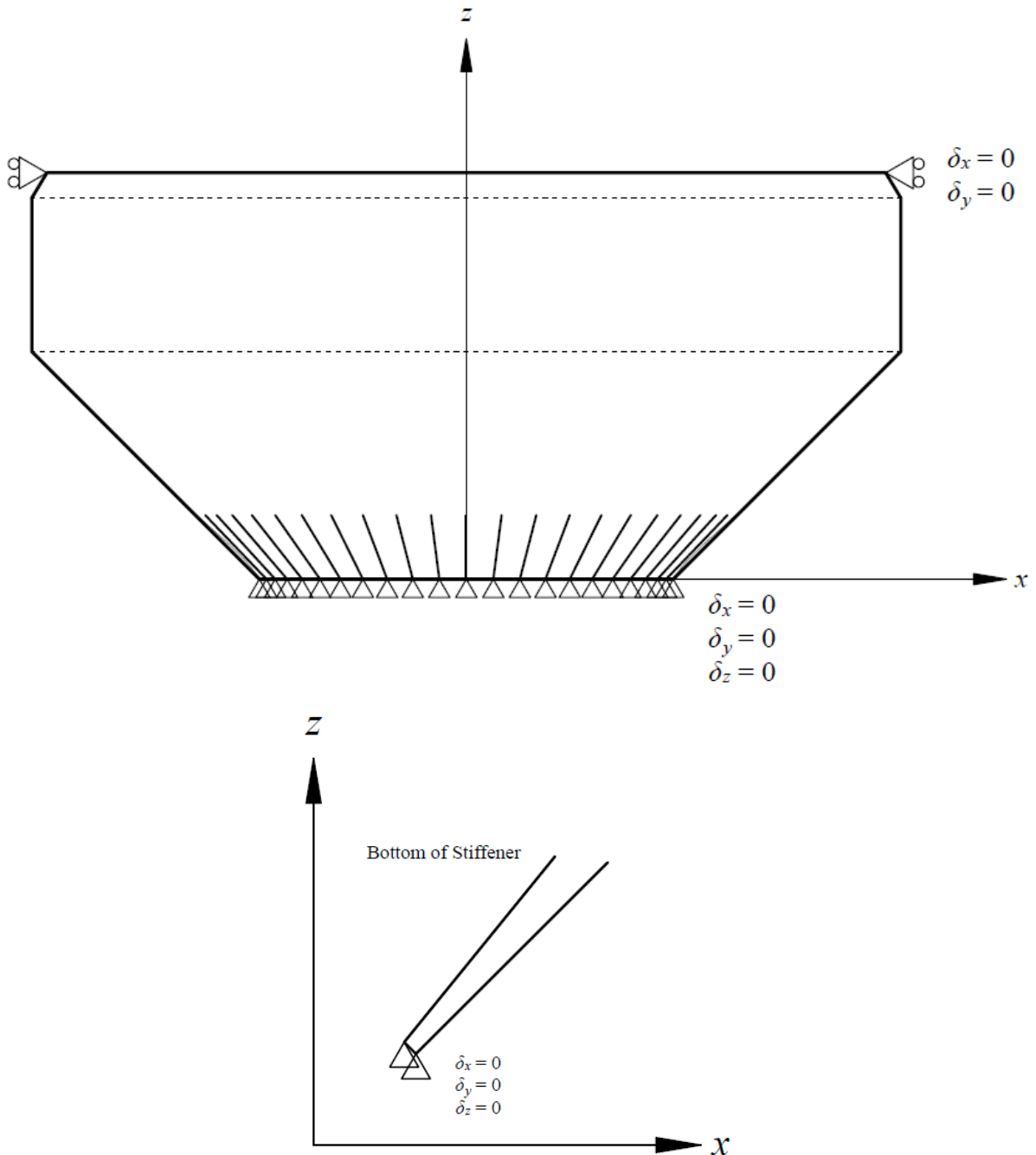


**Figure 0.32 Boundary conditions of the LFCT**

Loads are factored according to NBCC 2015 standard as dead loads (shown in Table 3.11). Apart from the self-weight of this tank, the design hydrostatic load is applied following the requirements of AWWA D100 design criteria and, which is factored by multiplying water density as  $1.25/0.9 \times 1000 \approx 1400 \text{ kg/m}^3$ . The factors 1.25 and 0.9 are the partial safety factors for the dead load and reduction factor for steel yield strength, respectively (NBCC 2015, AWWA D100-11).

**Table 0.11 Loads applied on FEM model**

| Type                 | Amplitude (Pa) | Location   | Direction         |
|----------------------|----------------|--|-------------------|
| Hydrostatic Pressure | $1400gH$       | Inner Surface of Conical Shell with $z = 12.1$ m as Free Surface | Normal to Surface |

Where:

$g$  : gravitational acceleration, equals to  $9.81 \text{ m/s}^2$ .

$H$  : depth from free surface (m).

The von Mises yield criterion with associated flow rule, isotropic hardening rule, finite-strain configuration and arclength method are adopted in the analysis to maintain the same analyzing approach with verification analysis.

### 3.6.2 Mesh sensitivity

As indicated in verification analysis in section 3.4, results of FEA can be affected by the element size in the model. Therefore, a mesh sensitivity analysis is introduced to determine a mesh quality used in the following procedure. It is confirmed when solutions are converged to stable values.

The model is initially assigned with a coarse mesh. Mesh grading is considered by varying elements size from a coarse mesh with a minimum element size of 0.6 m at the top cylindrical part to a finer mesh at the upper part of the conical vessel with a minimum element size of 0.4 m. The most refined mesh is applied to the bottom part of conical vessel with minimum element size of 0.3 m. Triangular shell elements has been used to enable the mesh grading. Finer mesh used in the lower part of the conical vessel to yield towards more accurate prediction of the buckling capacity of the tank.

Multiple runs are employed to make sure that the result reaches convergence, where element size is decreased by 20% in each step. Local minimum element size and number of elements and nodes for each step is shown in Table 3.12. Generated mesh for each step is shown in Figures 3.33, 3.34, 3.35, 3.36 and 3.37.

**Table 0.12 Configurations of model in each step**

| Step Number     | Local Minimum Element Size (m) |                    |                                 | Number of Nodes | Number of Elements |
|-----------------|--------------------------------|--------------------|---------------------------------|-----------------|--------------------|
|                 | Cylindrical Cap                | Upper Part of Cone | Lower Part of Cone & Stiffeners |                 |                    |
| 1 <sup>st</sup> | 0.6                            | 0.4                | 0.3                             | 8026            | 15632              |
| 2 <sup>nd</sup> | 0.48                           | 0.32               | 0.24                            | 12002           | 23553              |
| 3 <sup>rd</sup> | 0.384                          | 0.256              | 0.192                           | 17819           | 35141              |
| 4 <sup>th</sup> | 0.3072                         | 0.2048             | 0.1536                          | 24523           | 48500              |
| 5 <sup>th</sup> | 0.24576                        | 0.16384            | 0.12288                         | 27831           | 55056              |

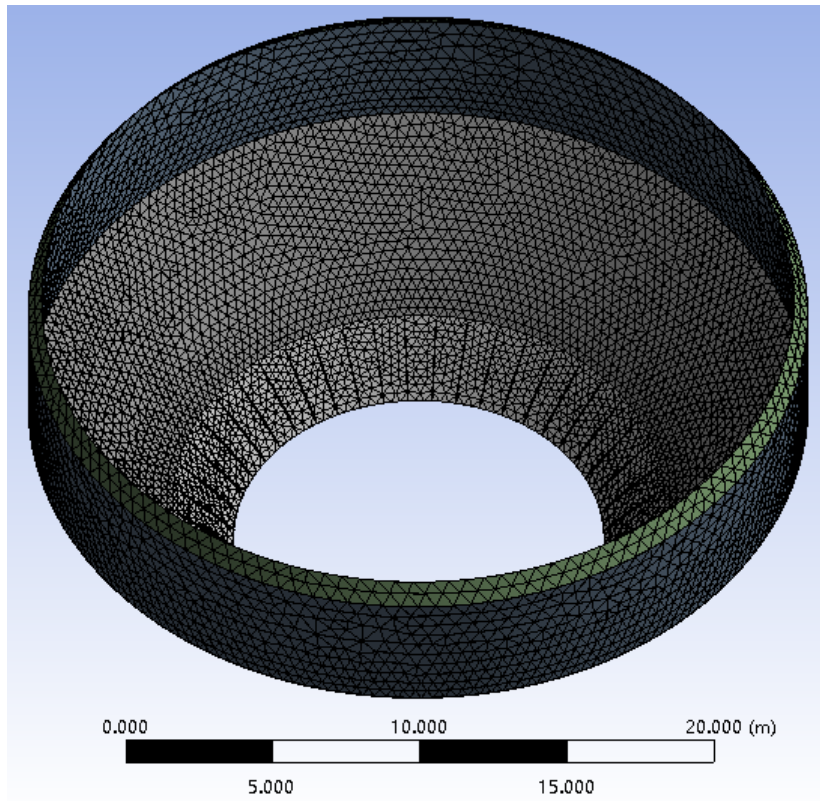


**Figure 0.33 Generated mesh for the 1<sup>st</sup> step**

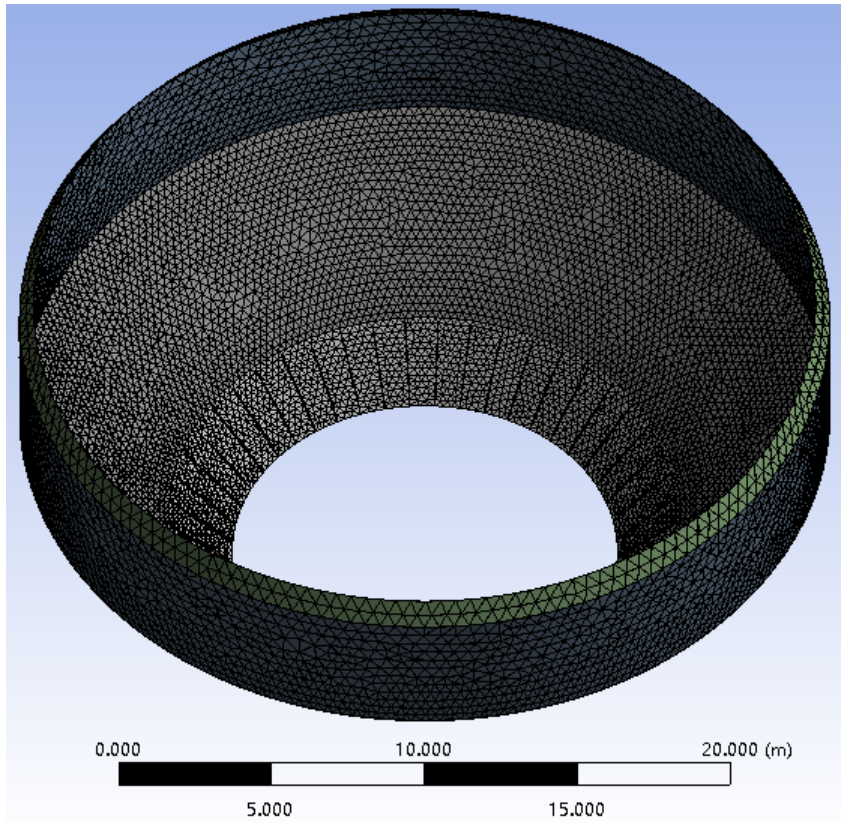


**Figure 0.34** Generated mesh for the 2<sup>nd</sup> step

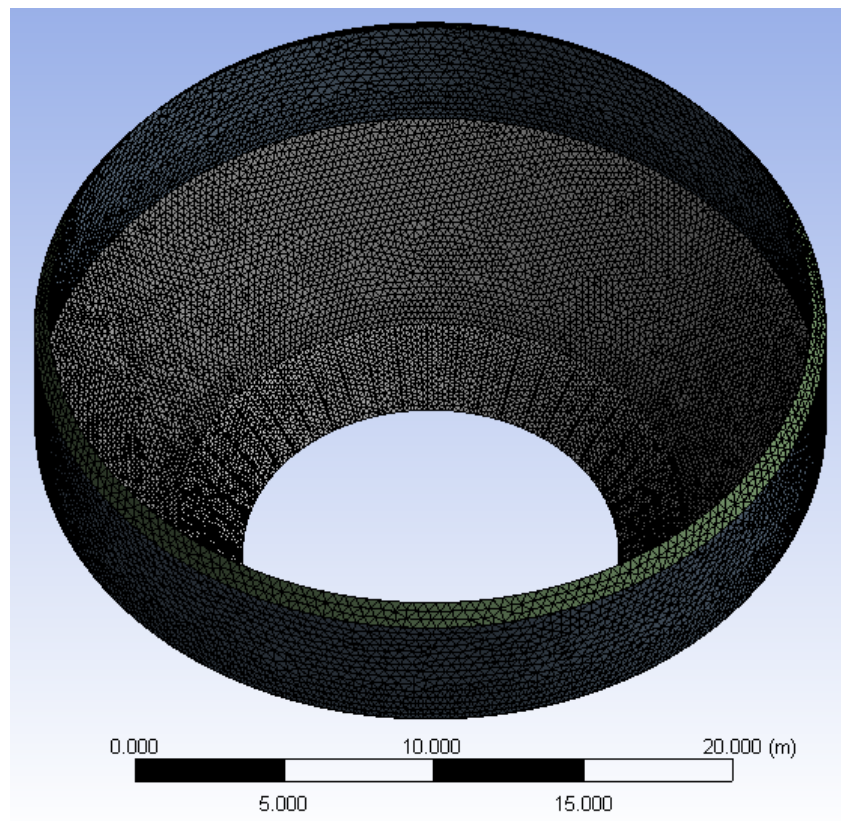


**Figure 0.35** Generated mesh for the 3<sup>rd</sup> step



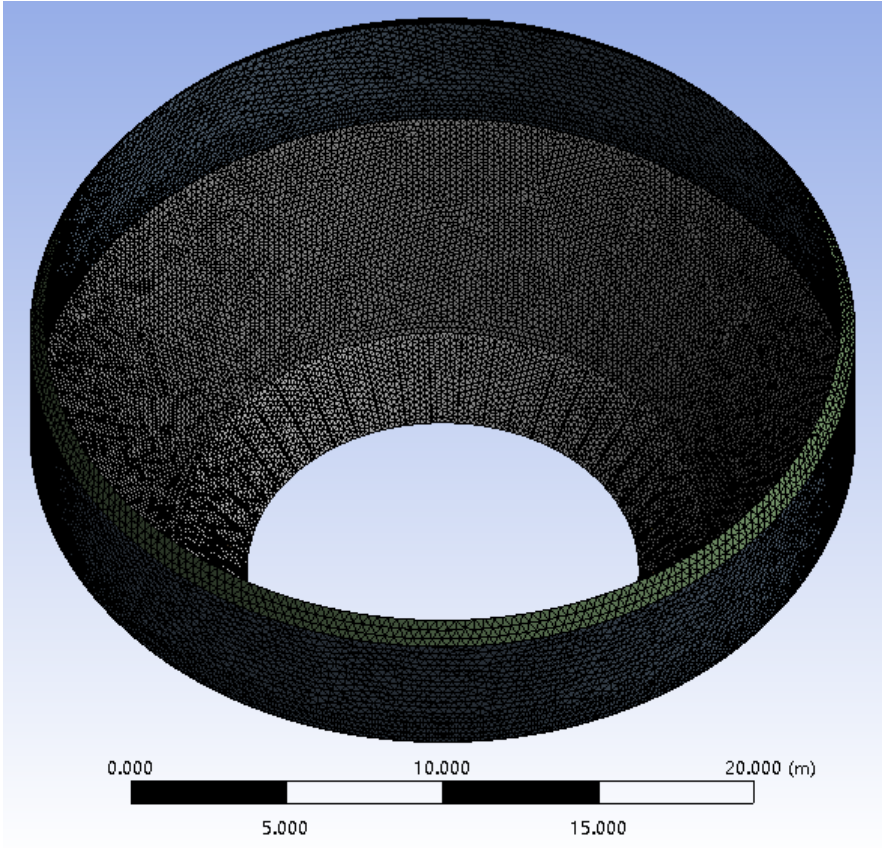


**Figure 0.36** Generated mesh for the 4<sup>th</sup> step

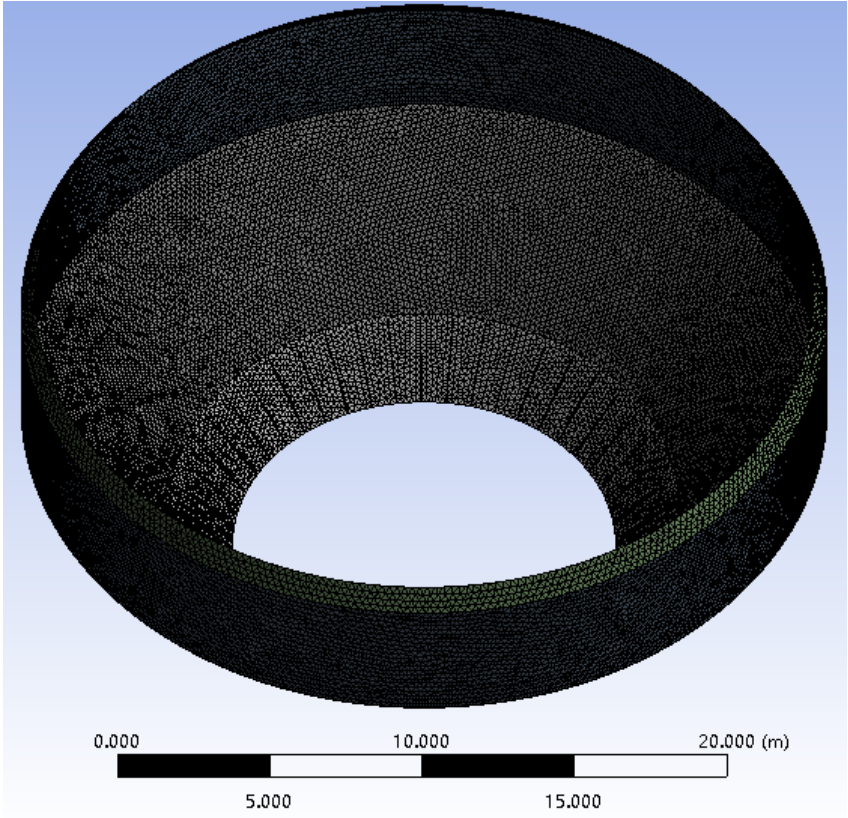


**Figure 0.37** Generated mesh for the 5<sup>th</sup> step

Since the plastic deformation is formed on an imperfect tank, the effect of initial geometric imperfections shall be included. This is done by generating a distorted mesh to simulate imperfection shape. The introduced imperfection pattern is specified by El Damatty et al. (2001) and is described in section 3.2.2. The amplitude is set to  $0.01L_b$ , corresponding to tank quality classified as a ‘poor cone’ (Vandepitte et al. 1982).

The critical load factor  $P_{cr}$  and maximum von Mises equivalent stress ( $\sigma_{v,max}$ ) at buckling are obtained to evaluate the convergence. ( $P_{cr} = n$  means the tank can exactly withstand  $n$  times the design load level.)

Results of analysis and convergence situation are shown in Table 3.13, Figures 3.38 and 3.39.

**Table 0.13 Sensitivity analysis results**

| Step Number     | $P_{cr}$ | Difference from last step | $\sigma_{v,max}$ (MPa) | Difference from last step |
|-----------------|----------|---------------------------|------------------------|---------------------------|
| 1 <sup>st</sup> | 1.876    | -                         | 332.92                 | -                         |
| 2 <sup>nd</sup> | 1.770    | 5.668%                    | 342.60                 | 2.908%                    |
| 3 <sup>rd</sup> | 1.688    | 4.643%                    | 359.22                 | 4.851%                    |
| 4 <sup>th</sup> | 1.674    | 0.840%                    | 356.61                 | 0.727%                    |
| 5 <sup>th</sup> | 1.667    | 0.401%                    | 357.91                 | 0.365%                    |

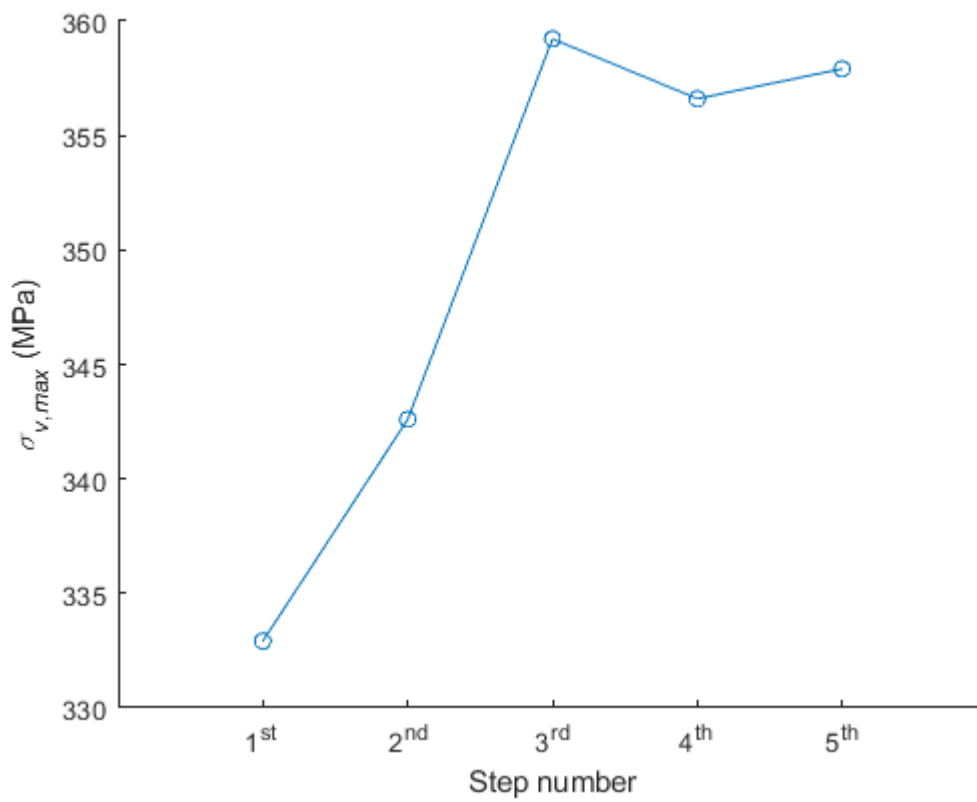
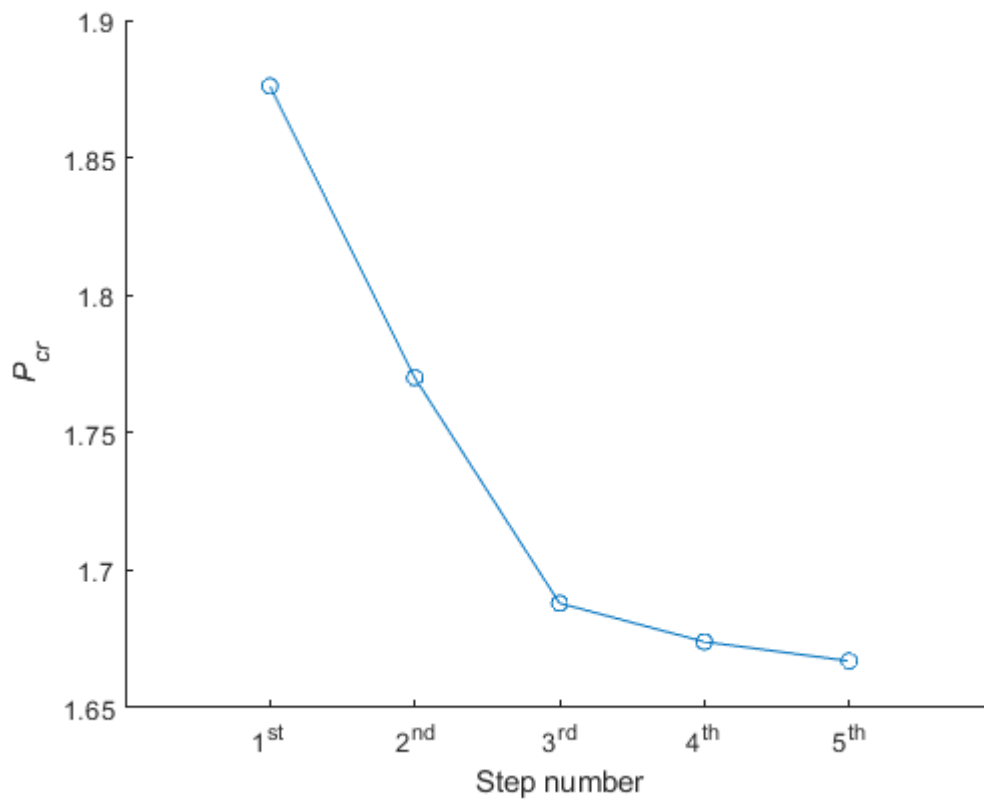


**Figure 0.38 Sensitivity analysis results**



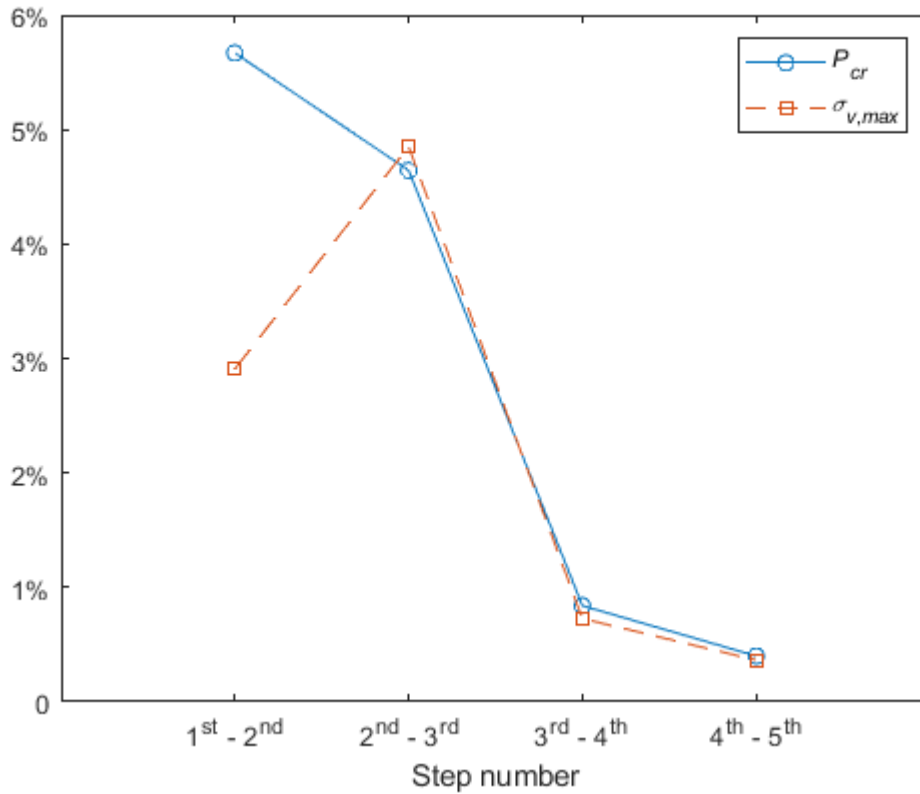


**Figure 0.39 Differences between steps**

It is clearly shown that both  $P_{cr}$  and  $\sigma_{v,max}$  reaches convergence at the 4<sup>th</sup> step since the difference between the results of the 4<sup>th</sup> and 5<sup>th</sup> steps is extremely small (less than 0.5%). Hence, the mesh quality generated in the 4<sup>th</sup> step is employed for the following analysis.

### 3.6.3 Multiple simulation & comparison

In this section, the impact of various geometric imperfections is simulated with the FEM model determined from convergence analysis. All types of geometric imperfections are applied on the model before fully loaded. The critical load factor  $P_{cr}$  is collected for the result of each simulation and compared with each other.

The simplified imperfection patterns for stiffened LFCT are suggested by El Damatty et al. (2001) with the amplitude tolerances of ‘good cone’ and ‘poor cone’ from the work by Vandepitte et al. (1982) (described in section 3.2.2). As a comparison, real imperfections are generated from the cloud data (described in section 3.3). Global imperfections, local imperfections and total geometric imperfections (global & local imperfections) are applied in

the FEM model. Analysis results are shown in Table 3.14.

**Table 0.14  $P_{cr}$  results of FEA**

| Imperfections in FEA Case                 |           | $P_{cr}$ | $\sigma_{v,max}$ (MPa) |
|---|-----------|----------|------------------------|
| Perfect Tank                              |           | 1.936    | 337.57                 |
| Assumption by El<br>Damatty et. al (2001) | Good cone | 1.705    | 345.08                 |
|   | Poor cone | 1.406    | 345.58                 |
| Global Imperfections from Measurements    |           | 1.516    | 326.58                 |
| Local Imperfections from Measurements     |           | 1.488    | 360.79                 |
| Total Imperfections from Measurements     |           | 1.653    | 335.36                 |

For the simplified imperfection pattern suggested by El Damatty et. al (1997, 2001),  $P_{cr}$  value obtained from FEA results is 88.07% (good cone) and 72.62% (poor cone) of the perfect tank. The capacities of the tank with real case imperfections are between those classified as ‘good cone’ (0.004 $L_b$  imperfection amplitude) and ‘poor cone’ (0.01 $L_b$  imperfection amplitude). The tank assigned with total measured imperfections has 85.38% capacity of the perfect tank. It drops to 78.31% when assigned with global imperfections only and 76.86% with local imperfections. The maximum von Mises stress in these results shows that critical load factor obtained from all cases are due to inelastic buckling.

The fact that higher capacity with total imperfections may be explained by several reasons:

1) Counteractions between global & local imperfections is a main effect in the coupling of individual components. Figures 3.6 and 3.7 show that directions of global & local imperfections are sometimes opposite, which makes the amplitude of total imperfection smaller than a component. In rest parts, locations where the imperfection concentrates are different

between global & local imperfections, which makes the total imperfection amplitude fails to exceed the component a lot in most positions.

2) Imperfection shape has a large effect on the buckling capacity. From meridional imperfections shown in Figure 3.7, compared to the smooth shape of total imperfections, sinusoidal waves with small wavelength are more obvious at the lower part of meridians ( $z = 2 \text{ m}$ ) with global or local imperfections only. Such locations are critical where buckling failure is easily to happen.

### 3.7 Conclusion

In this section, geometric imperfections extracted from laser scan cloud data are put into analysis with a verified FEA technique. The impact on LFCT buckling capacity is compared with specifications in literature. The following conclusions can be drawn from the results:

1) Imperfection shape suggested by El Damatty et. al (2001) leads to the most critical case with imperfection amplitude of  $0.01L_b$  ('poor cone' by Vandepitte 1982), The capacity decrease to 72.62% of the perfect case. Measured local imperfections have a smaller impact on the capacity (76.86%) even with the amplitude reaches 200% of the tolerance specified the 'poor cone' classification (Vandepitte et al. 1982). Based on the result, it is recommended that local imperfections can be deemed as the critical case. This introduces a conservative consideration in design procedures and help reducing complexity by ignoring global imperfections.

2) Coupling effects between global & local imperfections are complicated and cannot be simply estimated from amplitudes. In this case, the capacity of imperfect tank with global or local imperfections decreases by 21.69% and 23.14% respectively. However, the tank with total imperfection has a capacity only 14.62% less than the perfect tank.

The imperfection shape has a large influence on the impact of LFCT capacity. Several experiments has been reported in literatures (El Damatty et al. 1998). However, quantitative results are still lacking about complicated shapes measured from real tanks. It is recommended that more researches on the imperfection shapes to be carried out in the future.

### 3.8 References

*Ansys® Academic Research Mechanical, Release 16.1, ANSYS, Inc.*

Árbocz J., Babcock C.D. Jr. (1964). “The Effect of General Imperfections on the Buckling of Cylindrical shells.” *Journal of Structural Engineering*, Volume 36, Issue 1, 879-890.

AWWA D100-11 Welded Carbon Steel Tanks for Water Storage. (2011). American Water Works Association, Denver, Colorado.

El Damatty A. A., Korol R. M., Mirza F. A. (1997a). “Stability of Imperfect Steel Conical Tanks under Hydrostatic Loading.” *Journal of Structural Engineering*, Volume 123, Issue 6, 703–712.

El Damatty A. A., Marroquin E. G., El Attar M. (2001). “Behavior of Stiffened Liquid-Filled Conical Tanks.” *Thin-Walled Structures*, Volume 39, 353–373.

Hafeez G., El Ansary A. M., El Damatty A. A. (2010). “Stability of Combined Imperfect Conical Tanks under Hydrostatic Loading.” *Journal of Construction Steel Research*, Volume 66, Issue 11, 1387 – 1397.

Hornung U., Saal H. (2002). “Buckling Loads of Tank Shells with Imperfections.” *International Journal of Nonlinear Mechanics*, Volume 37, 605–621.

National Building Code of Canada. (2015). Ottawa: Associate Committee on the National Building Code, National Research Council.

Riks E. (1979). “An Incremental Approach to the Solution of Snapping and Buckling Problems.” *International Journal of Solids and Structures*, Volume 15, Issue 7, 529-551.

Vandepitte D., Rathe J., Verhegghe B., Paridaens R., Verschaeve C. (1982). "Experimental investigation of hydrostatically loaded conical shells and practical evaluation of the buckling load." In: Ramm E. (ed.) *Buckling of shells*, Springer-Verlag KG, Berlin, Germany, 375-399.

Vandepitte D. (1992). "Report about the failure of a water tower, Fredericton, New Brunswick." *Technical Report*, Ghent University, Ghent, Belgium.

# Chapter 4 Conclusions

## 4.1 Summaries and conclusions

### 4.1.1 General

This thesis presents a series of analyses on the imperfection shape measured from real liquid-filled conical tank to evaluate the quality of imperfect tank with current design codes and compare the impact between the real case and conservative assumptions reported in literatures. Conclusions and summaries drawn from this thesis are presented as follows:

### 4.1.2 The evaluation of extracted circumferential & meridional geometric imperfection shapes from cloud data in amplitude and wavelength.

In chapter 2, a cloud data was introduced with 3,250,386 points distributed on the external surface of the conical tank. A sampling-homogenization procedure was introduced to obtain the measurement data evenly distributed along the height and circumference of the tank. Sampling resolution was checked from 0.02 m to 0.08 m in the height range and from  $0.36^\circ$  to  $1.44^\circ$  in angular range. The difference in sampling results is found as up to 30% in bottom circumferences and few meridians. Imperfection shapes on 10 circumferences and 12 meridians were collected from sampling results and were smoothed using the Savitzky-Golay filter. Based on a fitting process with the least-squares method, the global & local imperfection profiles are extracted on these circumferences and meridians.

Next, the wavelength and amplitude of global, local, and total imperfections were compared with tolerances and specifications in design standards, which are AWWA D100-11, EN 1993-1-6: 2007 and EN 1998-4: 2006. Critical shape assumptions literatures are also put into the comparison, including the assumed patterns by Vandepitte et al. (1982) and El Damatty et al. (2001). Tolerances of global imperfections are satisfied by the measured imperfections in AWWA D100-11 and EN 1993-1-6: 2007. The amplitude of local imperfections and total imperfections exceed the specified largest tolerances, where maximum local imperfection is 100% more than the tolerance of in AWWA D100-11 and maximum total imperfection is 150%

more than the tolerance in EN 1998-4: 2006. The wavelength is compared in the result of a Fourier analysis, where the main components of wavelength is larger than 1/15 of circumferences and 1/4 of meridians.

In Chapter 2, The amplitude of plastic deformation was evaluated based on a finite element analysis of the conical tank using ANSYS 16.1. Several imperfection shapes were assumed on the tank to collect a critical effect, which includes:

- 1) Assumed imperfections with sinewave patterns along meridians and circumferences, following specifications by El Damatty et al. (2001). The amplitudes are set to 0.4% and 1% of buckling wavelength calculated based on assumptions by Vandepitte et al. (1982).
- 2) Measured geometric deviations from a real tank. Considering effects from the imperfection amplitude, 40% and 100% amplitudes of measurements are applied (same proportion with assumptions by Vandepitte et al.)

Two maximum amplitude locations are found on the top edge of the cone (0.0007 m) and in the lower part of the cone (0.0014 m). The maximum amplitude at the top is less than 3% of the maximum total deviation amplitude at the same location. Even in the worst case (100% measured initial imperfection), the maximum plastic deformation only accounts for 2.85% of the imperfection recorded in the cloud data.

#### 4.1.3 Impact of real & simplified geometrical imperfections on the buckling capacity of a LFCT.

In Chapter 3, the finite element model of the considered conical tank is developed. The FEA modelling technique was verified with a benchmark analysis works. Mesh quality was checked and adjusted to yield the converged results. After successive mesh refinement in seven runs, Differences between failure loads and von Mises equivalent stress drops below 1.3%.

Nonlinear elastoplastic finite element analysis (FEA) was utilized to simulate the impact on the buckling capacity of this liquid-filled conical tank by considering multiple scenarios, including:

- 1) Perfect tank without initial imperfections.
- 2) Sinewave-shaped imperfections from El Damatty's assumptions, with the amplitudes of

0.4% and 1% of buckling wavelength calculated by Vandepitte's assumptions.

3) Global, local and total imperfection shapes extracted from measurements on a real tank. Buckling capacity of FEA results with simplified imperfection pattern drops to 88.07% (0.4%) and 72.62% (1%) compared with the perfect tank. The capacities of the tank with real measured imperfections are within the intermediate range. The tank assigned with total measured imperfections has 85.38% capacity of the perfect tank. It drops to 78.31% when assigned with global imperfections only and 76.86% with local imperfections. The conservativeness of the assumed simple geometric imperfection shape, reported in the literature, was confirmed to have the most significant impact on the tank's buckling capacity, compared to real imperfections. Despite the fact that the amplitudes of local components in measured imperfections are higher than tolerances, the overall imperfection considering global components didn't match the critical buckling shape. Especially in lower part of the meridians, similar patterns between global & local imperfections are usually in opposite directions, which resulted smoother overall shapes. When evaluating the effect of different components from the imperfection pattern of a real case, local components showed the largest impact while the total imperfections showed a lower effect even with the largest amplitude.

#### 4.1.4 Research significance and novelty

Geometric imperfection is an essential reason that impacts the buckling capacity of LFCT. Previous investigations on geometric imperfection on tanks usually assume initial imperfections following simplified procedures which only consider local imperfection effects. This thesis provided the first study on a tank with real measured imperfections. Different from the traditional way to deal with the imperfection pattern as an integral body, this study provided an example to decompose the imperfection cloud data into several components following classifications in design standards. With an LSQ fitting approach involving the inclined ellipse function, ovalization effects, central axis deviation as global imperfections and residual local imperfections were extracted and compared with tolerances in design codes. This will help to improve the way of dealing with measured imperfection recorded in scan points. A series of nonlinear FEM analysis were carried out to evaluate the capacity of an LFCT with various



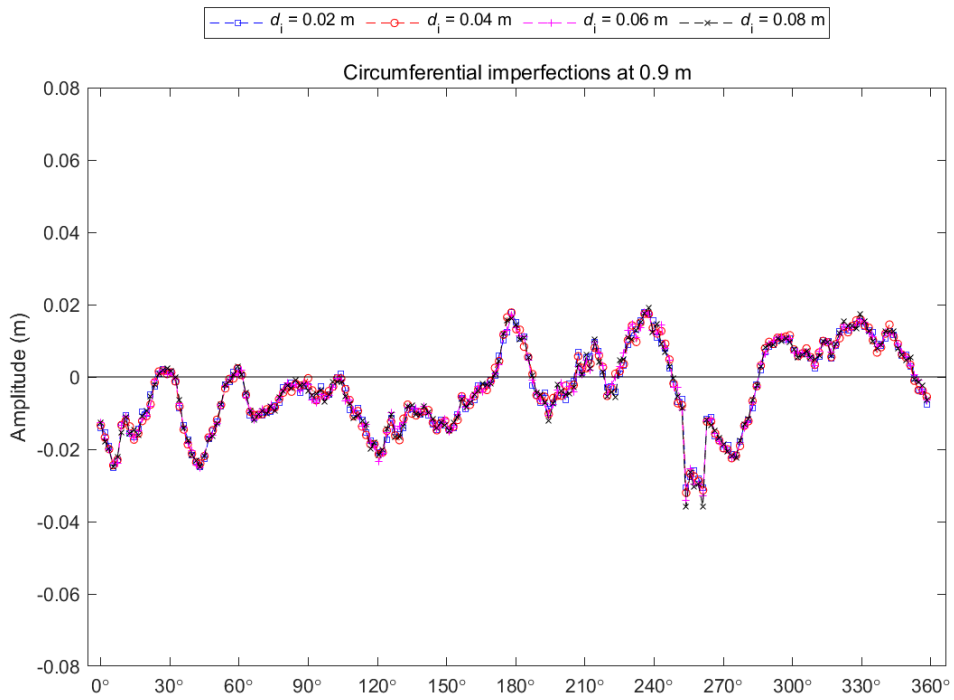
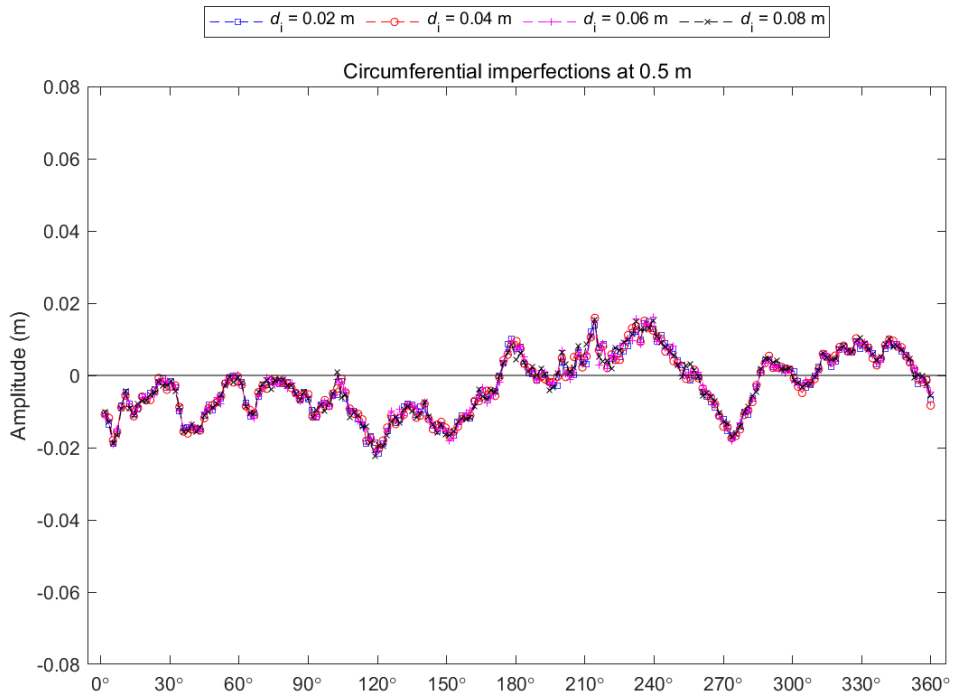
initial imperfections assigned to it. The impact of real imperfections was compared with imperfection from simplified assumptions. This helps the industry to evaluate conservativeness of the critical assumptions. Also, an example is given on evaluating the individual and combined effects of global & local imperfections from real measurements.

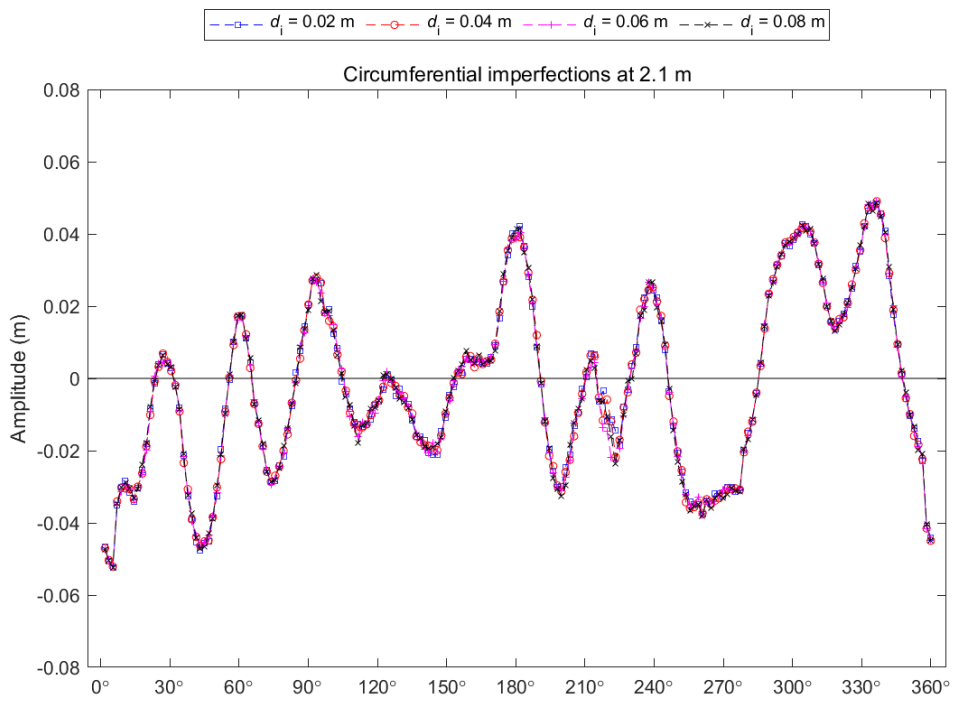
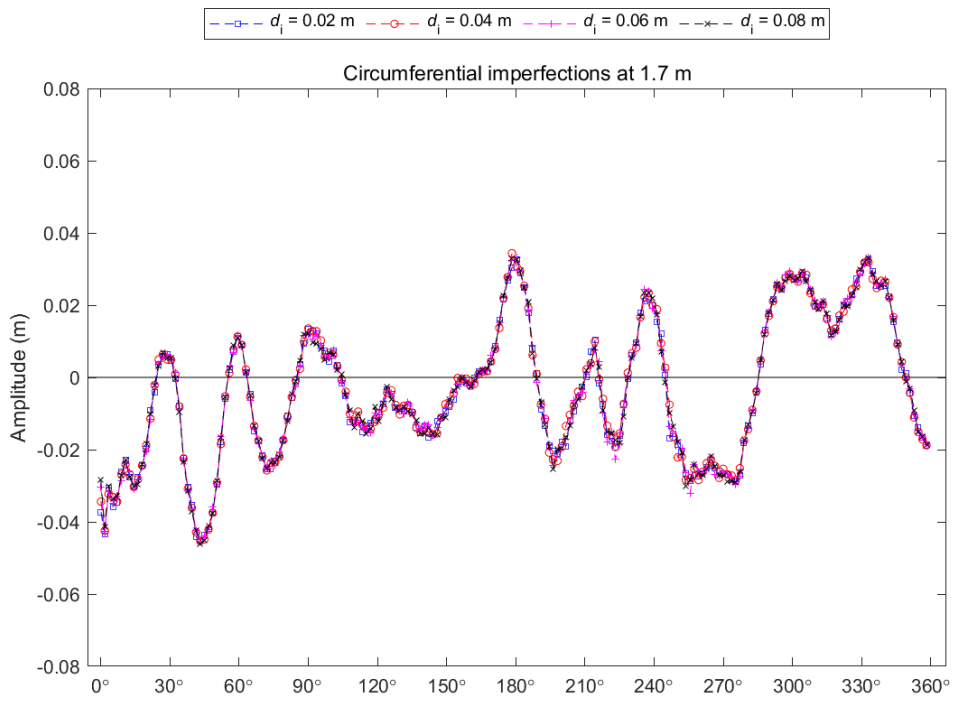
#### **4.2 Recommendations for future work**

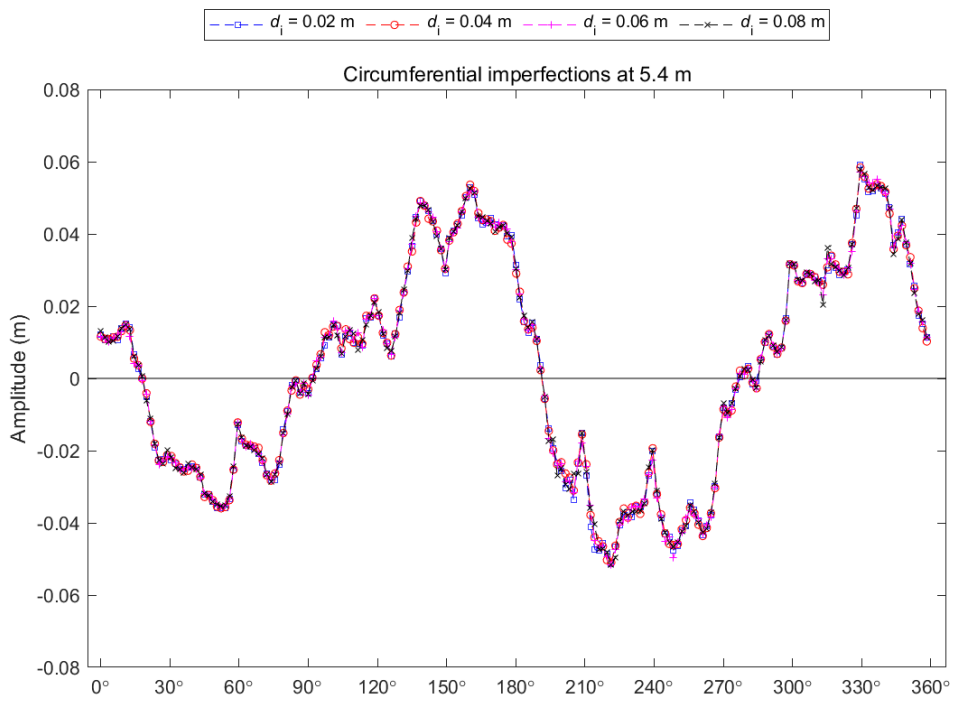
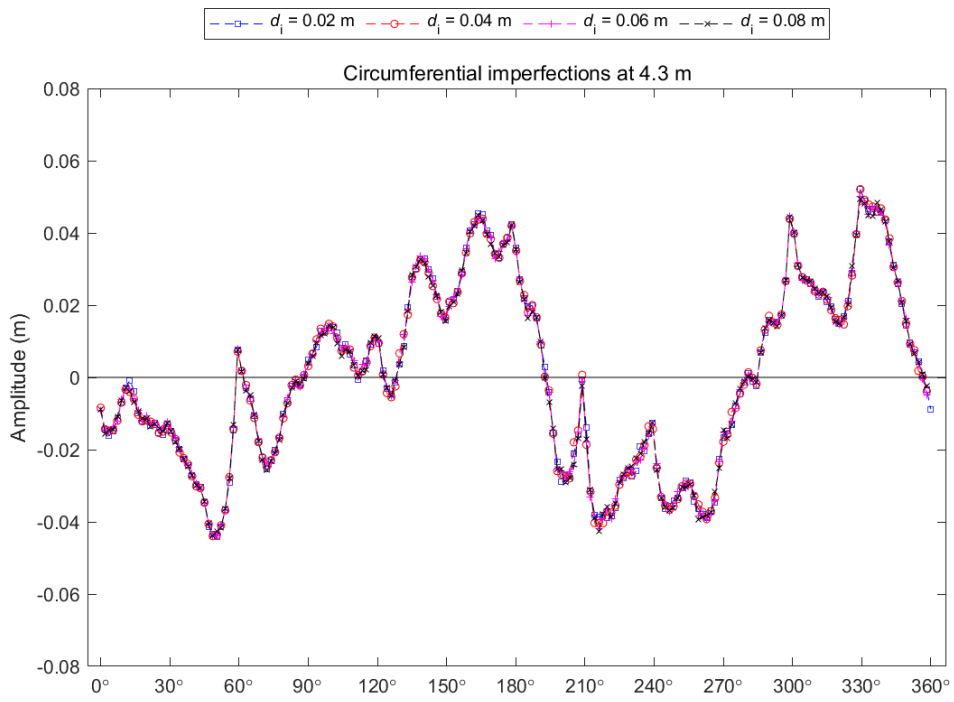
A novel study of geometric imperfections on the LFCT is presented in this thesis, where the need for future works is suggested as follows:

- 1) The complexity of a specific imperfection pattern from real measurements is demonstrated in this study together with its impact which differ a lot from simplified assumptions. A worthy topic in future works is to investigate the effect of shapes of various real measurements on the buckling capacity of LFCT.
- 2) Global & local imperfections are usually collected based on strict measurements from design codes and are evaluated with separate classifications. Conservative assumptions in the literature usually focus on single components of geometric imperfections. It is worthwhile to analyze the coupling effects of various imperfection components and their contributions to the overall impact on the buckling capacity of tanks.
- 3) Deviation of central axis shall be considered as part of global imperfections when decomposing the entire imperfection shape. It contributes to the overall shape of geometric imperfections although it cannot be detected by the measuring approaches from designs standards AWWA D100-11 and EN 1993-1-6: 2007.

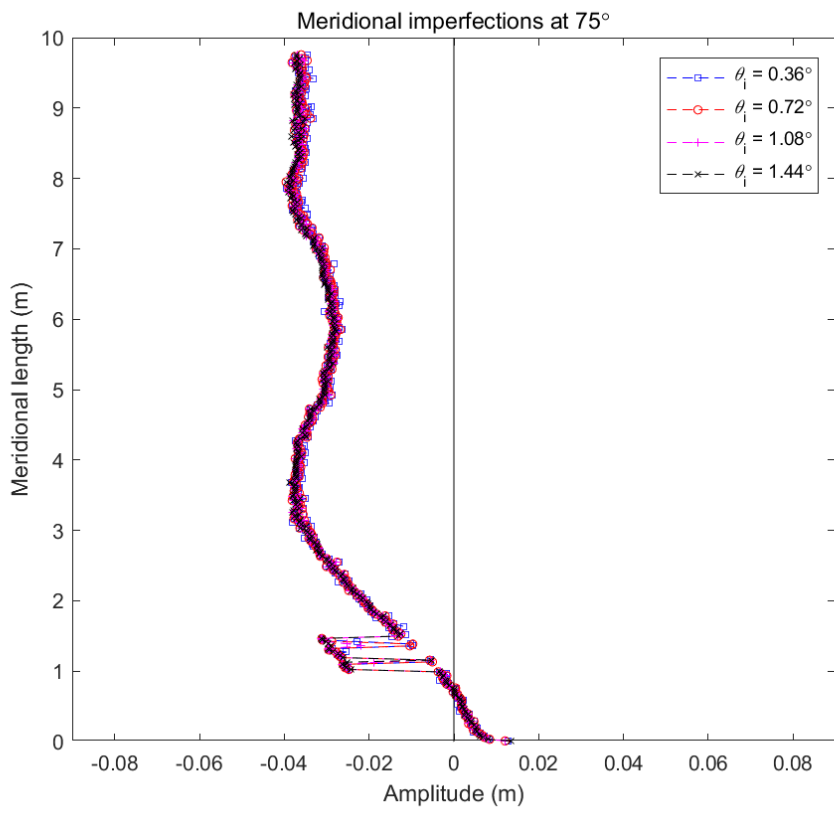
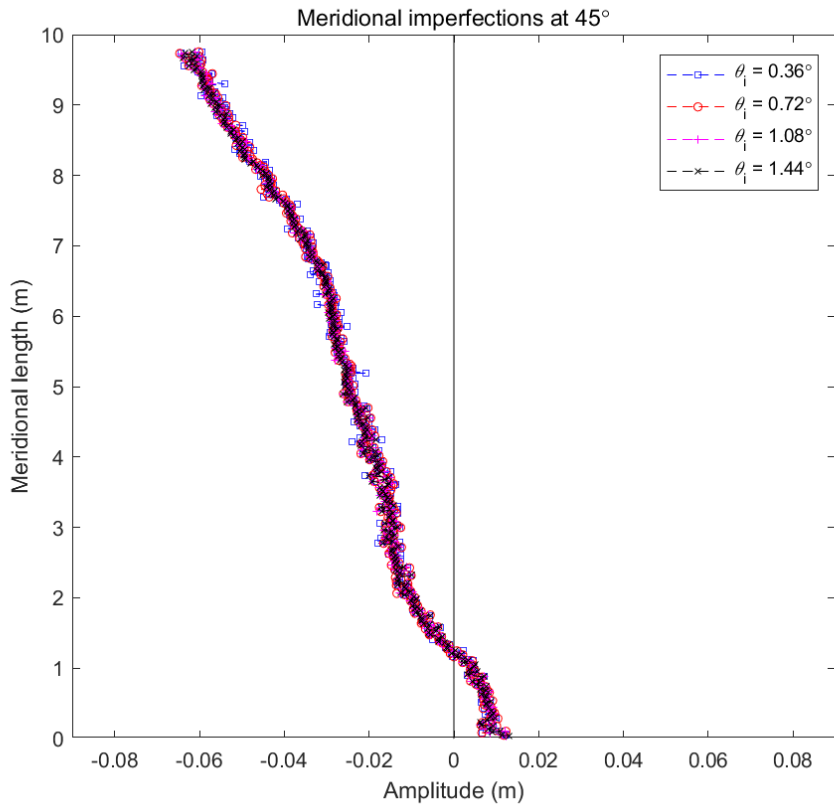
# Appendix

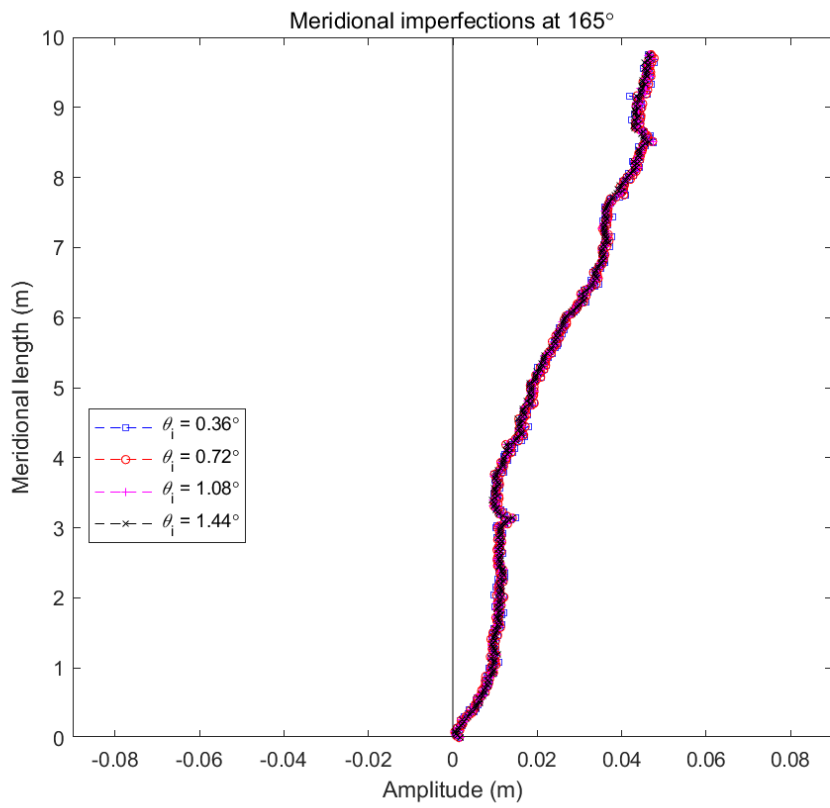
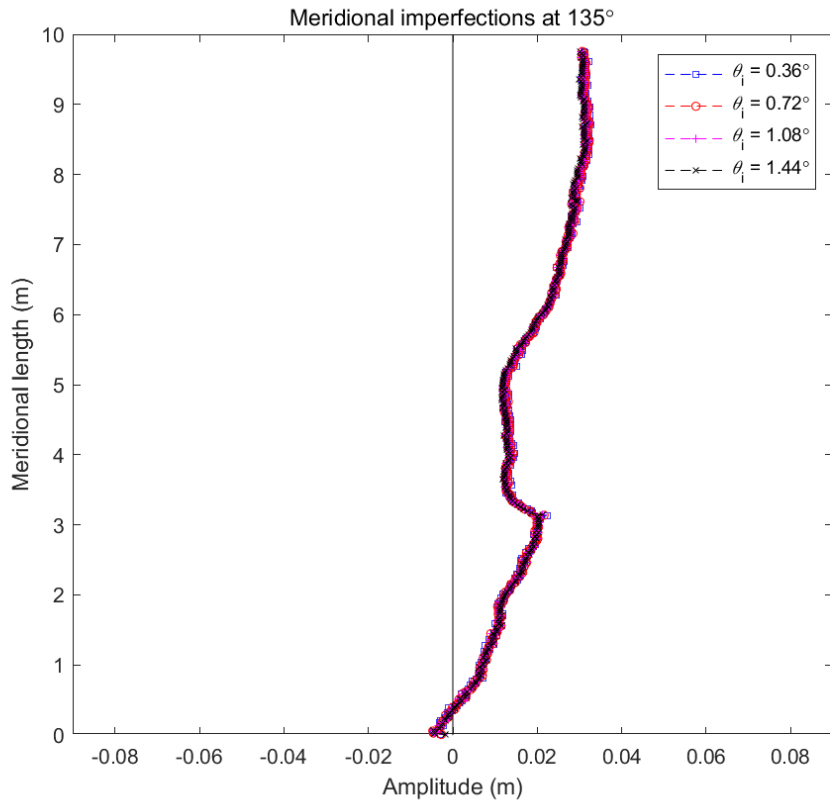


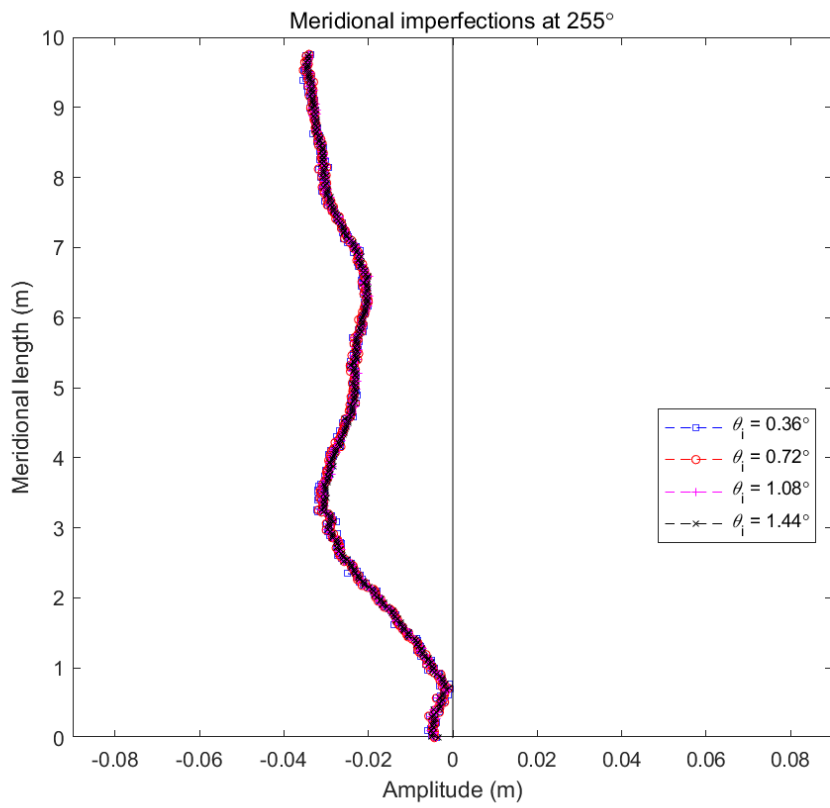
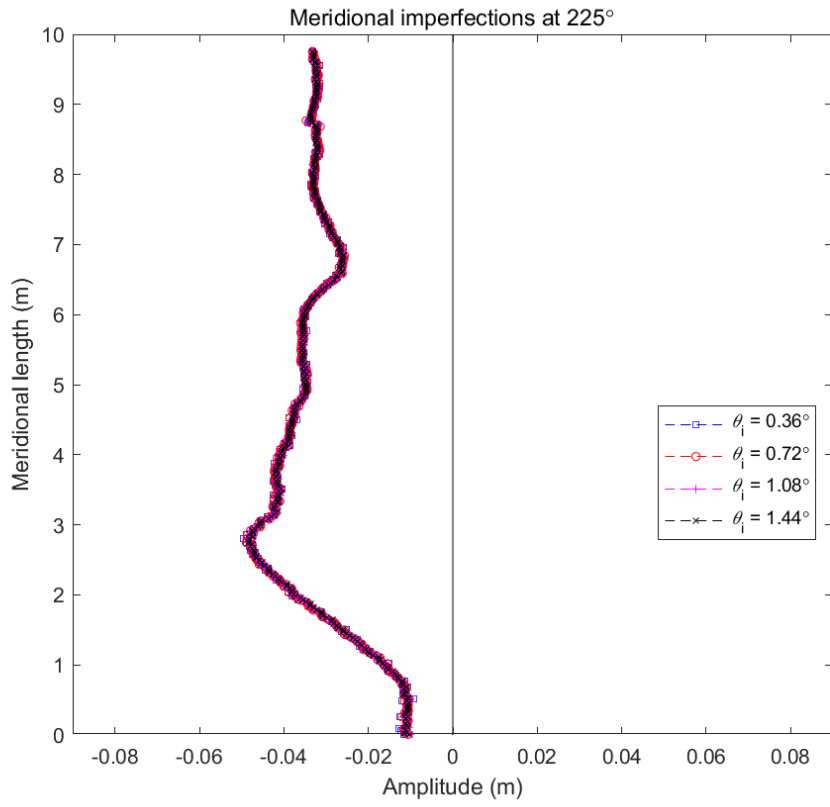


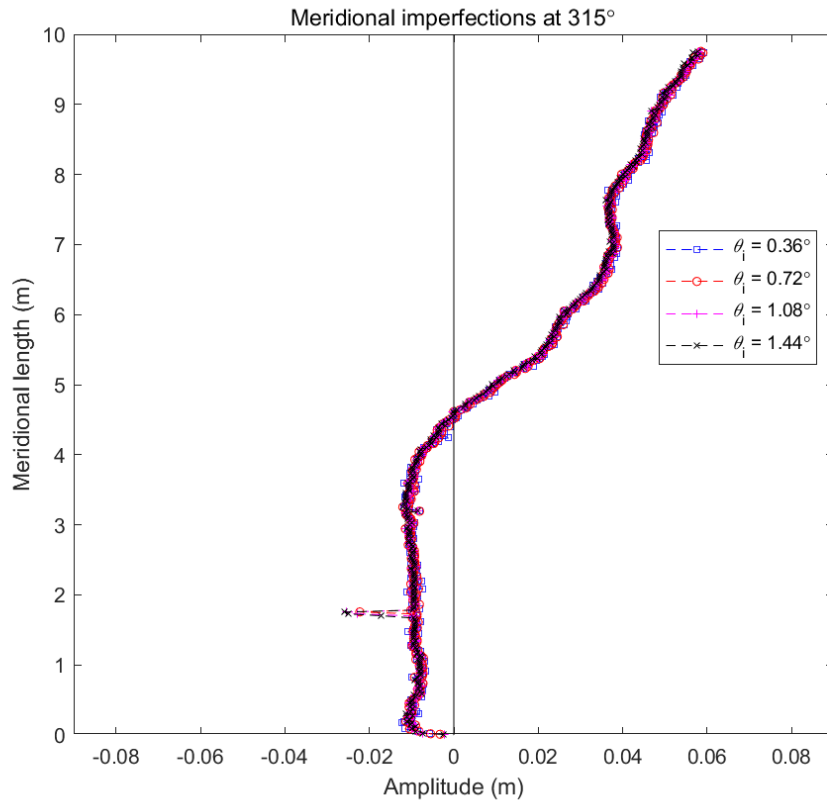


**Figure A.1** Calculated circumferential imperfections with  $d_i$  of 0.02 - 0.05 m



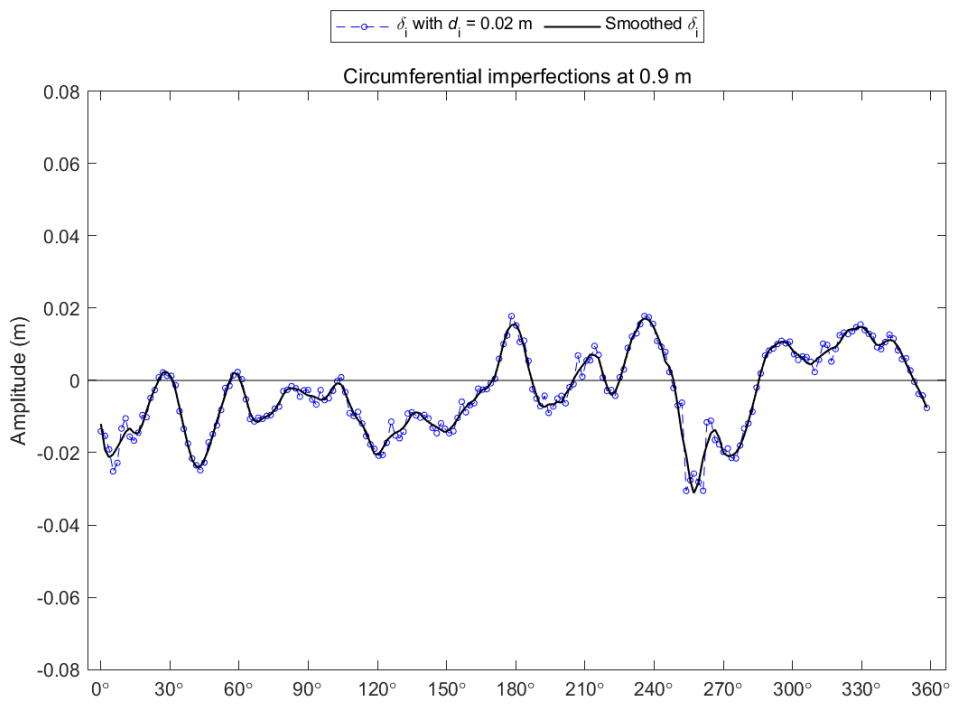
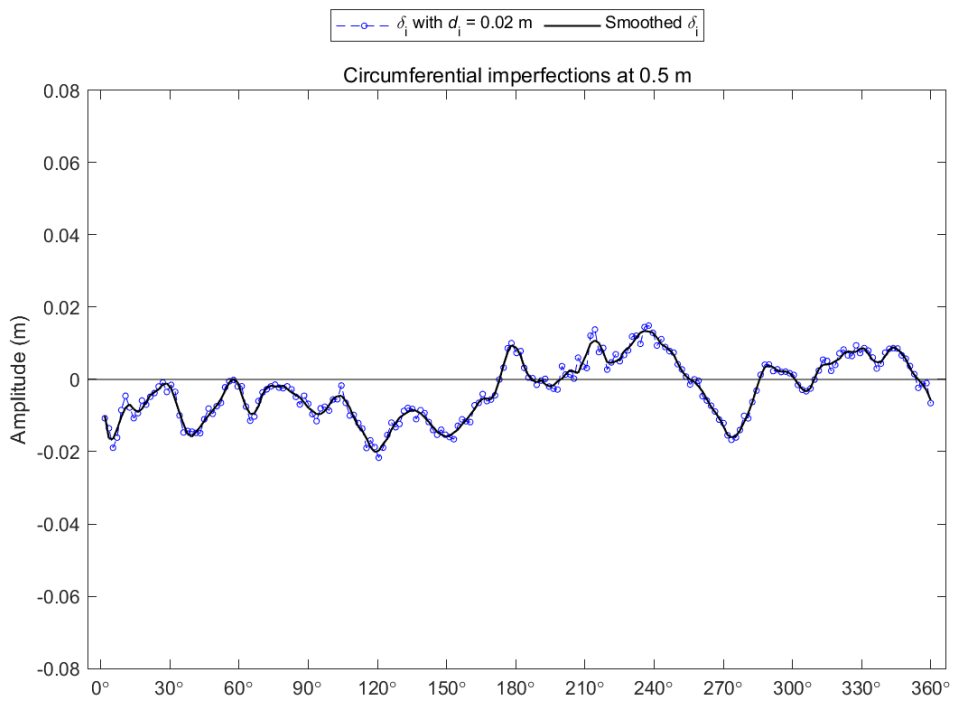


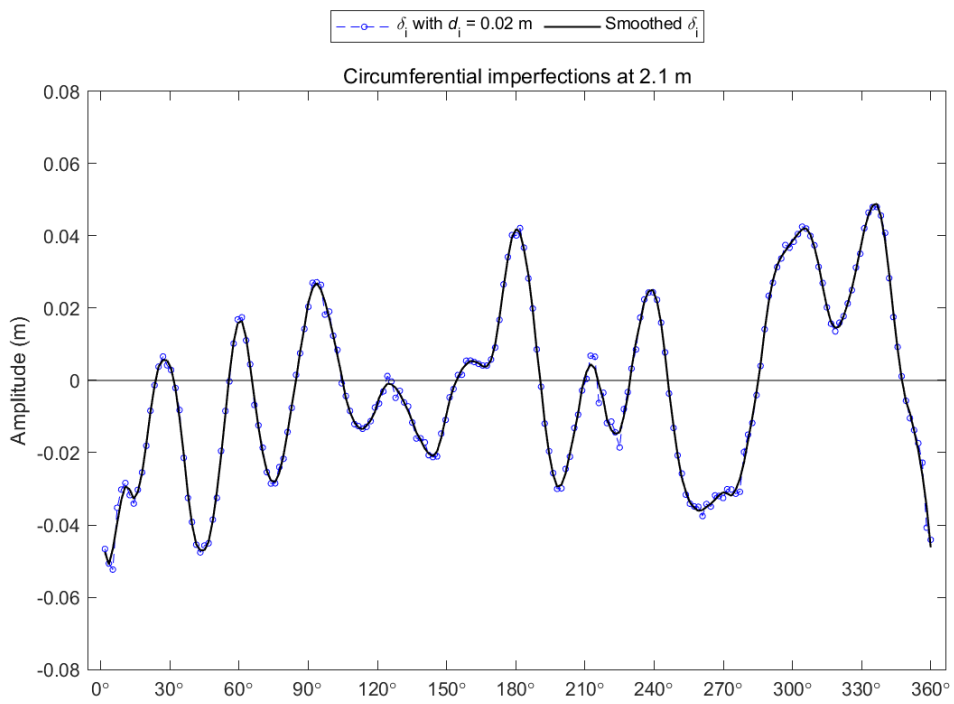
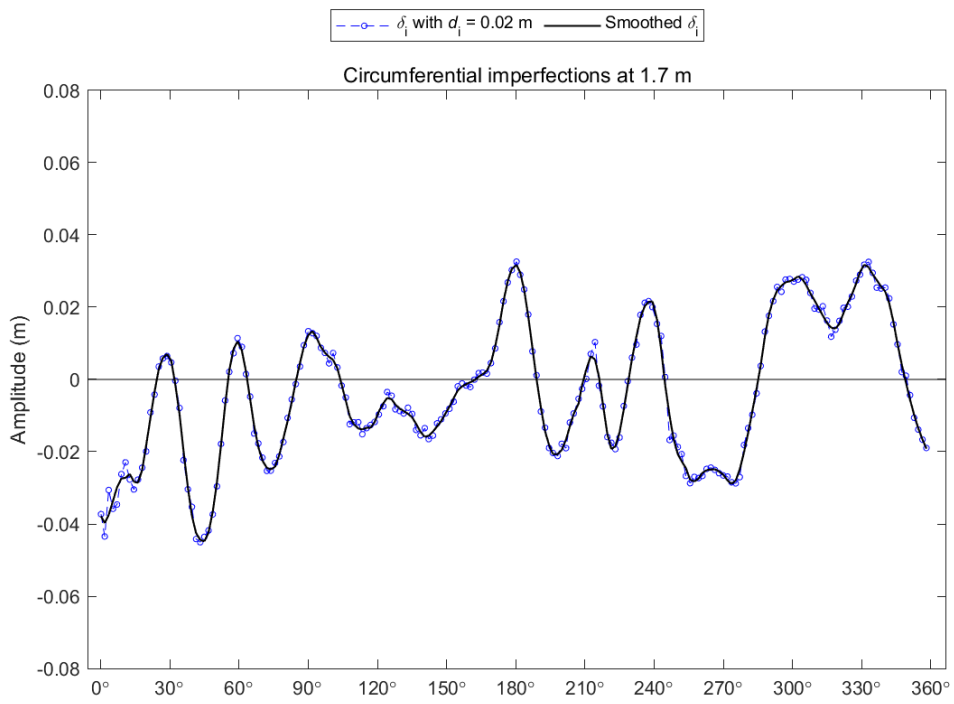


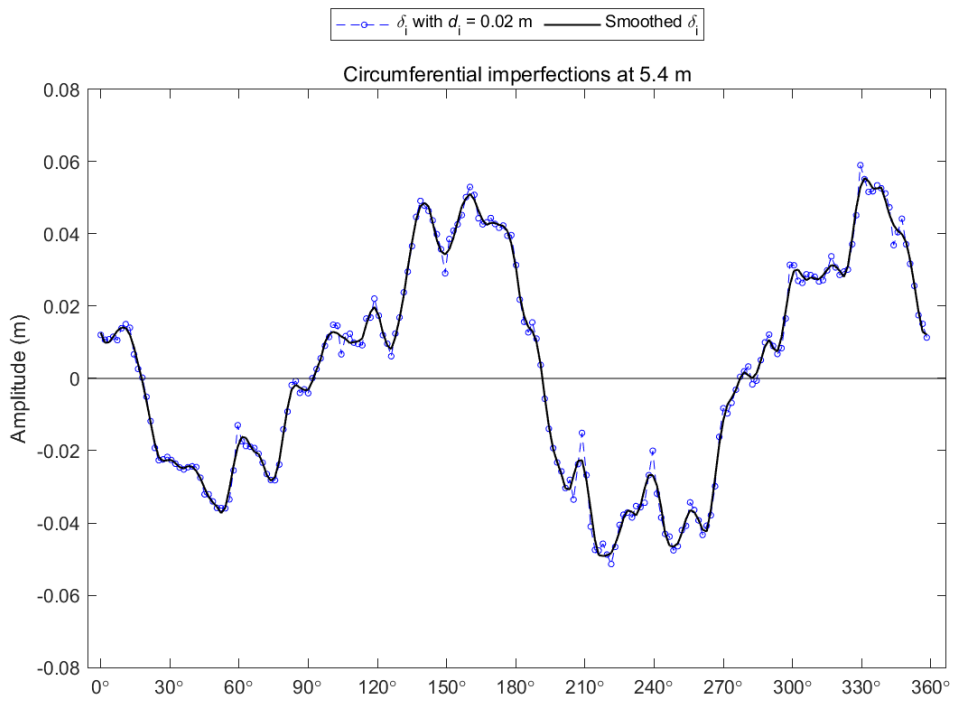
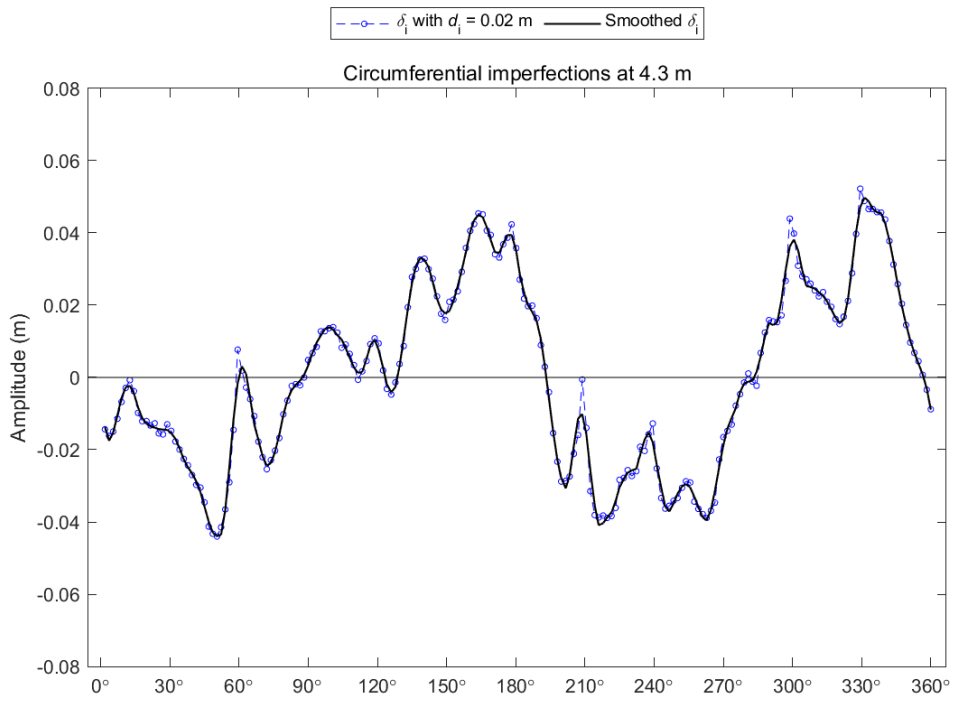


**Figure A.2** Calculated meridional imperfections with  $\theta_i$  of  $0.36^\circ$  -  $1.44^\circ$

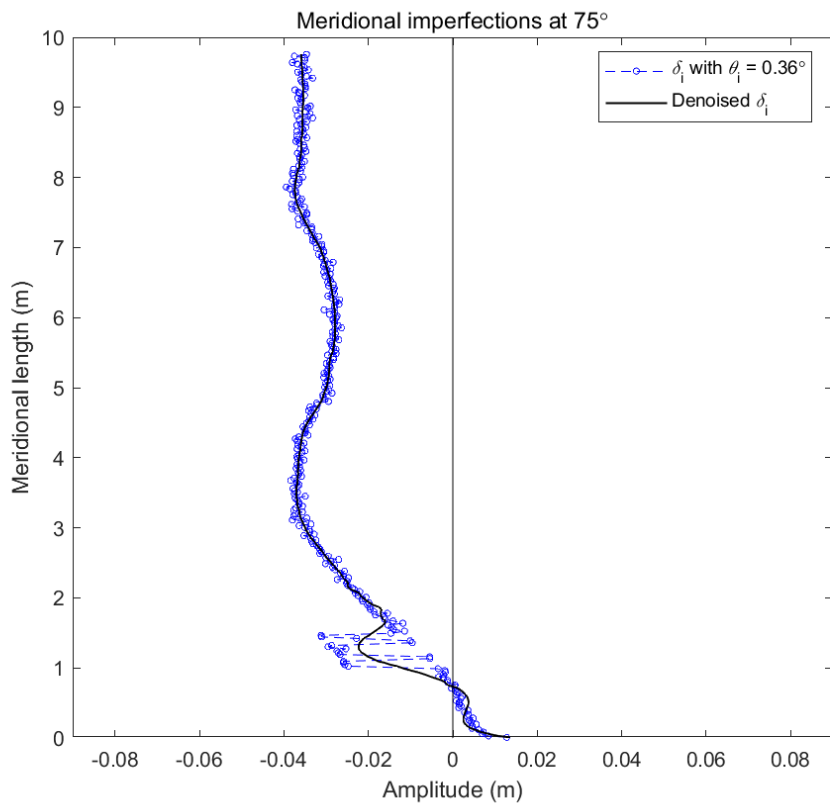
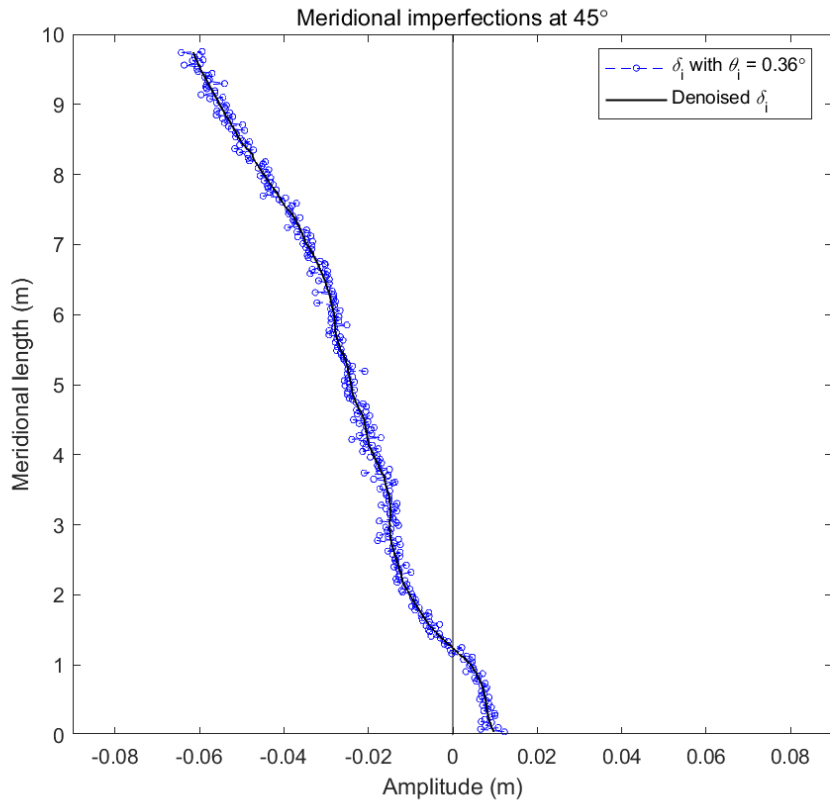


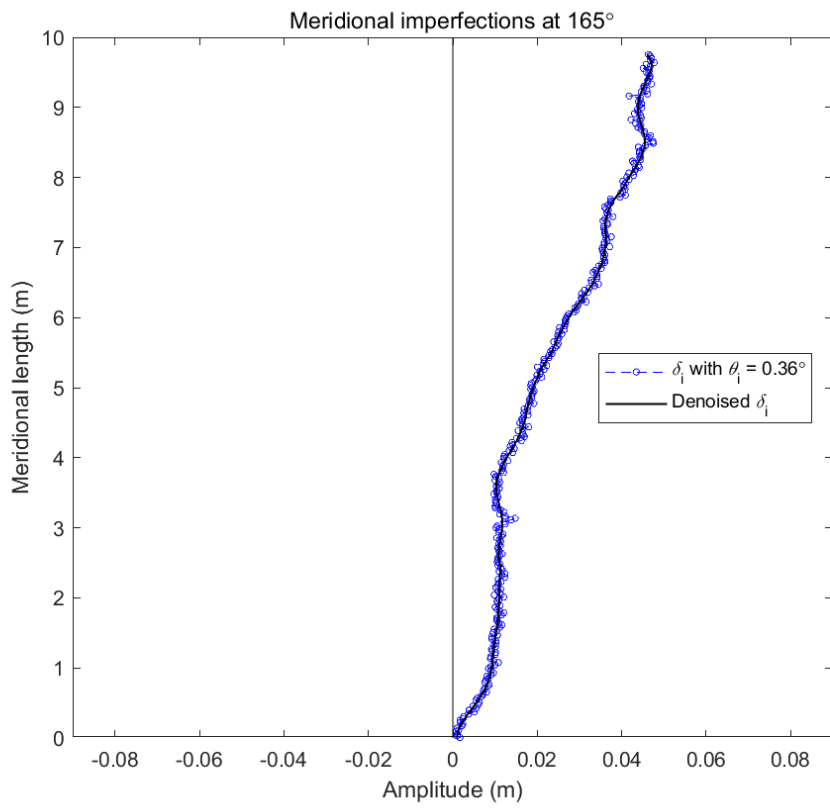
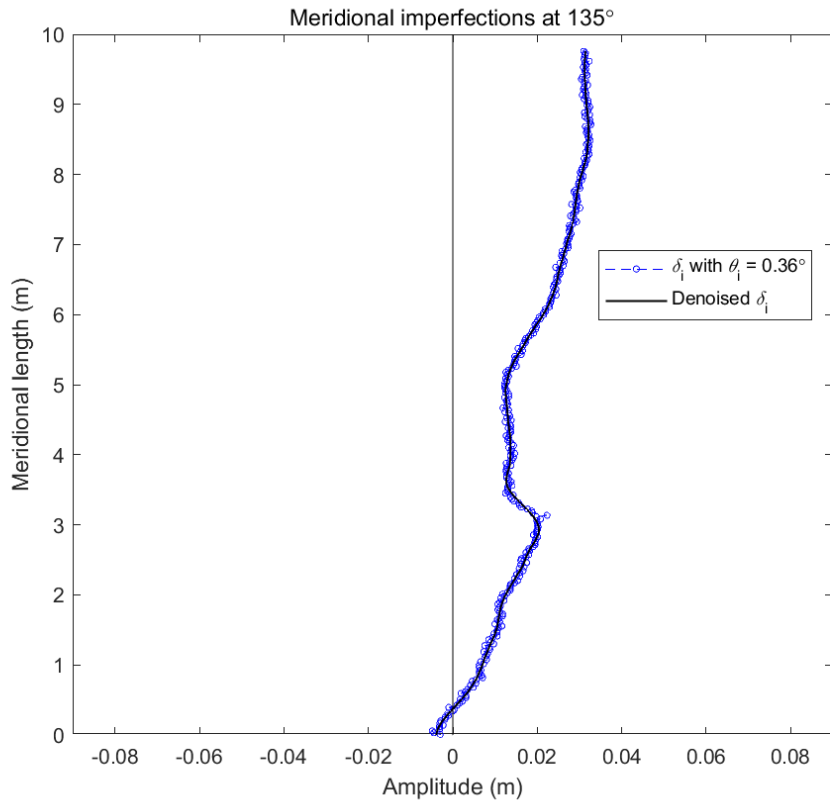


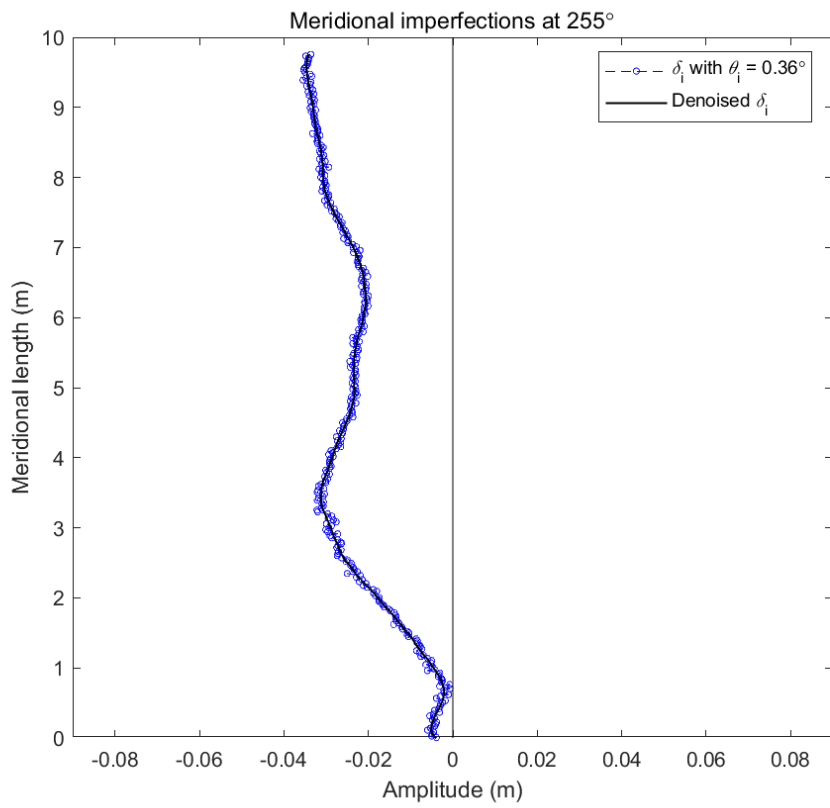
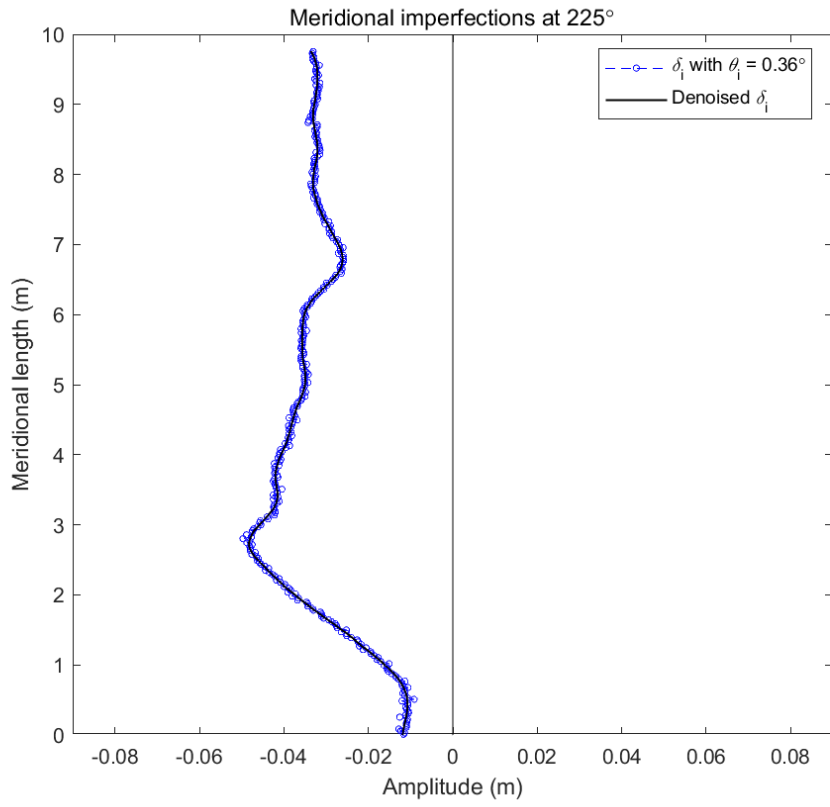


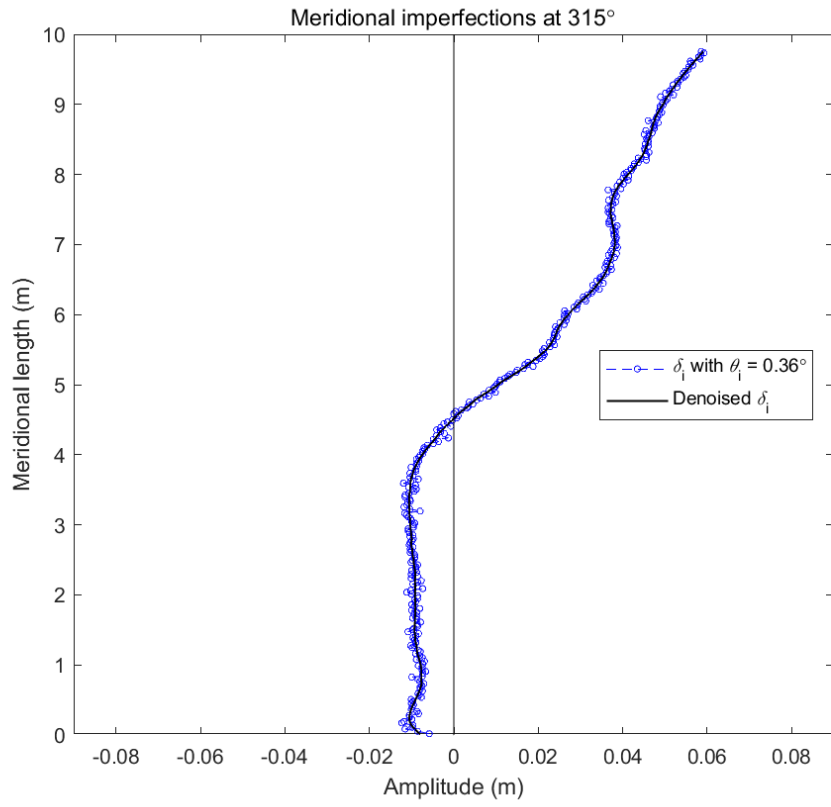


**Figure A.3 Denoised circumferential imperfections**

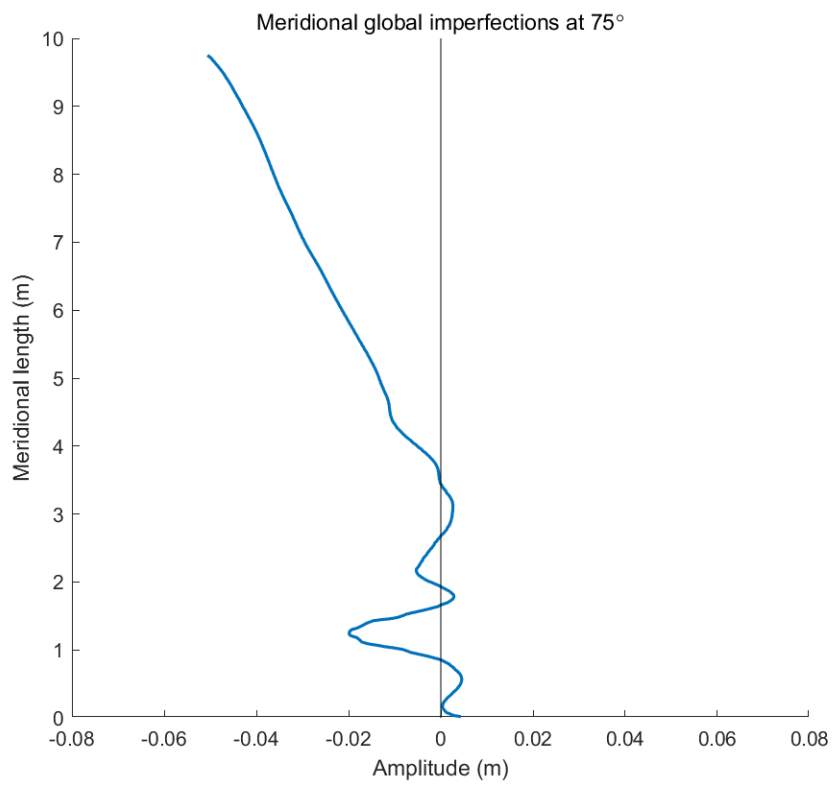
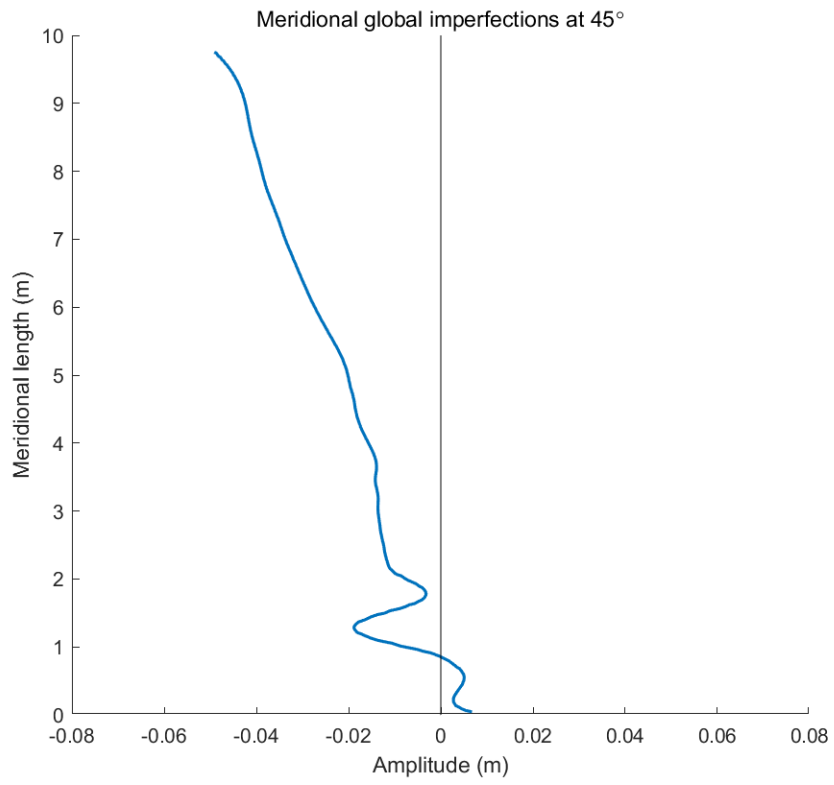




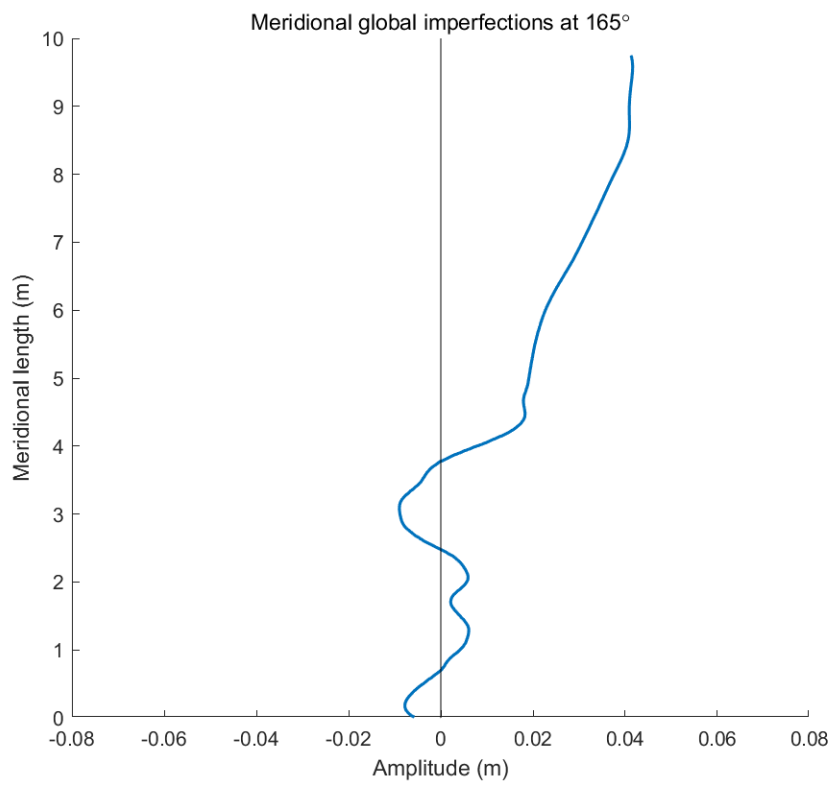
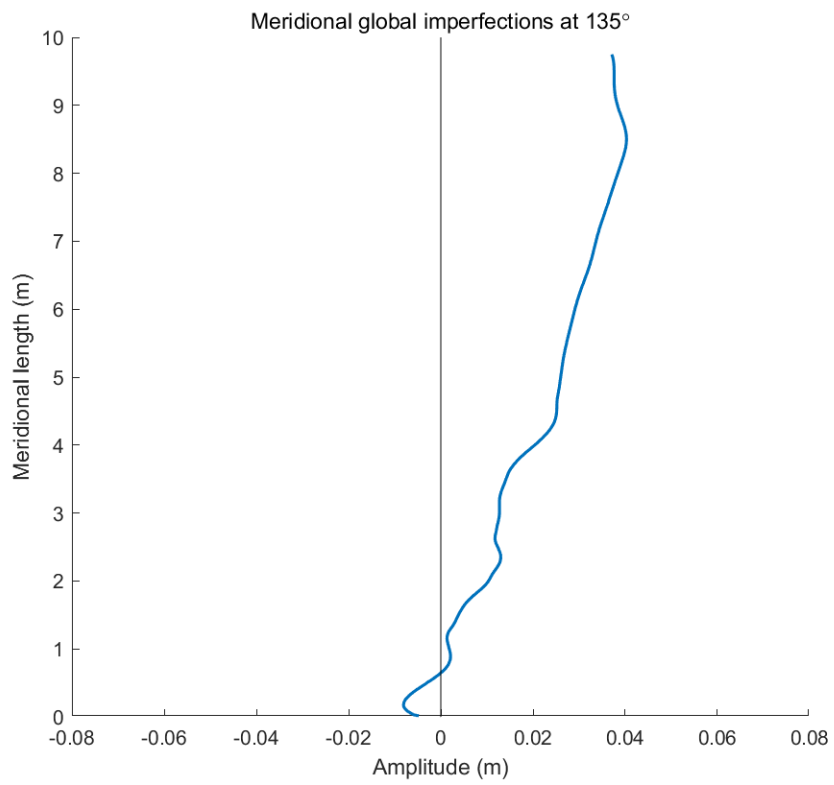


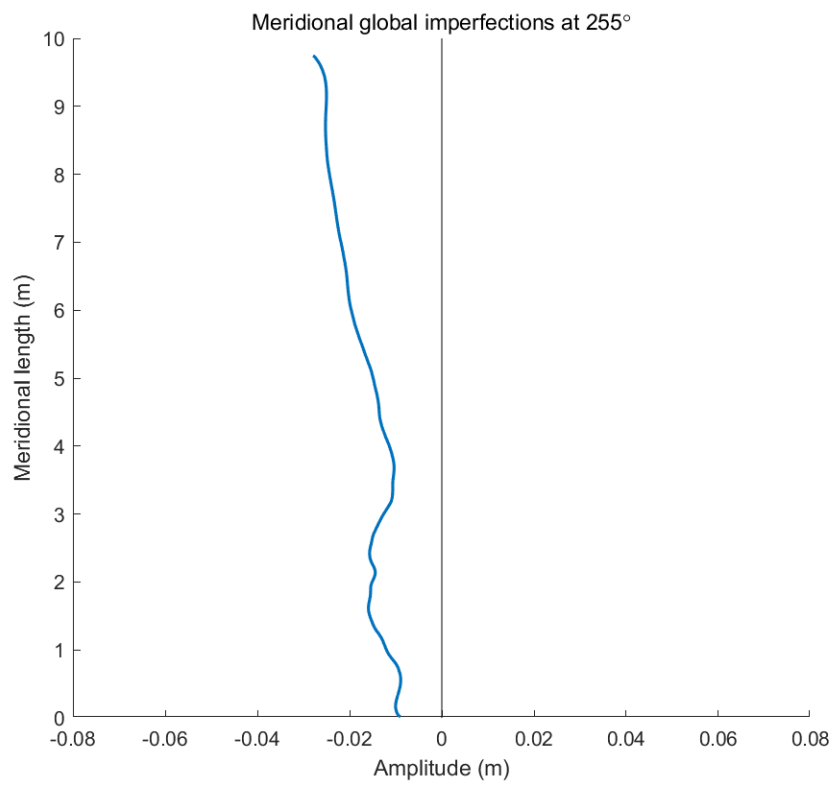
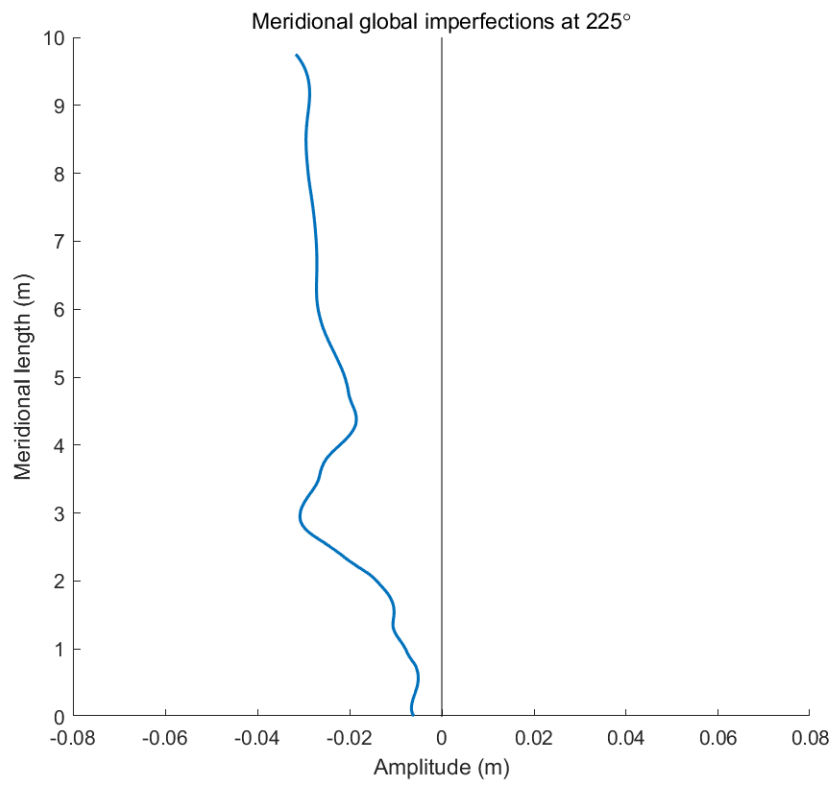


**Figure A.4 Denoised meridional imperfections**









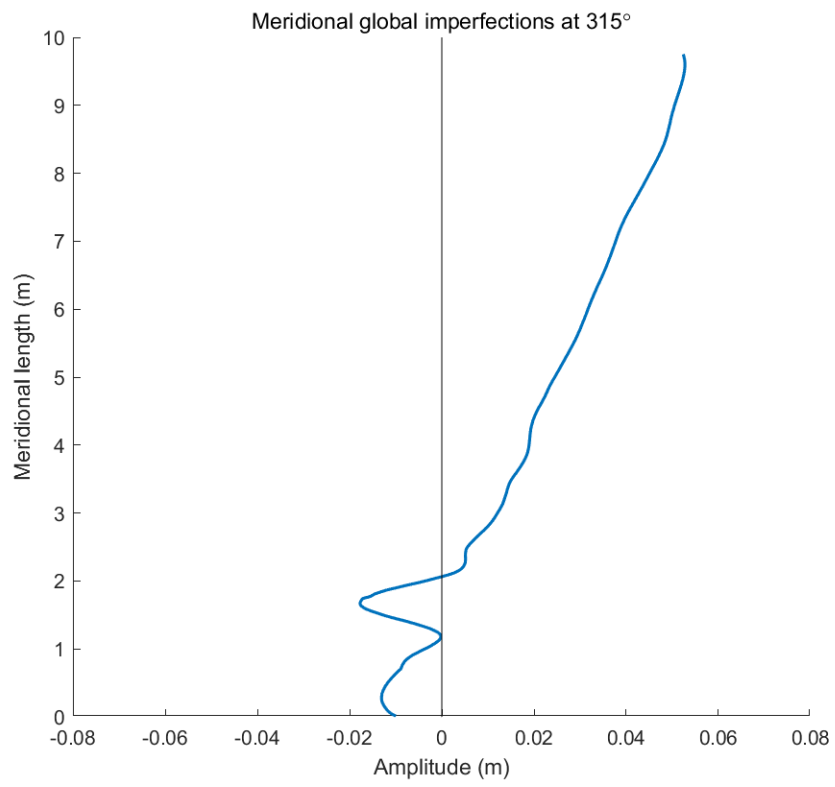
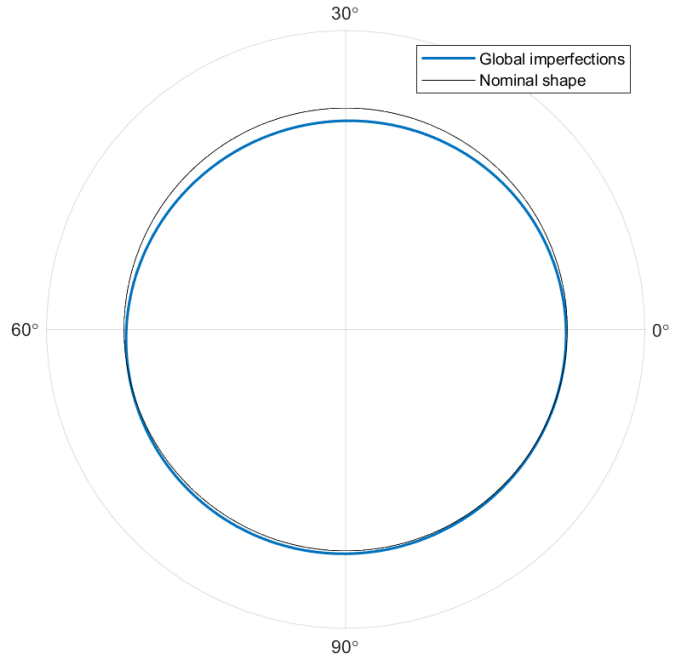
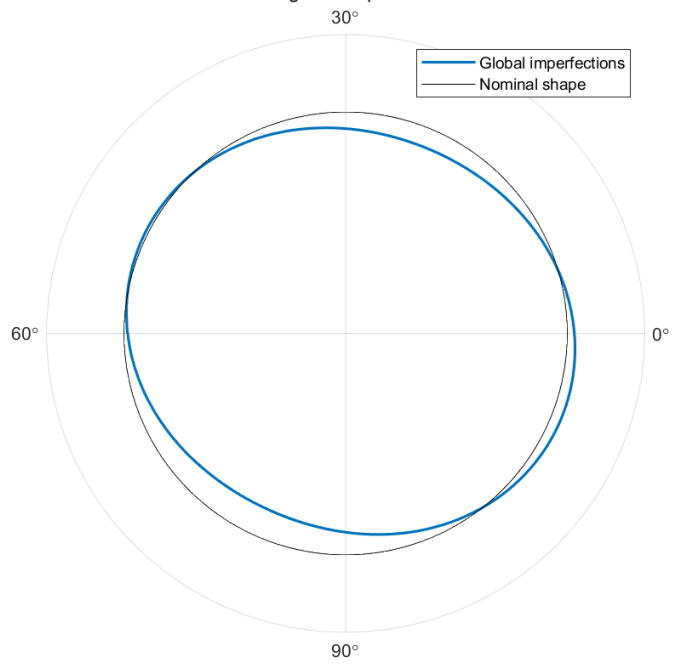


**Figure A.5 Meridional global imperfections**

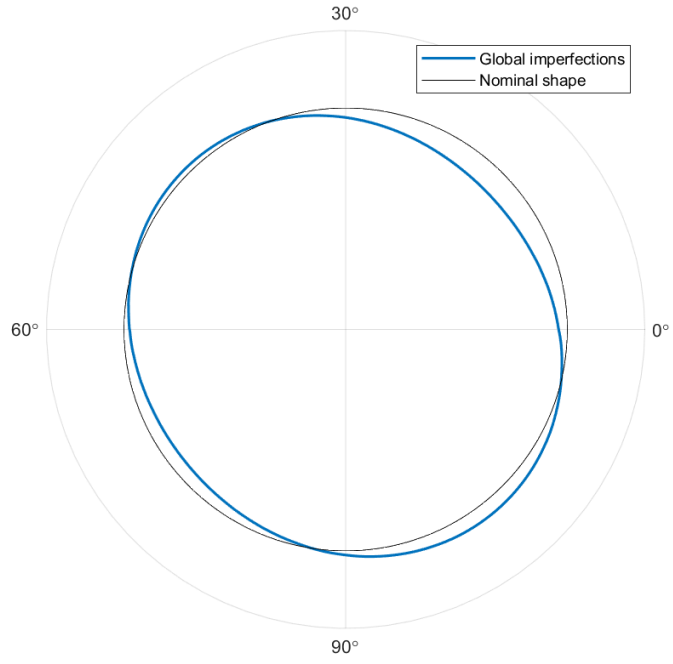
Circumferential global imperfections at 0.5 m



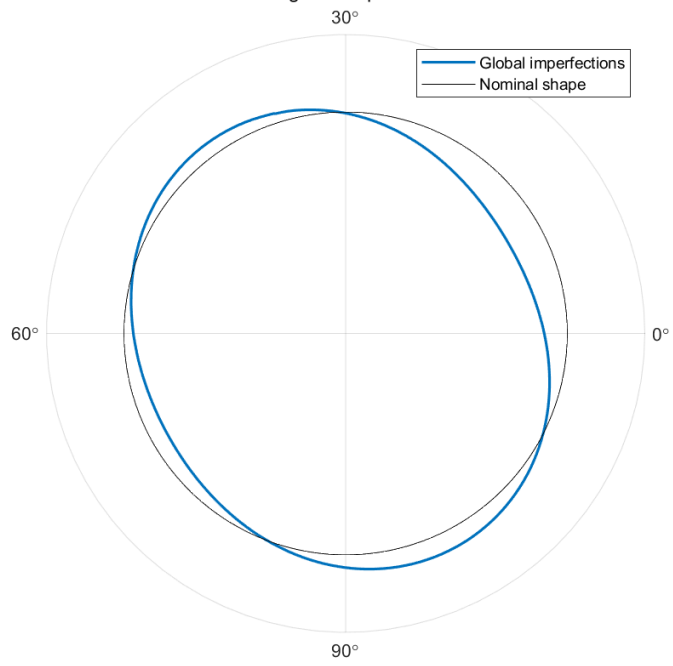
Circumferential global imperfections at 0.9 m

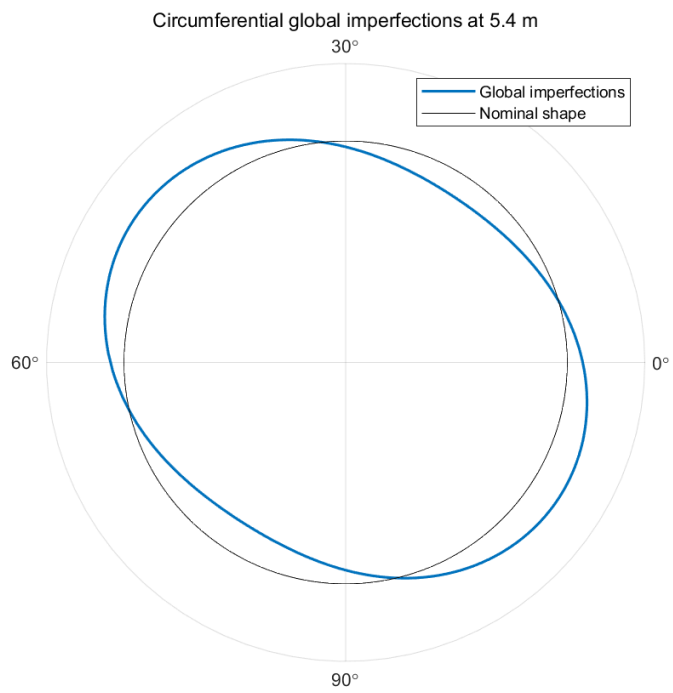
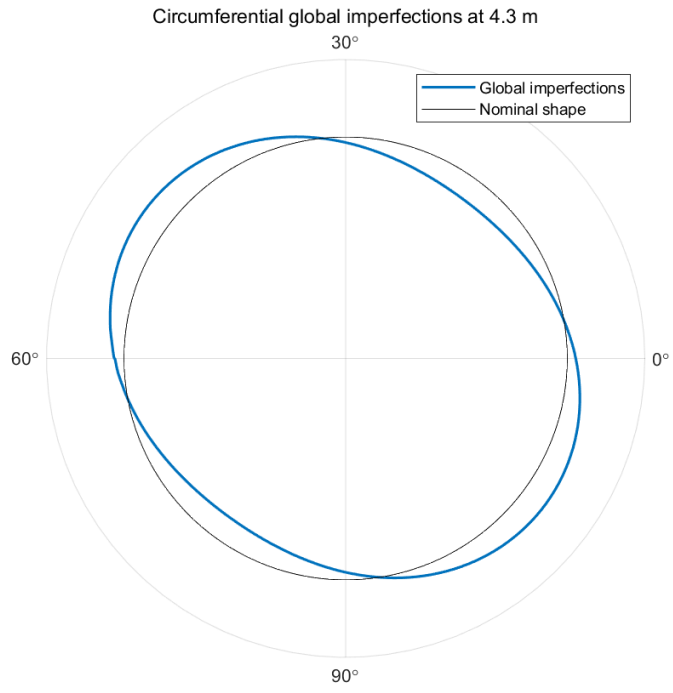


Circumferential global imperfections at 1.7 m

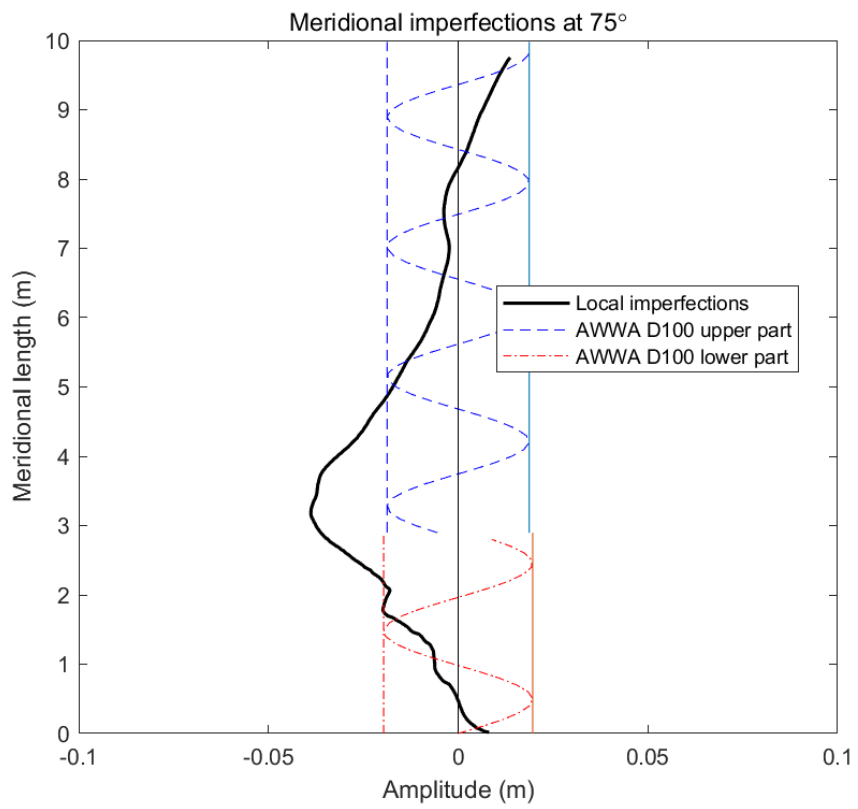
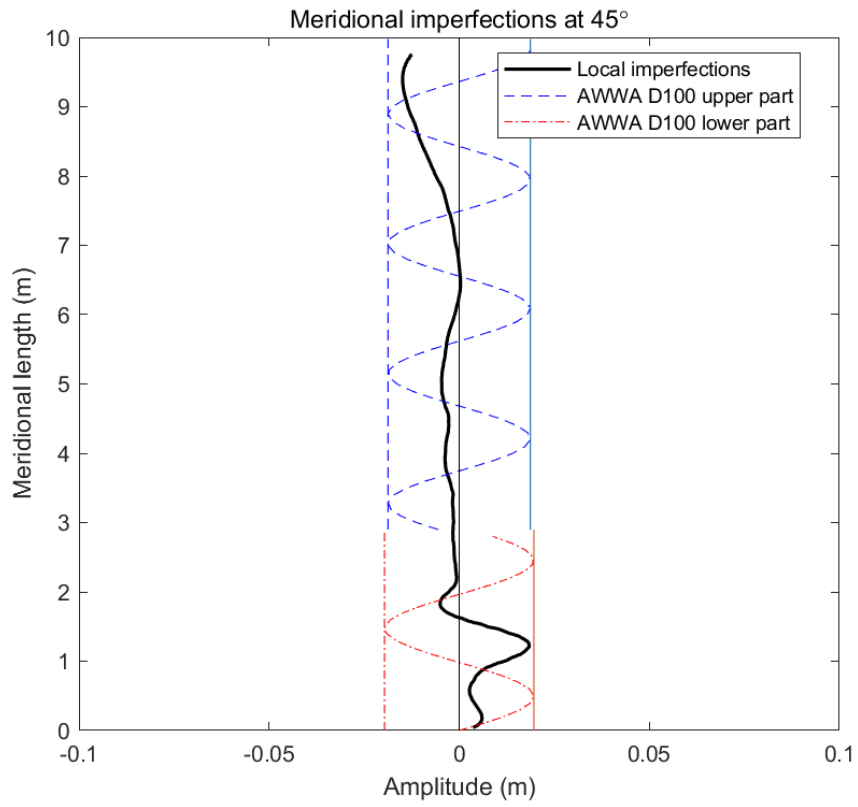


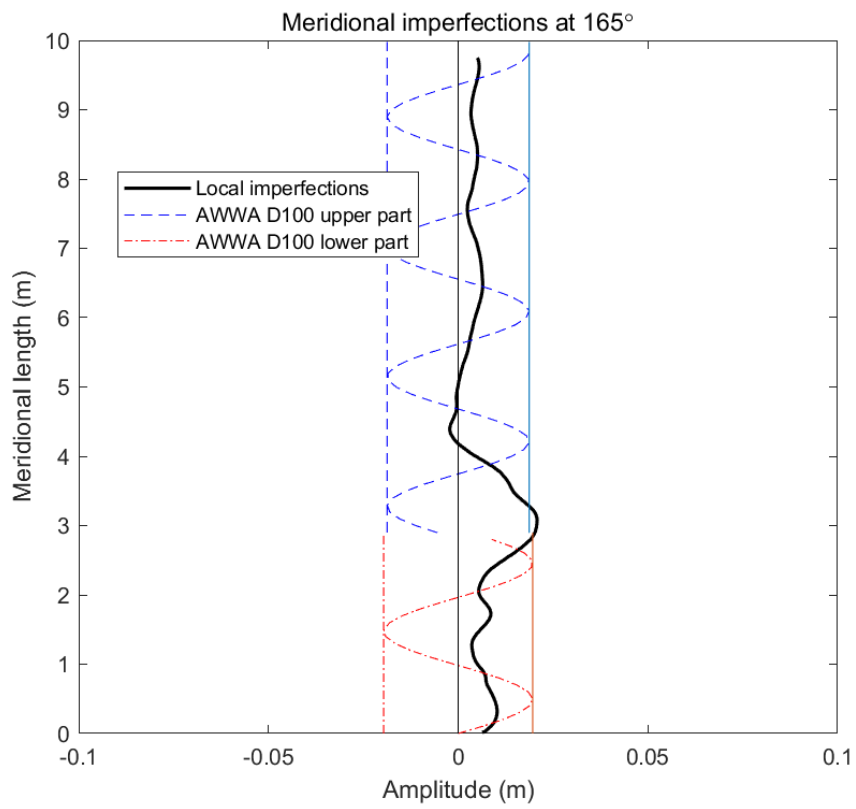
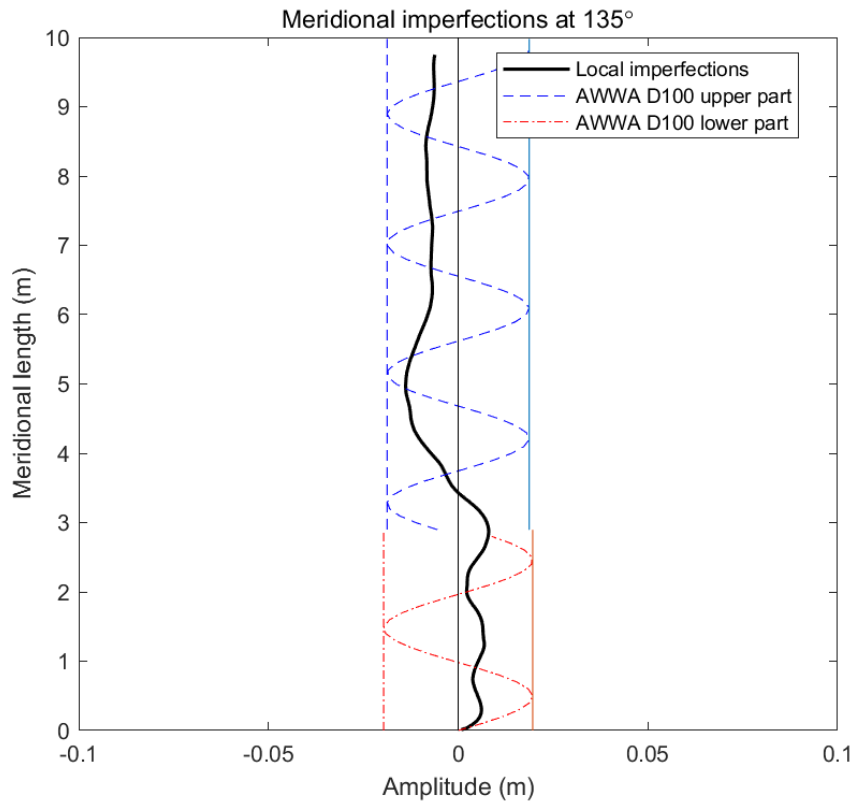
Circumferential global imperfections at 2.1 m



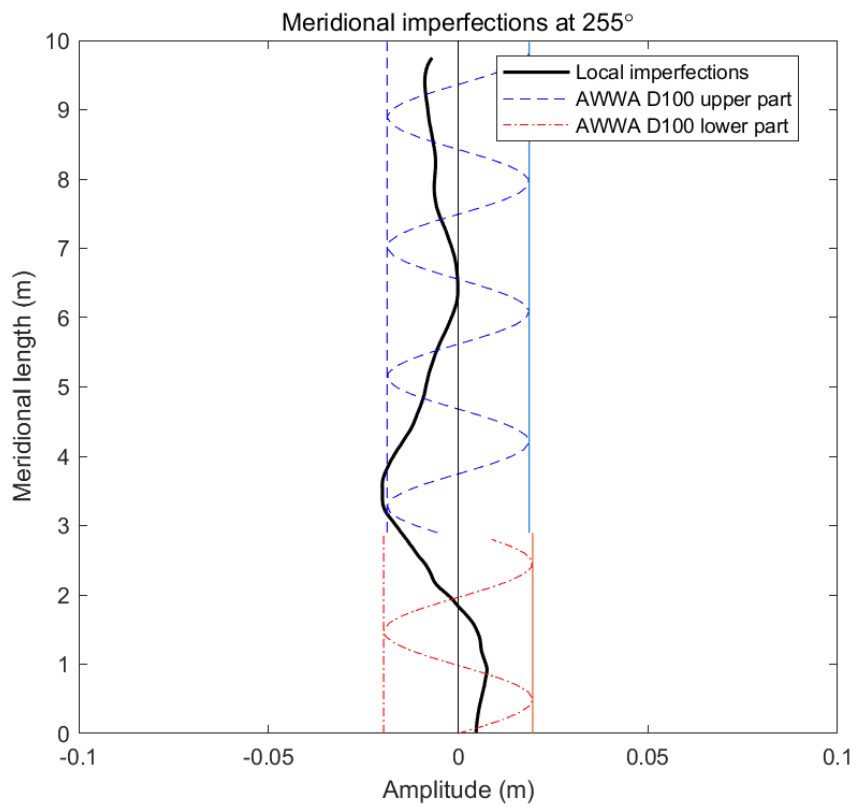
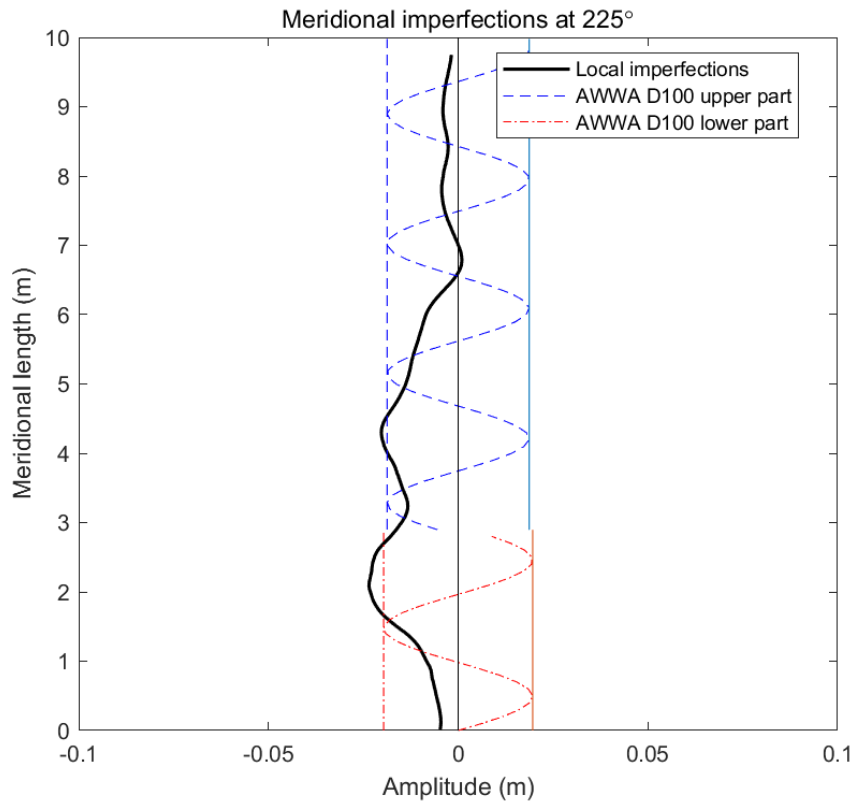


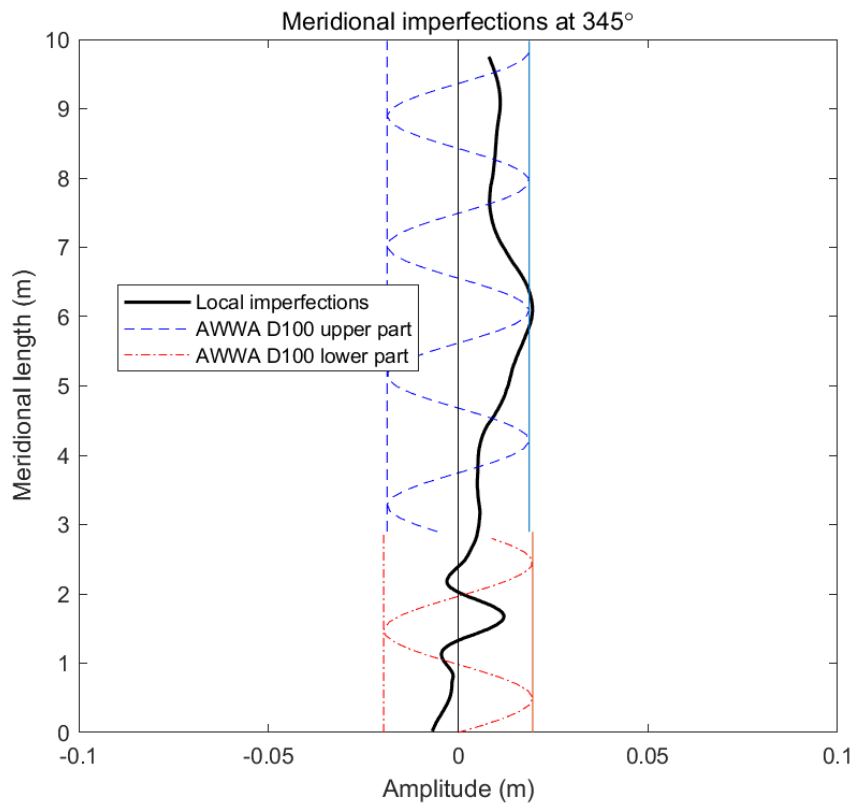
**Figure A.6 Circumferential global imperfections (40 times scaled)**



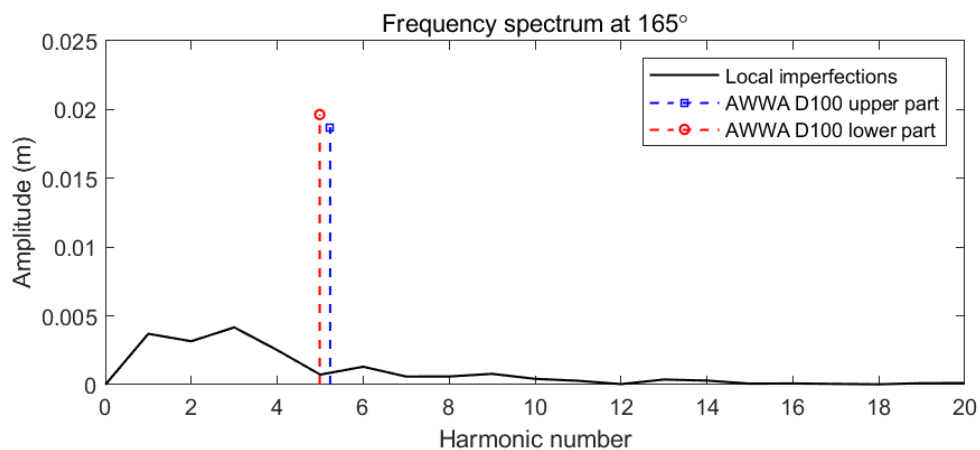
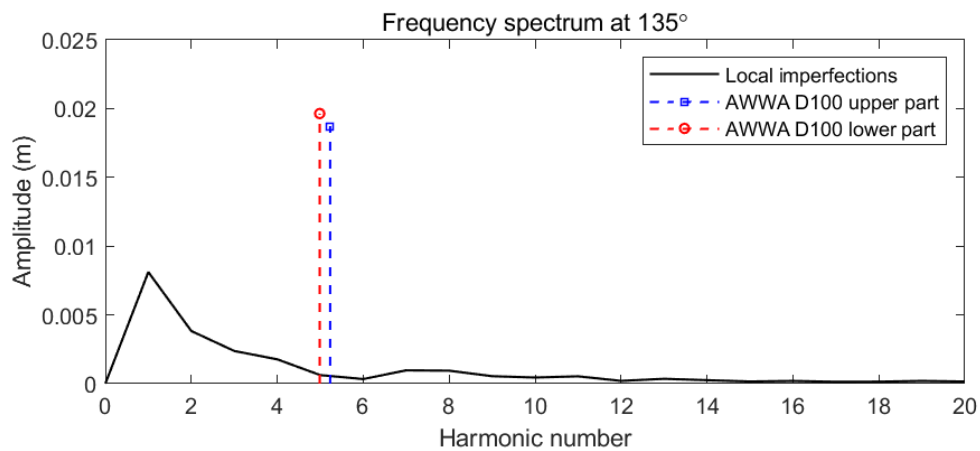
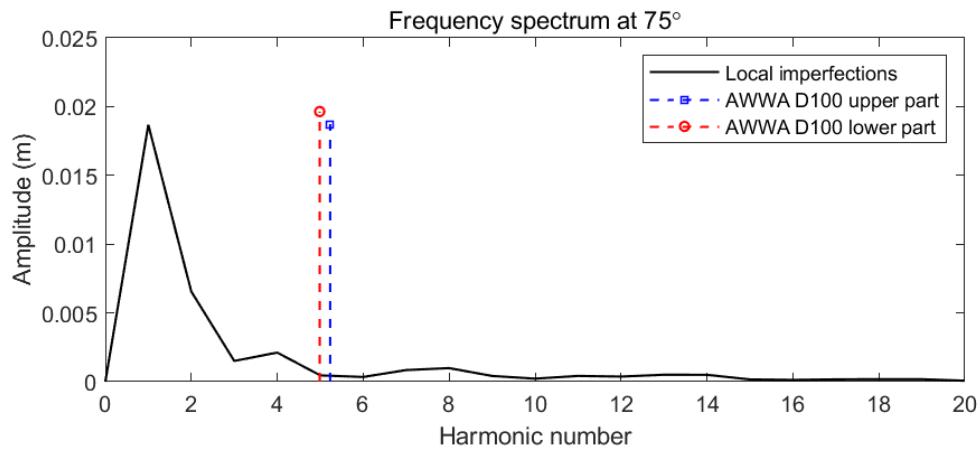
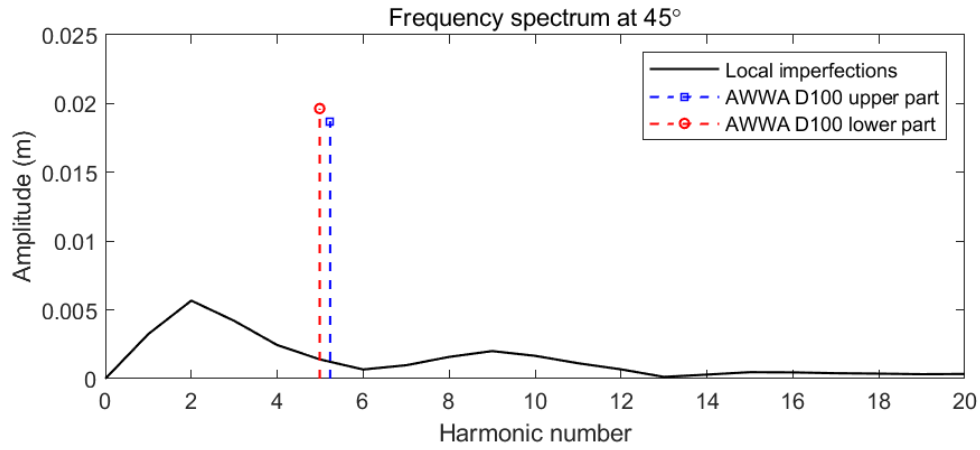


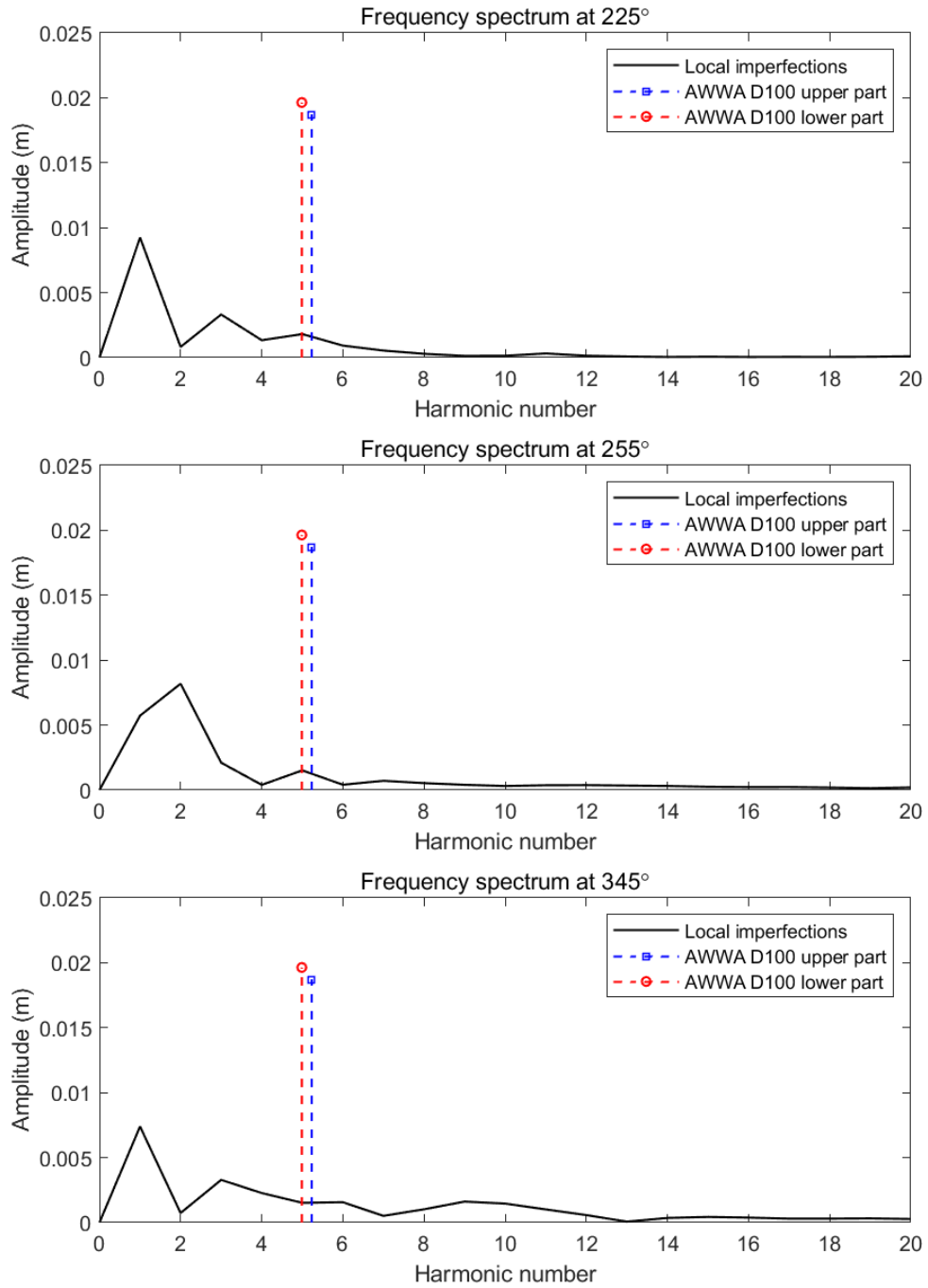




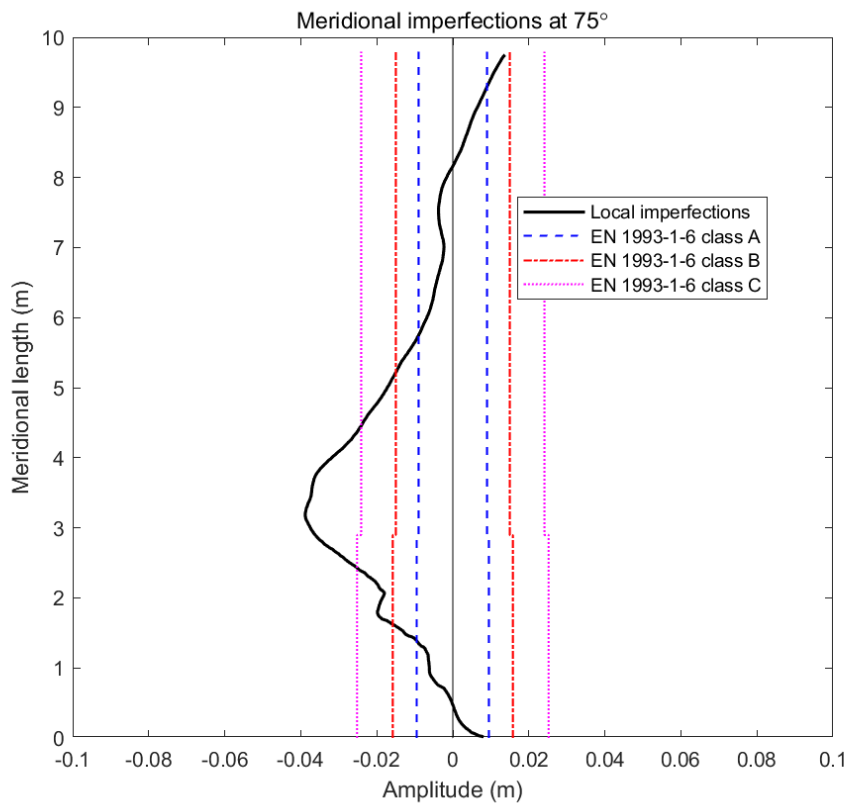
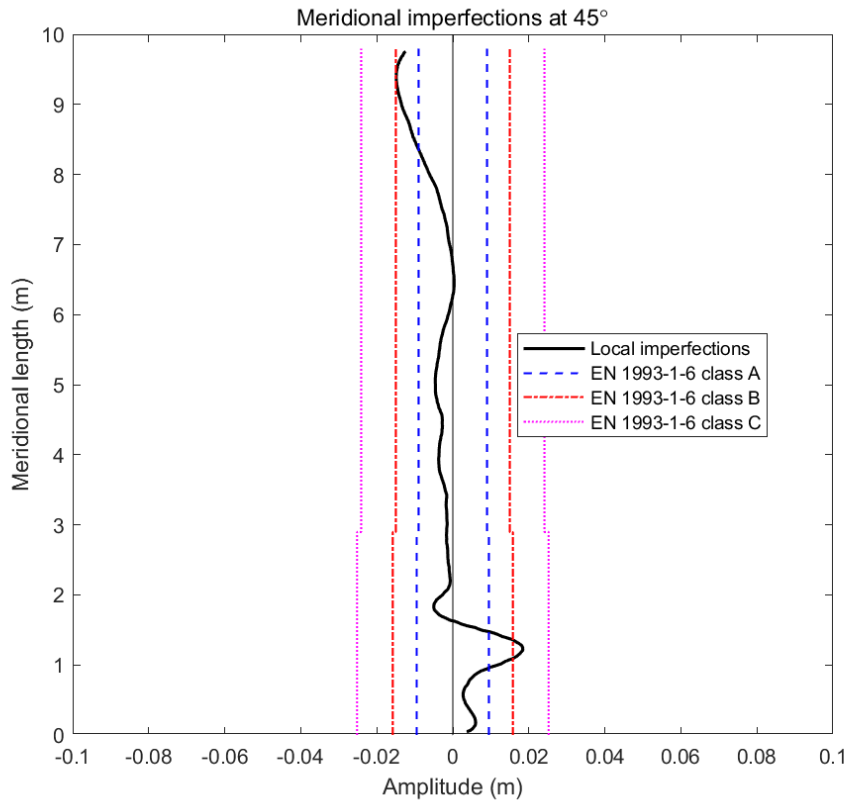


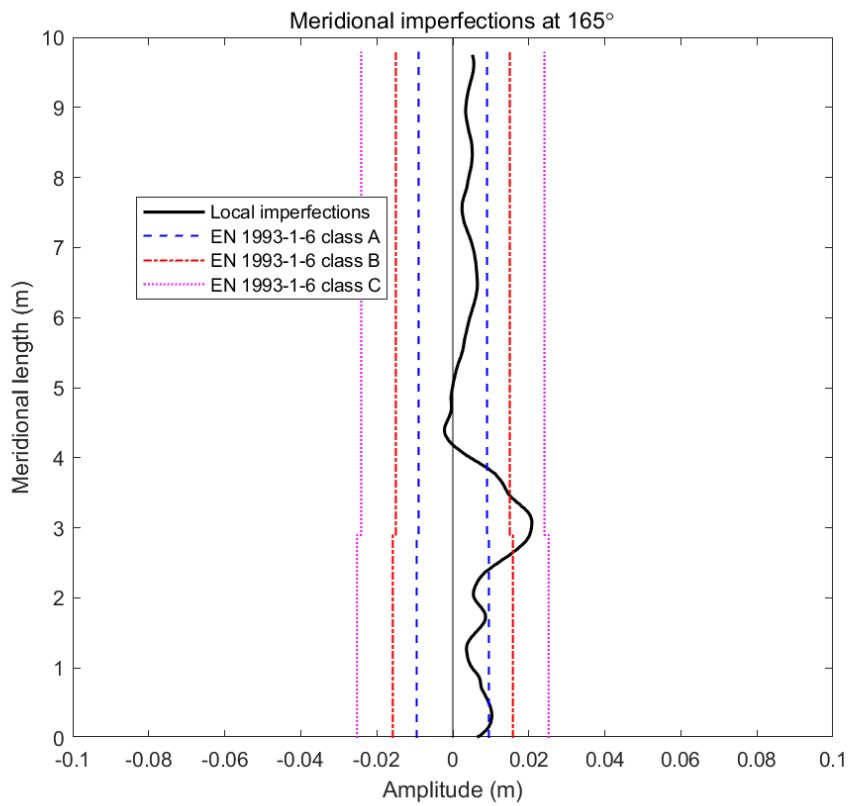
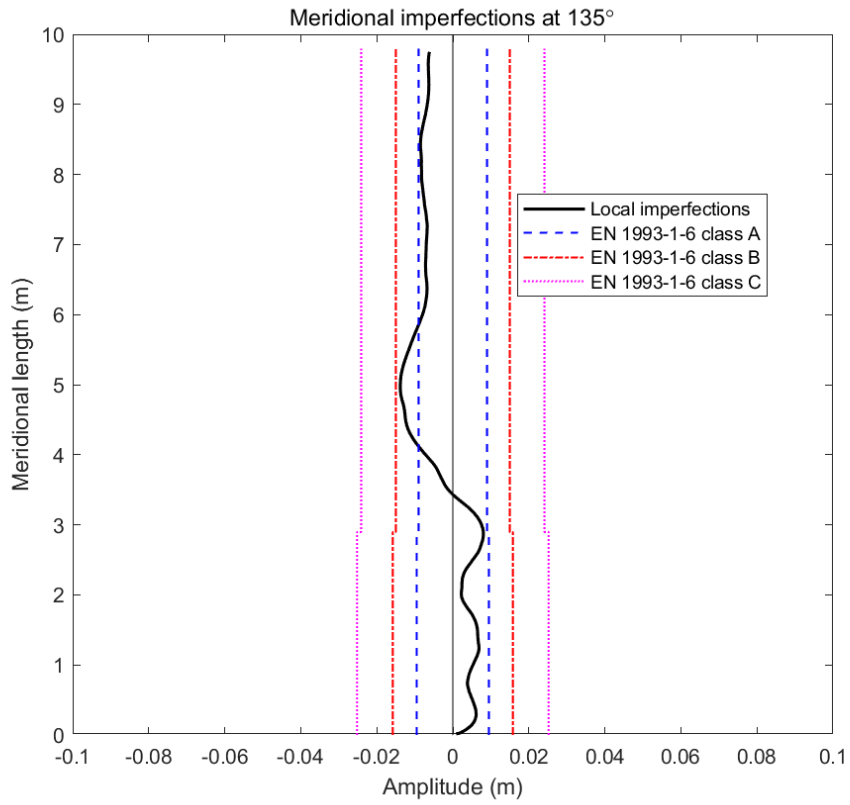
**Figure A.7 Evaluation of local imperfection amplitude with specifications in AWWA D100-11**

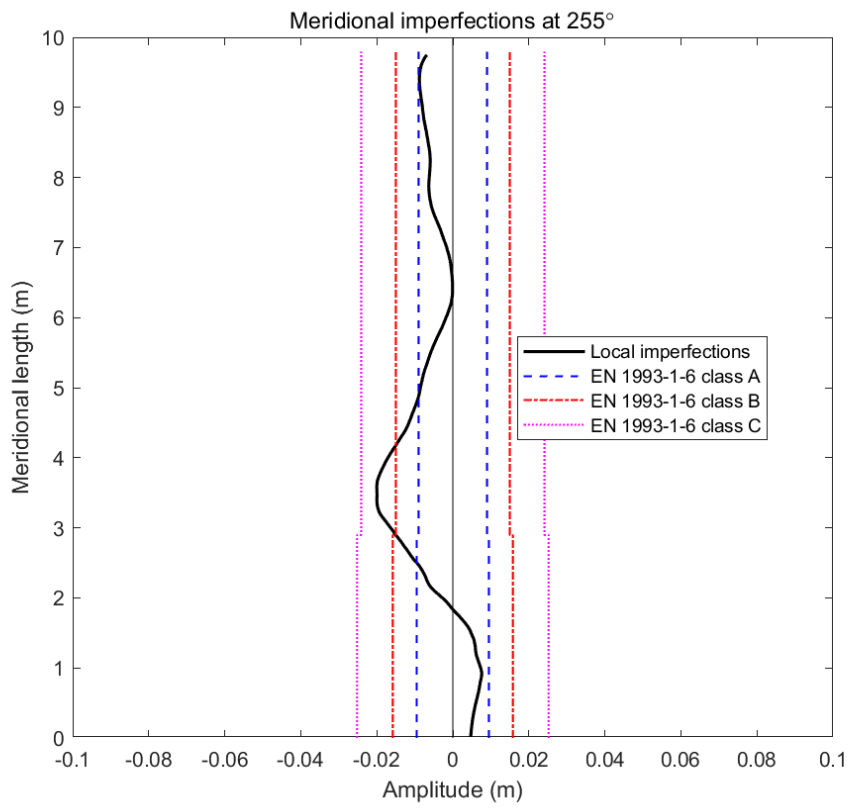
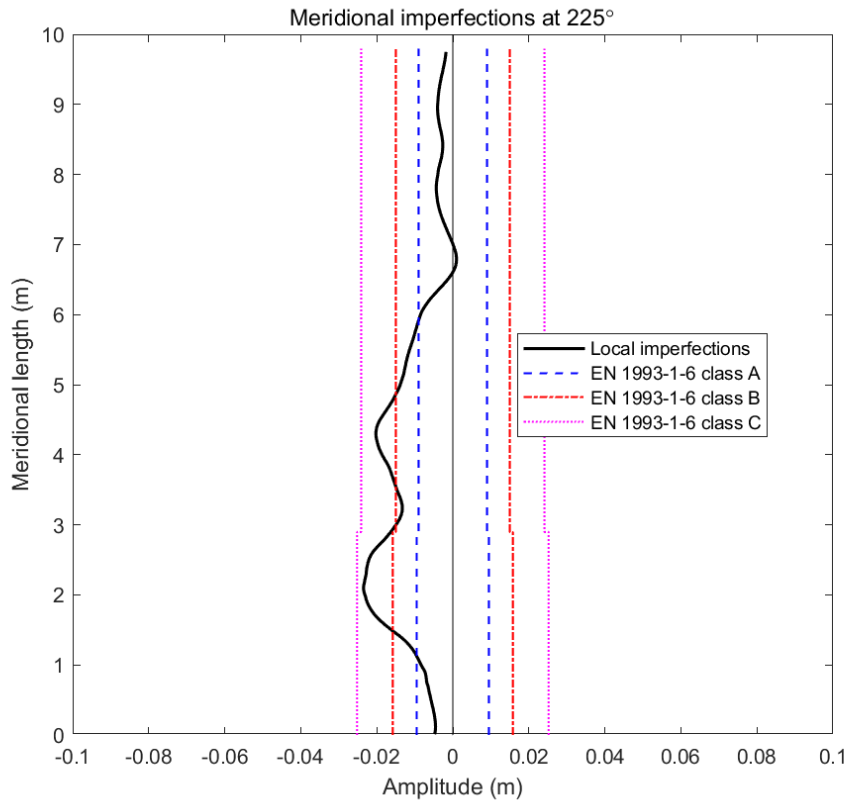


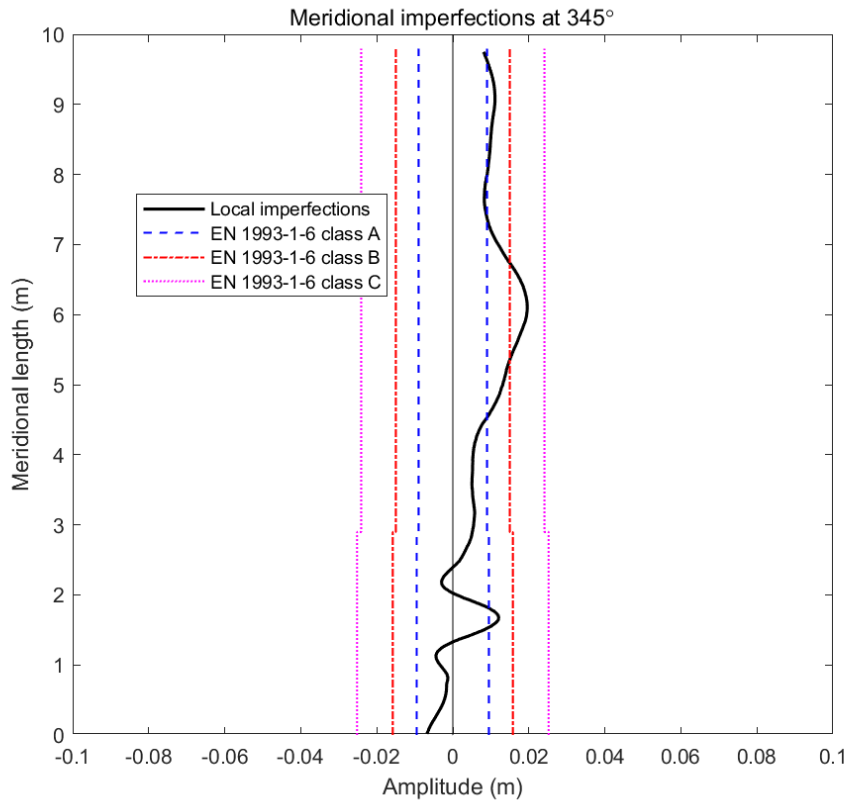


**Figure A.8 Evaluation of local imperfection wavelength with specifications in AWWA D100-11**



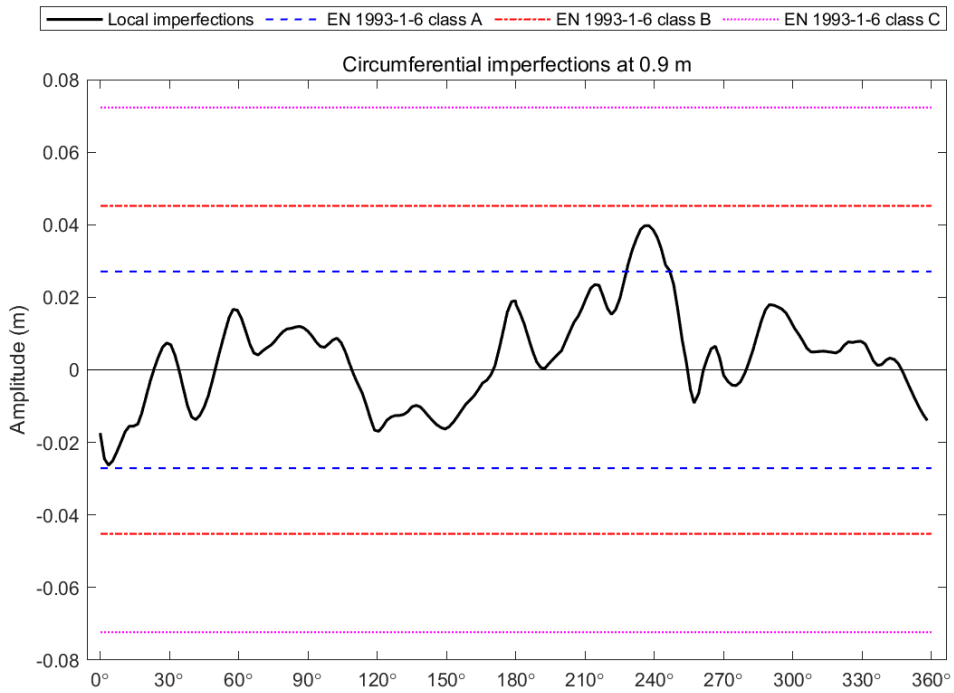
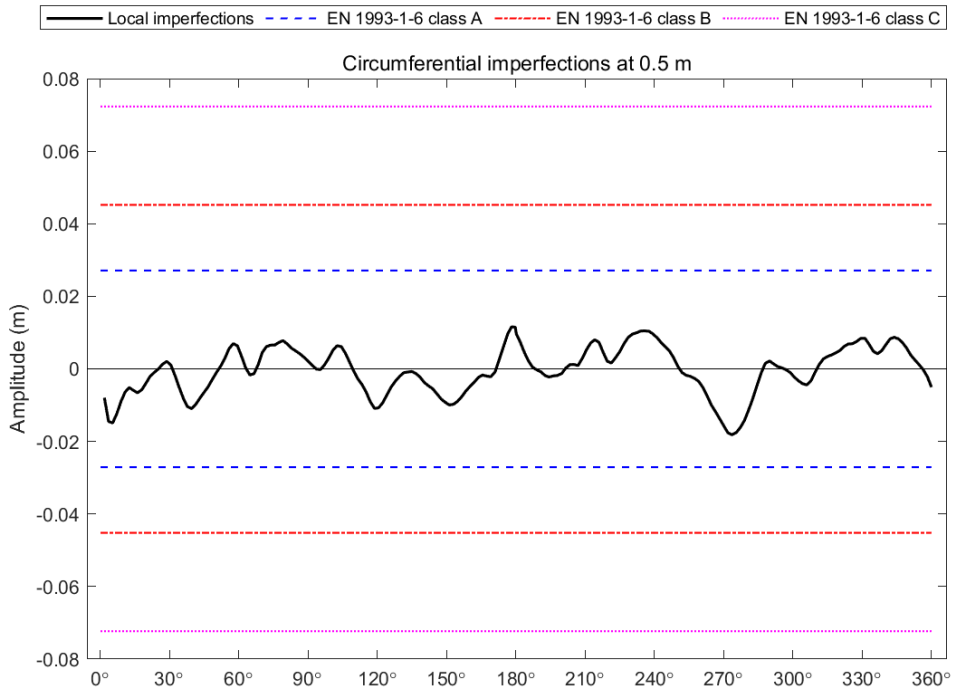


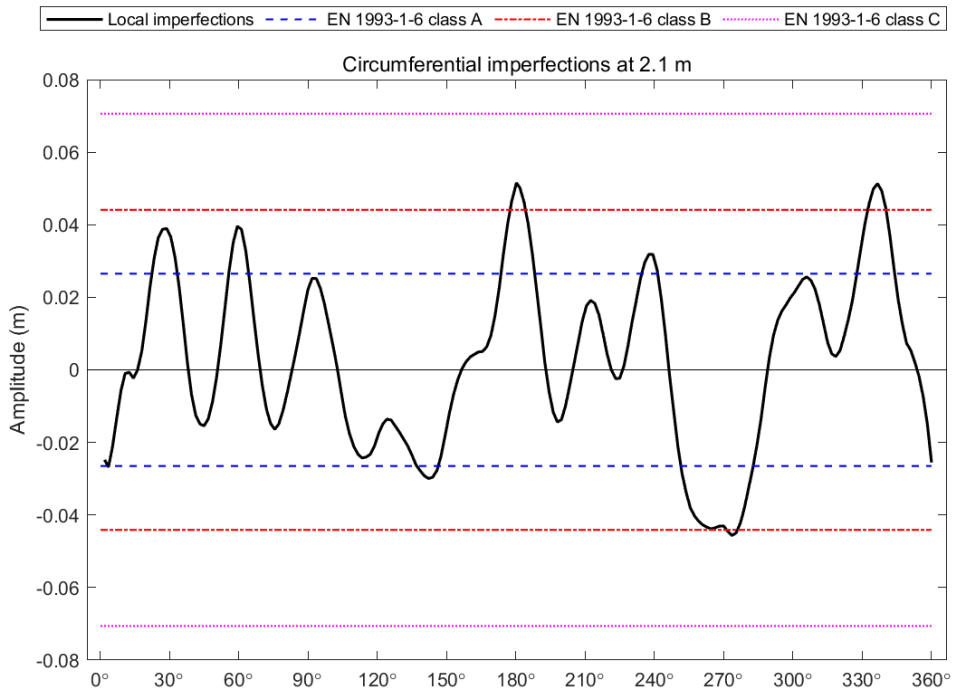
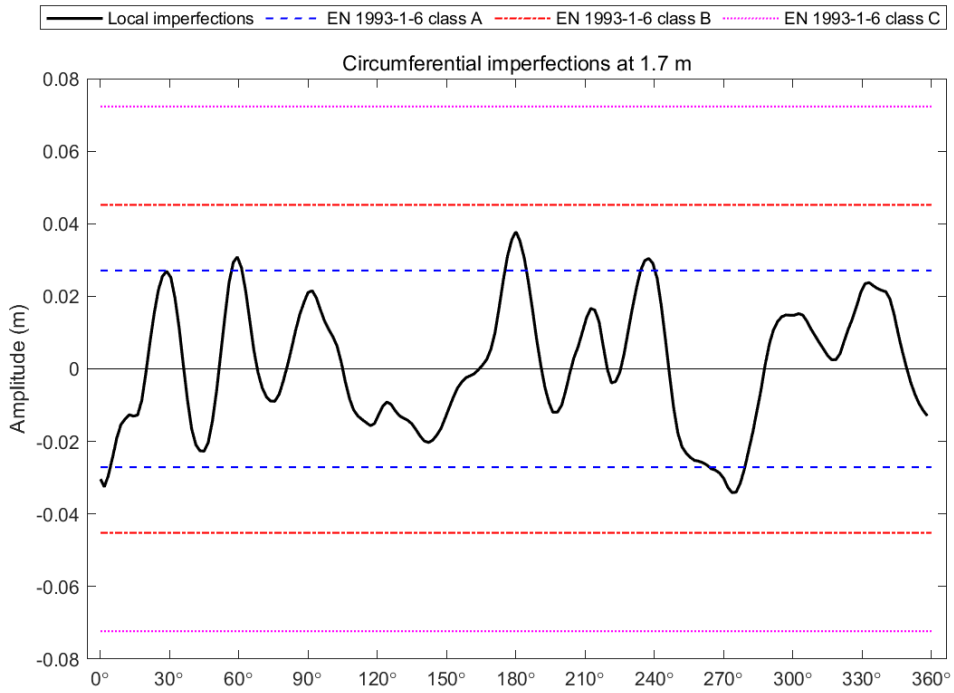


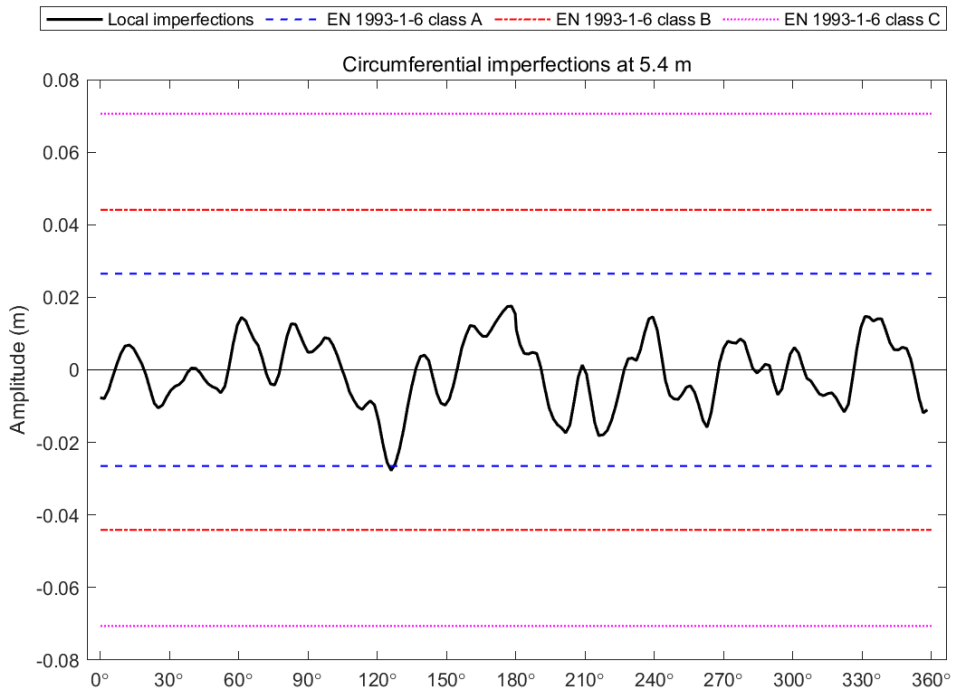
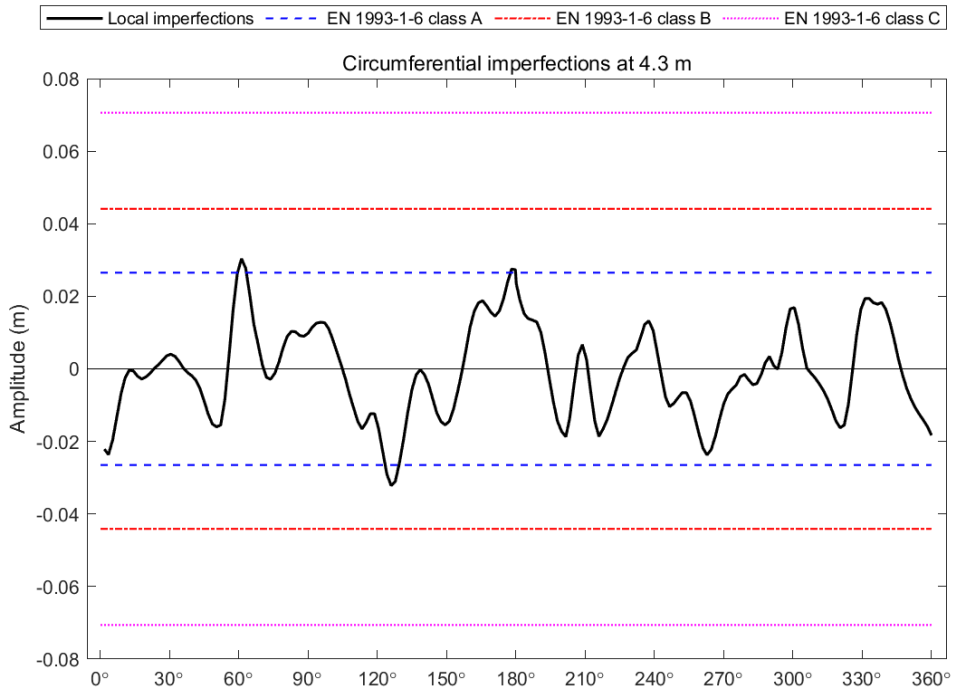


**Figure A.9 Evaluation of meridional local imperfection amplitude with specifications in EN 1993-1-6: 2007**

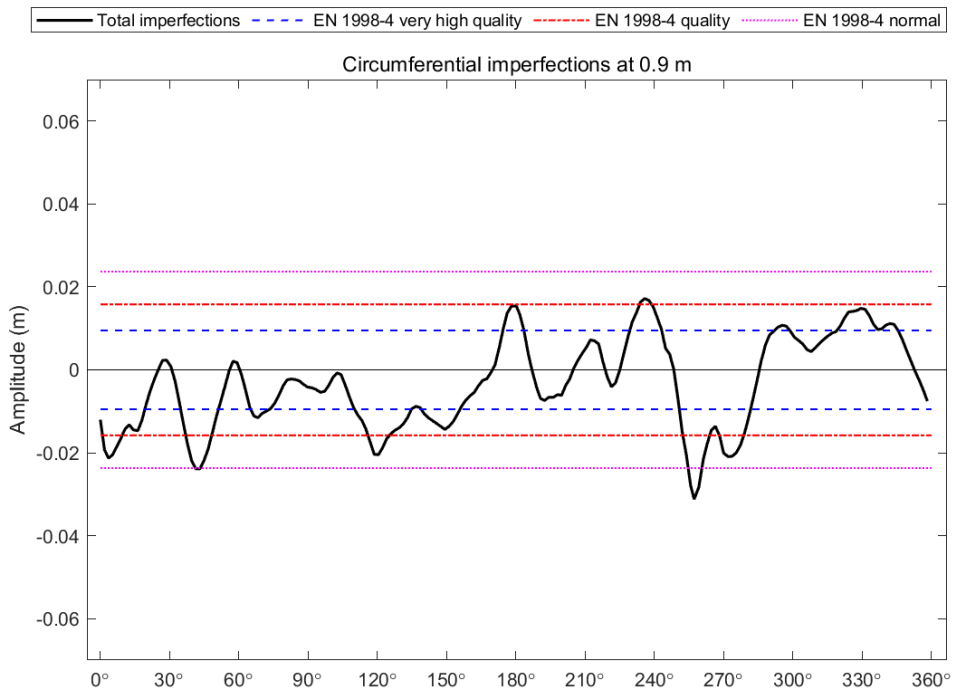
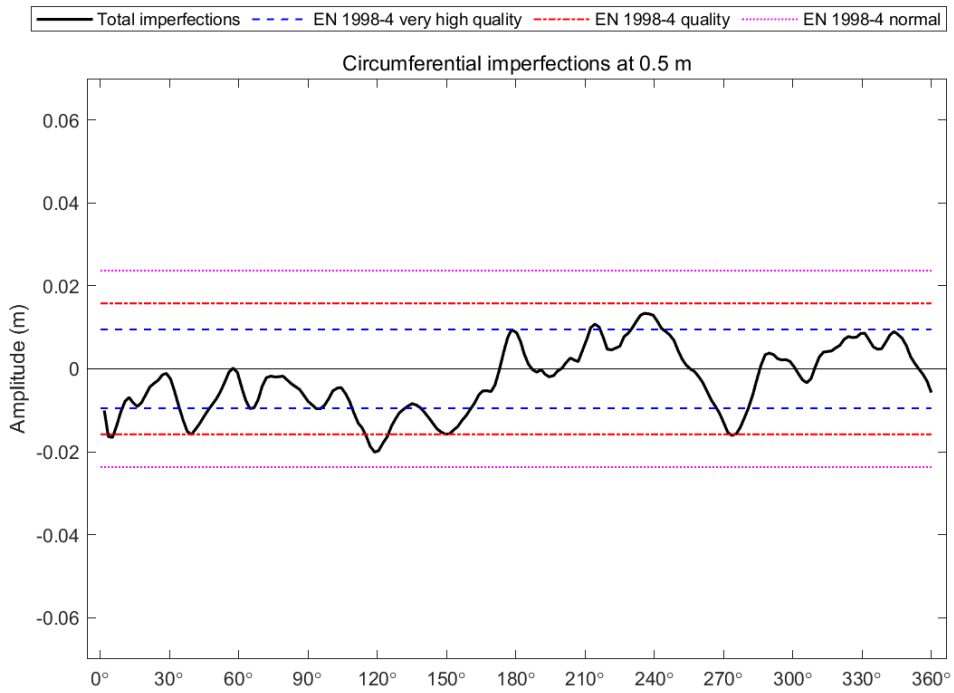


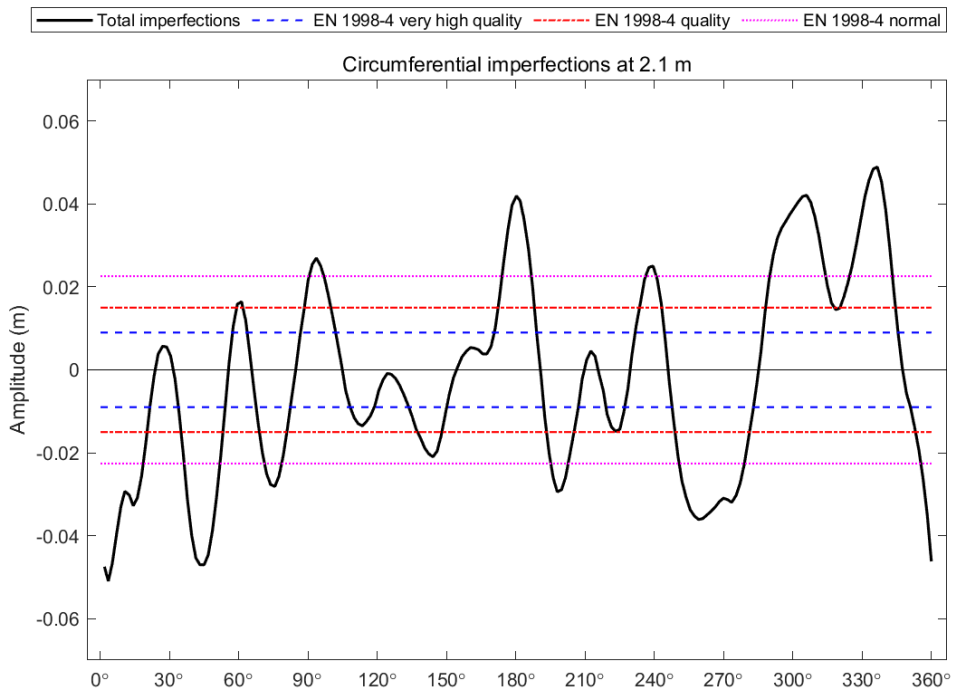
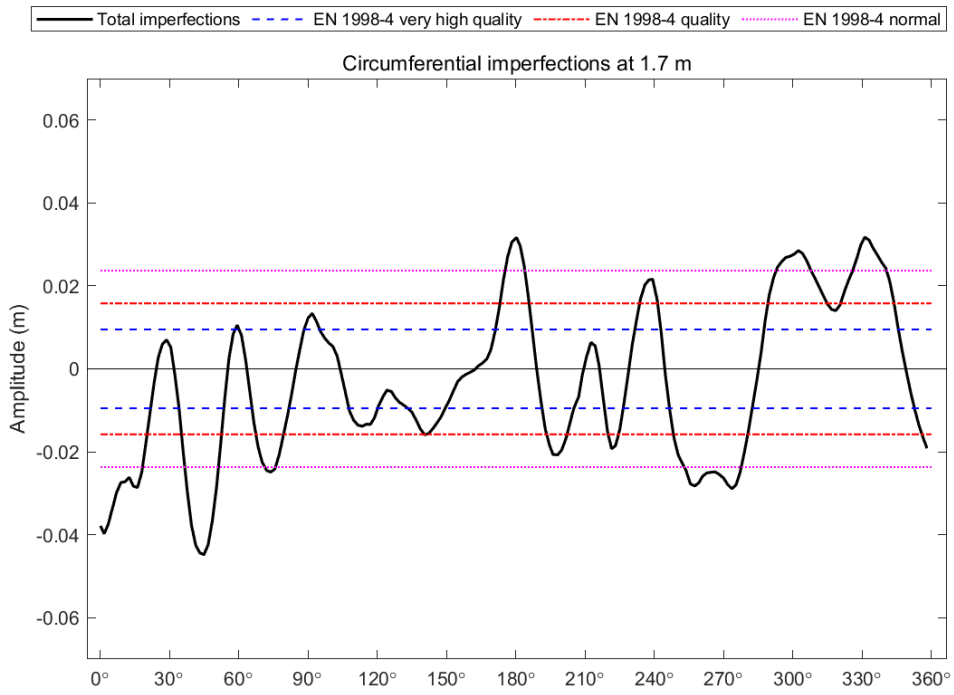


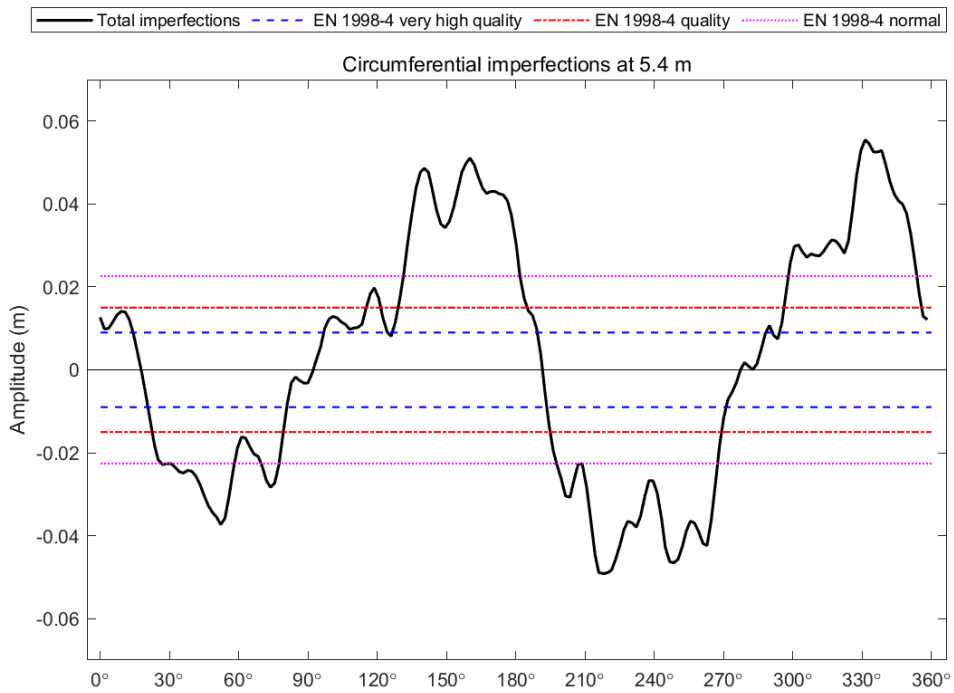
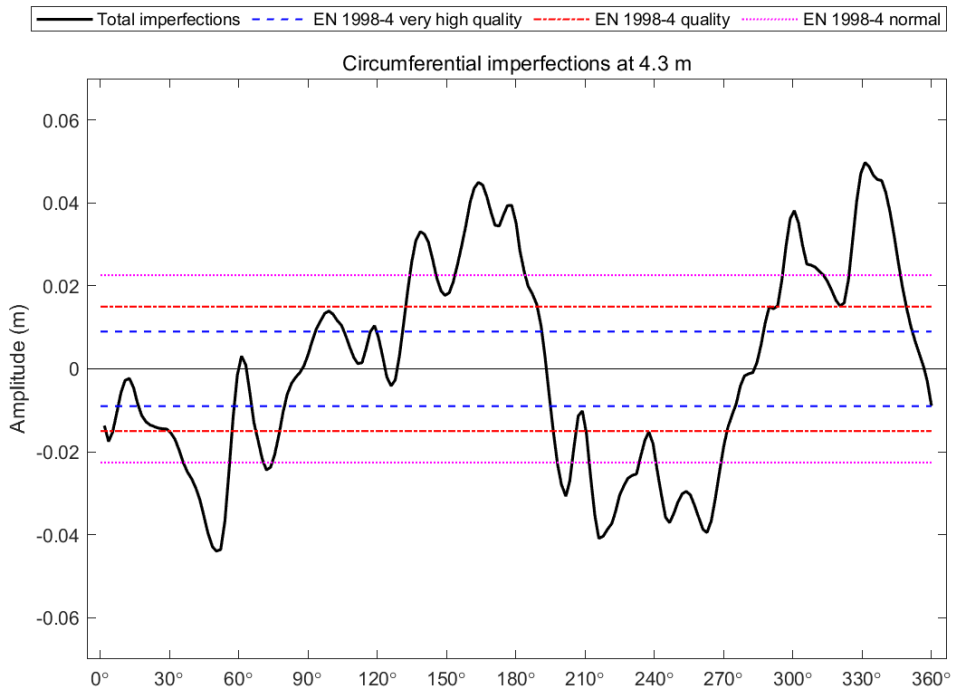


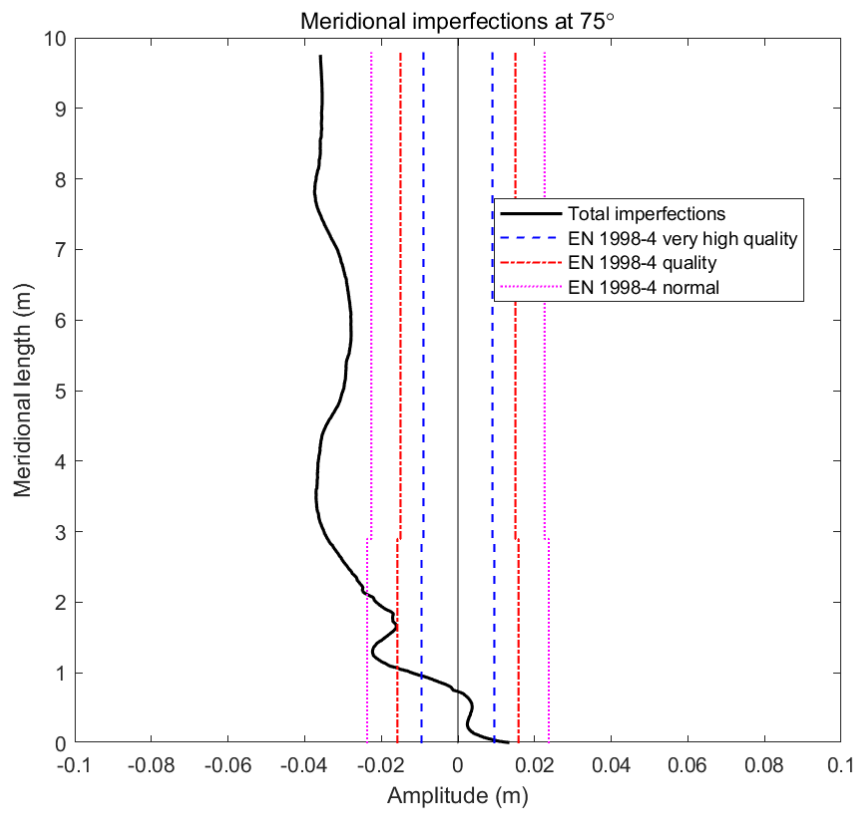
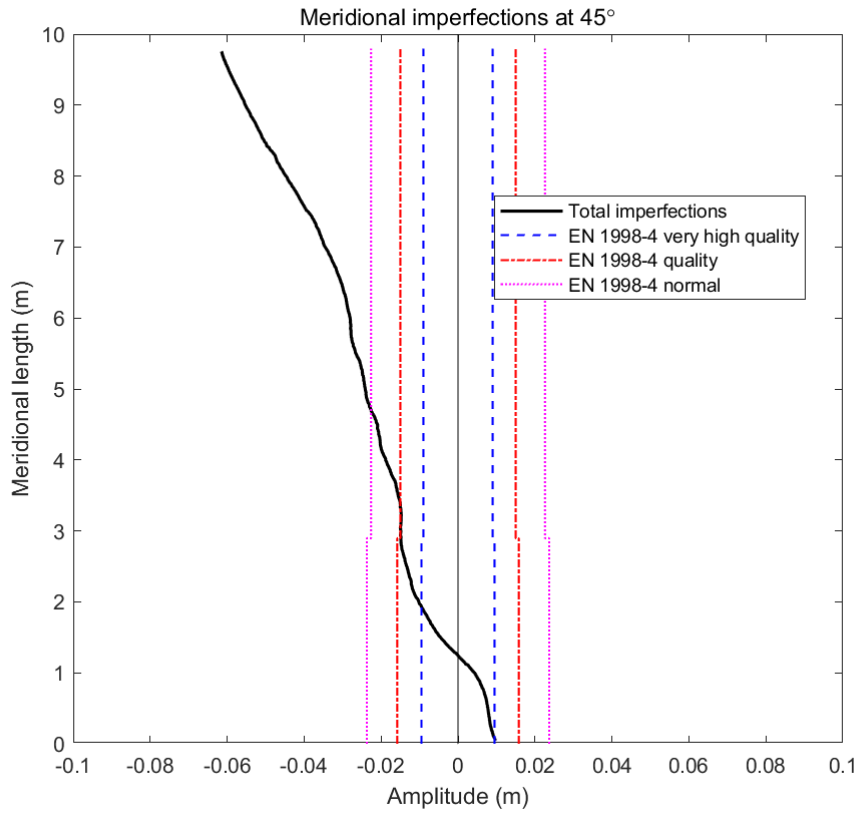


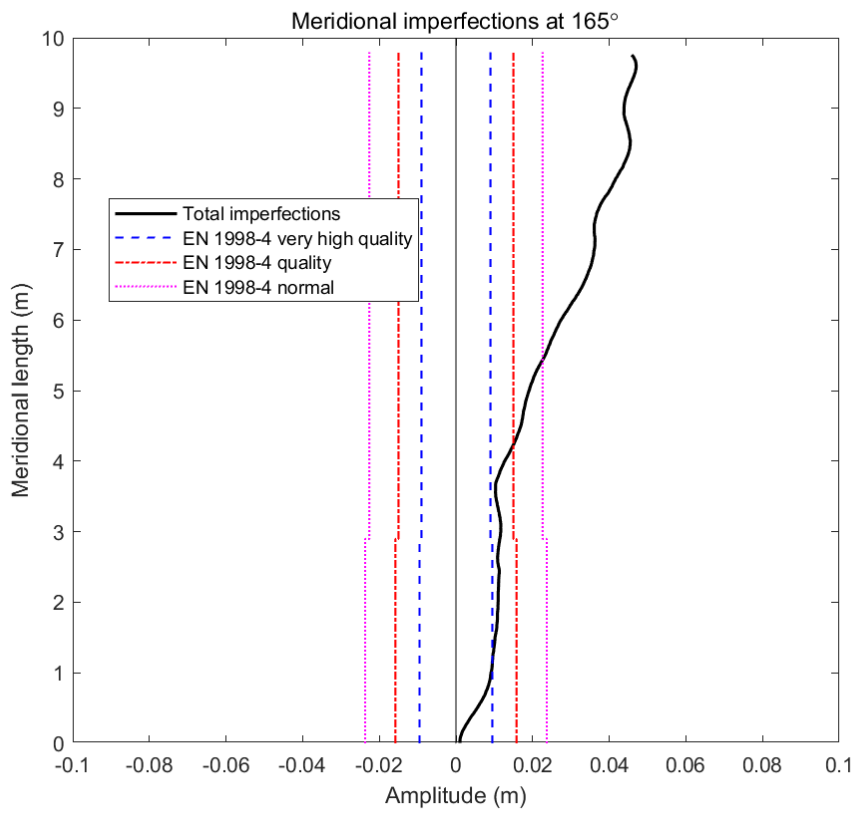
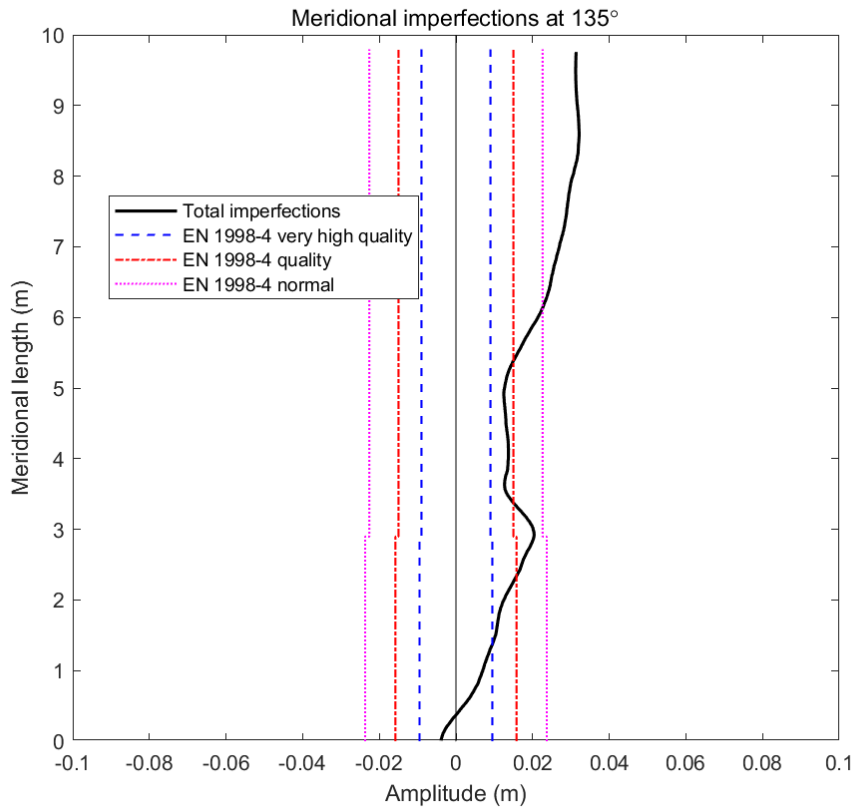
**Figure A.10 Evaluation of circumferential local imperfection amplitude with specifications in EN 1993-1-6: 2007**



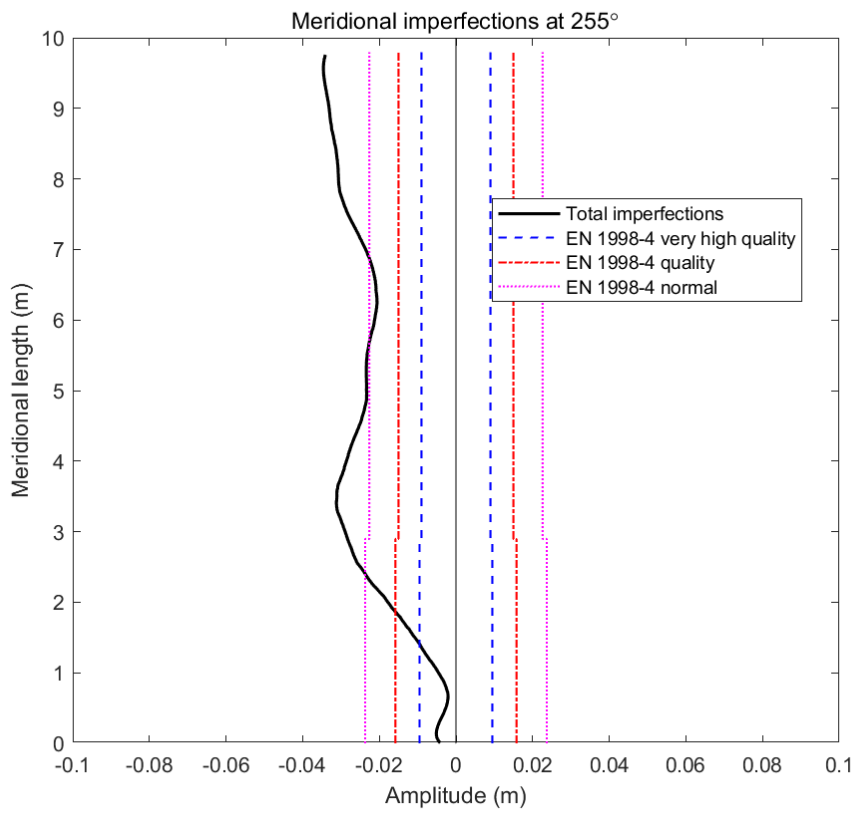
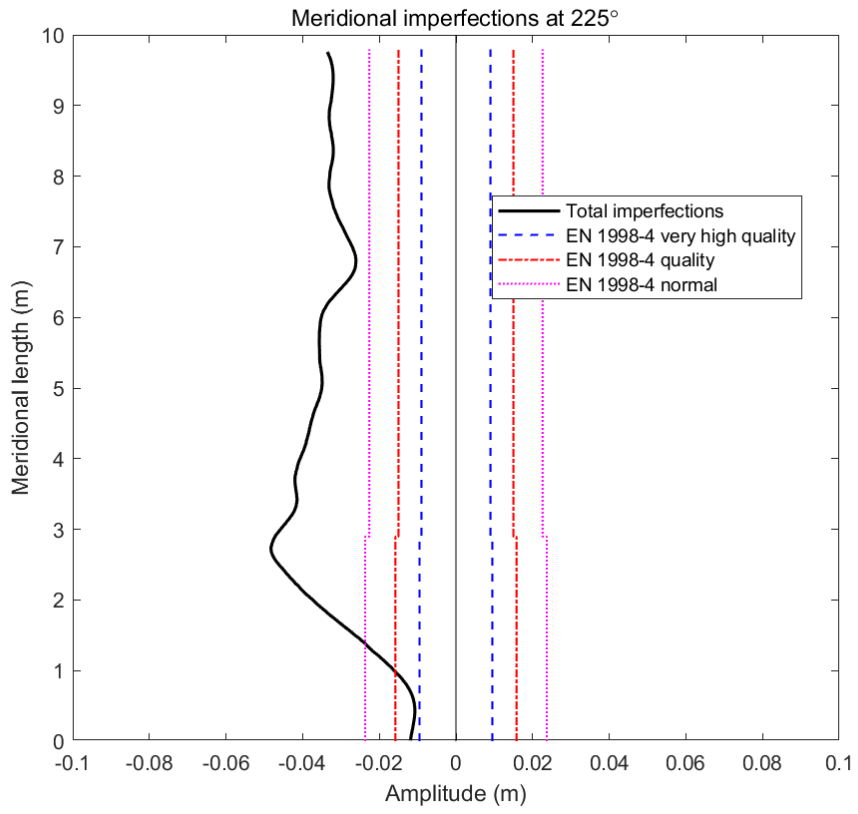


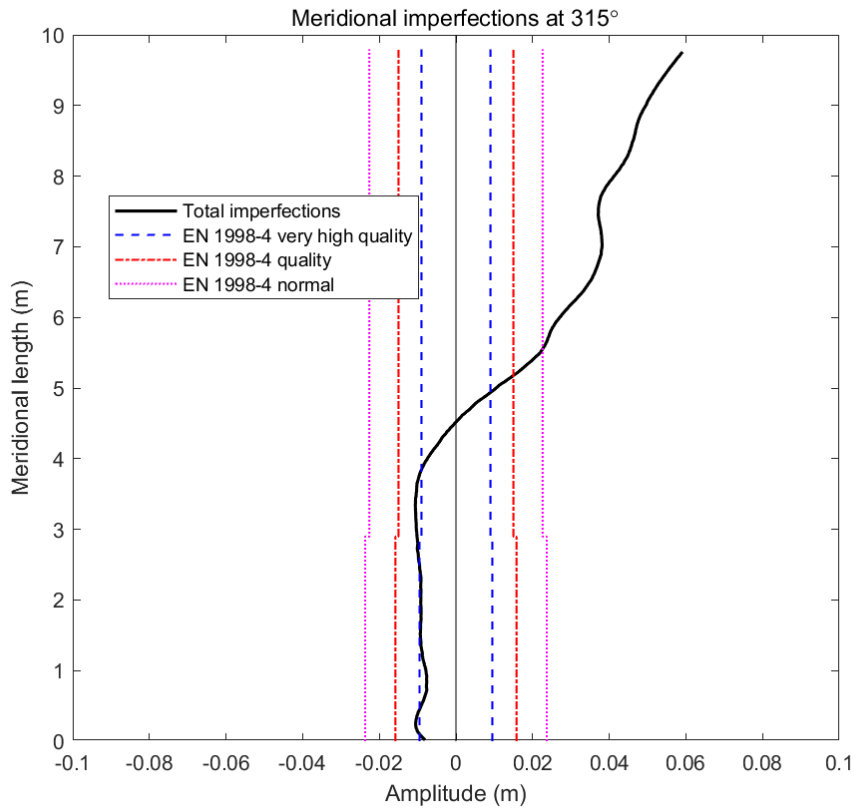




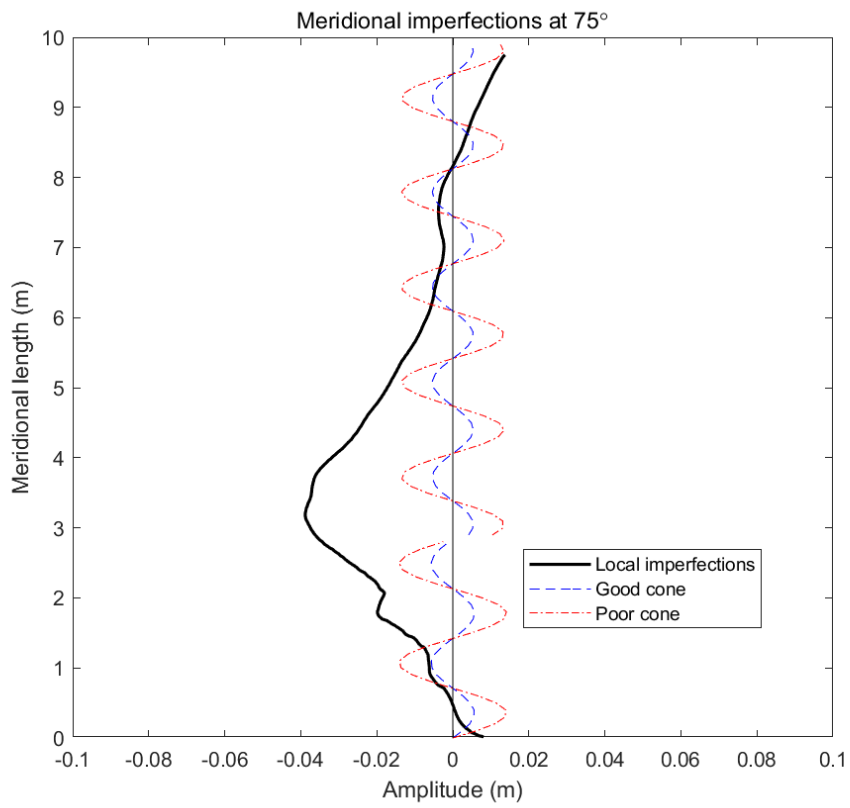
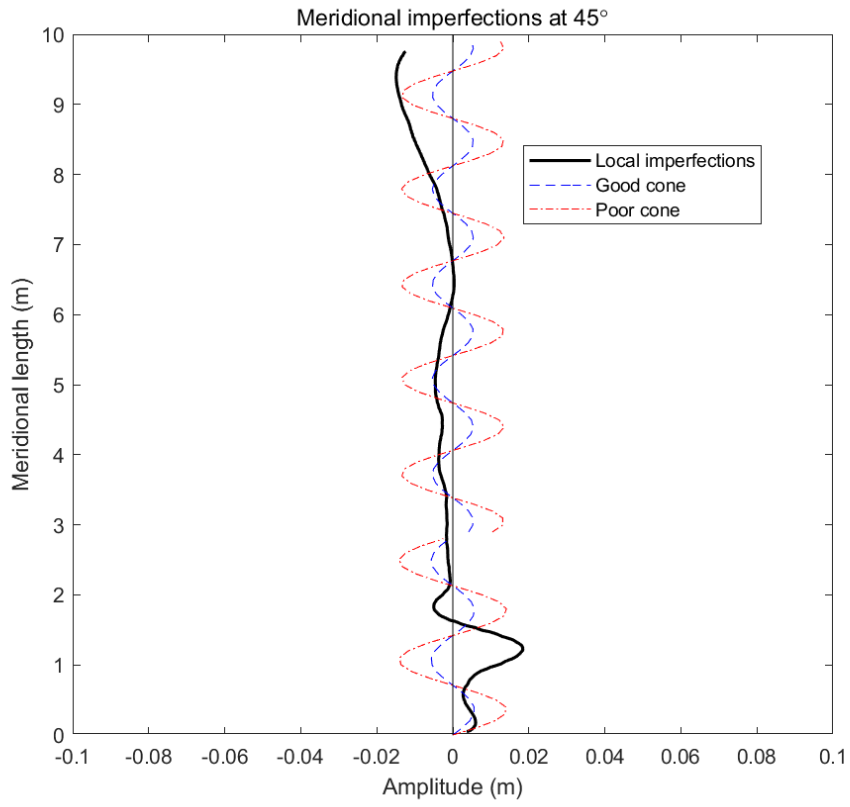


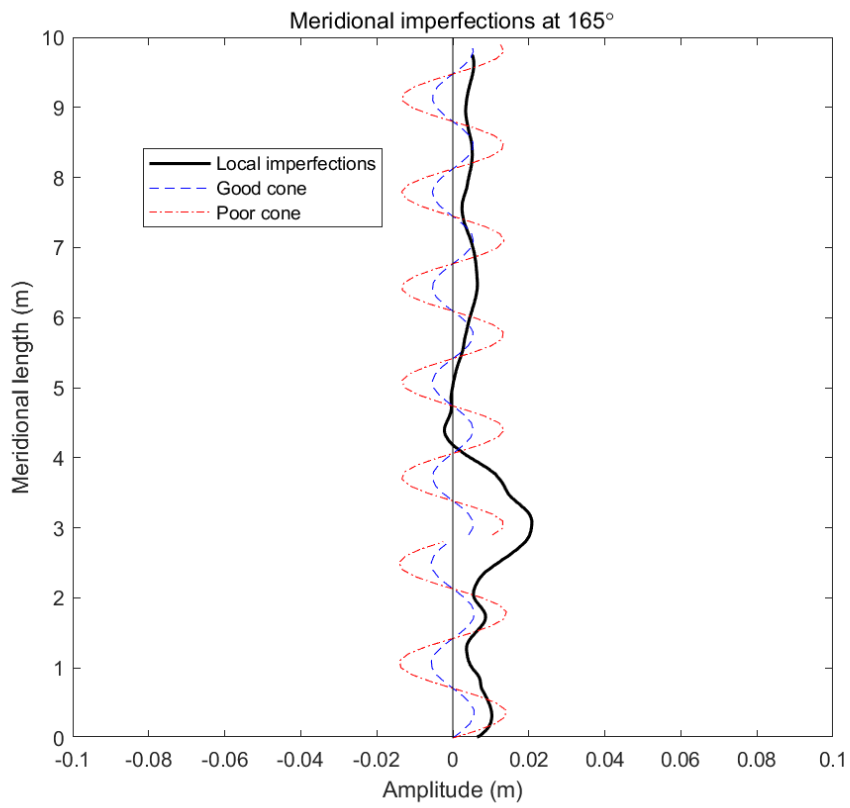
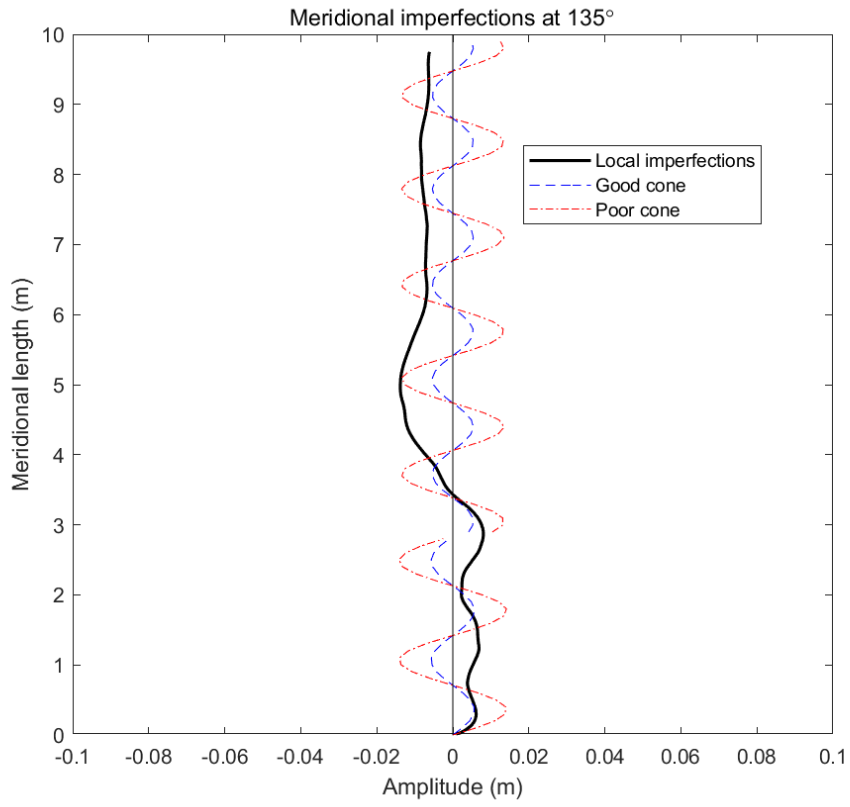


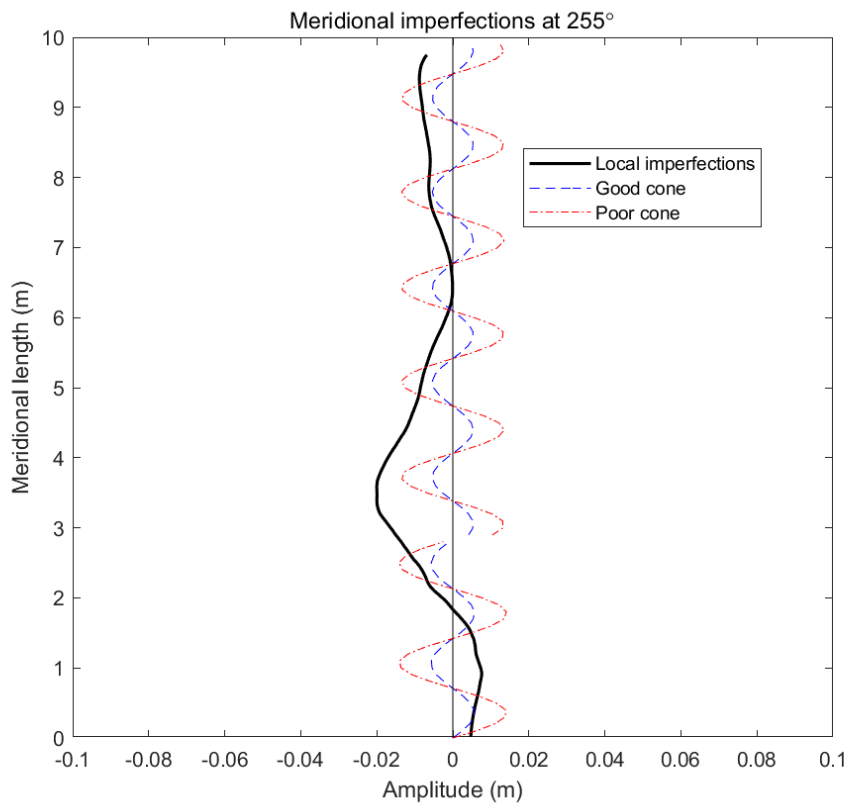
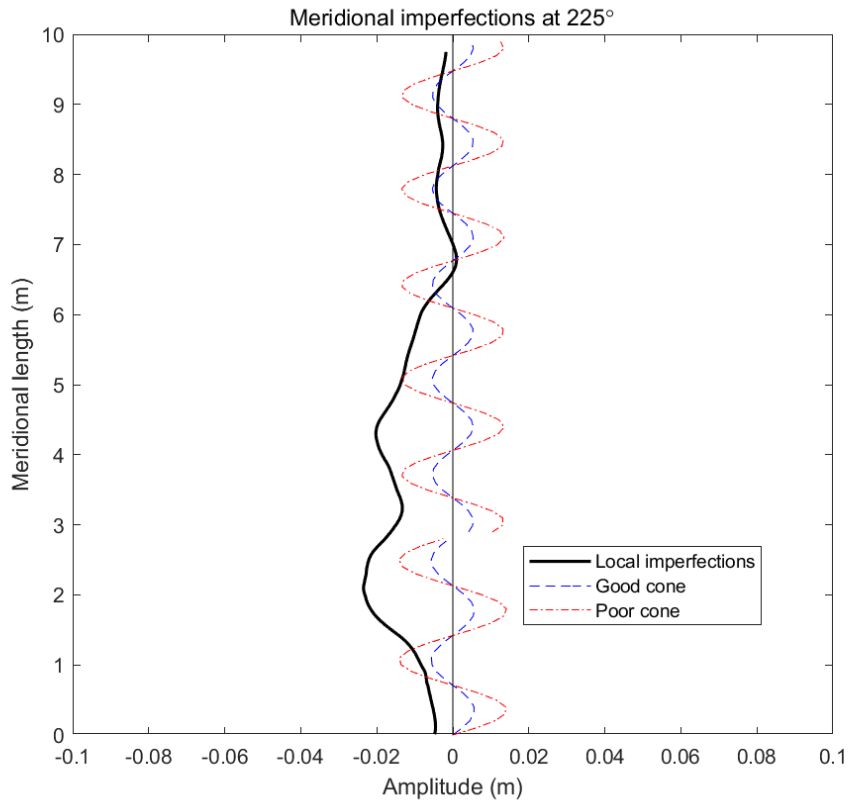




**Figure A.11 Evaluation of total imperfection amplitude with specifications in EN 1998-4: 2006**







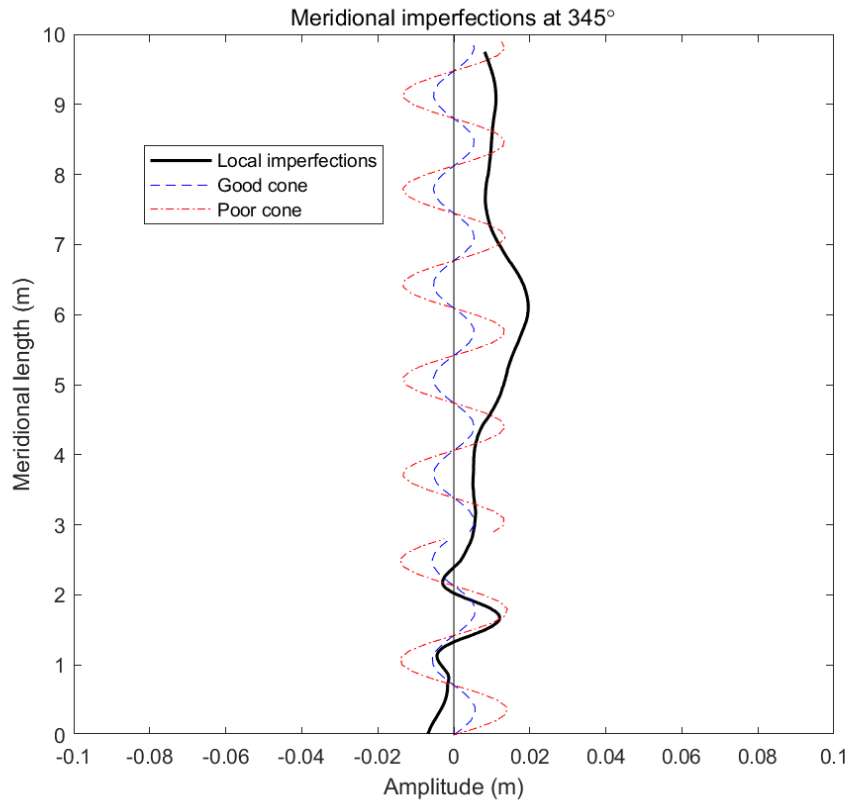


**Figure A.12 Evaluation of meridional local imperfection amplitude with specifications by Vandepitte et al. (1982)**



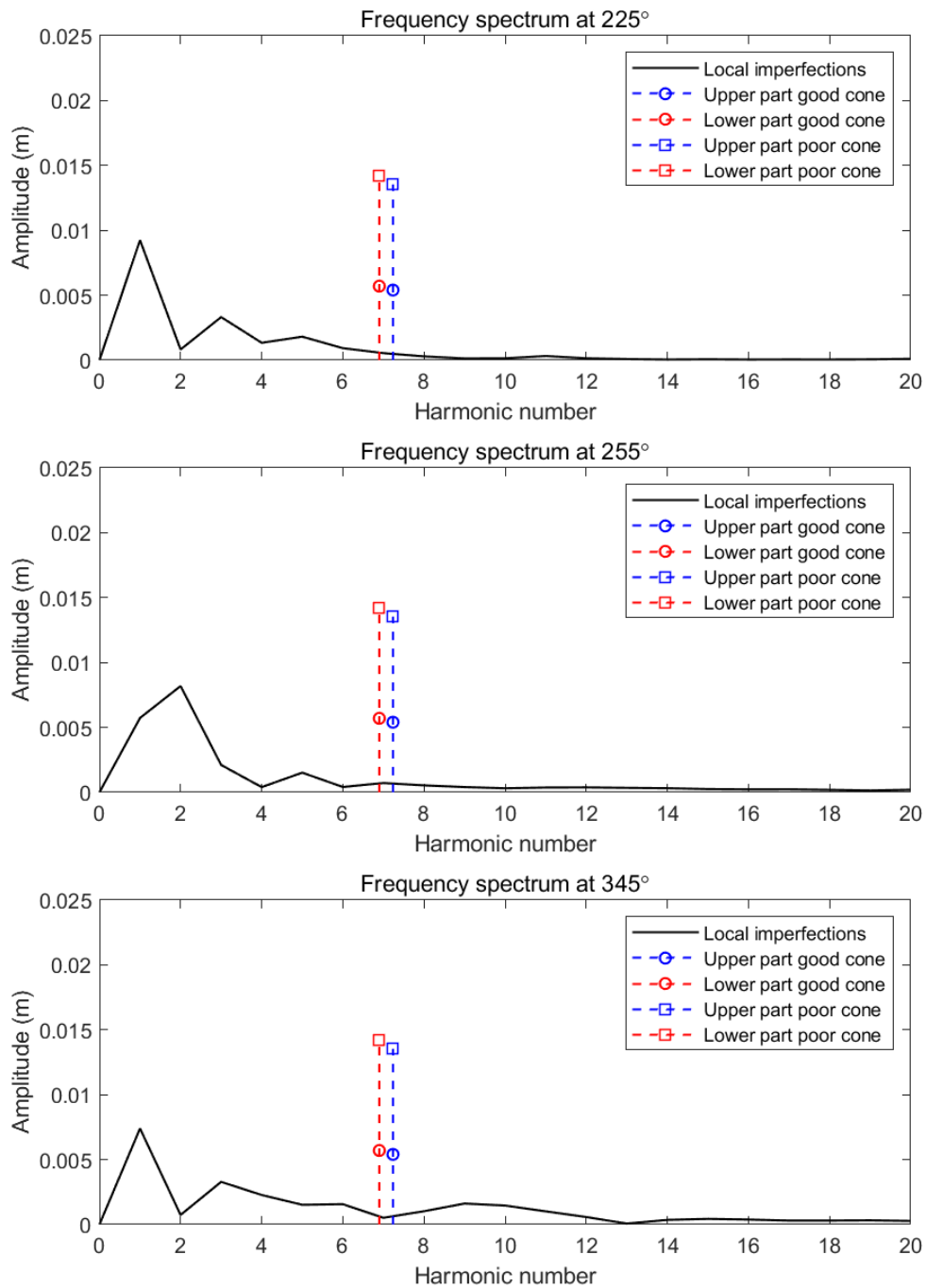
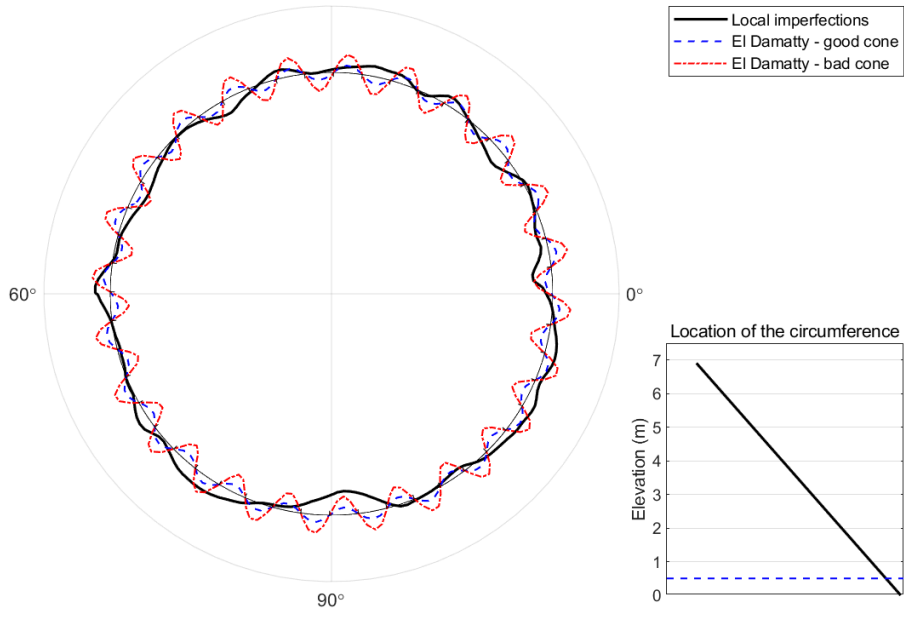


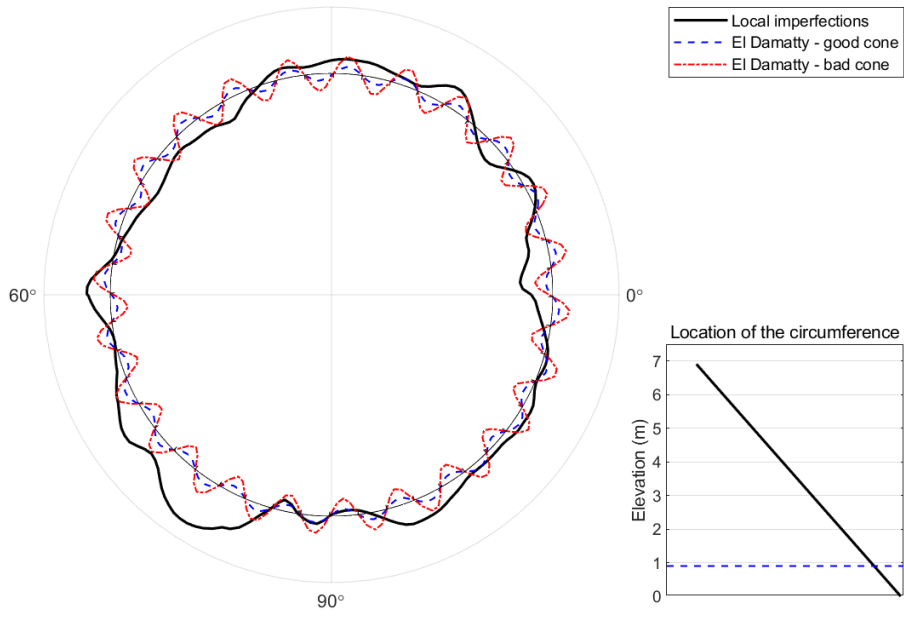
**Figure A.13 Evaluation of meridional local imperfection wavelength with specifications by Vandepitte et al. (1982)**



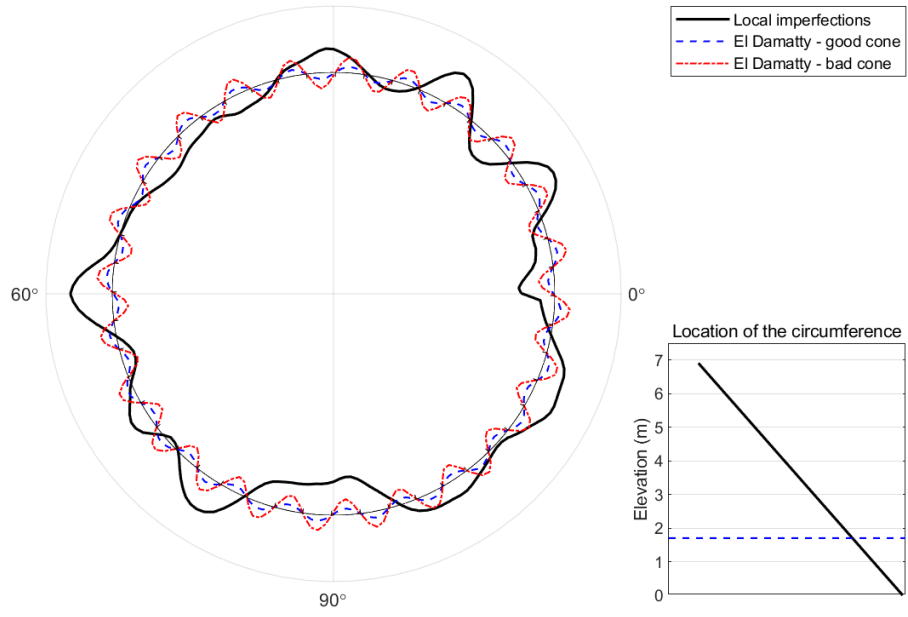
Circumferential imperfections at 0.5 m  
30°



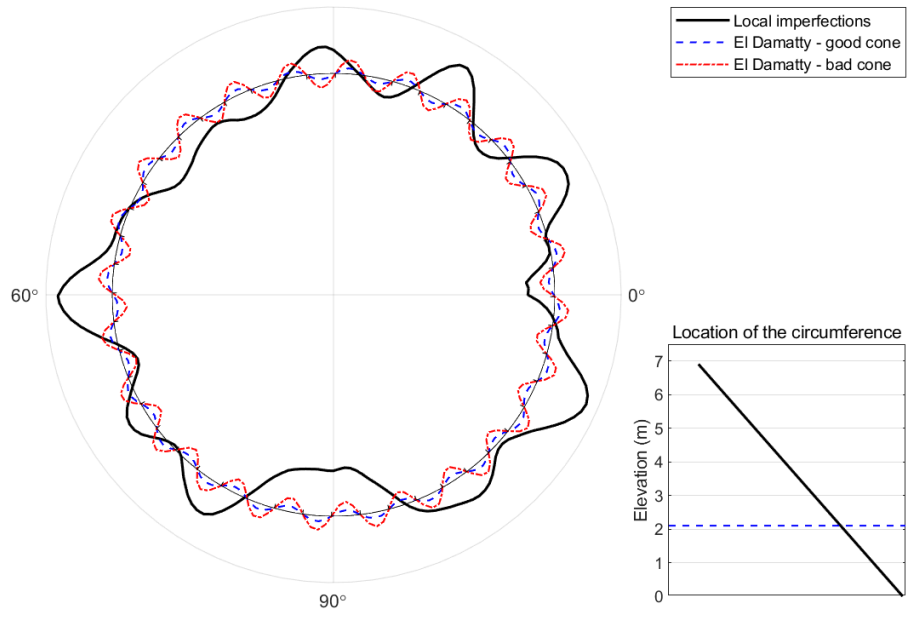
Circumferential imperfections at 0.9 m  
30°

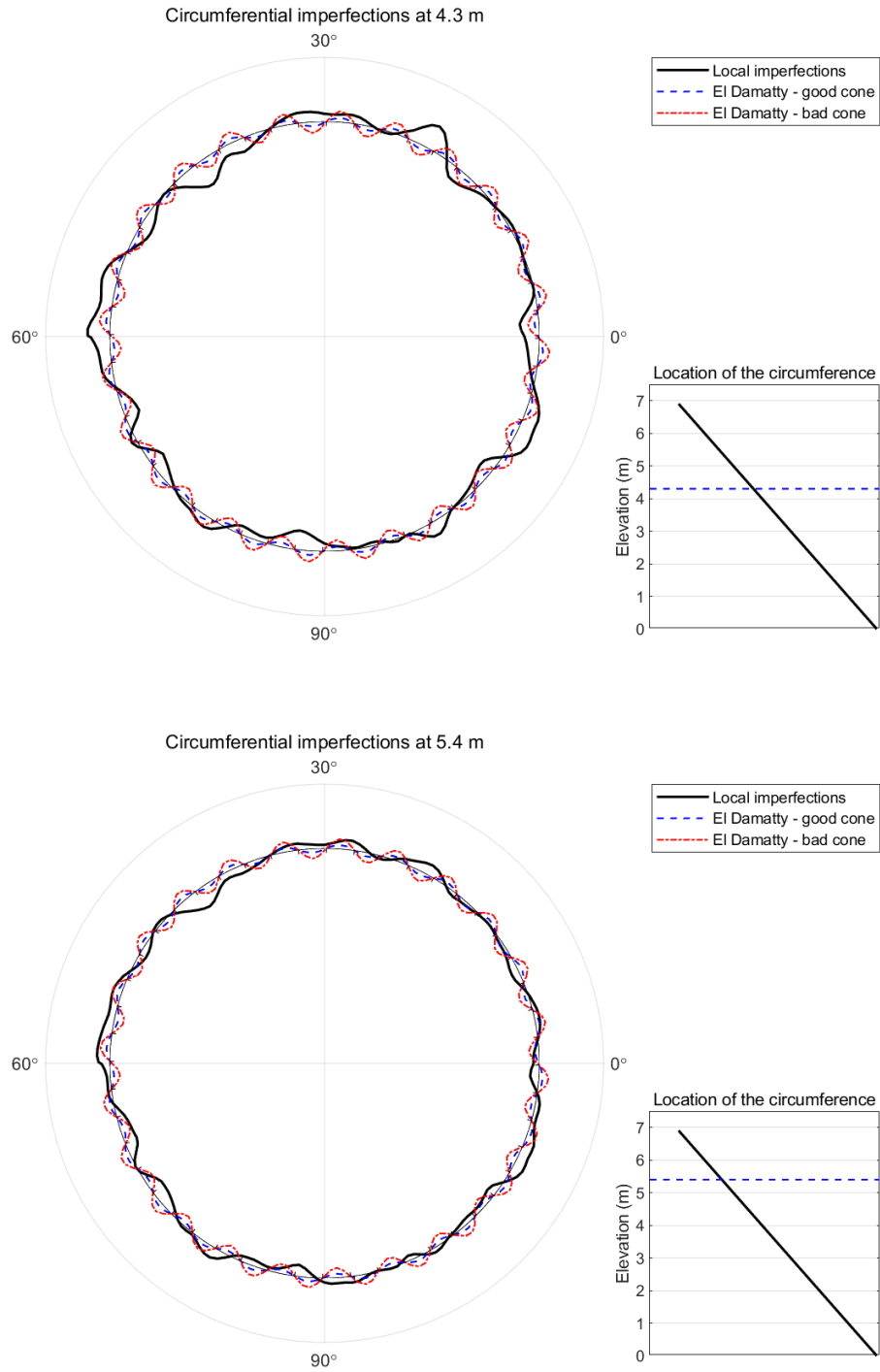


Circumferential imperfections at 1.7 m  
30°

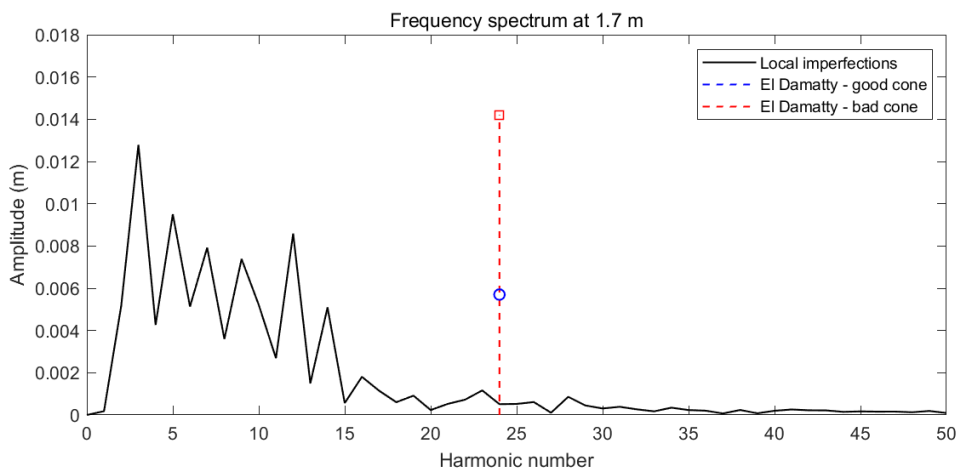
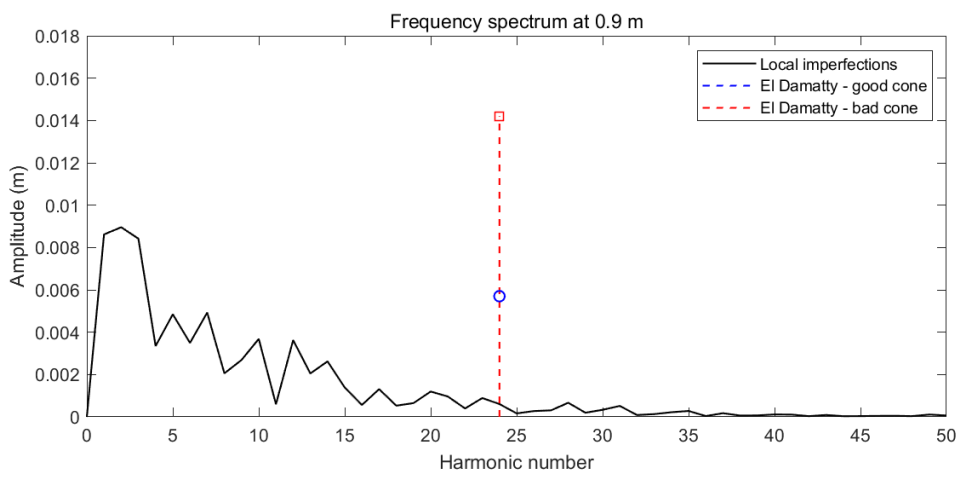
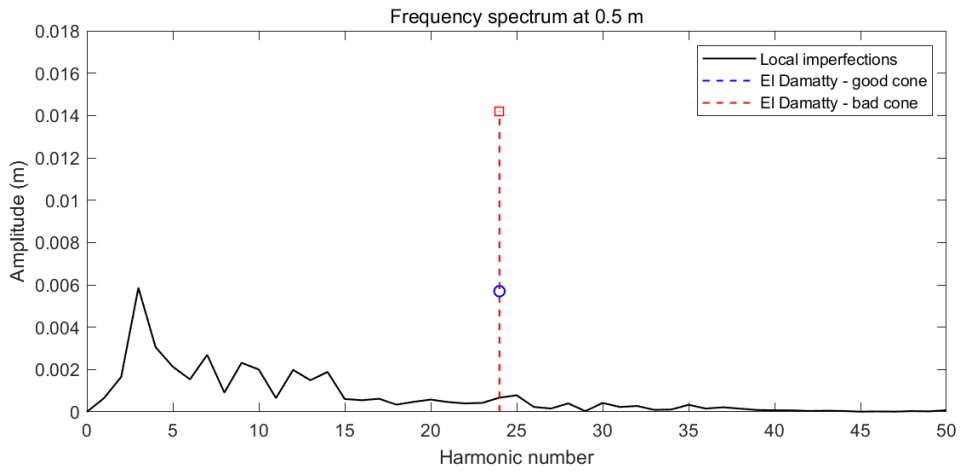


Circumferential imperfections at 2.1 m  
30°





**Figure A.14 Comparison of circumferential local imperfections with specifications by El Damatty et al. (2001) (40 times scaled)**



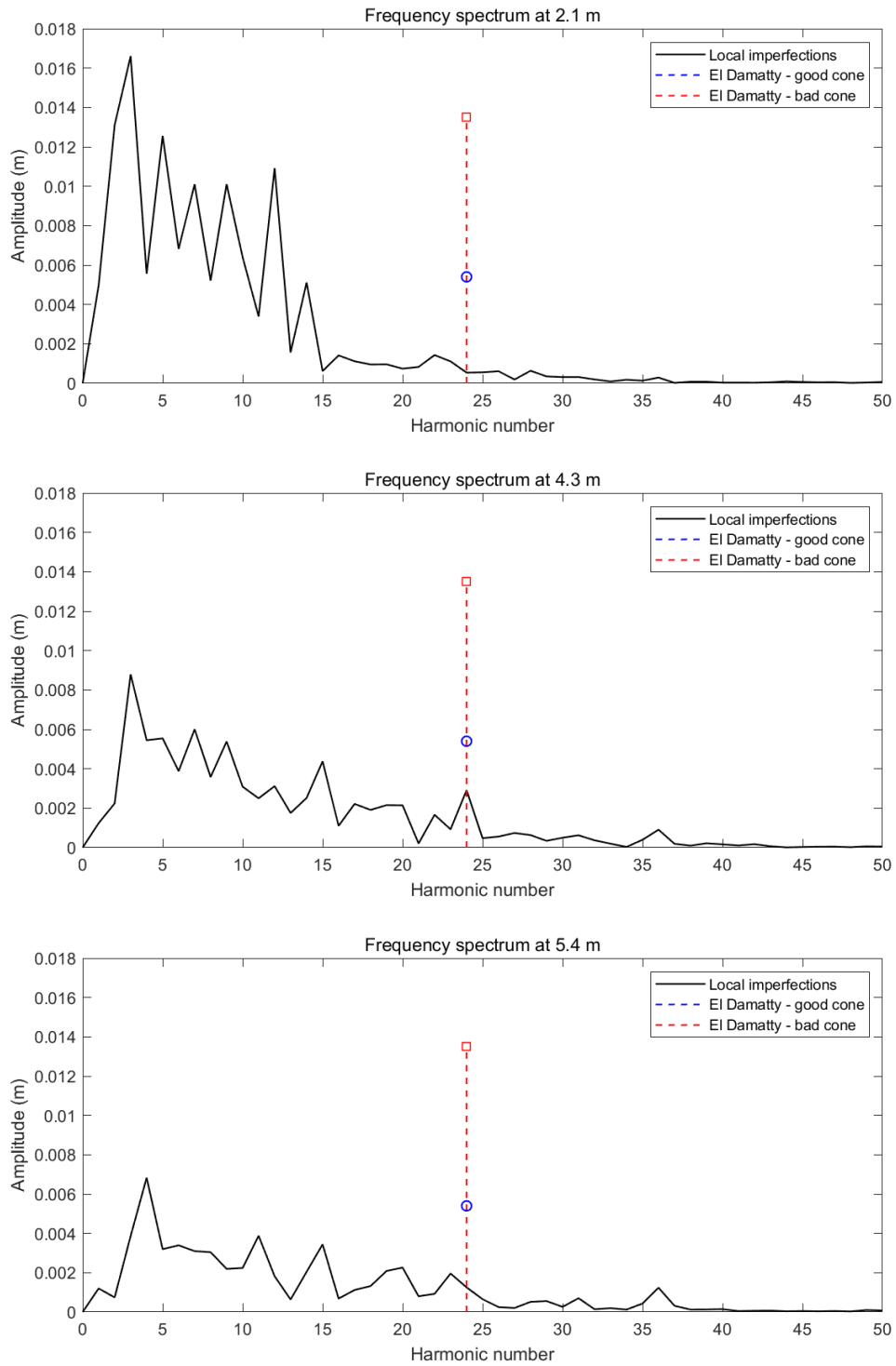
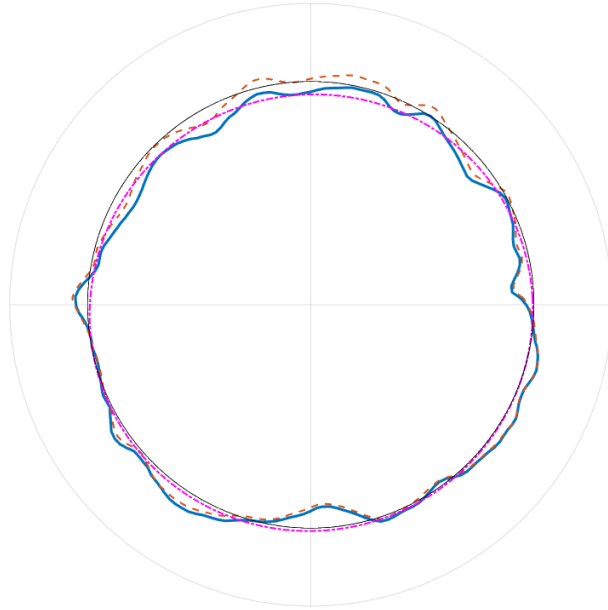
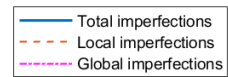
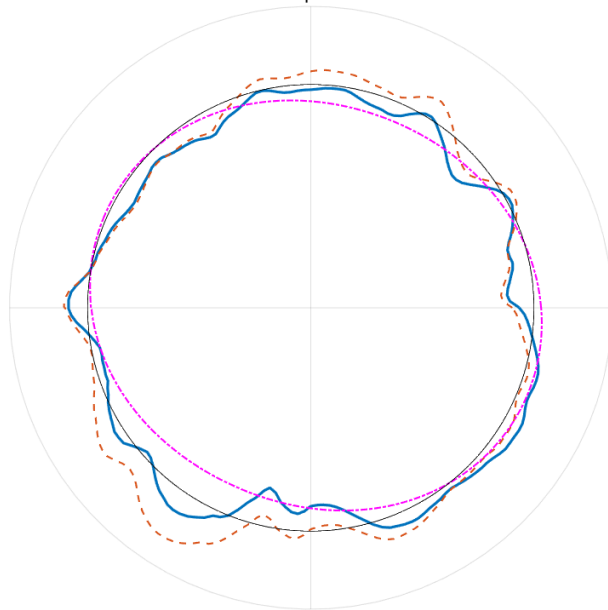


**Figure A.15 Evaluation of circumferential local imperfection wavelength with specifications by Vandepitte et al. (1982)**

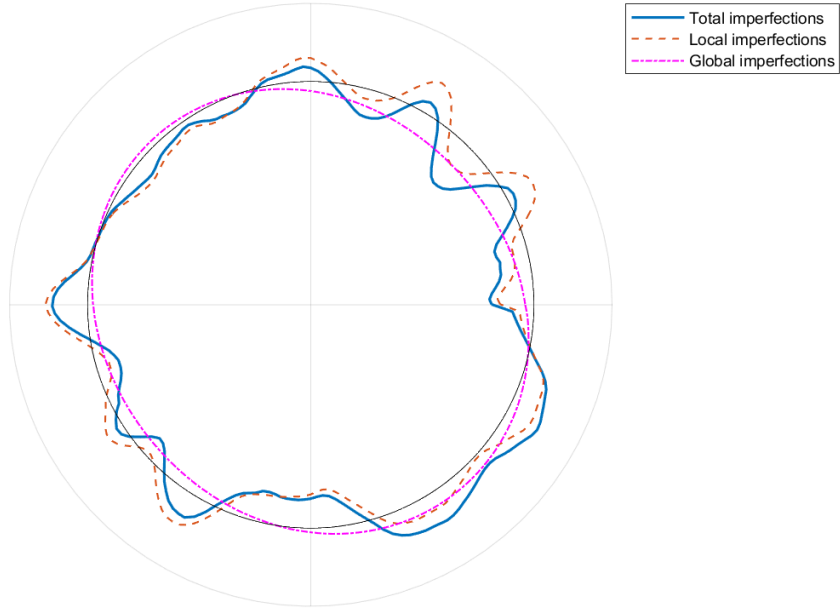
Circumferential imperfections at 0.5 m



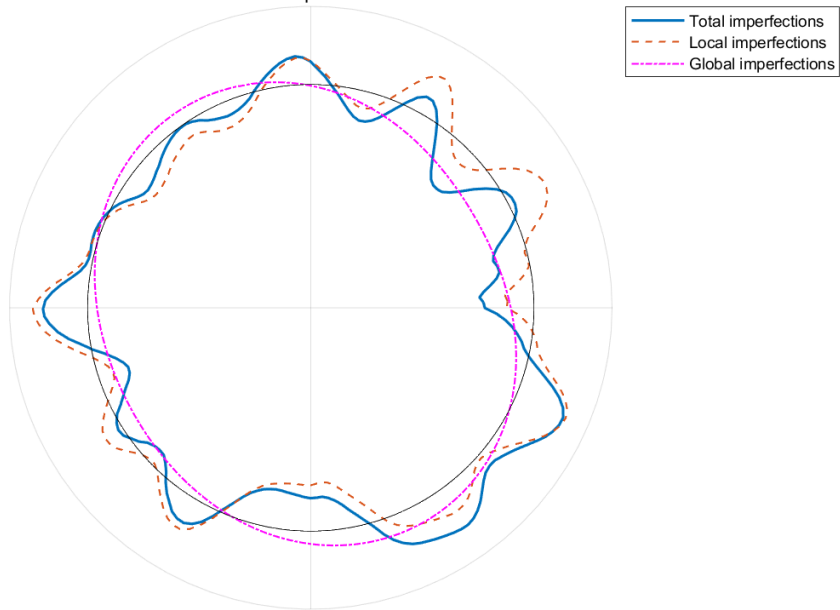
Circumferential imperfections at 0.9 m

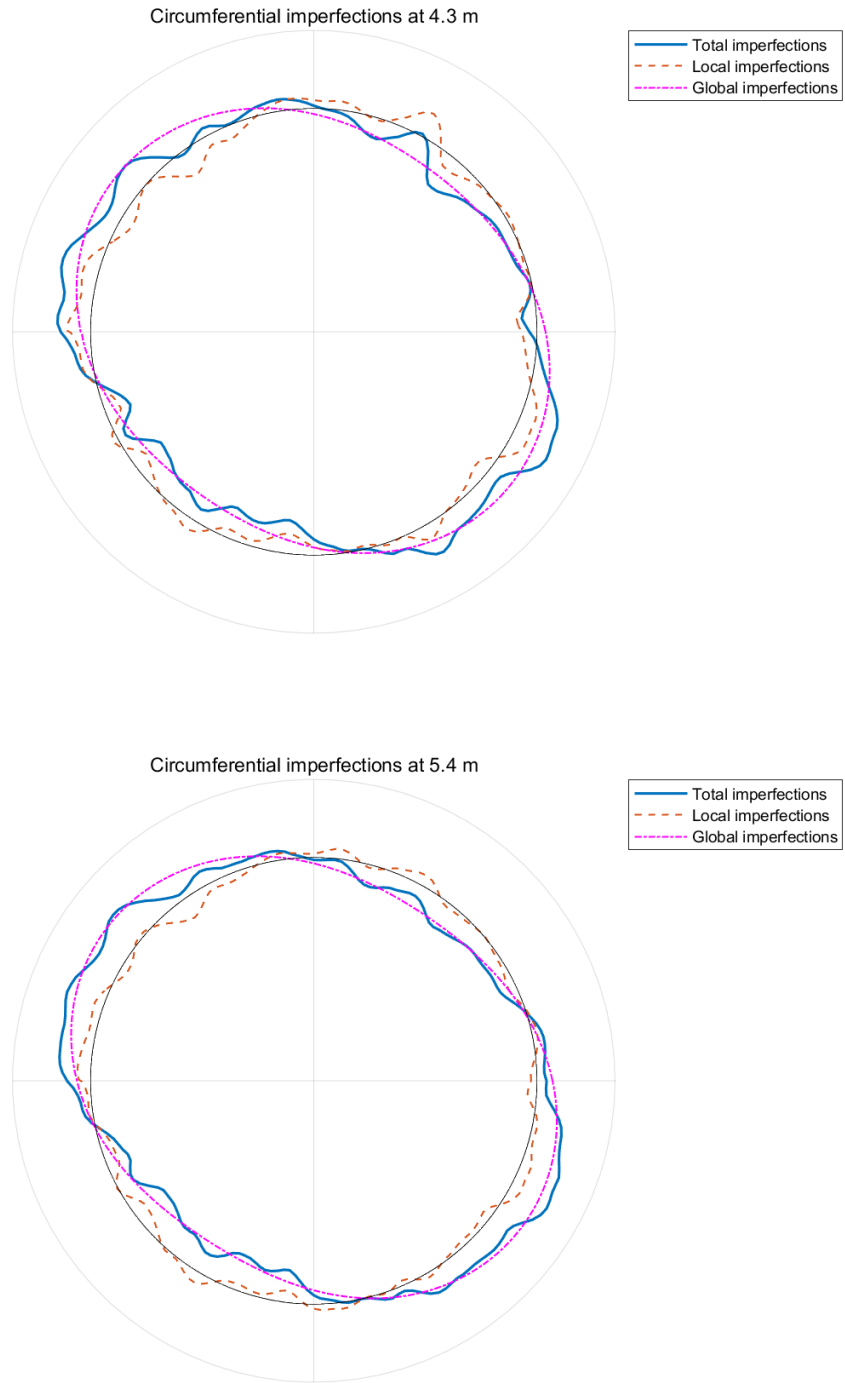


Circumferential imperfections at 1.7 m



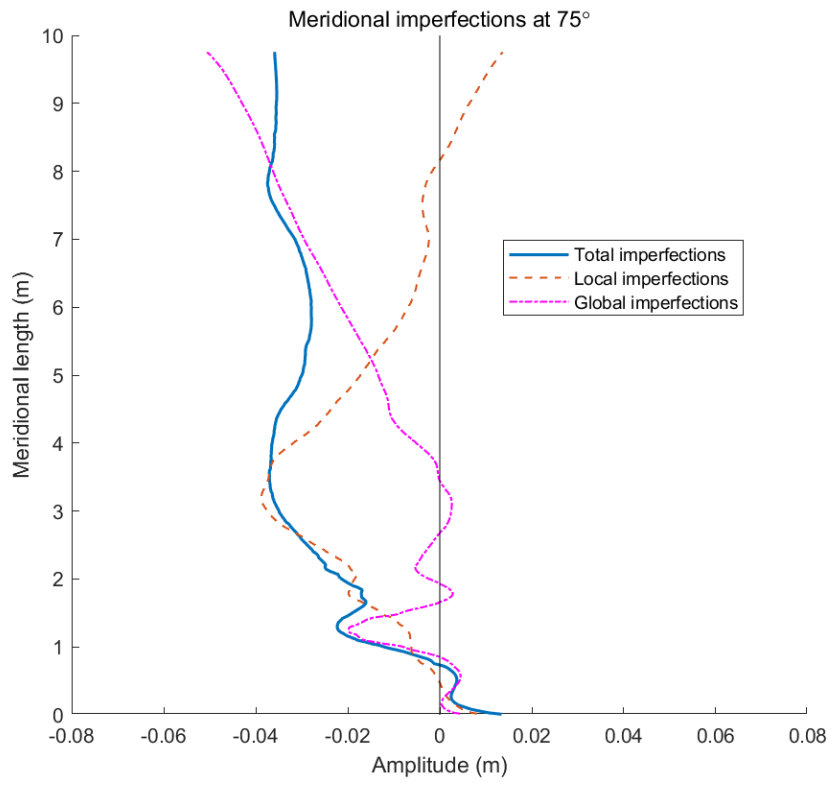
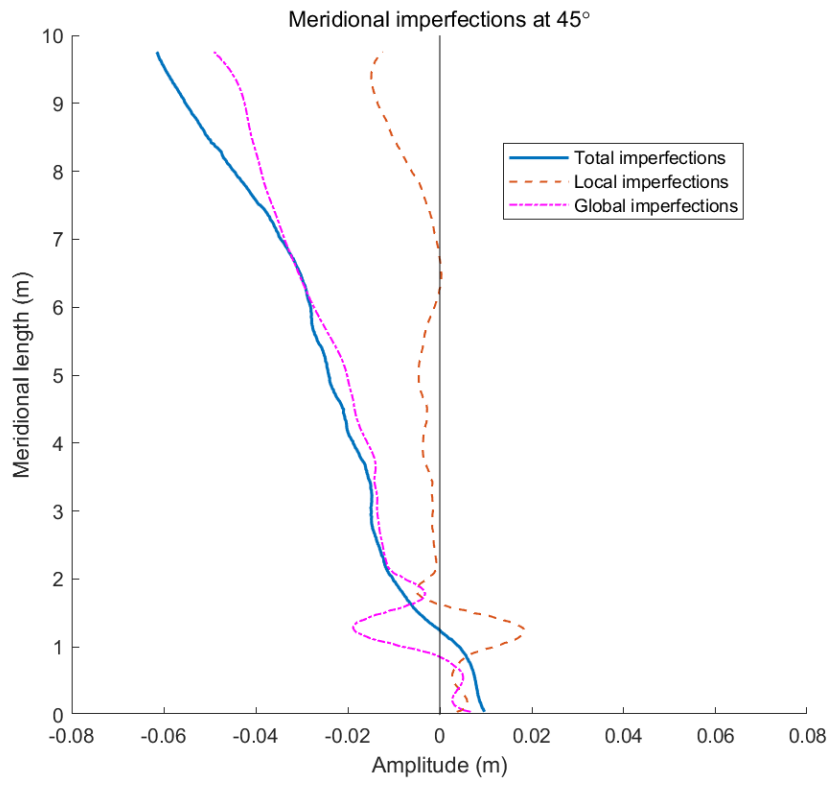
Circumferential imperfections at 2.1 m

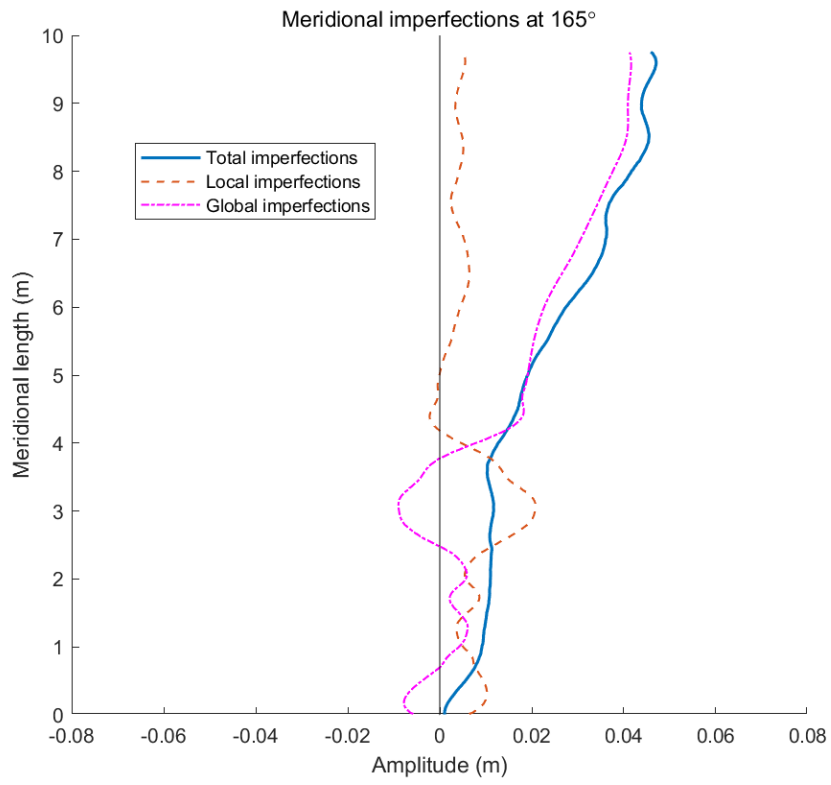
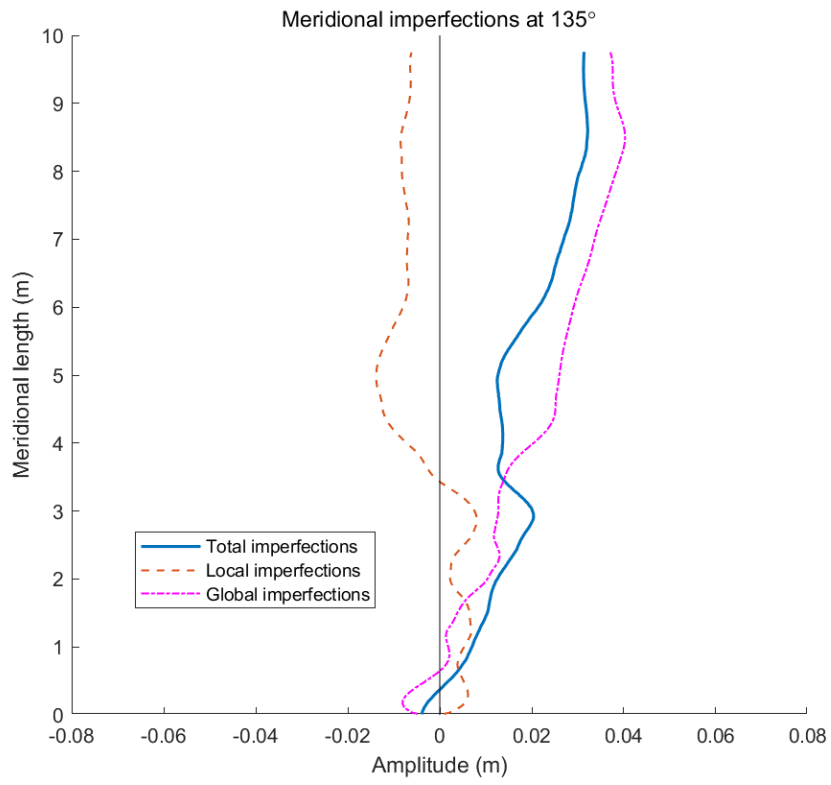


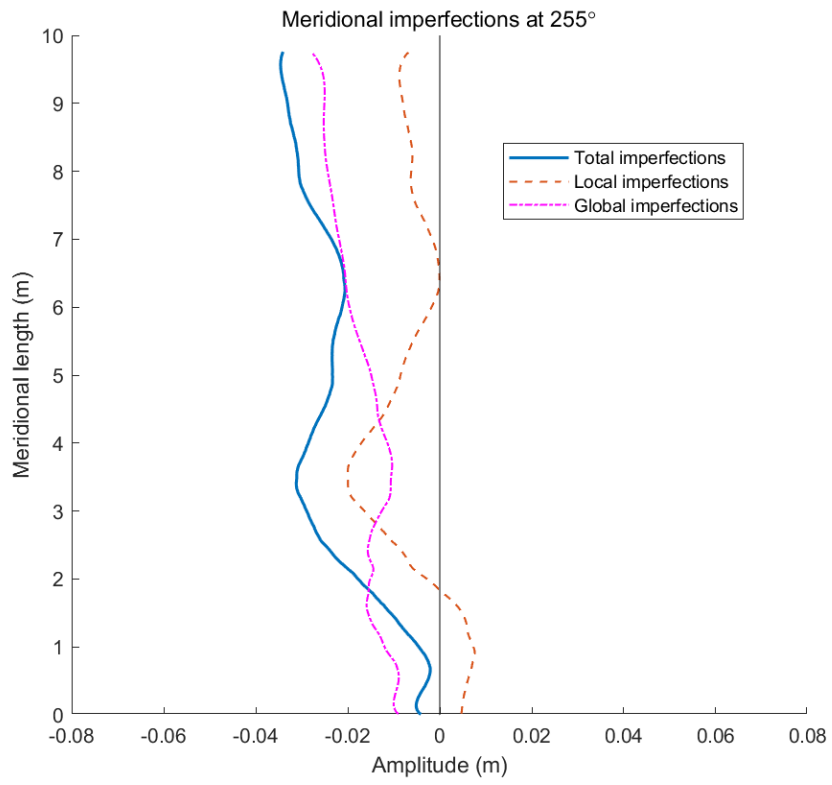
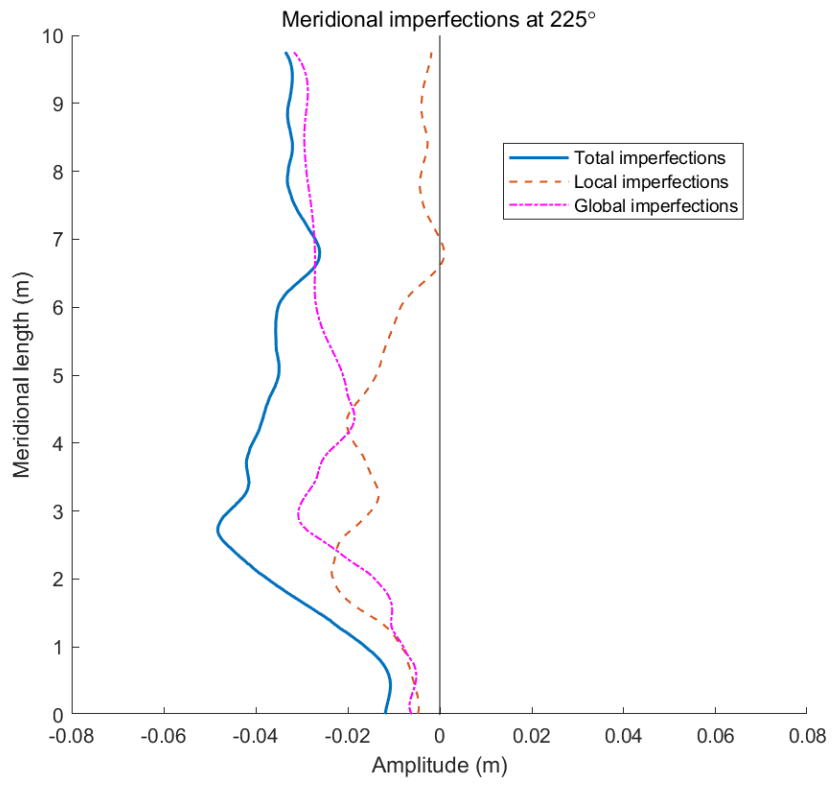


**Figure A.16 Circumferential imperfections from cloud data (40 times scaled)**









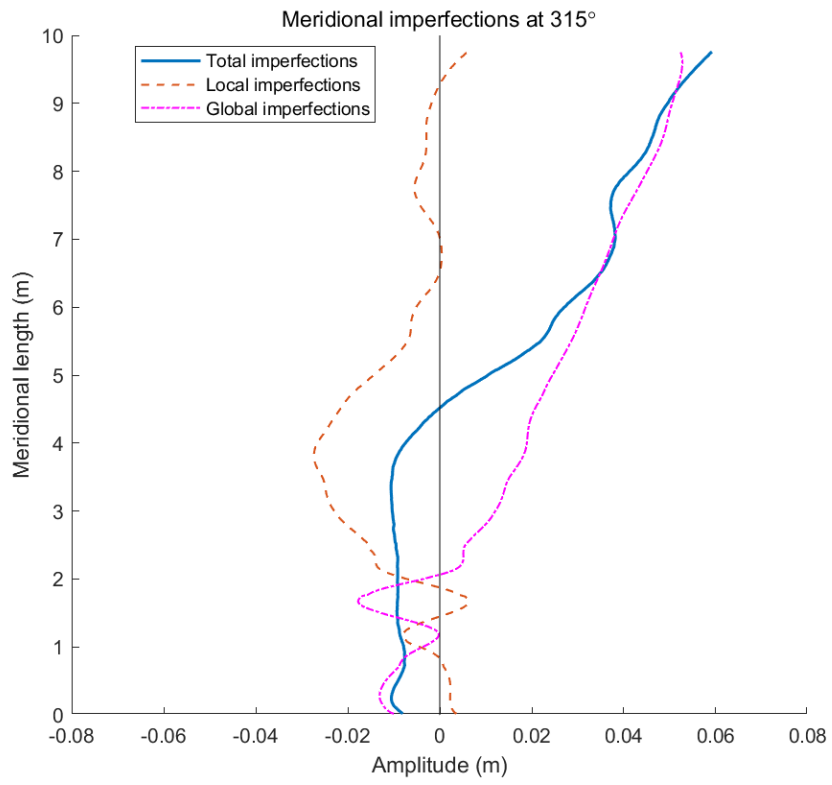


**Figure A.17 Meridional imperfections from cloud data**

# Curriculum Vitae

**Name:**

Haoyi Zhang

**Post-Secondary Education  
and Degrees:**

Harbin Institute of Technology  
Harbin, China  
2012-2016 BSc (Civil Engineering)

Western University  
London, Ontario, Canada  
2018-2020 MEng (Civil Engineering)

**Related Work Experience:**

Teaching Assistant  
Western University (2020)